

**FABRICATION OF COMPOSITE  
ELECTRODES AND SUPERCAPACITOR  
DEVICES**

By Yangshuai Liu, B.S., M.S.

A Thesis Submitted to the School of Graduate Studies in Partial Fulfillment of the  
Requirements for the Degree Doctor of Philosophy

Ph.D. Thesis, Yangshuai Liu      McMaster University, Materials Science & Engineering

DOCTOR OF PHILOSOPHY (2016)

McMaster University

Department of Materials Science & Engineering

Hamilton, Ontario

TITLE: Fabrication of composite electrodes and supercapacitor devices

AUTHOR: Yangshuai Liu, M.S., (Donghua University, Shanghai, China), B.S.,

(Donghua University, Shanghai, China)

SUPERVISOR: Igor Zhitomirsky, Distinguished Engineering Professor, Ph.D., P.Eng.

NUMBER OF PAGES: XXXVII, 238

## **Abstract**

Electrochemical supercapacitors (ECs) attract significant attentions for their unique characteristics of high power density, good cycling capability and low cost. This dissertation will focus on fabrication of composite materials for electrodes and devices of ECs. A conceptually new colloidal approach to the fabrication of metal oxide – multi-walled carbon nanotube (MWCNT) composites is proposed. The heterocoagulation of positively charged oxide nanoparticles and negatively charged MWCNT allows the fabrication of advanced nanocomposites with improved dispersion of individual components. The proof-of-principle was demonstrated by the fabrication of MnO<sub>2</sub>-MWCNT electrodes for ECs with excellent performance.

We proposed another novel concept based on electrostatic heterocoagulation of MnO<sub>2</sub>-MWCNT composites in aqueous environment. In this case, Benzyldimethylhexadecylammonium chloride (BAC) surfactant and caffeic acid (CA) were selected for adsorption and dispersion of MWCNT and MnO<sub>2</sub>, respectively, and this allowed the formation of stable aqueous suspensions of positively charged MWCNT and negatively charged MnO<sub>2</sub>. The asymmetric device showed high capacitance, high power-energy characteristics with enlarged voltage window of 1.8 V, good capacitance retention at high charge-discharge rates and cyclic stability.

A novel capacitive material BiMn<sub>2</sub>O<sub>5</sub> was firstly discovered and synthesized for ECs applications in our studies. The BiMn<sub>2</sub>O<sub>5</sub> nanocrystals were prepared by a hydrothermal

method. We demonstrated for the first time that  $\text{BiMn}_2\text{O}_5$  – MWCNT composite can be used as a new active material for positive electrodes of ECs. The composite electrode with high mass loading showed a capacitance of  $6.0 \text{ F cm}^{-2}$  ( $540 \text{ F cm}^{-3}$ ) at a scan rate of  $2 \text{ mV s}^{-1}$  and excellent capacitive behavior at high scan rates. As-fabricated device showed good cyclic stability in a voltage window of  $1.8 \text{ V}$  with energy density of  $13.0 \text{ Wh L}^{-1}$  ( $9.0 \text{ Wh kg}^{-1}$ ) and power density of  $3.6 \text{ kW L}^{-1}$  ( $2.5 \text{ kW kg}^{-1}$ ).

We firstly discovered that Poly[1-[4-(3-carboxy-4-hydroxyphenylazo)benzenesulfonamido]-1,2-ethanediyl, sodium salt] (PAZO) can be used as an universal dispersant for various materials and its thin film fabricated by electrophoretic deposition (EPD) exhibited photo-induced birefringence. Our new findings indicated that PAZO is good candidate for diverse materials dispersing because it contains diaromatic monomers with salicylate ligands, which can provide multiple adsorption sites for efficient adsorption on particles and impart electrical charges to the particles. Additionally, the use of PAZO polymer offers the advantages of improved steric stabilization.

We discovered that Celestine blue (CB) can be developed as an efficient dispersing agent for the nanoparticles. We found that CB includes a catechol ligand, which can provide CB adsorption on inorganic nanoparticles. The relatively large size of the CB molecules is beneficial for the electrosteric dispersion. The benefits of cathodic EPD for nanotechnology were demonstrated by the formation of nanostructured  $\text{MnO}_2$  films on commercial high surface area current collectors for energy storage in ECs.

Key words: manganese dioxide, carbon nanotubes, supercapacitor, colloids, dispersion, bismuth manganese oxide, hybrid, voltage window, activated carbon, EPD

## **Acknowledgement**

Undertaking this Ph. D has been a truly challenging and interesting experience for me and it would not have been possible to make it without the help and support from many people.

First and foremost, I would like to express my special appreciation and thanks to my supervisor Professor Igor Zhitomirsky (Ph.D., P.Eng) for his full support and encouragements during my Ph. D studies. Without his constant and brilliant advices and guidance on both of my research and career this Ph. D would not be achievable. I really appreciate your patience and tolerance and I also enjoy this experience working with you.

I would also like to thank my committee members, Dr. Shiping Zhu and Dr. Adrin Kitai for their professional advices and guidance on my research and career. I'd also like to thank them for the efforts they put into my proposal exam, comprehensive exam and committee meetings. I also want to thank Dr. Tony Petric, Dr. Oleg Rubel, Dmitri Malakhov and Dr. Hatem Zurob for participating my comprehensive exams and proposal exam and the tough questions they raised.

I hereby also sincerely thank the graduate course teachers Dr. Igor Zhitomirsky, Dr. Gu Xu, Dr. James Britten and Dr. Hatem Zurob. I obtained more than I thought from these courses.

I spent a lot of time on my experiment but I can't make it without help from many people. I really appreciate the help from Dr. James Britten and Victoria Jarvis for XRD training

and characterization. I also thank Steve Kornic and Megan Fair for FTIR and UV-Vis analysis. I thank Chris Butcher and Glynis de Silveira for their help on SEM characterization. Special thanks go to Dr. Gianluigi Botton and Dr. Guozhen Zhu for their help in TEM characterization. I also want to thank Dr. Changqing Xu and his Ph. D student Qianli Ma for their help in laser system setup.

My fellow groupmates help and support me so much, here I'd like to thank Dr. Xin Pang, Dr. Yaohui Wang, Yanchao Sun, Lijia Yang, Mustafa Ata, Dr. Yisong Su, Dr. Shilei Chen, Kaiyuan Shi, Yeling Zhu, Dan Luo, Tianshi Zhang, Patrick Wojtal and Cameron Wallar.

I'd like to gratefully thank my family members for their understanding and support of my Ph. D studies. Thank you for always believing in me and encouraging me to follow my dreams. And finally to my fiancée Linda Zhu, who has been by my side throughout the good and challenging time, and without whom, I would not have had the courage to embark on this journey.

## **Declaration of Academic Achievements**

This dissertation was used to fulfill the requirements of Ph.D. degree. The major research project was undertaken from September 2012 to April 2016.

The author of this dissertation and the supervisor are the major contributor to the presented materials. As the primary author, contributions included but not limited to literature review, proposal and approaches, experiments setup, materials synthesis, film preparation, electrochemical tests, materials characterization, data analysis, and journal article writing.

The results of this dissertation were published in 9 papers in peer-reviewed journals, which were listed below:

1. Yangshuai Liu, Kaiyuan Shi, Igor Zhitomirsky, Azopolymer triggered electrophoretic deposition of MnO<sub>2</sub>-carbon nanotube composites and polypyrrole coated carbon nanotubes for supercapacitors, *J. Mater. Chem. A*, 3 (2015) 16486 -16494.
2. Yangshuai Liu, Dan Luo, Mustafa S. Ata and Igor Zhitomirsky, Electrochemical supercapacitor based on multiferroic BiMn<sub>2</sub>O<sub>5</sub>, *J. Power Sources*, 284 (2015) 377-382
3. Yangshuai Liu and Igor Zhitomirsky, Universal dispersing agent for electrophoretic deposition of inorganic Materials with improved adsorption, triggered by chelating monomers, *J Colloid Interface Sci*, 462 (2015) 1-8
4. Yangshuai Liu, Dan Luo, Tianshi Zhang, Kaiyuan Shi, Patrick Wojtal, Cameron J. Wallar, Qianli Ma, Eric Gustave Daigle, Adrian Kitai, Chang-Qing Xu and Igor

Zhitomirsky, Film deposition mechanisms and properties of optically active chelating polymer and composites, *Colloids and Surfaces A*, 487 (2015) 17-25.

5. Yangshuai Liu, Dan Luo, Mustafa S. Ata, Tianshi Zhang, Cameron J. Wallar, Igor Zhitomirsky, Aqueous electrostatic dispersion and heterocoagulation of multiwalled carbon nanotubes and manganese dioxide for the fabrication of supercapacitor electrodes and devices, *RSC Adv*, 4 (2014) 45481-45489.

6. Y.Liu, M.S.Ata, K.Shi, G.-Z.Zhu, G.Botton and I.Zhitomirsky, Surface modification and cathodic electrophoretic deposition of ceramic materials and composites using Celestine blue dye, *RSC Adv*, 4 (2014) 29652-29659.

7. Yangshuai Liu, Kaiyuan Shi, and Igor Zhitomirsky, New colloidal route for electrostatic assembly of oxide nanoparticle-carbon nanotube composites, *Colloids and Surfaces A*, 446 (2014) 15-22.

8. Yaohui Wang, Yangshuai Liu and Igor Zhitomirsky, Surface modification of MnO<sub>2</sub> and carbon nanotubes using organic dyes for nanotechnology of electrochemical supercapacitors, *J. Mater. Chem. A*, 1 (2013) 12519-12526.

9. M. S. Ata, Y. Liu and I. Zhitomirsky, A review of new methods of surface chemical modification, dispersion and electrophoretic deposition of metal oxide particles, *RSC Adv.*, 4 (2014) 22716-22732.

## Table of contents

Abstract .....	III
Acknowledgement .....	V
Declaration of Academic Achievements.....	VII
Table of contents.....	IX
List of Figures .....	XV
List of Tables .....	XXXI
List of Abbreviations and Symbols.....	XXXII
Chapter 1 Introduction .....	1
1.1 Global energy issue and next-generation energy storage devices .....	1
1.2 Comparison of different energy storage devices .....	3
1.3 Major objectives and achievements of this work .....	4
References.....	5
Chapter 2 Literature review .....	7
2.1 Development and advantages of electrochemical supercapacitors.....	7
2.2 Categories of supercapacitors .....	8
2.2.1 Electrochemical double-layer supercapacitors .....	8
2.2.1.1 Energy storage mechanism for EDLCs .....	8
2.2.1.2 Models of the Double Layer .....	11
2.2.1.3 Equivalent circuit representation of double-layer electrical behavior .....	15
2.2.2 Faradaic (pseudo)supercapacitors.....	16

2.2.2.1 Origin of Pseudocapacitance .....	16
2.2.2.2 Types of pseudocapacitance .....	17
2.2.2.3 Equivalent circuit representation of pseudocapacitor behavior .....	22
2.2.3 Hybrid electrochemical capacitors .....	23
2.2.3.1 Symmetric hybrids.....	24
2.2.3.2 Asymmetric hybrids .....	26
2.2.4 Summary of different types of supercapacitors .....	28
2.3 Materials for supercapacitors.....	29
2.3.1.1 EDLCs based on AC (activated carbon).....	30
2.3.1.2 Electrodes based on carbon nanotubes (CNTs).....	32
2.3.1.3 Summary of data for electrodes based on carbon materials .....	34
2.3.2 Redox-based materials.....	34
2.4 Dispersion and electrophoretic deposition (EPD) .....	43
2.4.1 Categorization and mechanism of dispersion .....	43
2.4.1.1 Electrostatic stabilization.....	44
2.4.1.2 Polymeric stabilization .....	49
2.4.2 Electrophoretic deposition (EPD) and dispersants .....	51
References.....	57
Chapter 3 Problem statements and objectives .....	76
3.1 Dispersion of carbon nanotubes and MnO <sub>2</sub> .....	76
3.1.1 Challenges on dispersion of CNTs .....	76
3.1.2 Difficulties in fabrication of MnO <sub>2</sub> -CNT composite.....	78

3.2 Low voltage window for symmetric supercapacitor .....	79
3.3 Low mass loading of MnO <sub>2</sub> -CNTs electrode .....	80
3.4 Objectives .....	81
References.....	83
Chapter 4 Experimental procedures.....	88
4.1 Materials synthesis.....	88
4.2 Electrophoretic deposition and adhesion characterization .....	92
4.3 Materials characterization techniques.....	93
4.4 Electrode fabrication procedure.....	94
4.4.1 Electrode fabrication using EPD .....	94
4.4.2 Electrodes fabrication based on heterocoagulation .....	95
4.4.3 Electrodes fabrication based on colloidal route and slurry.....	96
4.4.4 Fabrication of activated carbon-carbon black for negative electrode.....	97
4.5 Cell fabrication .....	97
4.6 Electrochemical characterization.....	98
4.6.1 Cyclic voltammetry .....	99
4.6.2 Electrochemical Impedance Spectroscopy .....	100
4.6.3 Galvanostatic charge–discharge .....	101
References.....	102
Chapter 5. Colloidal route for electrostatic assembly of MnO <sub>2</sub> -MWCNTs composites for supercapacitors.....	103
5.1 Proposed approach based on electrostatic heterocoagulation in ethanol.....	103

5.2 Charging and dispersion of MWCNTs.....	104
5.2.1 Adsorption mechanism, involving $\pi$ - $\pi$ interaction .....	104
5.2.2 EPD and characterization of MWCNTs with CS .....	105
5.3 Charging and dispersion of MnO <sub>2</sub> .....	107
5.3.1 Mechanism for charging and dispersion of MnO <sub>2</sub> .....	107
5.3.2 EPD and characterization of MnO <sub>2</sub> with PE.....	109
5.4 Fabrication and characterization of MnO <sub>2</sub> -MWCNTs composite electrodes.....	112
5.4.1 Morphology characterization.....	112
5.4.2 Electrochemical characterization for single electrode.....	113
5.4.3 Electrochemical characterization for device.....	118
5.5 Conclusions .....	119
References.....	121
Chapter 6 Aqueous electrostatic dispersion and heterocoagulation of MnO <sub>2</sub> -MWCNTs composite for supercapacitor .....	125
6.1 New approach based on electrostatic heterocoagulation in aqueous suspension	125
6.2 Molecular structure comparison of BAC and CTAB .....	126
6.3 Adsorption mechanism of BAC on MWCNT .....	128
6.4 Adsorption mechanism of CA on MnO <sub>2</sub> particles.....	130
6.5 Formation of MnO <sub>2</sub> -MWCNT composite and morphology studies .....	132
6.6 Electrochemical characterization of composite electrode .....	134
6.7 Electrochemical characterization for device.....	138
6.8 Conclusions .....	142

References.....	144
Chapter 7. BiMn <sub>2</sub> O <sub>5</sub> -MWCNTs composite for supercapacitor .....	147
7.1 BiMn <sub>2</sub> O <sub>5</sub> as a capacitive material .....	147
7.2 Phase and morphology characterization of BiMn <sub>2</sub> O <sub>5</sub> .....	148
7.3 Celestine blue as dispersing agent .....	149
7.4 Electrochemical characterization for composite electrodes .....	150
7.5 Electrochemical characterization of a device .....	153
7.6 Conclusions .....	158
References.....	159
Chapter 8 Azopolymer triggered electrophoretic deposition of MnO <sub>2</sub> -MWCNTs composites for supercapacitors .....	163
8.1 Motivation and origin .....	163
8.2 Materials synthesis and morphology characterization.....	164
8.3 Dispersion mechanism and stability characterization.....	167
8.4 EPD and adsorption characterization.....	170
8.4 Electrode fabrication and morphology characterization.....	175
8.5 Electrochemical characterization.....	176
8.6. Conclusions .....	181
References.....	183
Chapter 9 Fabrication and testing of asymmetric devices based on manganese dioxide positive electrode and iron oxide negative electrode formed by EPD on rGO.....	186
9.1 Synthesis of materials and current collectors .....	186

9.2. Electrochemical testing of electrodes and devices .....	191
9.3 Conclusions .....	201
References.....	202
Chapter 10 Functional properties of PAZO and fabrication of composites using PAZO as an universal dispersing agent .....	203
10.1 PAZO as universal dispersant for optics and supercapacitor application.....	203
10.2 EPD of PAZO thin films from different solvents.....	204
10.3 Adsorption and phase characterization of different materials with PAZO.....	209
10.4 Electrochemical characterization.....	213
10.5 Conclusion .....	214
References.....	216
Chapter 11 Proposed approach for dispersing MnO <sub>2</sub> using Celestine blue .....	218
11.1 Motivation of using Celestine blue.....	218
11.2 Materials synthesis & morphology characterization .....	219
11.3 EPD and Adsorption mechanism.....	220
11.4 Morphology and adsorption characterization .....	223
11.5 Electrochemical characterization.....	228
11.6 Conclusions .....	231
References.....	232
Conclusions.....	235
Future works .....	237

## List of Figures

Fig. 1.1 Sketch of Ragone plot for various energy storage and conversion devices. The indicated areas are rough guide lines. ....	3
Fig. 2.1 Schematic structure and principles of a single cell EDLC .....	9
Fig. 2.2 Models of the double layer: (a) Helmholtz model, (b) Gouy-Chapman point charge model, (c) Stern model with thermal distribution, combining Helmholtz model and Gouy-Chapman models .....	11
Fig. 2.3 an equivalent circuit of Stern model, consisted of $C_H$ and $C_{diff}$ .....	14
Fig. 2.4 Equivalent circuit for a. ideally polarized electrode and b. electrode with a Faradaic leakage resistance .....	16
Fig. 2.5 Schematic of intercalation pseudocapacitance based on $Nb_2O_5$ electrodes .....	18
Fig. 2.6 Schematic of redox pseudocapacitance based on $RuO_2$ electrodes .....	19
Fig. 2.7 Schematic of underpotential deposition based on Au electrodes .....	21
Fig. 2.8 Equivalent circuit of pseudocapacitance .....	22
Fig. 2.9 Ragone plot of three major electrochemical energy storage devices. Time constants are shown in dashed line, by dividing the specific energy by the specific power .....	24
Fig. 2.10 Configuration of symmetric supercapacitor .....	25
Fig. 2.11 Configuration of asymmetric supercapacitor .....	26
Fig. 2.12 Normalized capacitance change vs the pore size of the CDC samples prepared at different temperatures .....	31

Fig 2.13. Various conducting polymer structures. A, polypyrrole (PPy), B, poly(3,4-ethylenedioxythiophene) (PEDOT), C, polythiophene (PTh), D, polyaniline (PAni).....35

Fig. 2.14 The charge-discharge process of PPy .....37

Fig. 2.15 Cyclic voltammetry for a MnO<sub>2</sub>-electrode cell in mild aqueous electrolyte (0.1 M K<sub>2</sub>SO<sub>4</sub>) shows the successive multiple surface redox reactions leading to the pseudo-capacitive charge storage mechanism.....39

Fig. 2.16 Possible strategies to improve both energy and power densities for ECs. a) carbon activation and b) decorating with pseudo-capacitive materials on porous carbon; c) highly ordered high surface area carbon nanotubes and d) deposit of pseudo-capacitive materials on carbon nanotubes.....41

Fig. 2.17 Cyclic voltammograms in (A) a three-electrode cell using MnO<sub>2</sub> or activated carbon as working electrode, (B) an asymmetric MnO<sub>2</sub>/activated carbon cell.....42

Fig. 2.18 Electrical double layer and potential drop around a colloidal particle .....45

Fig. 2.19 Configuration of two colloidal particles in an ionic electrolyte suspension.....47

Fig. 2.20 Energy variation with distance between two colloidal particle surfaces.....49

Fig. 2.21 Schematics of steric stabilization.....50

Fig. 2.22 Schematics of depletion stabilization .....51

Fig. 2.23 Schematics of electrosteric stabilization: (a) charged particles with nonionic polymers; (b) polyelectrolytes attached to uncharged particles.....51

Fig. 2.24 Schematic of electrophoretic deposition.....52

Fig. 2.25 Adsorption mechanism of catechol group on metal surface, structure of dopamine and dopa .....54

Fig. 2.26 a. molecular structure of PAZO and b. attaching mechanism of PAZO to inorganic particle.....	55
Fig 3.1. A. Polymer wrapping on surface of CNTs, B. covalent sidewall functionalization on CNTs .....	78
Fig. 4.1 Schematic of MnO <sub>2</sub> particles synthesis procedure .....	88
Fig. 4.2. Hydrothermal process for producing BiMn <sub>2</sub> O <sub>5</sub> nanocrystals .....	89
Fig. 4.4 Schematic of MnO <sub>2</sub> -MWCNTs composite electrode fabrication based on herocoagulation.....	96
Fig. 4.5 Schematic of coin cell fabrication procedure .....	98
Fig. 4.6 38 PARSTAT 2273 Potentiostat (A) and three-electrodes testing system (B).....	99
Fig. 5.1 Schematic configuration of colloidal route for fabrication of MnO <sub>2</sub> -CNT composite electrode in ethanol.....	103
Fig 5.2 Mechanism of CS charging and dispersing MWCNTs in ethanol suspension....	104
Fig. 5.3 A deposit mass versus deposition time at CS concentration of 1 g L <sup>-1</sup> for 1 g L <sup>-1</sup> MWCNT suspension in ethanol at a deposition voltage of 100 V; (B) SEM image of deposited MWCNT film .....	106
Fig. 5.4 (A) FTIR and (B) UV-vis spectra for (a) as-received CS, (b) as-received MWCNT and (c) deposited MWCNT .....	106
Fig. 5.5 Chemical structures of (a) mono- and (b) di-alkyl phosphate esters .....	108
Fig. 5.6 Mechanism of PE charging and dispersing MnO <sub>2</sub> .....	109
Fig. 5.7 (A,B,C) Deposit mass of MnO <sub>2</sub> from 10 g L <sup>-1</sup> MnO <sub>2</sub> suspensions versus (A) PE concentration in the suspensions at a deposition voltage of 40 V and deposition time of 2	

min, (B) deposition time at a deposition voltage of 40V and PE concentration of 1 g L<sup>-1</sup>, inset shows MnO<sub>2</sub> deposit on a stainless steel foil, (C) deposition voltage at PE concentration of 1 g L<sup>-1</sup> and deposition time of 1 min and (D) current versus time dependence at a voltage of 100 V for (a) 1 g L<sup>-1</sup> PE solution (b) 10g L<sup>-1</sup> MnO<sub>2</sub> suspension (c) 10g L<sup>-1</sup> MnO<sub>2</sub> suspension, containing 1g L<sup>-1</sup> PE..... 110

Fig. 5.8 Fabrication of MnO<sub>2</sub>-MWCNT composite by mixing of MnO<sub>2</sub> suspension, containing PE dispersant, and MWCNT suspension, containing CS dispersant ..... 112

Fig. 5.9 SEM images of (A) MnO<sub>2</sub>, (B) MWCNT and (C,D) composite MnO<sub>2</sub>-MWCNT composite, prepared using PE and CS, at different magnifications..... 113

Fig. 5.10 CVs for electrodes with mass loading of 40 mg cm<sup>-2</sup>, prepared (A,B) using PE and CS dispersants and (C,D) without dispersants, containing (A,C) 83% MnO<sub>2</sub>, 15% MWCNT and 2% PVB and (B,D) 78% MnO<sub>2</sub>, 20% MWCNT and 2% PVB at scan rates of (a) 2, (b)5, (c)10 and (d) 20 mV s<sup>-1</sup> ..... 114

Fig. 5.11 (A) C<sub>s</sub> and C<sub>m</sub>, calculated from the CV data, (B) Nyquist plot of complex impedance and components of complex capacitance (C) C<sub>s</sub>' and (D) C<sub>s</sub>" versus frequency for electrodes with mass loading of 40 mg cm<sup>-2</sup>, prepared (a,b) using PE and CS dispersants and (c,d) without dispersants, containing (a,c) 83% MnO<sub>2</sub>, 15% MWCNT and 2% PVB and (b,d) 78% MnO<sub>2</sub>, 20% MWCNT and 2% PVB..... 115

Fig. 5.12 Capacitance retention of MnO<sub>2</sub> -MWCNT composite electrode, containing 15% MWCNT, prepared using PE and CS dispersants at a scan rate of 50 mV s<sup>-1</sup> in 0.5 M Na<sub>2</sub>SO<sub>4</sub> electrolyte ..... 117

Fig. 5.13. Galvanostatic charge-discharge behavior of a hybrid coin cell (A) at current

densities of (a) 2, (b) 3, (c) 4, (d) 7 and (e) 10 mA cm<sup>-2</sup> and (B) multiple cycling at 10 mA cm<sup>-2</sup>, inset shows a bulb powered by a coin cell..... 119

Fig 6.1 Procedure of fabrication of MnO<sub>2</sub>-MWCNT composite using CA and BAC as dispersants, for MnO<sub>2</sub> and MWCNT, respectively ..... 126

Fig. 6.2. Molecular structures of (A) BAC and (B) caffeic acid (CA) ..... 127

Fig. 6.3 Comparison of chemical structures of (BAC) and hexadecyltrimethylammonium CTAB ..... 128

Fig. 6.4 Deposit mass for 1 g L<sup>-1</sup> MWCNT suspension in water at a deposition voltage of 20 V: (A) versus BAC concentration at a deposition time of 3 min and (B) versus deposition time at BAC concentration of 1 g L<sup>-1</sup> ..... 129

Fig. 6.5 Comparison of the deposition yield obtained from 1 g L<sup>-1</sup> MWCNT suspension in water at a deposition voltage of 20 V and deposition time of 3 min: (a) versus BAC concentration and (b) versus CTAB concentration..... 130

Fig. 6.6 Deposit mass for 4 g L<sup>-1</sup> MnO<sub>2</sub> suspension in water at a deposition voltage of 20 V: (A) versus CA concentration at a deposition time of 3 min and (B) versus deposition time for CA concentration of 0.4 g L<sup>-1</sup>..... 132

Fig. 6.7 Fabrication of MnO<sub>2</sub>-MWCNT composite by dispersion of MWCNT using cationic BAC, dispersion of MnO<sub>2</sub> using anionic CA and electrostatic heterocoagulation ..... 133

Fig. 6.8 SEM images of MnO<sub>2</sub>-MWCNT composite, prepared with (A) and without (B) CA and BAC ..... 133

Fig. 6.9 CVs for electrodes with mass loading of  $40 \text{ mg cm}^{-2}$ , prepared (A, B and C) without CA and BAC dispersants and (D, E and F) with dispersants, containing (A and D) 85%  $\text{MnO}_2$ , 15% MWCNT, (B and E) 80%  $\text{MnO}_2$ , 20% MWCNT and (C and F) 75%  $\text{MnO}_2$ , 25% MWCNT at scan rates of (a) 2, (b) 5, (c) 10 and (d)  $20 \text{ mV s}^{-1}$  in 0.5 M aqueous  $\text{Na}_2\text{SO}_4$  electrolyte .....134

Fig. 6.10  $C_s$  and  $C_m$ , calculated from the CV data, for different electrodes with mass loading of  $40 \text{ mg cm}^{-2}$ : (a) pure  $\text{MnO}_2$  and (b-g) different composite electrodes, prepared (b, c and d) without dispersants, (e, f and g) using BAC and CA dispersants, containing (b and e) 85%  $\text{MnO}_2$  and 15% MWCNT, (c and f) 80%  $\text{MnO}_2$  and 20% MWCNT and (d and g) 75%  $\text{MnO}_2$  and 25% MWCNT.....135

Fig. 6.11 Nyquist plot of complex impedance and components of complex capacitance of (A) pure  $\text{MnO}_2$  and (B) different composite electrodes, (C)  $C_s'$  and (D)  $C_s''$  versus frequency for electrodes with mass loading of  $40 \text{ mg cm}^{-2}$ , prepared (a) pure  $\text{MnO}_2$ , (b, c and d) without dispersants, (e, f and g) using CA and BAC dispersants and containing (b and e) 85%  $\text{MnO}_2$ , 15% MWCNT, (c and f) 80%  $\text{MnO}_2$ , 20% MWCNT and (d and g) 75%  $\text{MnO}_2$ , 25% MWCNT .....137

Fig. 6.12 CVs for two-electrode, which is composed by a  $\text{MnO}_2$ -MWCNT electrode, containing 80%  $\text{MnO}_2$  and 20% MWCNT and a AC-CB electrode with 85% PICA and 10% CB (5% binder). Scan rate are  $2 \text{ mV s}^{-1}$  (a),  $5 \text{ mV s}^{-1}$  (b),  $10 \text{ mV s}^{-1}$  (c), and  $20 \text{ mV s}^{-1}$  (d) in 0.5 M  $\text{Na}_2\text{SO}_4$  electrolyte.....138

Fig. 6.13 Frequency dependencies of components of complex capacitance (A)  $C_s'$ ,  $C_m'$  and (B)  $C_s''$ ,  $C_m''$ , calculated from the impedance data for the two electrode asymmetric cell,

containing a positive MnO<sub>2</sub>-MWCNT electrode (80% MnO<sub>2</sub> and 20% MWCNT) and a negative AC-CB electrode (90 % AC and 10% CB). ..... 139

Fig. 6.14 (A) Galvanostatic charge–discharge behavior of an asymmetric coin cell at currents of (a) 1, (b) 2, (c) 3, (d) 4, (e) 5, (f) 6, (g) 8, and (h) 10 mA, (B) cell capacitance C<sub>s</sub> and C<sub>m</sub> versus current, inset shows coin cells. .... 140

Fig. 6.15 (A) Ragone plot and (B) capacitance retention versus cycle number for an asymmetric coin cell, inset shows multiple charge-discharge cycles at a constant current of 10 mA. .... 141

Fig. 6.16 Two envelope asymmetric cells power 19 LED bulbs with a nominal current of 20 mA cm<sup>-2</sup> for each bulb ..... 142

Fig. 7.1 X-ray diffraction pattern of as-prepared BiMn<sub>2</sub>O<sub>5</sub> powder and corresponding JCPDS file..... 148

Fig. 7.2 (A,B) SEM images of as-prepared BiMn<sub>2</sub>O<sub>5</sub> powder at different magnifications ..... 149

Fig. 7.3 (A) CVs for BiMn<sub>2</sub>O<sub>5</sub> - MWCNT electrode at scan rates of (a) 10, (b) 20, (c) 50, (d) 100, and (e) 200 mV s<sup>-1</sup> in 0.5 M aqueous Na<sub>2</sub>SO<sub>4</sub> electrolyte, (B) C<sub>s</sub> and C<sub>v</sub>, calculated from the CV data at different scan rates ..... 151

Fig. 7.4 (A) Nyquist plot of complex impedance, inset shows high frequency range, (B) C<sub>s</sub>' and (C) C<sub>s</sub>'' components of complex capacitance versus frequency for BiMn<sub>2</sub>O<sub>5</sub>-MWCNT electrode..... 152

Fig. 7.5 Schematic of BiMn<sub>2</sub>O<sub>5</sub>-MWCNTs/activated carbon-carbon black hybrid device ..... 154

Fig. 7.6 CVs for the two electrode asymmetric cell, containing a positive BiMn<sub>2</sub>O<sub>5</sub>-MWCNT electrode and a negative AC-CB electrode at scan rates of (a) 2 (b) 5 (b), (c)10 and (d) 20 mV s<sup>-1</sup> in 0.5 M Na<sub>2</sub>SO<sub>4</sub> electrolyte, (B) Cs calculated from the CV data at different scan rates. .... 154

Fig. 7.7 (A) Nyquist plots of complex impedance, inset shows high frequency range and (B) Cs' and (C) Cs'' components of complex capacitance versus frequency for two electrode asymmetric cell, containing a positive BiMn<sub>2</sub>O<sub>5</sub>-MWCNT electrode and a negative AC-CB electrode ..... 155

Fig. 7.8 Galvanostatic charge-discharge behavior of an asymmetric cell at currents of (a) 1, (b) 2, (c) 4, (d) 5, (e) 8 and (f) 10 mA cm<sup>-2</sup>..... 155

Fig. 7.9. Capacitance retention versus cycle number for an asymmetric cell, inset shows multiple charge-discharge cycles at a constant current of 10 mA cm<sup>-2</sup>. ..... 156

Fig 7.10. Ragone plot for an asymmetric cell, inset shows five LED bulbs powered by two asymmetric cells in series. .... 157

Fig. 8.1 Schematic of PAZO as dispersant for charging and EPD of MnO<sub>2</sub> and PPy fibers ..... 164

Fig. 8.2 (A) SEM image, (B) TEM image, inset shows electron diffraction pattern, (C) high resolution TEM image and (D) X-ray diffraction pattern of MnO<sub>2</sub> nanofibers..... 165

Fig. 8.3 (A) Chemical structure of BT dopant, (B) SEM image of pristine MWCNT, (C) SEM image of PPy particles prepared using BT dopant, (D) SEM image of PPy coated MWCNT, prepared using BT as a dopant for PPy and dispersant for MWCNT ..... 166

Fig. 8.4 TEM images (A and B) at different magnifications of the PPy coated MWCNT,

prepared using BT as a dopant for PPy and dispersant for MWCNT, inset in (B) shows interface of PPy coating and MWCNT.....167

Fig. 8.5(A) Molecular structure of PAZO, (B) schematic of adsorption of PAZO on MnO<sub>2</sub> nanofiber, involving the complexation of a Mn atom with a salicylate ligand of a PAZO monomer; (C) (a) PAZO solution, and suspensions of (b) 1 g L<sup>-1</sup> MWCNTs, (c) 1 g L<sup>-1</sup> MWCNTs and 1 g L<sup>-1</sup> PAZO, (d) 1 g L<sup>-1</sup> MnO<sub>2</sub>, (e) 1 g L<sup>-1</sup> MnO<sub>2</sub> and 1 g L<sup>-1</sup> PAZO, (f) 1 g L<sup>-1</sup> MnO<sub>2</sub>, 1 g L<sup>-1</sup> MWCNTs and 1 g L<sup>-1</sup> PAZO, (g) 1 g L<sup>-1</sup> PPy, (h) 1 g L<sup>-1</sup> PPy and 1 g L<sup>-1</sup> PAZO, (i) 1 g L<sup>-1</sup> PPy coated MWCNTs, (j) 1 g L<sup>-1</sup> PPy coated MWCNTs and 1 g L<sup>-1</sup> PAZO in an ethanol–water solvent. ....168

Fig. 8.6 (A–C) Deposit mass at a deposition voltage of 5 V: (A) versus deposition time in 0.1 g L<sup>-1</sup> PAZO solutions in (a) water, (b) ethanol–water solvent, measured by QCM; (B) versus PAZO concentration in ethanol–water solvent at a deposition time of 5 min; (C) versus time for 1 g L<sup>-1</sup> PAZO solution in ethanol–water solvent, (D–F) SEM images of films prepared from 1 g L<sup>-1</sup> PAZO solutions in (D) water and (E and F) ethanol– water solvent, (E) surface, (F) cross section. ....171

Fig. 8.7 FTIR spectra of (a) as-received PAZO and deposits, prepared from (b) 1 g L<sup>-1</sup> PAZO, (c) 4 g L<sup>-1</sup> MnO<sub>2</sub> and 1 g L<sup>-1</sup> PAZO, (d) 1 g L<sup>-1</sup> MWCNT and 1 g L<sup>-1</sup> PAZO in a mixed ethanol–water solvent .....173

Fig. 8.8 Deposit mass versus (A) PAZO concentration at a deposition time of 5 min and (B) time at PAZO concentration of 1 g L<sup>-1</sup> for suspensions of (a) 2 g L<sup>-1</sup> MnO<sub>2</sub> nanofibers, (b) 1 g L<sup>-1</sup> MWCNT, (c) 1 g L<sup>-1</sup> PPy powder, (d) 1 g L<sup>-1</sup> PPy coated MWCNT in a mixed ethanol– water solvent .....174

Fig. 8.9 (A–C) SEM images of deposits, prepared at a deposition voltage of 100 V from suspensions of (A) 1 g L<sup>-1</sup> MWCNT and 1 g L<sup>-1</sup> PAZO, (B) 4 g L<sup>-1</sup> MnO<sub>2</sub> nanofiber and 1 g L<sup>-1</sup> PAZO (C) 4 g L<sup>-1</sup> MnO<sub>2</sub> nanofiber, 1 g L<sup>-1</sup> MWCNT and 1 g L<sup>-1</sup> PAZO, (D) composite, prepared by filtration of 4 g L<sup>-1</sup> MnO<sub>2</sub> nanofiber and 1 g L<sup>-1</sup> MWCNT suspension, dispersed using 1 g L<sup>-1</sup> PAZO in ethanol–water solvent. .... 175

Fig. 8.10 SEM images of deposits prepared from 4 g L<sup>-1</sup> suspensions of (A) PPy and (B) PPy coated MWCNT, containing 1 g L<sup>-1</sup> PAZO in ethanol–water solvent at a deposition voltage of 100 V. .... 176

Fig. 8.11 (A–C) CVs for 3 mg cm<sup>-2</sup> electrodes of (A) of pure MnO<sub>2</sub> prepared by EPD using PAZO, (B) MnO<sub>2</sub>-MWCNT, prepared by slurry impregnation method without PAZO, (C) MnO<sub>2</sub>-MWCNT, prepared by EPD using PAZO at scan rates of (a) 2, (b) 5, (c) 10, (d) 20, and (e) 50 mV s<sup>-1</sup>, the mass ratio of MWCNT : MnO<sub>2</sub> in the suspensions (B and C) was 1 : 4, (D) C<sub>s</sub> and C<sub>m</sub> versus scan rate, calculated from the CV data, for (a) pure MnO<sub>2</sub>, prepared by EPD using PAZO (b) MnO<sub>2</sub>-MWCNT, prepared by slurry impregnation (c) MnO<sub>2</sub>-MWCNT, prepared by EPD using PAZO. .... 178

Fig. 8.12 (A) Nyquist plot of complex impedance for 3 mg cm<sup>2</sup> electrodes and (B and C) components of complex capacitance, calculated the impedance data versus frequency, for (a) of pure MnO<sub>2</sub> prepared by EPD using PAZO, (b) MnO<sub>2</sub>-MWCNT, prepared by slurry impregnation method without PAZO (c) MnO<sub>2</sub>-MWCNT, prepared by EPD using PAZO, the mass ratio of MWCNT : MnO<sub>2</sub> in the suspensions (b and c) was 1 : 4. .... 179

Fig 8.13 Electrochemical testing data for 3 mg cm<sup>2</sup> electrodes prepared by EPD using PAZO: (A and B) CVs for (A) PPy and (B) PPy coated MWCNT at scan rates of (a) 2, (b)

5, (c) 10, (d) 20, and (e) 50  $\text{mV s}^{-1}$ , (C)  $C_s$  and  $C_m$ , calculated from the CVs for (a) PPy and (b) PPy coated MWCNT, (D–F) impedance data for (a) PPy and (b) PPy coated MWCNT: (D) Nyquist plot of complex impedance and (E and F) components of complex capacitance, calculated from the impedance data versus frequency. .... 179

Fig. 8.14 Capacitance retention versus cycle number for (A)  $\text{MnO}_2$ - MWCNT and (B) PPy coated MWCNT electrodes, prepared by EPD using PAZO..... 180

Fig. 9.1 Schematic of asymmetric supercapacitor composed by a  $\text{MnO}_2$ -rGO positive electrode and a  $\text{Fe}_2\text{O}_3$ -rGO negative electrode ..... 186

Fig. 9.2 (A) X-ray diffraction pattern, (B) SEM image, (C) TEM image, inset shows electron diffraction pattern and (D) high resolution TEM image of  $\text{MnO}_2$  nanotubes, arrows show inner diameter. .... 187

Fig. 9.3 (A) X-ray diffraction pattern, (B)SEM image, (C) TEM image, inset shows electron diffraction pattern and (D) high resolution TEM image of  $\text{Fe}_2\text{O}_3$  nanotubes. ... 188

Fig. 9.4 (A) Molecular structure of PAZO, (B) and (C) schematic of adsorption of PAZO on  $\text{MnO}_2$  and  $\text{Fe}_2\text{O}_3$  nanotubes, respectively, involving the complexation of a Mn and Fe atoms with a salicylate ligand of a PAZO monomer; (D) UV-Vis data for (a) pure PAZO, and deposits prepared from 2  $\text{g L}^{-1}$  suspensions of (b)  $\text{MnO}_2$ , (c)  $\text{Fe}_2\text{O}_3$ , containing 0.5  $\text{g L}^{-1}$  PAZO at a deposition voltage of 20 V in 25% water and 75% ethanol; E(d) 0.5  $\text{g L}^{-1}$  PAZO solution, and suspensions of (e) 2  $\text{g L}^{-1}$   $\text{MnO}_2$ , (f) 2  $\text{g L}^{-1}$   $\text{MnO}_2$  and 0.5  $\text{g L}^{-1}$  PAZO, (g) 2  $\text{g L}^{-1}$   $\text{Fe}_2\text{O}_3$  and (h) 2  $\text{g L}^{-1}$   $\text{Fe}_2\text{O}_3$  and 0.5  $\text{g L}^{-1}$  PAZO. .... 189

Fig. 9.5 (A) SEM image of rGO after freeze drying; (B), (C) are lateral and plan view of as-prepared rGO hydrogel before freeze drying; (D), (E) are lateral and plan view of rGO

hydrogel after freeze drying; F(a) and (b) are X-ray diffraction pattern of as- prepared rGO and GO, respectively..... 190

Fig. 9.6 (A) CVs for rGO electrode with mass loading of  $1 \text{ mg cm}^{-2}$ , at scan rates of (a) 2, (b) 5, (c) 10 and (d)  $20 \text{ mV s}^{-1}$  in  $0.5 \text{ M}$  aqueous  $\text{Na}_2\text{SO}_4$  electrolyte. (B)  $C_s$  and  $C_m$ , calculated from the CV data; (C)  $C'$  and (D)  $C''$  components of complex capacitance versus frequency. .... 191

Fig. 9.7 SEM image of EPD of  $2 \text{ g L}^{-1} \text{ MnO}_2$  with  $0.5 \text{ g L}^{-1}$  PAZO (A) onto stainless steel and (B) into rGO substrate (white arrows show rGO and black arrows show  $\text{MnO}_2$  tubes) under 10V for 5 min in 75% ethanol and 25% water. .... 192

Fig. 9.8 (A) CVs for  $\text{MnO}_2$  electrode prepared by EPD of  $2 \text{ g L}^{-1} \text{ MnO}_2$  with  $0.5 \text{ g L}^{-1}$  PAZO onto stainless steel with  $\text{MnO}_2$  mass loading of  $1 \text{ mg cm}^{-2}$ , at scan rates of (a) 2, (b) 5, (c) 10 and (d)  $20 \text{ mV s}^{-1}$  in  $0.5 \text{ M}$  aqueous  $\text{Na}_2\text{SO}_4$  electrolyte. (B)  $C_s$  and  $C_m$ , calculated from the CV data; (C)  $C'$  and (D)  $C''$  components of complex capacitance versus frequency. .... 193

Fig. 9.9 (A) CVs for  $\text{MnO}_2$  electrode prepared by EPD of  $2 \text{ g L}^{-1} \text{ MnO}_2$  with  $0.5 \text{ g L}^{-1}$  PAZO into rGO with total mass loading of  $2 \text{ mg cm}^{-2}$ , at scan rates of (a) 2, (b) 5, (c) 10 and (d)  $20 \text{ mV s}^{-1}$  in  $0.5 \text{ M}$  aqueous  $\text{Na}_2\text{SO}_4$  electrolyte. (B)  $C_s$  and  $C_m$ , calculated from the CV data; (C)  $C'$  and (D)  $C''$  components of complex capacitance versus frequency. .... 194

Fig. 9.10 SEM image of EPD of  $2 \text{ g L}^{-1} \text{ Fe}_2\text{O}_3$  with  $0.5 \text{ g L}^{-1}$  PAZO (A) onto stainless steel and (B) into rGO substrate (white arrows show rGO and black arrows show  $\text{Fe}_2\text{O}_3$  tubes) under 10V for 5 min in 75% ethanol and 25% water..... 195

Fig. 9.11 (A) CVs for Fe<sub>2</sub>O<sub>3</sub> electrode prepared by EPD of 2 g L<sup>-1</sup> Fe<sub>2</sub>O<sub>3</sub> with 0.5 g L<sup>-1</sup> PAZO onto stainless steel with Fe<sub>2</sub>O<sub>3</sub> mass loading of 1 mg cm<sup>-2</sup>, at scan rates of (a) 2, (b) 5, (c) 10 and (d) 20 mV s<sup>-1</sup> in 0.5 M aqueous Na<sub>2</sub>SO<sub>4</sub> electrolyte. (B) C<sub>s</sub> and C<sub>m</sub>, calculated from the CV data; (C) C' and (D) C'' components of complex capacitance versus frequency. ....196

Fig. 9.12 (A) CVs for Fe<sub>2</sub>O<sub>3</sub> electrode prepared by EPD of 2 g L<sup>-1</sup> Fe<sub>2</sub>O<sub>3</sub> with 0.5 g L<sup>-1</sup> PAZO into rGO with total mass loading of 2 mg cm<sup>-2</sup>, at scan rates of (a) 2, (b) 5, (c) 10 and (d) 20 mV s<sup>-1</sup> in 0.5 M aqueous Na<sub>2</sub>SO<sub>4</sub> electrolyte. (B) C<sub>s</sub> and C<sub>m</sub>, calculated from the CV data; (C) C' and (D) C'' components of complex capacitance versus frequency. ....197

Fig. 9.13 (A) CVs for asymmetric device composed by EPD of 2 g L<sup>-1</sup> MnO<sub>2</sub> as positive electrode and Fe<sub>2</sub>O<sub>3</sub> as negative electrode with 0.5 g L<sup>-1</sup> PAZO into rGO with total mass loading of 4 mg cm<sup>-2</sup>, at scan rates of (a) 2, (b) 5, (c) 10 and (d) 20 mV s<sup>-1</sup> in 0.5 M aqueous Na<sub>2</sub>SO<sub>4</sub> electrolyte. (B) C<sub>s</sub> and C<sub>m</sub>, calculated from the CV data; (C) C' and (D) C'' components of complex capacitance versus frequency. ....199

Fig. 9.14 Impedance data for (A) pure rGO, (B) pure MnO<sub>2</sub> nanotubes on stainless steel, (C) pure Fe<sub>2</sub>O<sub>3</sub> nanotubes on stainless steel, (D) MnO<sub>2</sub>-rGO, (E) Fe<sub>2</sub>O<sub>3</sub>-rGO and (F) asymmetric device. ....200

Fig. 9.15 (A) Galvanostatic charge–discharge behavior of an asymmetric coin cell at currents of (a) 0.5, (b) 1, (c) 3, (d) 4 and (e) 5mA, (B) capacitance retention versus cycle number for an asymmetric coin cell, inset shows multiple charge–discharge cycles at a constant current of 3 mA.....200

Fig. 10.1 Schematic of EPD for different materials using PAZO as dispersant .....203

Fig. 10.2 (A) (a) Structure of PAZO and (b) adsorption mechanism, involving complexation of salicylate ligands of PAZO with metal atom (M) on the particle surface, (B) time dependence of QCM mass gain during EPD from 0.1 g L<sup>-1</sup> PAZO solutions in (a) methanol and (b) ethanol-water solvent; arrow shows time, corresponding to application of cell voltage of 10V, (C) photoinduced birefringence for films prepared from 1 g L<sup>-1</sup> PAZO solutions in (a) methanol and (b) ethanol-water solvent, arrows show OFF times for writing laser. ....205

Fig. 10.3 SEM images of films, prepared from (A-F) 1 g L<sup>-1</sup> PAZO solutions and (G-I) 1 g L<sup>-1</sup> PAZO solutions, containing 0.5 g L<sup>-1</sup> PVDM in (A-C) methanol and (D-I) ethanol-water solvent at a deposition voltage of 10 V and deposition time of 3 min, (A,B,D,E,G,H) – surfaces at different magnifications, (C,F,I) - cross sections. ....206

Fig. 10.4 (A) Photoinduced birefringence versus time, arrow shows OFF time for writing laser, (B) saturated birefringence and birefringence buildup time versus power of the writing laser for films, prepared from 1 g L<sup>-1</sup> PAZO solutions in ethanol-water solvent, containing 0.5 g L<sup>-1</sup> PVDM. ....208

Fig. 10.5 (A) FTIR and (B) UV-Vis spectra for deposits, prepared from 1 g L<sup>-1</sup> PAZO solution in a mixed ethanol-water solvent: (a) without additives and containing 2 g L<sup>-1</sup> of (b) MnO<sub>2</sub>, (c) aluminium hydroxide, (d) Pd, (e) PPy nanofibers and (f) MWCNT, (C) UV-Vis spectrum of the deposit prepared from 1 g L<sup>-1</sup> PAZO solution, containing 1 g L<sup>-1</sup> AT dye (■ - absorption of AT, ● - absorption of PAZO). ....211

Fig. 10.6 (A) X-ray diffraction patterns and (B) corresponding SEM images of deposits,

prepared from 1 g L<sup>-1</sup> PAZO solution in a mixed ethanol-water solvent, containing (a) 2 g L<sup>-1</sup> Pd and 1 g L<sup>-1</sup> MWCNT, (b) 2 g L<sup>-1</sup> TiO<sub>2</sub> rutile and 1 g L<sup>-1</sup> MWCNT, (c) 2 g L<sup>-1</sup> TiO<sub>2</sub> anatase and 2 g L<sup>-1</sup> SiC, (d) 2 g L<sup>-1</sup> TiO<sub>2</sub> anatase and 2 g L<sup>-1</sup> alumina platelets, white arrows and black arrows in B(c) show SiC and TiO<sub>2</sub> anatase, respectively, inset in B(d) shows TiO<sub>2</sub> anatase. ....212

Fig. 10.7 (A) CVs at a scan rate of 20 mV s<sup>-1</sup>, (B) specific capacitance versus scan rate, (C) real and (D) imaginary components of AC capacitance, calculated from impedance data versus frequency for (a) PPy nanofibers and (b) PPy nanofibers(85%) – MWCNT(15%) composite deposits with active mass of 2 mg cm<sup>-2</sup>, prepared using PAZO. ....214

Fig. 11.1 Chemical structure of Celestine blue (adsorption on ceramic particles) .....218

Fig. 11.2 (A,B) TEM images of MnO<sub>2</sub> particles at different magnifications .....219

Fig. 11.3 (A,B) TEM images of Mn<sub>3</sub>O<sub>4</sub> particles at different magnifications .....220

Fig. 11.4 Deposit mass versus CB concentration in 4 g L<sup>-1</sup> suspensions of (A) MnO<sub>2</sub>, (B) Mn<sub>3</sub>O<sub>4</sub>, (C) TiO<sub>2</sub> and (D) BaTiO<sub>3</sub> at a deposition voltage of 20V and deposition time of 5 min. ....221

Fig. 11.5 Deposit mass versus deposition time for 4 g L<sup>-1</sup> suspensions of (A) MnO<sub>2</sub>, (B) Mn<sub>3</sub>O<sub>4</sub>, (C) TiO<sub>2</sub> and (D) BaTiO<sub>3</sub>, containing 0.5 g L<sup>-1</sup> CB at a deposition voltage of 20V. ....222

Fig. 11.6 SEM images of films, prepared from 4 g L<sup>-1</sup> suspensions of (A) MnO<sub>2</sub>, (B) Mn<sub>3</sub>O<sub>4</sub>, (C) TiO<sub>2</sub> and (D) BaTiO<sub>3</sub>, containing 0.5 g L<sup>-1</sup> CB at a deposition voltage of 20V .....223

Figure. 11.7 (A) FTIR and (B)UV-Vis data for deposits, prepared from 4 g L<sup>-1</sup> suspensions of (a) MnO<sub>2</sub>, (b) Mn<sub>3</sub>O<sub>4</sub>, (c) TiO<sub>2</sub> and (d) BaTiO<sub>3</sub>, containing 0.5 g L<sup>-1</sup> CB at a deposition voltage of 20V. ....224

Fig. 11.8 Mass gain, measured using QCM for the MnO<sub>2</sub> film deposited on a gold coated quartz crystal versus time after the injection of CB. Arrow shows injection time. ....225

Fig. 11.9 (A,B,C) SEM images of films and (D) corresponding X-ray diffraction patterns for films, prepared from mixed suspensions, containing 2 g L<sup>-1</sup> TiO<sub>2</sub> and (A), (D (a)) 2 g L<sup>-1</sup> MnO<sub>2</sub>, (B), (D(b)) 2 g L<sup>-1</sup> halloysite and (C), (D(c)) BaTiO<sub>3</sub> at a deposition voltage of 20 V (● - JCPDS file 21-1272, ◆-JCPDS file 44-1386, ■-JCPDS file 29-1487, ▼ - JCPDS file 5-0626).....226

Fig. 11.10 Deposit mass versus (A) CB concentration in suspensions at a deposition time of 5 min and (B) versus deposition time for CB concentration of 0.5 g L<sup>-1</sup> for suspensions of (a) zirconia I and (b) zirconia II at a deposition voltage 20 V.....227

Fig. 11.11 Schematic mechanism of CB adsorption on MnO<sub>2</sub> and halloysite nanotubes229

## **List of Tables**

Table 1. Comparison of different types of supercapacitors .....	28
Table 2. Onion-like carbon, carbon nanotubes, graphene, activated carbons, and carbide-derived carbons used in EDLCs.....	34
Table 3. Comparison of different polymers in electrochemical properties.....	36
Table 4. Different materials as electrode for supercapacitors.....	43

## List of Abbreviations and Symbols

A (unit)	Ampere
A	Specific surface area of electrode
AC	Activated carbon
APS	Ammonium Peroxydisulfate
aq.	Aqueous
BAC	Benzyltrimethylhexadecylammonium chloride
C	Capacitor
C (unit)	Coulomb
CA	Caffeic acid
CB	Celestine blue
CB	Carbon black
$C_{dl}$	Double-layer capacitance
$C_{diff}$	Capacitance corresponding to diffuse region
$C_H$	Hemholtz type capacitance
$C_m$	Mass normalized specific capacitance
cm (unit)	Centimeter
CNT	Carbon nanotubes
$C_s$	Areal normalized specific capacitance

CS	m-cresol purple sodium salt
CTAB	Hexadecyl-trimethyl-ammonium bromide
CV	Cyclic voltammetry
$C_{\varphi}$	Pseudocapacitance
$d$	Thickness of double layer
DA	Dopamine
DL	Double layer
DOPA	L-34-dihydroxyphenylalanine
$e$	Euler's number (2.71828...)
ECs	Electrochemical supercapacitors
Ed	Energy density
EDL	Electro-double-layer
EDLC	Electrochemical Double Layer Capacitor
EDX	Energy-dispersive X-ray spectroscopy
EIS	Electrochemical Impedance Spectroscopy
EPD	Electrophoretic Deposition
Eq.	Equation
ES	Electrochemical supercapacitor
ESR	Equivalent Series Resistance
F	Faraday constant
F (unit)	Farad
$\Delta F$	Frequency change

FTIR	Fourier transform infrared spectroscopy
g (unit)	Gram
h (unit)	Hour
$\eta$	Overpotential
HAADF	High angle annular dark field
IHP	Inner Helmholtz Plane
$k$	Boltzman constant
kg (unit)	Kilogram
L(unit)	Liter
LBL	Layer-by-layer
Li-ion	Lithium-ion Battery
M (unit)	Mole per liter
mM (unit)	Millimole per liter
m (unit)	Meter
mg (unit)	Milligram
min (unit)	Minute
mL (unit)	Millilitre
mV (unit)	Milli Volt
MWCNT	Multi-walled carbon nanotubes
Ni-MH	Nickel-Metal Hydride
nm (unit)	Nanometer
OHP	Outer Helmholtz Plane (OHP)

Ox	Oxidizing
PAni	Polyaniline
PAZO	Poly[1-[4-(3-carboxy-4-hydroxyphenylazo)benzenesulfonamido]-1
2- ethanediyl	sodium salt]
PBH	1-Pyrenebutyric Acid
Pd	Power density
PE	Phosphate ester
PEDOT	Poly(3-4-ethylenedioxythiophene)
PPy	Polypyrrole
<i>Pr</i>	Possibility (Poisson distribution)
PTh	Poly(thiophene)
PVB	Polyvinyl butyral
p.z.c.	Point of zero charge
Q	Electric charge
QCM	Quartz Crystal Microbalance
R	Ideal gas constant ( $8.314 \text{ J mol}^{-1} \text{ K}^{-1}$ )
Red	Reducing
rGO	reduced graphene oxide
RHE	Reversible hydrogen electrode
$R_f$	Faradaic leakage resistance
S (unit)	Siemens

s (unit)	Second
SC	Specific capacitance
SCE	Saturated calomel electrode
SEM	Scanning electron microscope
SHE	Standard hydrogen electrode
STEM	Scanning transmission electron microscope
T	Absolute temperature (K)
TEM	Transmission electron microscope
UV-vis	Ultraviolet-Visible spectroscopy
$U_e$	Electrostatic energy
$U_c$	Chemisorption energy
$v$	Speed of particle
V (unit)	Volt
$V_A$	Attraction energy
$V_R$	Repulsion energy
$V_T$	Total internal energy
W (unit)	Watt
Wh (unit)	Watt-hour
XRD	X-Ray diffraction
$\Omega$ (unit)	Ohm
$Z'$	Real impedance
$Z''$	Imaginary impedance

$\pi$	Pi (3.1416)
$\xi$	Zeta potential
$\mu\text{m}$ (unit)	Micrometer
$\mu\text{V}$ (unit)	Micro Volt
$^{\circ}\text{C}$ (unit)	Celsius degree
$\epsilon_0$	Permittivity of vacuum
$\epsilon_r$	Relative permittivity
$\lambda$	Average number of events per interval
$\delta$	Fraction ( $0 < \delta < 1$ )

## **Chapter 1 Introduction**

### **1.1 Global energy issue and next-generation energy storage devices**

In the 21st century, the topic of energy has secured a foothold as one of the most important technological issues that must be addressed to secure the sustainability of human societies[1]. With the rapid development of the global economy, the depletion of fossil fuels, and increasing environmental pollution, there is an urgent need for efficient, clean, and sustainable sources of energy, as well as new technologies associated with energy conversion and storage[2]. The market tendency in pure electric and hybrid electric vehicles raise urgent demands in energy storage devices with high capacity as well as high power density. Among the ideal candidates for electrochemical energy storage or conversion devices, supercapacitors, also called ultracapacitors, electrochemical capacitors (ECs), have become some of the most promising candidates for next-generation power devices because of their high power density, fast charging/discharging rate, sustainable cycling life (millions of cycles), and excellent cycle stability[3, 4]. With many thousands of times higher power density than lithium ion batteries and much larger energy density than conventional capacitors, ECs offer a promising approach to meeting the increasing power demands of energy storage systems[5].

In order to satisfy the requirements for large capacity as well as high power density, numerous attentions have been drawn in studies of hybrid asymmetric supercapacitors,

which are composed of an electric double layer supercapacitor (EDLC) and a pseudocapacitor electrodes. EDLCs origin from electrostatic storage and separated charges at Helmholtz double layer, where one layer at electrode and another layer in electrolyte. Pseudocapacitance is caused by redox reaction at electrode in a Faradaic process. The voltage window of hybrid supercapacitor can be broaden from 0.9V to 1.8V due to over potential in aqueous environment[7]. Thus energy and power density can be greatly increased according to  $E=1/2 CV^2$  and  $P=V^2/4R$ .

The EDLC electrode can be fabricated using diverse carbon-based materials such as activated carbon (AC), carbon nanotubes (CNTs), graphene or their composites. These materials should have high specific surface area (SSA) for accommodation of more ions adsorption/departure on its surface during charge and discharge.

Pseudocapacitors are based on transitional metal oxides such as  $MnO_2$ ,  $RuO_2$ ,  $NiO_2$  or polymers. Recent studies in complex oxide compounds also raise numerous interests due to their specific properties. Charge and discharge process always involves redox reaction between various valence states of specific elements in these oxides. Pseudocapacitors possess relatively higher energy density than that of EDLCs, on the other hand, EDLCs have higher power density.

By combination of EDLC and pseudocapacitor, a hybrid supercapacitor exhibits both double-layer as well as pseudocapacitive properties, where it compensates the drawbacks of lower power density for batteries, or lower energy density for symmetric capacitors[8]. This dissertation will focus on fabrication of advanced asymmetric supercapacitors.

## 1.2 Comparison of different energy storage devices

The reason why ECs were able to raise considerable attention are visualized in Fig. 1.1, in which the so called “Ragone plot” exhibits variation of specific energy density vs. power density of typical energy storage devices. ECs fill the gap between batteries and conventional capacitors such as the electrolytic capacitors or metallized film capacitors,

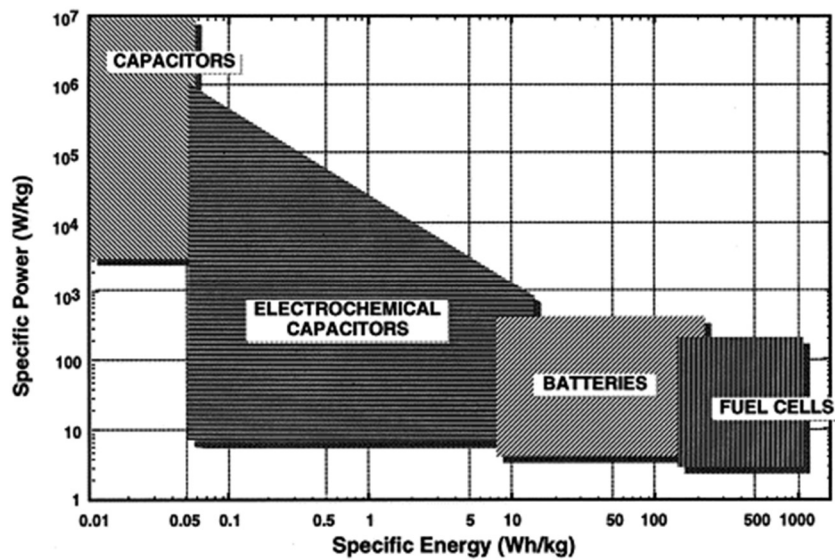


Fig. 1.1 Sketch of Ragone plot for various energy storage and conversion devices. The indicated areas are rough guide lines [9].

occupying an important position in terms of the specific energy as well as the specific power. The conventional capacitors may achieve a power density beyond 10<sup>6</sup> W/kg at extremely low energy density, whereas batteries and low temperature fuel cells compensate that for a higher energy density with drawbacks of low power densities. Comparing to batteries and fuel cells, ECs have evident advantage in much higher power, which can reach up to 10<sup>6</sup> W/kg, as well as higher energy densities than conventional

capacitors. Additionally, ECs show extraordinarily good cycling capability (up to  $10^6$  cycles), and have longer life time and fast recharging rate.

### **1.3 Major objectives and achievements of this work**

Specific surface area (SSA) is critical for nanotechnology and ECs fabrication. A high SSA is beneficial for electrodes utilized in ECs, which facilitates electrolyte diffusing into more active materials and results in high energy storage or conversion. Therefore, fabrication of well dispersed composite materials with a high SSA for ES electrode becomes first priority of our work. Moreover, energy density is the major limitation for application of ECs. Development of ECs with larger voltage window is an effective way for enhancing energy density of ECs. Organic electrolyte offers opportunities for broadening voltage window of ECs. However, there are many disadvantages for utilizing organic electrolyte because they are environmentally unfriendly, flammable and toxic, which are harmful to environment and human been. Hence it's better to propose approaches based on aqueous suspensions for ECs.

In this dissertation, many goals have been achieved. Novel dispersants have been developed for dispersing of  $\text{MnO}_2$  - MWCNTs composite electrode for ECs. EPD has been employed for characterizing colloidal properties of dispersants and particles. Voltage window has been successfully enlarged in aqueous suspension by introducing activated carbon as negative electrode for fabrication of asymmetric ECs. Novel material  $\text{BiMn}_2\text{O}_5$  nanocrystals have been firstly synthesized and investigated for their capacitive properties as ES electrode, which shows excellent areal and volumetric capacitance.

## References

- [1] D. Higgins, P. Zamani, A. Yu, Z. Chen, The application of graphene and its composites in oxygen reduction electrocatalysis: a perspective and review of recent progress, *Energy & Environmental Science*, (2016) DOI: 10.1039/C5EE02474A.
- [2] G. Wang, L. Zhang, J. Zhang, A review of electrode materials for electrochemical supercapacitors, *Chemical Society reviews*, 41 (2012) 797-828.
- [3] L. Bao, J. Zang, X. Li, Flexible Zn<sub>2</sub>SnO<sub>4</sub>/MnO<sub>2</sub> core/shell nanocable-carbon microfiber hybrid composites for high-performance supercapacitor electrodes, *Nano letters*, 11 (2011) 1215-1220.
- [4] B.E. Conway, *Electrochemical Supercapacitors: Scientific Fundamentals and Technological Applications*, Kluwer Academic/ Plenum Publisher, New York, 1999.
- [5] B.E. Conway, Transition from “Supercapacitor” to “Battery” Behavior in Electrochemical Energy Storage, *Journal of The Electrochemical Society*, 138 (1991) 1539-1548.
- [6] V.K. E. Frackowiak , K. Jurewicz, K. Lota, F. Béguin, Supercapacitors based on conducting polymers/nanotubes composites, *Journal of Power Sources*, 153 (2006) 413-418.
- [7] E.R.-P. V. Khomenko, E. Frackowiak, F. Béguin, High-voltage asymmetric supercapacitors operating in aqueous electrolyte, *Appl. Phys. A*, 82 (2006) 567-573.
- [8] P. Yang, Y. Ding, Z. Lin, Z. Chen, Y. Li, P. Qiang, M. Ebrahimi, W. Mai, C.P. Wong, Z.L. Wang, Low-Cost High-Performance Solid-State Asymmetric Supercapacitors Based on MnO<sub>2</sub> Nanowires and Fe<sub>2</sub>O<sub>3</sub> Nanotubes, *Nano letters*, 14 (2014) 731-736.

[9] R.K.t. a, M. Carlen, Principles and applications of electrochemical capacitors, *Electrochimica Acta*, 45 (2000) 2483-2498.

## **Chapter 2 Literature review**

### **2.1 Development and advantages of electrochemical supercapacitors**

ECs have been known since many years. Becker for the first time described a capacitor based on high surface area carbon in his patent in 1957[1]. SOHIO tried to market such devices later in 1969[2]. ECs have started drawing attentions only in the 90s when hybrid electric vehicles become popular. The U.S. Department of Energy (DOE) ultracapacitor development program was initiated in 1989, and it proposed a short term and long term goals for 1998–2003 and after 2003, respectively[3]. The EC was supposed to support the batteries or fuel cells with a higher power for acceleration of vehicles when it's necessary in a hybrid energy system, and additionally allow for recuperation of brake energy. There are more and more companies such as Maxwell Technologies, ATL, NEC, Panasonic, Siemens Matsushita (now EPCOS), ELNA, TOKIN invest in the supercapacitor technology development. The applications envisaged are principally boost components supporting batteries or replacing batteries primarily in electric vehicles. In addition, alternative applications of EC do not compete with batteries but show considerable market potential[4].

Besides bridging the gap between capacitors and batteries, ECs also possess a number of desirable properties that make them an attractive energy storage option. Charge and discharge of electrochemical double-layer capacitors (EDLCs) are completely reversible, so EDLCs are extremely efficient and can withstand a large number of charge/discharge

cycles. EDLCs have advantages of the use of low cost and environmental friendly raw materials and extremely long cycle life etc. Moreover, ECs can store or release energy very quickly, and can operate over a wide range of temperatures. They also have a high charge and discharge efficiency. The energy loss to heat during each cycle is relatively small. Furthermore, in general, ECs do not contain toxic materials and are much safer than batteries and fuel cells.

## **2.2 Categories of supercapacitors**

Based on their charge storage mechanisms, supercapacitors can be generally classified to three types: electrochemical double-layer supercapacitors (EDLC), Faradaic supercapacitors (FS) or pseudocapacitors, and hybrid supercapacitors.

### **2.2.1 Electrochemical double-layer supercapacitors**

#### **2.2.1.1 Energy storage mechanism for EDLCs**

The energy stored in the ECs is either double-layer capacitive or pseudocapacitive in nature. For EDLCs, the capacitive (non-Faradaic) process is based on charge accumulation and separation at the electrode/electrolyte interface, as shown in Fig. 2.1. These processes operate solely on the electrostatic accumulation of surface charge[5]. The so called EDLC was first described and modeled by Von Helmholtz in the 19th century. In the Helmholtz double layer model, it states that two layers of opposite charge form at the electrode/electrolyte interface and are separated by an atomic distance. Due to the inaccuracy of calculation of capacitance, this model was further modified by others[6]. EDLCs are usually fabricated from carbon materials, such as activated carbon, carbon

aerogel, CNTs, graphene or their composites, since these materials are able to provide higher conductivity, as well as larger specific surface area and possess low electrochemical activity[7].

As shown in Fig. 2.1, the mechanism of charge generation includes surface dissociation as well as ion adsorption from both the electrolyte and crystal lattice defects[8]. The accumulation of electrons at the electrode is a non-Faradaic process. During the process of charging, the electrons travel from the negative electrode to the positive electrode through an external load. Within the electrolyte, cations move towards the negative elect-

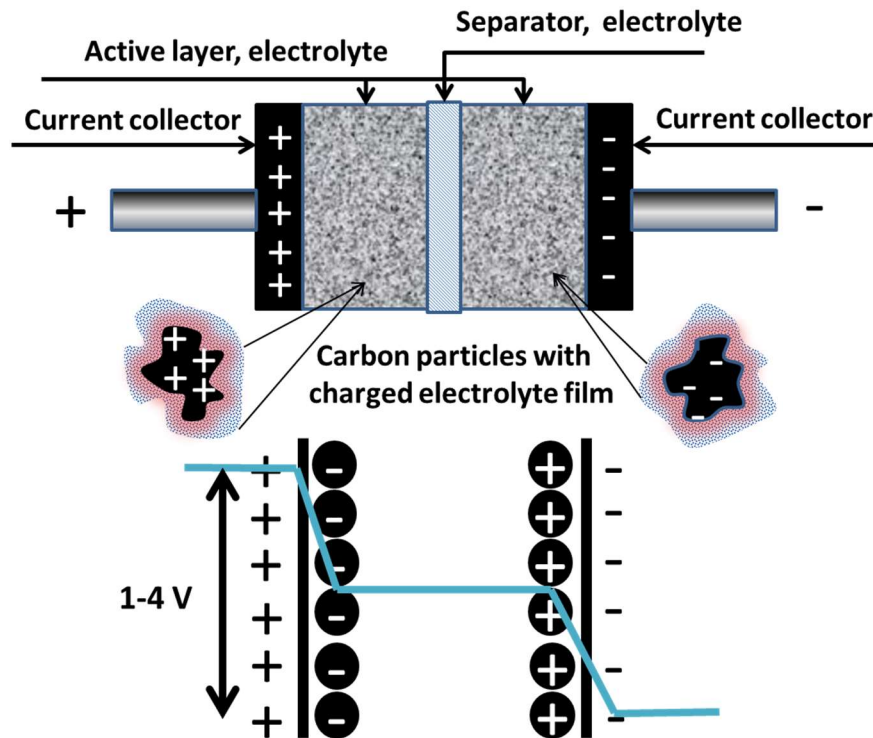


Fig. 2.1 Schematic structure and principles of a single cell EDLC[5]

-rode while anions move towards the positive electrode. During discharge, the reverse processes take place. In this type of ES, no charge transfers across the electrode/

electrolyte interface, and no net ion exchanges occur between the electrode and the electrolyte. This implies that the electrolyte concentration remains constant during the charging and discharging processes. In this way, energy is stored in the double-layer interface. Calculation of capacitance for EDLC can be generally assumed following the parallel-plate capacitor as[9]

$$C = \frac{\varepsilon_r \varepsilon_0}{d} A \quad (\text{Eq.2.1})$$

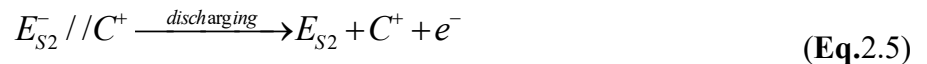
In equation 2.1,  $\varepsilon_r$  is the relative permittivity of the medium in the electrical double-layer,  $\varepsilon_0$  is the permittivity of vacuum,  $A$  is the specific surface area of the electrode, and  $d$  is the effective thickness of the electrical double-layer.

If the two electrode surfaces can be expressed as  $ES_1$  and  $ES_2$ , an anion as  $A^-$ , a cation as  $C^+$ , and the electrode/electrolyte interface as  $//$ , the electrochemical processes for charging and discharging can be expressed as equations (2.2)–(2.5) [10, 11].

For the positive electrode,



For the negative electrode,



The electrodes of EDLCs are made of high surface-area materials such as porous carbon or carbon aerogels in order to maximise the surface-area of the double-layer. The reason is that porous electrodes have a very small distance between the electronic and ionic charge at the electrode surface. Indeed, the surface-area of the porous carbon electrodes has been reported to be as large as 1000–2000 m<sup>2</sup>/g [12, 13].

### 2.2.1.2 Models of the Double Layer

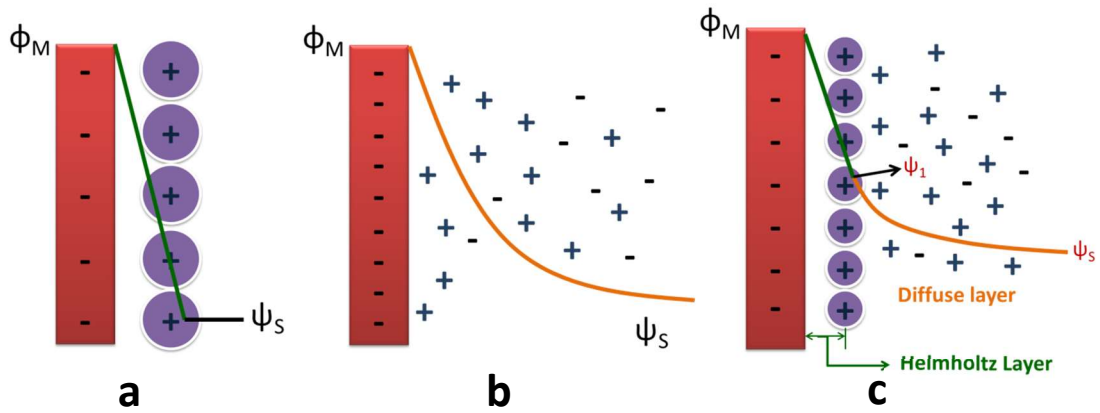


Fig. 2.2 Models of the double layer: (a) Helmholtz model, (b) Gouy-Chapman point charge model, (c) Stern model with thermal distribution, combining Helmholtz model and Gouy-Chapman models[14].

The definition of double layer refers to configuration composed of two arrays of layers consisting of opposite charges that are separated by an atomic scale of distance. The opposite charges are facing each other as on the plates of a two-plate hardware capacitor shown in Fig. 2.1 [14]. Von Helmholtz proposed the first double layer model [15], as shown in Fig 2.2 (a). Due to an excess or deficiency of electrons of the delocalized plasma of the metal, a corresponding and controllable density of positive or negative

charges will arise for neutralization on the metal side. Due to the high free electron density (approximately 1 e per atom) in the metal, any net charge of electrons at the surface is strongly screened. In this case, the gradient of electron density at a charged metal interface is highly localized over a distance only, the so-called Thomas-Fermi screening distance. There is significant spillover of electron density into the double layer on the solution side of the interface. The effect is potential dependent, since the wave function amplitudes of the conduction-band electrons retain significant but diminishing magnitudes outside the formal electrode surface plane [16].

After Von Helmholtz proposed his model, people started to realize that the ions on the solution side should be more randomly distributed than stay compact and static because of thermal fluctuation according to the Boltzmann principle. The thermal fluctuation greatly depends on the electrostatic energy  $U_e$  and chemisorption energy  $U_c$  of the ions' interactions with the charged metal surface exceeded, or were exceeded by, the average thermal energy,  $kT$ , at temperature,  $T$ , K, i. e., the ratio  $(U_e+U_c)/kT$ .

The addressed thermal fluctuation factor was introduced by Gouy[17] into a modified representation of the double layer some time later. In his model, the equal and opposite charges corresponding to the electron charge of the metal surface were considered as a 3-dimensional diffusely distributed population of cations and anions of the electrolyte.

In Gouy's model, shown in Fig. 2.2(b), the major reason causing its failure is that the ions were assumed to be point charges. Because this assumption led to (1) an incorrect potential profile and local field near electrode surface and (2) a too-large capacitance being predicted consequently. The quantity of predicted capacitance was defined as the

rate of variation of net ionic charge on the solution side with the change of potential difference between metal-solution interphase. The so-called “diffuse” double-layer capacitance refers to the capacitance generated in inter-phase of this model.

In 1913, Chapman gave a full mathematical treatment of the Gouy diffuse-layer[18], based on the combination of Boltzmann’s energy distribution equation and Poisson’s equation:

$$f(v) = \sqrt{\left(\frac{m}{2\pi kT}\right)^3} 4\pi v^2 e^{-\frac{mv^2}{2kT}}, \quad (\text{Eq.2.6})$$

$$f(k; \lambda) = \Pr(X = k) = \frac{\lambda^k e^{-\lambda}}{k!}, \quad (\text{Eq.2.7})$$

where  $v$  is the velocity of particles,  $m$  is particle mass,  $k$  is Boltzmann constant in (Eq.2.6),  $T$  is thermodynamic temperature,  $Pr$  is the possibility,  $k$  takes the value 0, 1, 2... in (Eq.2.7),  $\lambda$  is is the average number of events per interval. It should be noted that these principles proposed by Chapman predicted the approach taken by Debye and Huckel in 1923[19]. In their approach, the three dimensional distribution of charge around a given ion was determined with their treatment of activity coefficients and conductance of electrolytes.

Combination of Boltzmann’s energy distribution function and Poisson’s electrostatic equation (so-called “Poisson-Boltzmann” equation) is the key approach in both Chapman’s and Debye and Huckel’s treatments of ionic charge distribution. This approach was also used in semiconductors for determining band profiles and space charge effects.

Overestimation of double-layer capacitance is the main drawback in Gouy-Chapman's model, and this problem had been overcome by Stern in 1924[20]. In Stern's model (Fig. 2.2(c)) and derivation, an adsorption process resulted from Langmuir's adsorption isotherm was introduced to the inner region of the ion distribution. The region into the solution, which is beyond the inner layer, was considered as a diffuse region of distributed ionic charge. Since these ionic charges have finite size, including the annular thickness of their hydration shells, it was easy to define a geometrical limit to the compact region of adsorption of ions at the electrode surface. Stern's model proposed a total double layer capacitance  $C_{dl}$  composed by a Helmholtz type compact double layer capacitance  $C_H$  and a diffusion capacitance  $C_{diff}$ . The later one is caused by the remaining ionic charge density beyond the compact ion array. The overall double layer capacitance  $C_{dl}$  can be written as the following equation:

$$\frac{1}{C_{dl}} = \frac{1}{C_H} + \frac{1}{C_{diff}} \quad (\text{Eq.2.8})$$

and the equivalent circuit corresponding to this capacitance can be represented by Fig. 2.3:

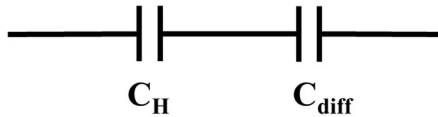


Fig. 2.3 an equivalent circuit of Stern model, consisted of  $C_H$  and  $C_{diff}$

Since  $C_H$  and  $C_{diff}$  are in series as in the equivalent circuit, it should be noted that  $C_{dl}$  will be determined by the smaller one of these two components. The properties of the double layer greatly depend on this characteristic, which is critical for determining the capacitance as function of electrode potential and ionic concentration of solution.

The reason of the overestimated capacitance arisen by the Gouy-Chapman treatment is caused by the improper assumption of charges as points, since the capacitance of two separated arrays of charges increases inversely as their separation distance. Thus the infinitesimally small distance of two charge points will result in a huge capacitance. Stern's model totally avoids the overestimation capacitance arisen in the Gouy-Chapman treatment by introducing a distance of closest approach. The finite-sized ions are critical for geometrically defining a compact Helmholtz inner region of the double layer.

#### 2.2.1.3 Equivalent circuit representation of double-layer electrical behavior

Fig. 2.4 represents the equivalent circuit of electrode interphases of an ideal and non-ideal double layer capacitors. The ideally polarized electrode can be simply represented by a capacitance (Fig. 2.4a) with a potential-dependent value. In case of a Faradaic process, the current will pass through a Faradaic leakage resistance  $R_F$ , as it's shown in Fig. 2.4b.  $R_F$  is exponential with the electrode potential  $E$  and it is approximately linear function of  $\Delta V$  or overpotential,  $\eta$  for small excursions. The so-called "micropolarization" experiments or complex impedance measurements can be utilized for observing  $R_F$ 's variation with various constant electrode potentials. The Faradaic leakage resistance plays critical role for both ECs and batteries.

For electrodes based on non-noble metals, it involves nonideal polarization due to anodic corrosion or oxide film. In the case of electrodes based on metals, the possibility of anodic corrosion or oxide film formation at potentials near the  $H_2$  evolution potential would cause nonideal polarizability, which results Faradaic leakage currents in parallel with double-layer charging. In addition, such metals usually have larger exchange current

density for H<sub>2</sub> evolution from water, so they can't be polarized very far cathodically to the reversible hydrogen electrode (RHE) or standard hydrogen electrode (SHE) potentials without appreciable H<sub>2</sub> evolution currents arising.

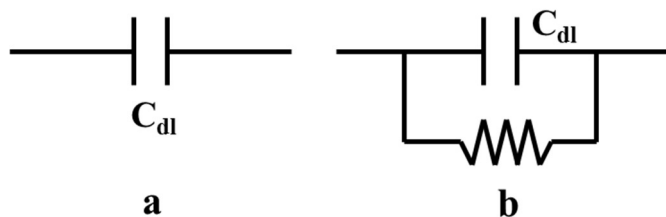


Fig. 2.4 Equivalent circuit for a. ideally polarized electrode and b. electrode with a Faradaic leakage resistance

## 2.2.2 Faradaic (pseudo)supercapacitors

### 2.2.2.1 Origin of Pseudocapacitance

Compared to EDLCs, charge storage mechanism in pseudocapacitors is completely different. Different from EDLCs, where charges accumulate or separate between electrode/electrolyte interface, charges pass across the double layer in pseudocapacitor. For pseudocapacitor, electrosorption processes for some thermodynamic reasons result in yield of capacitance. A derivative  $d(\Delta q)/d(\Delta V)$  or  $dq/dV$ , in which  $\Delta q$  is the extent of charge acceptance, and  $\Delta V$  is the change of potential, can be employed to evaluate a pseudocapacitance. The variations can be formulated and experimentally measured by dc, ac, or transient techniques.

From a thermodynamic point of view, pseudocapacitance originates whenever some property,  $y$ , proportional to charge passed, is related to potential by an equation of the

form

$$y/(1-y)=K \exp(VF/RT) \quad (\text{Eq.2.9})$$

Where the parameters  $K$ ,  $F$ ,  $R$  and  $T$  are Faraday's constant, ideal gas constant and temperature, respectively. And  $y$  (or  $\theta$  and  $X$ ) is the variate of fractional specie that adsorbed on the electrode surface, intercalated into the material by absorption, or converted through an oxidation/reduction coupling system. Each of the above mechanism involves the charge transfer of an electron ( $s$ ) between the ionic species that measured by an extent  $Q$ . The mentioned reactions above depend on the applied potential, which can be related as  $dQ/dV$ . This description is analogous to that of the electric double-layer capacitance.

Grahame proposed the term “pseudocapacity” to describe the reversible discharge of ions (e.g., of  $\text{Na}^+$ ) at high negative potentials at Hg in his 1947 review[21]. The concept is different from that employed here, where extents of Faradaically delivered charges are a function of potential but no continuous currents pass in time. EDLCs exhibit much lower specific capacitance compared to that of pseudocapacitors. On the other hand, pseudocapacitor devices always exhibit some electrostatic double-layer capacitance component proportional to their electrochemically accessible interfacial areas.

#### 2.2.2.2 Types of pseudocapacitance

Conway suggested that pseudocapacitive behavior can result from mainly three mechanisms: (1) intercalation pseudocapacitance, (2) redox pseudocapacitance and (3) underpotential deposition[14, 22].

(i) Intercalation pseudocapacitance

Porous pseudocapacitive electrodes provide spaces for the diffusion and intercalation of ions from the electrolyte. Intercalation pseudocapacitance occurs when ion intercalate into

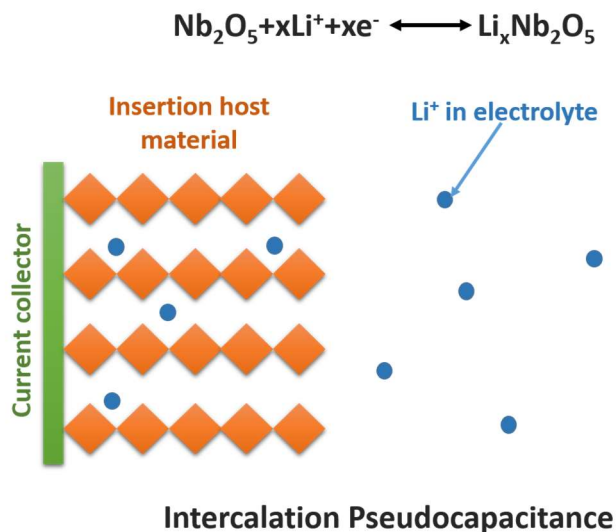


Fig. 2.5 Schematic of intercalation pseudocapacitance based on  $\text{Nb}_2\text{O}_5$  electrodes[22]

to the tunnels or layers of a redox-active material accompanied by a Faradaic charge-transfer without crystallographic phase change. As illustrated in Fig. 2.5, which shows a schematic of intercalation pseudocapacitance based on  $\text{Nb}_2\text{O}_5$  electrodes,  $\text{Li}^+$  ions are able to diffuse and intercalate into the host materials of  $\text{Nb}_2\text{O}_5$  with applying an external potential during charge process, involving charges/electrons transfer. During discharge, a reverse faradaic process occurs that  $\text{Li}^+$  ions departure and separate from the host materials accompanied with donation of electrons to external circuit, and these  $\text{Li}^+$  ions reenter into the electrolyte as their original state. The faradaic process of intercalation pseudocapacitor can be presented by the redox reaction given in Fig. 2.5.

## (ii) Redox pseudocapacitance

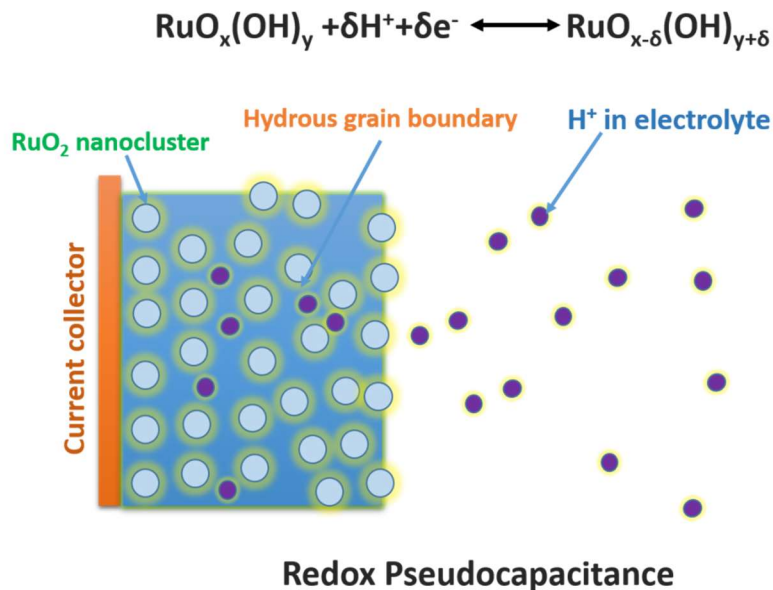


Fig. 2.6 Schematic of redox pseudocapacitance based on  $\text{RuO}_2$  electrodes[22]

The so-called redox pseudocapacitance refers to the electrochemical adsorption of ions onto or near the surface of an active electrode material with a concomitant faradaic charge-transfer. Different with intercalation pseudocapacitance mentioned above, redox pseudocapacitance mainly results from the ions adsorbing onto surface of active materials instead of insertion onto them, and this process is determined by the structure and properties of active materials such as  $\text{RuO}_2$  and  $\text{MnO}_2$ , etc. Electrode material with a higher specific surface area (SSA) is beneficial for accommodating more ions to obtain higher redox pseudocapacitance during charge process. For a typical charge phase of redox pseudocapacitance based on  $\text{RuO}_2$  electrodes, as illustrated in Fig. 2.6, hydrogen ions in electrolyte move towards and electrochemically adsorb onto or near the negatively charged  $\text{RuO}_2$  nanocluster electrode with applying an external potential. A charge transfer

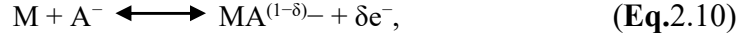
process occurs accompanied with valence state variation of Ru element and electrons obtainment from external circuit in the meantime. Oppositely with charge process, during discharge, hydrogen ions re-enter into electrolytes accompanied with electrons released to external circuit to generate current, and Ru element returns to its origin valence state. The redox reaction for describing the charge-discharge process is given in Fig. 2.6.

### (iii) Underpotential deposition

Underpotential deposition (UPD) occurs when metal ions form an adsorbed monolayer at a different metal's surface well above their redox potential. The process of UPD involves the electrodeposition of metal monolayers on a different metal substrate at certain potentials. The potentials for deposition of metal monolayers on the same metal surface as the sorbate can be significantly more positive than UPD potentials. This phenomena offers benefits for reproducible and precise control of the surface coverage. It also provides possibility for the study of coverage dependent properties including the structure of the metallic adlayer and its electronic properties[23-25].

Lead on the surface of a gold electrode is a classic example of UPD[26]. As it is shown in Fig. 2.7, for an underpotential deposition based on Au electrodes, lead UPD processes take place at potentials that overlap with the onset of hydrogen evolution on gold electrodes. However, the presence of lead on the electrode surface greatly inhibits the hydrogen evolution reaction, as would be expected given the high overpotential for hydrogen evolution on bulk lead electrodes. Lead and gold have very different atomic sizes (lead is ca. 20% larger than gold), which favors the formation of incommensurate adlayers.

Electrosorption occurs when chemisorption of electron-donating anion such as  $\text{Cl}^-$ ,  $\text{B}^-$ ,  $\text{I}^-$ , or  $\text{CNS}^-$  takes place in a process such as:



where M is the electroactive redox materials such as  $\text{RuO}_2$ ,  $\text{NiO}$ ,  $\text{Co}_3\text{O}_4$ ,  $\text{MnO}_2$  or conducting polymers[14, 27-29]. Such an electrosorption reaction of  $\text{A}^-$  anions at the surface of an electrode, and the quantity  $\delta\text{e}^-$  are related to the so-called “electrosorption valence”. Secondly, the exchange of charge across the DL, rather than a static separation of charge across a finite distance, results in oxidation–reduction reactions (indicated as:  $\text{O}_{\text{ad}} + \text{ne}^- \rightarrow \text{R}_{\text{ed}}$ ). The charge,  $\text{ne}^-$ , exchanged in this reaction, and the energy storage is analogous to that of a battery[30].

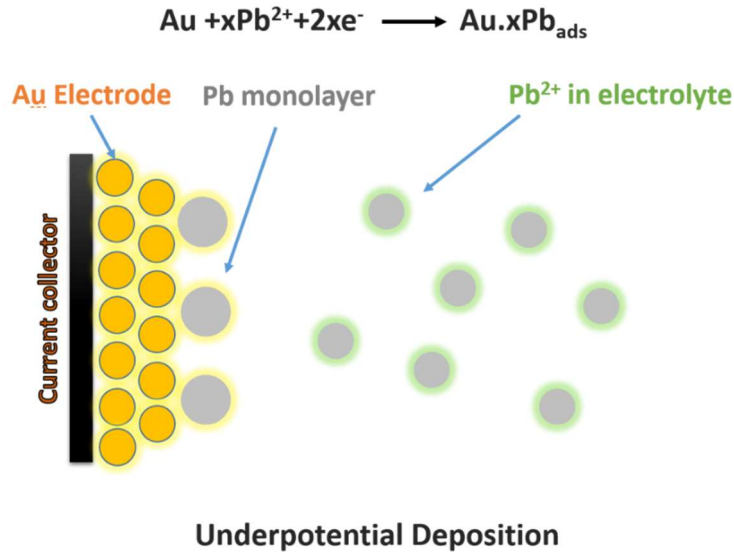


Fig. 2.7 Schematic of underpotential deposition based on Au electrodes[22]

As mentioned above, the most widely used active electrode materials are metal oxides, such as  $\text{RuO}_2$ [31],  $\text{IrO}_2$ [32],  $\text{NiO}$ [33],  $\text{Co}_3\text{O}_4$ [34] and  $\text{MnO}_2$ [35], as well as conducting

polymers (polypyrrole and polyaniline) [36], which are typical examples of pseudocapacitors under extensive research. Three types of faradic processes occur at pseudocapacitor electrodes: reversible adsorption, redox reactions of transition metal oxides and reversible electrochemical doping–dedoping in conductive polymer based electrodes[5].

2.2.2.3 Equivalent circuit representation of pseudocapacitor behavior

For pseudocapacitor, as Fig. 2.8 shows, a Faradaic impedance,  $R_F$ , representing deposition or desorption of an electroactive species (e.g., H or metal adatoms in an underpotential deposition process) is involved in parallel with the double layer capacitance,

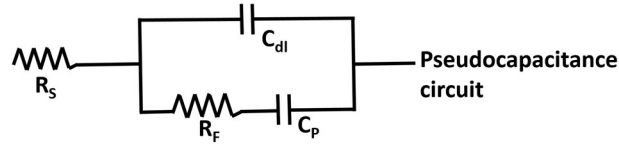


Fig. 2.8 Equivalent circuit of pseudocapacitance

-ce,  $C_{dl}$ . In the simplest analysis, the configuration contains a Faradaic charge transfer resistance  $R_F$  in series with a pseudocapacitance  $C_p$ . The pseudocapacitance is usually potential dependent and determined by the derivative, with respect to potential, of the coverage,  $\theta$ , of adatom species, or more precisely, the charge associated with their deposition or desorption. Alternatively,  $C_p$  can rise in a potential-dependent redox reaction where the relative quantities of Ox and Red species are dependent on potential according to a thermodynamic Nernst equation:

$$E = E^0 + (RT/zF) \ln [Ox]/[Red] \tag{Eq.2.11}$$

Where  $E$  is the potential of an ion of charge  $z$  across a membrane,  $E^0$  is standard potential,  $R$  is ideal gas constant,  $T$  is the temperature in Kelvin,  $F$  is Faradaic's constant, Ox and Red are oxidizing and reducing species, respectively. As in the equivalent circuit discussed earlier, a  $C_P$  can also arise when an overpotential deposition (OPD) process is taking place as a result of the potential dependence of the coverage by an adsorbed intermediate, e.g., H in cathodic  $H_2$  evolution. Then the equivalent circuit must include a desorption equivalent resistance,  $R'_F$  in the above circuit, which may be dependent on the overvoltage.

### 2.2.3 Hybrid electrochemical capacitors

The so-called hybrid supercapacitor contains two types: 1. symmetric hybrids, composed of two similar electrodes that are based on composites such as metal oxides and carbon materials; 2. asymmetric hybrids composed of different positive and negative electrode materials. In the case of asymmetric hybrids the overall cell potential can be increased, resulting in higher energy and power densities[37]. Asymmetric electrode designs are most frequently associated with the combination of electrodes with different storage mechanisms, typically, a capacitive electro-double-layer (EDL) electrode and a battery-type faradaic or pseudocapacitive electrode.

As the Ragone plot shows in Fig. 2.9, hybrid supercapacitors fill the gap of energy density and power density between Li-ion batteries and ordinary symmetric supercapacitors. Its maximum specific power and energy can reach up to approximate 10 kW/kg and 50 Wh/kg, respectively, which are much higher than Li-ion batteries' 500 W/kg and symmetric supercapacitors' 8 Wh/kg. The essential reason is that the

combination of a redox and a double layer electrode will result in “over potential” for the entire device, thus it will largely broaden the voltage window to increase the energy density and power density according to  $E=CV^2/2$ ,  $P=V^2/4ESR$ , where ESR is the equivalent series resistance of the hybrid cell.

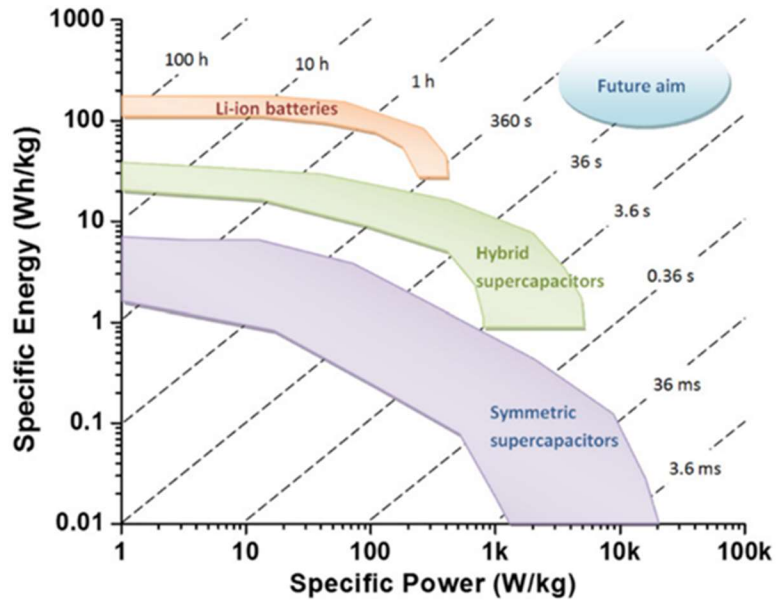


Fig. 2.9 Ragone plot of three major electrochemical energy storage devices. Time constants are shown in dashed line, by dividing the specific energy by the specific power[38].

### 2.2.3.1 Symmetric hybrids

Symmetric hybrid supercapacitors are the most common types of ESs, as shown in Fig. 2.10. Such ECs are composed of two similar composite electrodes, electrolyte between two electrodes, current collector and a separator for avoiding direct contact of the two electrodes. Their electrodes of symmetric cell are usually fabricated using a composite hybrid materials. In pursuit of high capacitance and high energy density storage devices,

hybrid materials have quickly attracted attention based on their power to merge complementary components and properties.

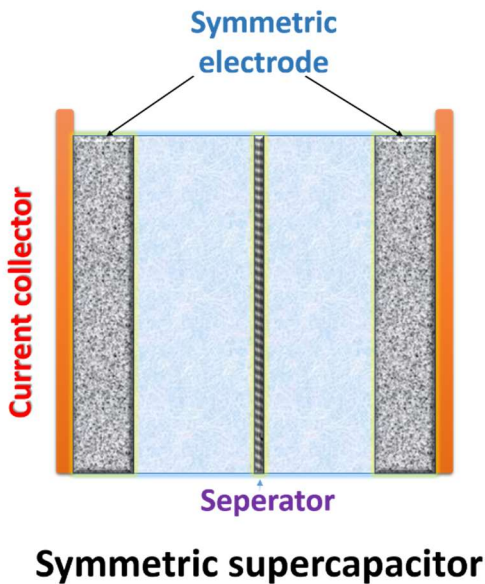


Fig. 2.10 Configuration of symmetric supercapacitor[37]

The pseudocapacitive materials mainly include transition metal oxides and conducting polymers, which involve electrochemical redox reaction as main mechanisms of energy storage, and they are employed in diverse hybrid electrodes. For most of pseudocapacitive materials, poor conductivity becomes a major problem, limiting their performance, thus it greatly decreases their energy conversion efficiency or capacitance retention at high voltage scan rate. Consequently, double layer capacitive materials are utilized for enhancing conductivity and boosting power density of the device.

Many works on fabrication of composite electrodes of hybrid supercapacitors have been reported. The most widely studied composite electrodes are  $\text{MnO}_2/\text{CNTs}$ ,  $\text{MnO}_2/\text{graphene}$  (or reduced graphene oxides),  $\text{MnO}_2/\text{activated carbon}$ , polypyrrole/CNTs, graphene (or

rGO)/CNTs and activated carbon/CNTs, etc[39-44]. Meanwhile, highly conductive noble metals are also utilized for enhancing capacitance of composite electrodes. Meng et, al[45] demonstrated the design and facile fabrication of an ultrathin flexible all-solid-state symmetric hybrid supercapacitor with a total thickness of less than one micrometer, based on an interesting nanocomposite structure of polypyrrole (PPy)-decorated nanoporous gold (NPG) in a leaf form. Because of the fast responses to ions and electrons, this device exhibits extraordinary volumetric capacitance and high power and energy densities.

### 2.2.3.2 Asymmetric hybrids

In recent years, several types of so-called hybrid electro-chemical capacitors (HECs) with an asymmetrical configuration, as shown in Fig. 2.11, containing a double layer carbon

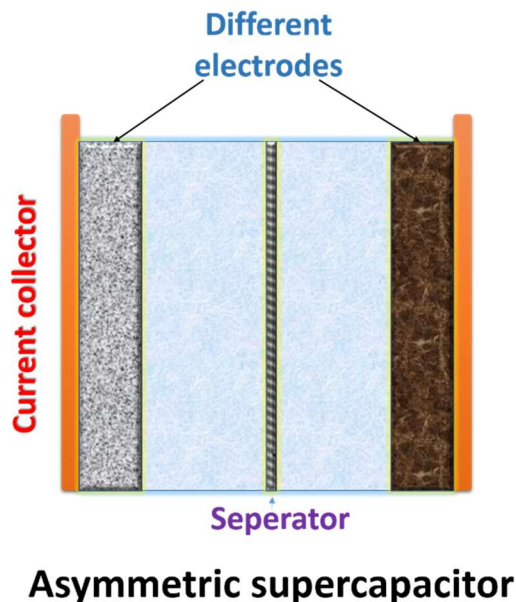


Fig. 2.11 Configuration of asymmetric supercapacitor[37]

material and a pseudocapacitive material, have attracted significant attentions. Most of

the HECs developed to date have used pseudocapacitive materials as the cathode and double-layer capacitive materials as the anode. The pseudocapacitive electrodes accumulate charge through faradic electrochemical process (redox reaction), which can not only increase the specific capacitance of the capacitor, but also extends the working voltage. In an advanced HEC, the potential range at the cathode is extended to the whole potential window of activated carbon (AC), specifically from 1.5 to 4.5 V vs. Li/Li<sup>+</sup>, which is a wide potential range compared with conventional EC, where the potential ranges from 0.8 to 2.7 V vs. Li/Li<sup>+</sup>. HECs can also be assembled using two non-similar mixed metal oxides or conducting polymers.

Asymmetric hybrid capacitors include various combinations of positive and negative electrode materials such as conducting polymer/metal oxide, metal oxide/carbon and conducting polymer/carbon material[30, 46].

By introducing a carbon-based electrode, asymmetric supercapacitor is able to extend to a much wider voltage window due to overpotential of carbon electrode[47]. The energy density of an EC is equal to  $CV^2/2$ , where  $C$  is capacitance and  $V$  is the working voltage window. In this case, energy and power density of the device would be largely enhanced comparing to that of symmetric supercapacitors. Hong et al.[48] demonstrated for the first time a hybrid system based on MnO<sub>2</sub> as positive electrode and activated carbon as negative electrode, allowing the operating voltage in aqueous medium to be extended up to 2 V. V. Khomenko et al. [49] presented a deep analysis of the storage mechanism of activated carbon under negative polarisation and manganese oxide under positive polarisation. The understanding of the processes taking place in both electrodes of the

asymmetric capacitor during charge and discharge allowed optimization of the system. The unique pseudocapacitive properties of activated carbons under negative polarisation in aqueous medium were observed. The voltammetric analysis showed that high overpotential values for H<sub>2</sub> evolution could be reached, that allowed significant increase in the potential window. Hydrogen produced by water decomposition at potentials lower than the thermodynamic value is immediately adsorbed in the carbon porosity, being reversibly electrooxidized during the anodic scan. In this case, the pseudocapacitive properties of activated carbon are related with the redox mechanism of hydrogen in the pores.

#### 2.2.4 Summary of different types of supercapacitors

The Table 1 demonstrates characteristics of different types of ES. EDCLs have relatively lower capacitance but with better cycling ability, while pseudocapacitors have higher capacitance but with lower rate capability and hybrid capacitor compromises between EDCLs and pseudocapacitors with moderate power and energy density.

Table 1. Comparison of different types of ECs[50]

Type of supercapacitor	Electrode material	Charge storage mechanism	Merits/shortcomings
EDLCs	Carbon	Electrochemical double layer, non-Faradaic process	Good cycling stability, good rate capability, low specific capacitance, low energy density
Pseudocapacitors	Redox metal oxide or redox polymer	Redox reaction, Faradaic process	High specific capacitance, relatively

				high energy density, relatively high power density, relatively low rate capability
<b>Hybrid capacitors</b>	<b>Asymmetric hybrid</b>	Anode: pseudocapacitance materials, cathode: carbon	Anode: redox reaction, Cathode: EDL	High energy density, high power density and good cyclability
	<b>Symmetric composite hybrid</b>	Redox metal oxide/carbon or redox polymer/carbon	Redox reaction plus EDL	High energy density, moderate cost and moderate stability

## 2.3 Materials for supercapacitors

The selection of electrode materials for fabrication of ES is critical in determining the electrochemical performance of ES. Material's structure, electrochemical properties, microstructure and morphology are important selection criterion. For EDCLs, the charge storage is a surface process, and the surface characteristics of the electrode greatly influence the capacitance of the cell. Carbon is the most widely used electrode material in EDLC for their high SC, good conductivity and low chemical activity. On the other hand, transition metal oxides or conducting polymers are most used in pseudocapacitors for their promising electrochemical activity. Hybrid supercapacitors combine both double-layer and redox-based materials.

### 2.3.1 Carbon materials for electrode of EDLCs

Mechanism of double-layer capacitor is based on the accumulation or separation of

charges at the electrode/electrolyte interface, thus it requires a high specific surface area, low electrochemical activity and high porosity electrode. The most widely used materials for EDLCs are activated carbon (AC), carbon nanotubes (CNTs), graphene, carbon aerogel (CAGs), template carbons and carbon-based composites. Carbon materials can provide better conductivity as well as higher specific surface area but with a drawback of relatively low capacitance.

Numerous works have been conducted in various carbon-based materials such as ACs[44], CAGs [51], graphites[52], CNTs[7, 9, 44, 53], graphene[40, 53, 54], carbon nanofibers (CNFs) [55, 56] and nano-structured carbons [57, 58] for use as the electrode materials of ECs because of their accessibility, easy process ability, relatively low cost, non-toxicity, high chemical stability, and wide temperature range. Based on these materials, different methodologies have been applied to increase their SSA or tailoring pore size distribution (PSD). This has resulted in considerable improvement of energy, power, and operation parameters of ECs.

#### 2.3.1.1 EDLCs based on AC (activated carbon)

ACs are among the best candidates for utilization in ES fabrication due to their good electrical properties, high SC and low cost. The abundant source of carbonaceous materials (including wood, nutshell and coal, etc.) provides possibility for production of ACs through physical (thermal) and/or chemical activation process. During physical activation, carbon precursors are treated with oxidation gases such as ammonia, steam and air at high temperature (from 700 to 1200 °C). For chemical activation process, the fabrication temperature is usually lower in the range from 400 °C to 700 °C with addition

of activating agents such as potassium hydroxide, sodium hydroxide, phosphoric acid and zinc chloride. ACs with different physicochemical properties possessing high surface areas reaching up to  $3000 \text{ m}^2 \text{ g}^{-1}$  have been produced. A broad pore size distribution including micropores ( $< 2 \text{ nm}$ ), mesopores ( $2\text{-}50 \text{ nm}$ ) and macropores ( $450 \text{ nm}$ ) inside of ACs produced by activation have been developed and studied[59-63].

Treatment of activated carbon materials influences the structure and electrochemical performance of the electrode. The accessibility of the pores by the electrolyte is very important for EDLCs[64]. Micropores have been proved to play a critical role in benefiting electrolyte ions diffusion for improving capacitance performance by numerous studies. Largeot et al. recently demonstrated the proof that a comparable pore size and ion size resulted a maximum EDL capacitance for an EDLC fabricated by carbide-derived-carbons (CDCs) using a neat  $\text{EMI}^+, \text{TFSI}^-$  solution (EthylMethyl Immidazolium, trifluoro-sulfonate Imide, shown in Fig. 2.12[65].

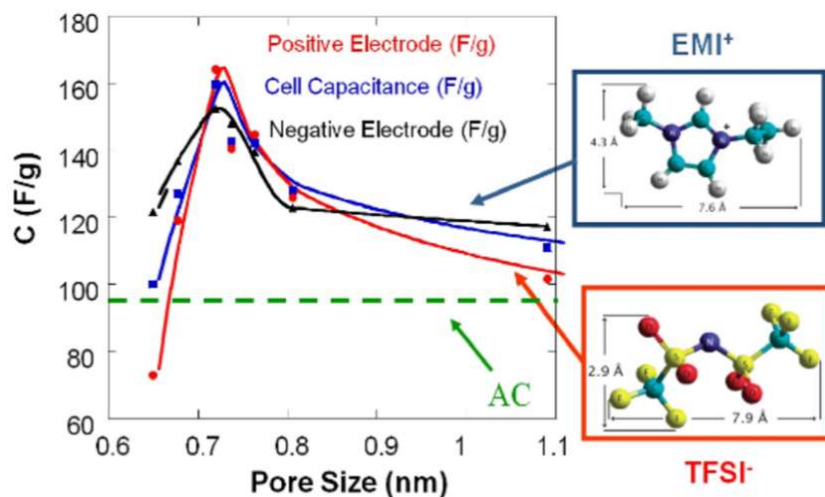


Fig. 2.12 Normalized capacitance change vs the pore size of the CDC samples prepared at

different temperatures [65]

Since solvation shell is not defined by the presence of solvent molecules, the size of the ions is defined by the bare ion size in this electrolyte. The maximum capacitance, which was found when the pore size of carbon matches with that of ions (as shown in Fig. 2.12), is 60% higher than the capacitance of commercial ACs (dashed line in Fig. 2.12). These results explained the charge storage mechanism in EDL materials, where both pore walls are covered by adsorbed ions and partially desolvated ions can be considered as aligned in the pores.

#### 2.3.1.2 Electrodes based on carbon nanotubes (CNTs)

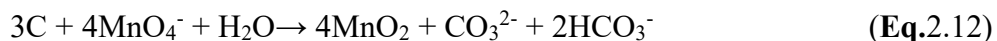
Carbon nanotubes (CNTs) have emerged as the wonder materials of the new century due to their unique physical and chemical properties. In addition to the advantages conferred by miniaturization, carbon based nanoelectronics promise greater flexibility compared to conventional silicon electronics, one example being the extraordinarily large variety of carbon structures exemplified in organic chemistry[66].

With nanotubes, the percolation of the active particles is more efficient than with the traditional carbon blacks which are generally used for the manufacturing of electrodes. Additionally, the ions are much easier to diffuse into active surface through the channel resulted from the open mesoporous network because of the unique morphology of CNTs. These properties are beneficial for lowering the equivalent series resistance (ESR), thus CNTs have been widely utilized in ES application. Finally, since the nanotubular materials are characterized by a high resiliency, the composite electrodes can easily adapt

to the volumetric changes during charge and discharge, that improves drastically the cycling performance [67].

The specific capacitance of CNTs is too low to be utilized as ES electrode, thus the interest in CNT is related to their application as a conductive additive attributed to their high conductivity and low percolation limit. Therefore, many investigations were focused on the combination of CNTs and metal oxides/polypyrrole as composite electrodes for ECs [68-72].

Many approaches have been developed for fabrication of CNTs based composite materials. The composite materials were prepared by reduction of  $\text{Mn}^{7+}$  species in  $\text{KMnO}_4$  solutions, containing CNT, to form  $\text{MnO}_2$  coated CNT[73-75]:



Further development of this method allowed the fabrication of flexible ES devices[76]. The composites with various  $\text{MnO}_2$  contents were obtained[75]. It was demonstrated[77] that reaction (2.12) results in a chemical degradation and reduced electrical conductivity of CNT. In order to reduce the chemical degradation of CNT, ethanol was used as a reducing agent[77] for  $\text{KMnO}_4$ . In another strategy, cathodic electrosynthesis of  $\text{MnO}_2$  was performed from  $\text{KMnO}_4$  solutions on CNT coated substrates, prepared by a chemical vapor deposition[78]. However, relatively low active mass loading was achieved in this method[78].

It was found that  $\text{MnO}_2$  and composite  $\text{MnO}_2$ -CNT electrodes showed ideal capacitive behavior in a voltage window of 1 V in aqueous electrolytes. The development of

asymmetric cells[79, 80], containing MnO<sub>2</sub> positive electrodes and activated carbon (AC) negative electrodes, allowed enlarged voltage window and improved power-energy characteristics of the ES devices. In order to achieve high SC, CNT must be well dispersed in the metal oxide matrix and CNT concentration in the composites must be optimized.

### 2.3.1.3 Summary of data for electrodes based on carbon materials

Table 2 Onion-like carbon, carbon nanotubes, graphene, activated carbons, and carbide-derived carbons used in EDLCs[60]

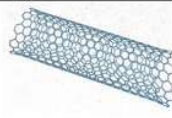
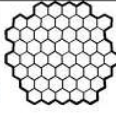
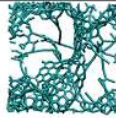
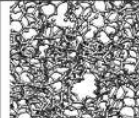
Material	Carbon onions	Carbon nanotubes	Graphene	Activated carbon	Carbide derived carbon	Templated carbon
Dimensionality	0-D	1-D	2-D	3-D	3-D	3-D
Conductivity	High	High	High	Low	Moderate	Low
Volumetric Capacitance	Low	Low	Moderate	High	High	Low
Cost	High	High	Moderate	Low	Moderate	High
Structure						

Table 2 is a summary for properties of carbon based materials. AC has relatively higher specific capacitance than other carbon materials but with lower conductivity, while CNT and graphene have lower SC with higher conductivity, thus carbon black, CNT or graphene are always used as additives to enhance AC's conductivity in EDLC electrodes.

### 2.3.2 Redox-based materials

As elaborated above, materials based on an electrical double-layer mechanism have limited specific capacitance, typically in the range of 10-50  $\mu\text{F cm}^{-2}$ , for a real electrode surface. Because pseudocapacitance may be 10–100 times greater, ECs made of redox-

active materials bearing pseudocapacitance are highly desirable as the next generation of ES. They not only store charges in the double layer, as a conventional ES electrode does, but also undergo fast and reversible surface redox reactions (faradaic reactions). Therefore, considerable efforts have been devoted in recent years to developing electrode materials with pseudocapacitance [5]. This kind of material is generally classified into two types: conducting polymers and electroactive metal oxides.

### 2.3.2.1 Conducting polymers

Conducting polymers are rendered conductive through a conjugated bond system along the polymer backbone. They are typically formed either through chemical oxidation of the monomer (for example with iron chloride) [81] or electrochemical oxidation of the monomer. Two oxidation reactions occur simultaneously—the oxidation of the monomer

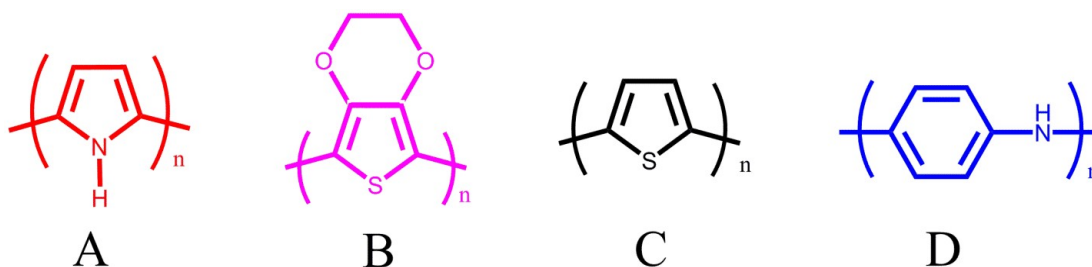


Fig 2.13. Various conducting polymer structures. A, polypyrrole (PPy), B, poly(3,4-ethylenedioxythiophene) (PEDOT), C, polythiophene (PTh), D, polyaniline (PAni)

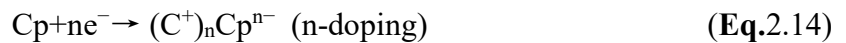
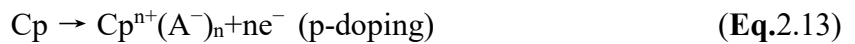
and the oxidation of the polymer with the coincident insertion of a dopant/counter ion (e.g.  $\text{Cl}^-$ ). The dopant or doping level (in this p-type conducting polymer) is typically below 1 dopant per polymer unit: approximately 0.3-0.5, i.e., 2-3 monomer units per dopant. This is limited by how closely the positive charges (so-called polarons) can be spaced along

the polymer chain. The polymers that are most commonly studied for use in ES devices are polypyrrole, polyaniline, and derivatives of polythiophene [81-83], and their chemical structures are showing in Fig. 2.13. The typical dopant level for these polymers, as well as their typical specific capacitances and voltage ranges, are given in Table 3.

Table 3. Comparison of different polymers in electrochemical properties[82]

Polymer	Potential limits (V)	Specific capacitance (F g <sup>-1</sup> )	Conductivity (S cm <sup>-1</sup> )	Doping type
PPy	-0.5 - 0.4	620	40-200	P-doping
PEDOT	-0.4 - 0.6	210	300-500	n,P-doping
PTh	-0.2 - 0.6	485	300-400	n,P-doping
Pani	0 - 0.8	750	0.1-5	P-doping

Conducting polymers draw numerous attentions in the application for ECs due to their excellent conductivity, fast charge-discharge rate, low band gaps, suitable morphology and low cost. The noticeable advantages for conducting polymers are their ease for massive fabrication and flexibility in application. The mechanism of charge-discharge process for conducting polymer is based on doping-dedoping process. Conducting polymers can be p-doped with (counter) anions when oxidised and n-doped with (counter) cations when reduced. The simplified equations for these two charging processes are as follows [81]:



The discharge reactions are, of course, the reverse of the above equations. Complications can occur given that on oxidation a certain degree of cation inclusion (mixed doping) is possible under certain circumstances.

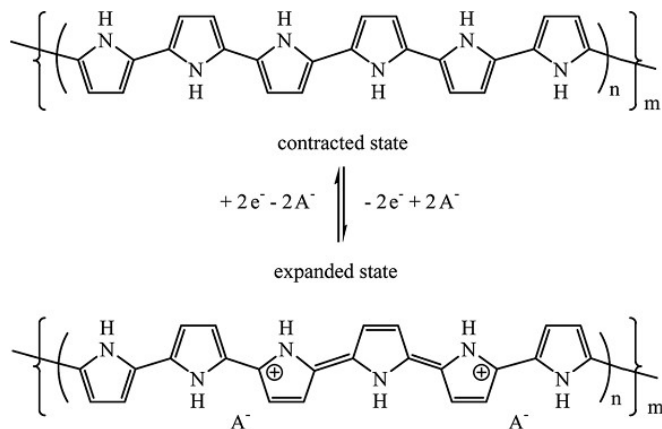


Fig. 2.14 The charge-discharge process of PPy [84]

PPy offers a greater degree of flexibility in electrochemical processing than most conducting polymers, and consequently the material has been the subject of much research as an ES or battery electrode. The fundamental mechanism of charge-discharge for polypyrrole hasn't been fully understood, here a hypothesis is described to elaborate the charge-discharge principle of conducting polymer being used as ES electrode. The following graph Fig. 2.14 demonstrates the doping-dedoping process of polypyrrole[43, 85].

### 2.3.2.2 Transition metal oxide materials

Another important type of redox-based materials for pseudocapacitor electrode fabrication are transition metal oxides, which can provide higher energy density for ES than conventional carbon materials and better electrochemical stability than polymer

materials. They not only store energy like electrostatic carbon materials but also exhibit electrochemical faradaic reactions between electrode materials and ions within appropriate potential windows [86].

The general requirements for metal oxides in ES applications are: (1) the oxide should be electronically conductive, (2) the metal can exist in two or more oxidation states that coexist over a continuous range with no phase changes involving irreversible modifications of a 3-dimensional structure, and (3) the protons can freely intercalate into the oxide lattice on reduction (and out of the lattice on oxidation), allowing facile interconversion of  $O^{2-}$  and  $OH^-$  [5]. The most widely used metal oxides in application of ES are ruthenium oxide, manganese oxide, cobalt oxide, nickel oxide, and vanadium oxide, among which, manganese oxides ( $MnO_2$ ) are demonstrated to be one of the most promising electrode materials for ECs because of such superior characteristics as large specific capacitance, environmentally benign nature, natural abundance and low cost [55]. The theoretical specific capacitance of  $MnO_2$  based on one-electron redox reaction per Mn atom is estimated to be 1370 F/g [87]. Thus  $MnO_2$  is selected as electrode material in our investigations, which will be addressed below in details.

The pioneering work on the pseudocapacitive behavior of manganese oxide in an aqueous solution was published in 1999 by Lee and Goodenough [88]. The charge storage mechanism of  $MnO_2$  has been elaborated by many people, Patrice Simon and Yury Gogotsi [8] presented excellent explanation in their review paper. They suggested that the charge storage mechanism of  $MnO_2$  is based on surface adsorption of electrolyte cations  $C^+$  such as  $K^+$ ,  $Na^+$  and proton incorporation. The redox reaction during charge-discharge

process is given as following:



The cations from electrolyte move forward to and adsorb on the  $\text{MnO}_2$  surface under the external electric field force during charge process (reduction process), which will result a valence decrease of  $\text{MnO}_2$ , thus the energy has been stored. The discharge is a quickly reversible process (oxidation process), which means a restoration of both  $\text{MnO}_2$  and the cations, and the motions of ions accumulate current for outputting.

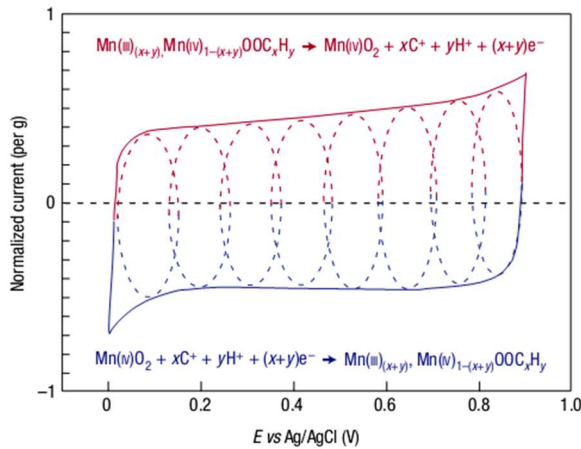


Fig. 2.15 Cyclic voltammetry for a  $\text{MnO}_2$ -electrode cell in mild aqueous electrolyte (0.1 M  $\text{K}_2\text{SO}_4$ ) shows the successive multiple surface redox reactions leading to the pseudo-capacitive charge storage mechanism [8].

The cyclic voltammogram of  $\text{MnO}_2$  film in aqueous electrolyte is shown in Fig. 2.15. The red (upper) part is related to the oxidation from Mn(III) to Mn(IV) and the blue (lower) part refers to the reduction from Mn(IV) to Mn(III). The main problem of  $\text{MnO}_2$  electrode is its low conductivity. High specific capacitance could only be achieved for thin films. To improve the rate capability of  $\text{MnO}_2$ , our group is studying the small-sized  $\text{MnO}_2$

particles uniformly dispersed on conductive and porous carbonaceous materials with a high SSA[8].

Besides  $\text{MnO}_2$ , another promising material  $\text{Bi}_2\text{O}_3$  and its composites also draw attentions for their novel capacitive properties as negative electrodes[89-94] of aqueous ES. The cyclic voltammogram of  $\text{Bi}_2\text{O}_3$  electrodes deviated significantly from ideal box shape and showed redox peaks[89, 90, 93]. Thin  $\text{Bi}_2\text{O}_3$  films, prepared by electrodeposition[89], showed a capacitance of  $98 \text{ F g}^{-1}$  ( $0.022 \text{ F cm}^{-2}$ ) in NaOH electrolyte. The specific capacitance of  $255 \text{ F g}^{-1}$  was reported for  $\text{Bi}_2\text{O}_3$  – graphene composite[90]. The charging mechanism[95, 96] of  $\text{Bi}_2\text{O}_3$  was described by the reaction:



where  $\text{A}^+ = \text{Li}^+, \text{Na}^+$ . Recently an asymmetric ES was reported[96], containing  $\text{MnO}_2$  positive electrode and  $\text{Bi}_2\text{O}_3$  negative electrode, which showed a specific capacitance of  $97 \text{ mF cm}^{-2}$ . The literature data on capacitive properties of Mn and Bi oxides have generated our interest in the investigation of complex oxides, such as  $\text{BiMn}_2\text{O}_5$ . The investigation of complex oxides is now an important avenue[97-99] for the development of advanced electrode materials for ES.

$\text{BiMn}_2\text{O}_5$  has been investigated for its multiferroic properties in the past[100-108]. The investigations of dielectric properties of  $\text{BiMn}_2\text{O}_5$  revealed high dielectric constant[107] in the range of  $10^5$ - $10^6$  at room temperature, which should be promising for applications in capacitors. In this dissertation,  $\text{BiMn}_2\text{O}_5$  and MWCNTs will be firstly used as ES positive electrode with expected higher specific areal capacitance and volumetric

capacitance due to its higher dielectric constant and better conductivity.

### 2.3.3 Composite electrodes and hybrid configurations

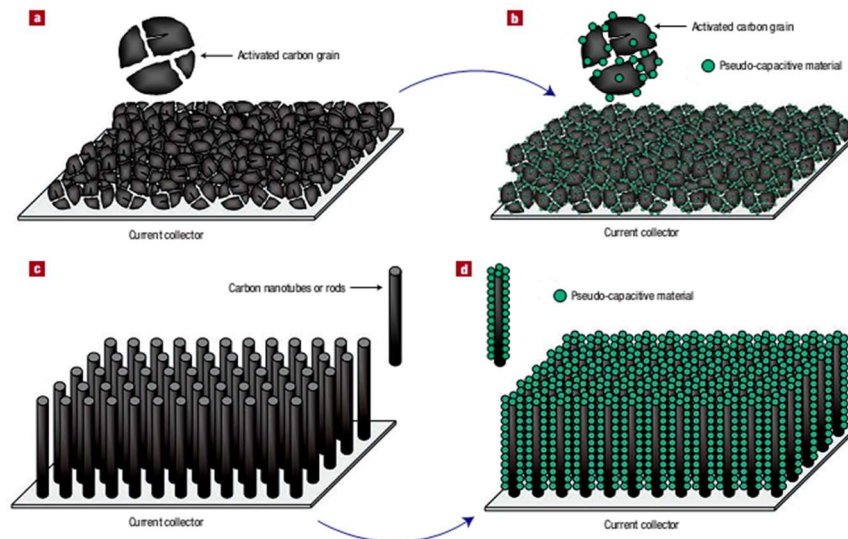


Fig. 2.16 Possible strategies to improve both energy and power densities for ECs. a) carbon activation and b) decorating with pseudo-capacitive materials on porous carbon; c) highly ordered high surface area carbon nanotubes and d) deposit of pseudo-capacitive materials on carbon nanotubes [8].

As stated before, carbon materials have many advantages but with drawback of low capacitance, the capacitive behavior could be further improved by combining carbon with pseudocapacitive materials. Such combination utilized the high specific area and high conductance of carbon materials as well as high capacitance of pseudocapacitive materials.

Composite electrodes consist of one type of materials incorporated into another within the same electrode. Thin film synthesis or high surface area capacitive material can decorate

with nano-sized pseudo-capacitive material. The typical strategies to make composite materials were shown in Fig. 2.16. These composite electrodes offer opportunities to increase energy density and compete with carbon-based EDLCs.

Hybrid electrode configurations consist of two different electrodes made of different materials. An appropriate electrode combination can increase the cell voltage, further contributing to improvement in energy and power densities. Currently, two different approaches to hybrid systems have suggested: (A) pseudo-capacitive metal oxides with a capacitive carbon electrode, and (B) lithium-insertion electrodes with a capacitive carbon electrode. In our case, the first approach is presented.

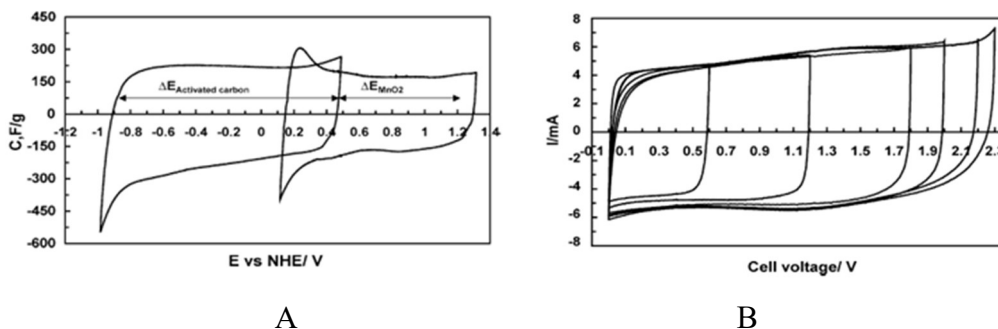


Fig. 2.17 Cyclic voltammograms in (A) a three-electrode cell using  $\text{MnO}_2$  or activated carbon as working electrode, (B) an asymmetric  $\text{MnO}_2$ /activated carbon cell [49]

The possibility to achieve a much broadened voltage window is the advantage of an asymmetric hybrid capacitor. As the cyclic voltammograms in Fig. 2.17 demonstrate, for a single activated carbon or  $\text{MnO}_2$  electrode, their voltage window only limits in no more than 1.2 V, since higher voltage would result in hydrogen/oxygen evolution around electrode due to decomposition of  $\text{H}_2\text{O}$ . By combination of activated carbon and  $\text{MnO}_2$ ,

Fig 2. 17 B, the voltage window for the whole device can reach up to 2.2 V with a box-like CV shape, which brings a much higher energy density and power density due to  $E=1/2 CV^2$  and  $P=V^2/4 ESR$ , where ESR is equivalent series resistance.

#### 2.3.4 Summary of different materials as electrode for supercapacitor

Table 4 Different materials as electrode for supercapacitor[1]

Electrode materials	Surface area	Pore size distribution	Specific capacitance	Conductivity	Rate capability	Stability	Cost
Carbon	High	Various ways to tailor	Low	High	High	Good	Low
Redox-based materials	Normally low	Difficult to tailor	High (metal oxide), moderate (conducting polymer)	Low (metal oxide), moderate (conducting polymer)	Low	Poor	High
Metal oxide-carbon composite	Normally controlled by a carbon support	Various ways to tailor	High	Tunable, depending on the carbon support	Good	Good	Moderate

## 2.4 Dispersion and electrophoretic deposition (EPD)

### 2.4.1 Categorization and mechanism of dispersion

Dispersion or stabilization is critical for nanomaterials synthesis and applications in ECs,

since a well dispersed material or composite electrode provides larger surface areas with more accommodation for ions diffusion and charges transfer. There are two major type of stabilization: electrostatic stabilization and steric stabilization.

Stability of colloids depends on the interaction between the particles during a collision, in which Brownian motion always causes colloidal particles to collide with each other frequently in a dispersion medium. Two basic interactions determine stability of colloids: attraction and repulsion. When the main interaction is dominated by attraction, the colloidal particles are easily adhered to each other and agglomerated together. When the other interaction dominates, the particles will be repulsive and dispersed to form stable suspension. These two interactions are caused by Van der Waals forces existing between colloidal particles. Colloidal dispersion can only be stable when a sufficiently strong repulsive force counteracts the Van der Waals attraction. Van der Waals forces are generated from three different origins including permanent dipole-induced dipole (Debye) interactions, permanent dipole-permanent dipole (Keesom) forces and transitory dipole-transitory dipole (London) forces. Comparing to the other two forces, London forces (VDWL) have longer range attractions, thus its magnitude and range (between 5-10 nm in normal colloidal systems) determines stabilization of colloidal particles.

#### 2.4.1.1 Electrostatic stabilization

Coulombic repulsion between colloidal particles provides an effective way to counterbalance the VDWL attraction in polar suspensions. Ionic groups from molecules or additives can attach and adsorb to particle surface to form a charged layer based on different mechanisms. Since charged particles naturally trend to electroneutrality, an

equal number of oppositely charges form surrounding the prior charges to give additional charge-neutral double layers.

(i) Electric double layers

Electric Double Layer is the layer surrounding a particle of the dispersed phase and including the ions adsorbed on the particle surface and a film of the countercharged dispersion medium. For instance, negatively charged ions in the dispersion medium move and adsorb on surfaces of colloidal particles, and the particles will attract positively charges layer surrounding the previous adsorbed negative charge layer. Electric double layers play critical role in determining stabilization of colloidal system.

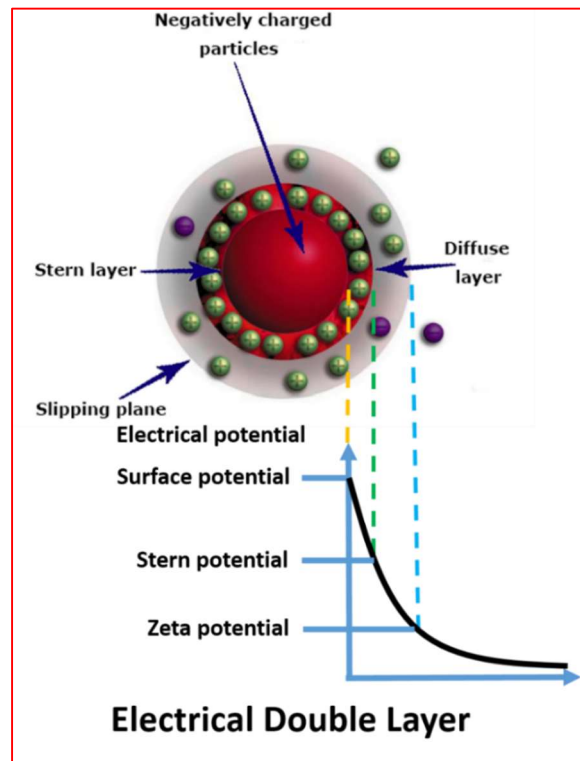


Fig. 2.18 Electrical double layer and potential drop around a colloidal particle[105]

As Fig. 2.18 shows, an electric double layer consists three parts: slipping plane (a conventionally introduced slipping plane forms to separate mobile fluid from fluid that remains attached to the surface), Stern layer - counterions (charged opposite to the surface charge) attracted to the particle surface and closely attached to it by the electrostatic force and diffuse layer - a film of the dispersion medium (solvent) adjacent to the particle. Diffuse layer contains free ions with a higher concentration of the counterions. The ions of the diffuse layer are affected by the electrostatic force of the charged particle.

The value of the electric potential at the slipping plane is called Zeta potential, which is very important parameter in the theory of interaction of colloidal particles. When all the particles have a large negative or large positive charge, they will repel each other, and so the suspension will be stable.

If the zeta potential is low the tendency for flocculation is increased. Another important consideration when discussing zeta potentials is pH; in fact, quoting a zeta potential without an accompanying pH is almost meaningless. The electrical potential within the Electric Double Layer has the maximum value on the particle surface (Stern layer). The potential drops with the increase of distance from the surface and reaches 0 at the boundary of the Electric Double Layer (Fig. 2.18).

#### (ii) DLVO theory

The DLVO theory is named after Boris Derjaguin and Lev Landau, Evert Verwey and Theodoor Overbeek. As discussed above, in liquid dispersion media, ionic groups can adsorb to the surface of a colloidal particle forming charged layer. To maintain

electroneutrality, an equal number of counter-ions with the opposite charge will surround

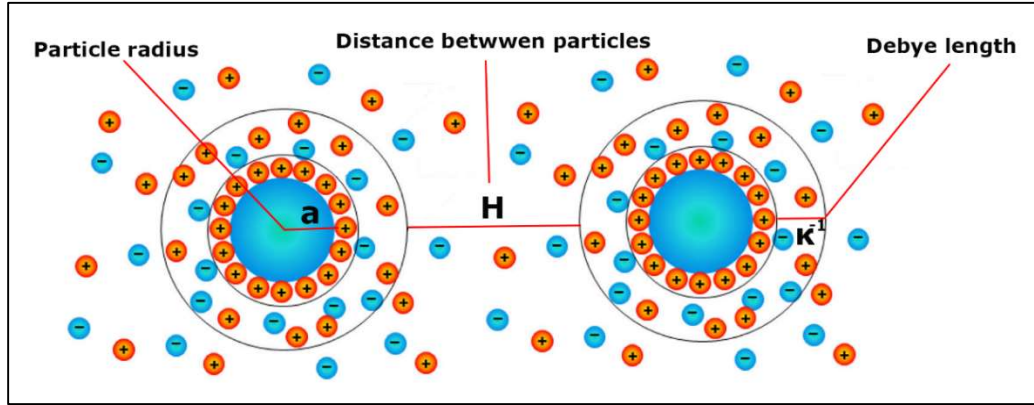


Fig. 2.19 Configuration of two colloidal particles in an ionic electrolyte suspension[109]

the colloidal particles and give rise to overall charge-neutral double layers. In charge stabilization, it is the mutual repulsion of these double layers surrounding particles that provides stability. Fig. 2.19 shows the general configuration of two adjacent colloidal particles[109].

Waals attraction energy ( $V_A$ ) and electrostatic double layer repulsion energy ( $V_R$ ) exist between two particles in the meantime. The total internal energy between the two particles ( $V_T$ ) in suspension was given in Eq.2.12.

$$V_T = V_A + V_R \quad (\text{Eq.2.17})$$

And the attraction energy ( $V_A$ ) and repulsion energy ( $V_R$ ) can be represented by the following equations:

$$V_A = -A \frac{a}{12\pi H} \quad (\text{Eq.2.18})$$

$$V_R = 2\pi\epsilon\epsilon_0 a\psi^2 \ln \left[ 1 + e^{-\kappa H} \right] \quad (\text{Eq.2.19})$$

Where  $A$  is the Hamaker constant,  $a$  is the particle radius,  $H$  is the distance between two slipping planes,  $\varepsilon$  and  $\varepsilon_0$  are relative permittivity and permittivity in vacuum, respectively,  $\pi$  is the solvent permeability,  $\psi$  is the zeta potential, and  $\kappa$  is a function of the ionic composition, which is defined as the reciprocal of Debye length:

$$\kappa = \left( \frac{e_0^2 \sum n_i z_i^2}{\varepsilon \varepsilon_0 k T} \right)^{1/2}, \quad (\text{Eq.2.20})$$

in which  $n_i$  is the concentration of ions with valence of  $z_i$ , and  $k$  is Boltzmann constant. The total energy of two particles can be represented by Fig. 2.20, which is composed by attraction energy and repulsion energy.

The combination of the two energies is a function of distance from the surface of a spherical particle. At a distance far from the solid surface, both van der Waals attraction potential and electrostatic repulsion potential reduce to zero. Near the surface is a deep minimum in the potential energy produced by the van der Waals attraction. A maximum is located a little farther away from the surface, as the electric repulsion potential dominates the van der Waals attraction potential. The maximum is also known as repulsive barrier.

It should also be noticed that Debye length will be decreased by increasing concentration of ions of the dispersion medium, resulting a thin electric double layer and shorter surface distance  $H$ . If the surface distance is decreased to the range which attraction energy dominates, particles are easy to have irreversible hard flocculation. This accounts for the fact that most charge-stabilized dispersions coagulate when increasing the ionic strength

of the dispersion medium [3]. Hence, one great disadvantage of charge stabilization of

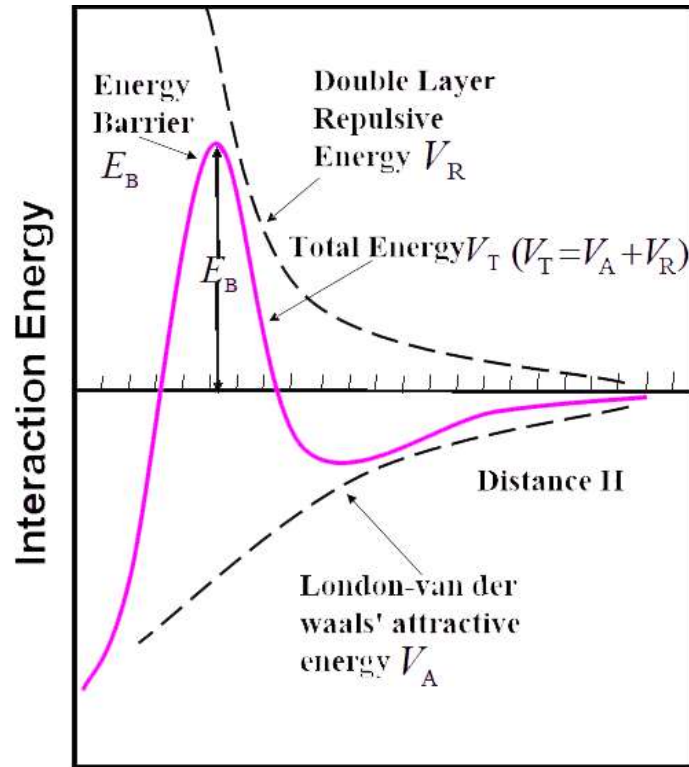


Fig. 2.20 Energy variation with distance between two colloidal particle surfaces

particles is its great sensitivity to the ionic strength of the dispersion medium. In addition, the DLVO theory only works in polar liquid which can dissolve electrolytes. However, due to the advantages in simplicity and cost price, charge stabilization is still widely used in stabilizing dispersions in aqueous media.

#### 2.4.1.2 Polymeric stabilization

Another principal stabilization mechanism is based on polymeric dispersion and stabilization. Different with electrostatic stabilization, polymers with molecular weights beyond 10000 D are in the excess of the range of the VDWL attraction, which means that

DLVO theory is not applicable for these polymer molecules. The end of long chain of these polymer molecules can easily attach to the surfaces of particles to impart colloidal stability [110]. For polymeric stabilization of colloidal dispersion, there are two basic mechanisms: steric stabilization and depletion stabilization.

(i) Steric stabilization

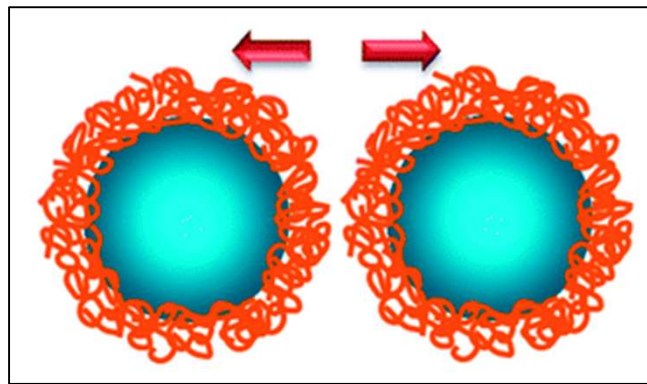


Fig. 2.21 Schematics of steric stabilization [111]

Fig. 2.21 shows mechanism of steric stabilization, which is achieved by attaching (grafting or chemisorption) the end of long chain of macromolecules to the surfaces of particles. The stabilization due to the adsorbed layers on the dispersed particle is generally called steric stabilization [111].

(ii) Depletion stabilization

Depletion stabilization of colloidal particles is imparted by macromolecules that are free in solution (Fig. 2.22). The study of this type of stabilization is still in its initial stage. Electrostatic and steric stabilization can be combined as electrosteric stabilization. The origin of the electrostatic component may be a net charge on the particle surface (Fig

2.23a) and/or charges associated with the polymer attached to the surface (i.e. through an-

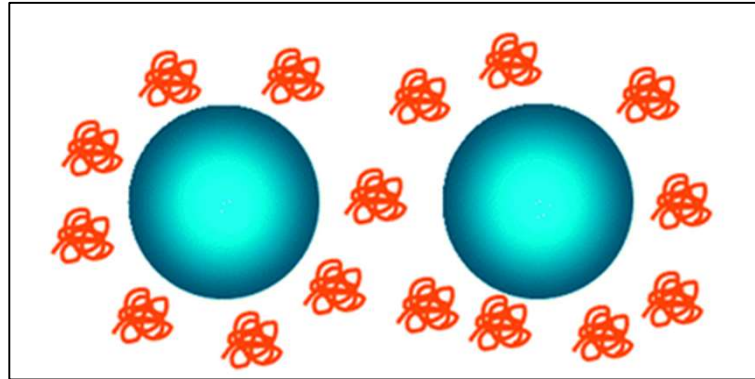


Fig. 2.22 Schematics of depletion stabilization[111]

attached polyelectrolyte) (Fig 2.23b). It is also possible to have combinations of depletion stabilization with both steric and/or electrostatic stabilization. The combination of depletion and steric stabilization is very common when there are high concentrations of free polymer in the dispersion medium [112].

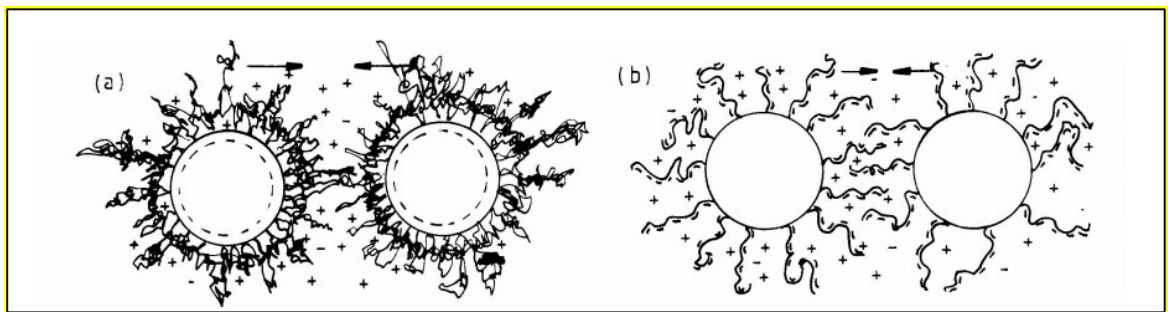


Fig. 2.23 Schematics of electrosteric stabilization: (a) charged particles with nonionic polymers; (b) polyelectrolytes attached to uncharged particles[112]

#### 2.4.2 Electrophoretic deposition (EPD) and dispersants

Electrophoretic deposition (EPD) refers to that colloidal particles suspended in a liquid

medium migrate under the influence of an electric field (electrophoresis) and are deposited onto an electrode (as Fig. 2.24 shows) [113, 114]. All colloidal particles that can be used to form stable suspensions and that can carry a charge can be used in electrophoretic deposition. This includes materials such as polymers, pigments, dyes, ceramics and metals [109].

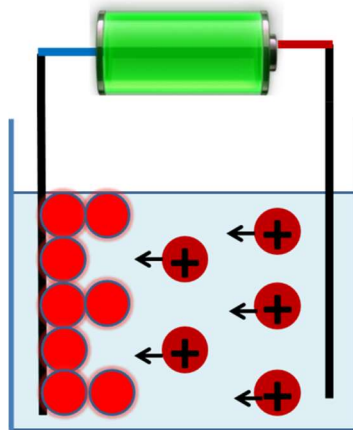


Fig. 2.24 Schematic of electrophoretic deposition

Cathodic deposition has important advantages for industrial applications. EPD is an important tool for the preparation of thick ceramic films.

One of the major issues in the development of EPD technology is the selection of dispersants. The particles must be well dispersed and charged in the bulk of the suspensions. Recent studies highlighted the importance of dispersant adsorption on the particle surface[115]. Despite the impressive progress achieved in the EPD of various materials[116-120], there is a need in the development of advanced additives and bath formulations for EPD. Dispersing agents typically show adsorption on limited number of materials of specific groups, such as metal oxides[121, 122] or carbon materials[123].

However, the development of composite films require the use of efficient co-dispersants for all the individual components. Small organic molecules from catechol, salicylic acid and gallic acid families with one chelating ligand per molecule show relatively weak adsorption on metal oxide particles. Relatively limited progress was achieved in the EPD of other functional materials, such as hydroxides, nitrates, metals, neutral polymers and other organic molecules.

Many investigations have focused on studying new dispersants for efficient dispersion and deposition of inorganic particles for various applications. Of particular importance are investigations of new adsorption and adhesion mechanism. Fundamental investigations showed[124-127] that strong mussel adhesion to different surfaces in saline water involves protein macromolecules, containing catecholic amino acid, L-3,4-dihydroxyphenylalanine (DOPA). The adhesion mechanism is attributed to the complexation of metal atoms on material surfaces by the OH groups of the catechol ligands. It was found that catechol is a powerful complexing agent, which is able to coordinate metal atoms in acidic or basic pH solutions. Previous investigation on DOPA reported a strong adhesion pull-off force reaching up to > 500 pN between DOPA and TiO<sub>2</sub> [127]. Driven by DOPA investigations, other chemicals from catechol family have been studied, the representative one is dopamine (DA). Structure of DA (Fig. 2.25) is analogous with that of DOPA, and many studies showed that adsorption of DA on inorganic particles can improve their electronic and photovoltaic properties [128-130].

The DA modified magnetic Fe<sub>3</sub>O<sub>4</sub> nanoparticles showed enhanced magnetization and increased superparamagnetic blocking temperature[131, 132]. It was found that DA

adsorption changed the microstructure of the magnetic dead layer on the nanoparticle

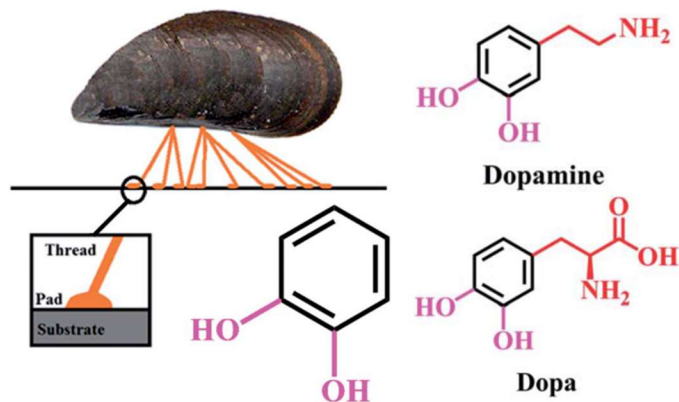


Fig. 2.25 Adsorption mechanism of catchol group on metal surface, structure of dopamine and dopa [115]

surface and promoted magnetic ordering in the surface layer. DA was used as an anchor for the functionalization of Fe<sub>3</sub>O<sub>4</sub> nanoparticles using a ‘click’ chemistry method[133]. Especially interesting are the investigations of DA adsorption on TiO<sub>2</sub>, which showed significant changes in the structure of the surface layer[134, 135] and revealed the enhanced electronic and photovoltaic properties of the TiO<sub>2</sub> nanoparticles[128-130]. The DA sensitized TiO<sub>2</sub> showed improved charge transfer at the organic –inorganic interface. The DA modified TiO<sub>2</sub> nanoparticles and films were investigated for the application in biosensors, photoelectrochemical transducers and optical devices[128-130, 135, 136]. The adsorption of DA resulted in enhanced luminescence properties[137] of ZnO. The strong adsorption of DOPA and DA on the surface of inorganic nanoparticles is of special interest for applications in electrophoretic nanotechnology of thin films.

The use of DOPA as a charging and dispersing agent for inorganic particles presents

difficulties attributed to zwitterionic properties of this molecule. Several investigations[138-140] were focused on the use of DA for cathodic EPD of ZnO, TiO<sub>2</sub> and MnO<sub>2</sub> nanoparticles. However, the use of DA for particle dispersion generates some problems, related to the small size of the DA molecule and self-polymerization of DA in the solutions. It is important to note that amino group of DA must be protonated in order to impart a charge to the DA molecules in the solutions. Therefore, in the previous investigations[138-140] DA was used in the form of dopamine hydrochloride (DA-HCl). In this case, competitive adsorption of the protonated DA and free H<sup>+</sup> ions from the acidic solutions on the particle surface can be expected. Inspired from DA, other promising molecules from catechol family should be proposed here to disperse inorganic particles especially for MnO<sub>2</sub> particles and CNTs composite electrode fabrication, and it's supposed the adhesion of this dispersant can help enhance capacitive properties of the composites.

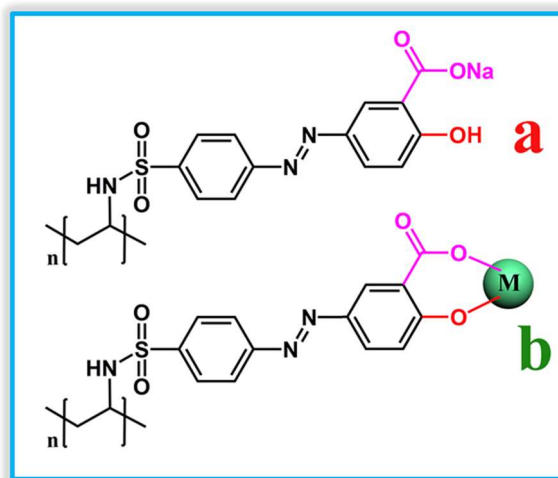


Fig. 2.26 a. molecular structure of PAZO and b. attaching mechanism of PAZO to inorganic particle

Besides using dispersants for MnO<sub>2</sub>-MWCNT composite fabrication, some dispersants can exhibit unique properties themselves, thus make them more promising and significant for functional applications. A significant amount of research was focused on the analysis of optical storage and photochromic properties, surface-relief grating[141-144], azobenzene *trans-cis-trans* transitions and birefringence[141]. Poly[1-[4-(3-carboxy-4-hydroxyphenylazo)benzenesulfonamido]-1,2-ethanediyl, sodium salt] (PAZO) has drawn attentions for its unique birefringence properties. It was found that the transformation from the *trans* form to the *cis* form results in a change of the dipole moment of the PAZO molecules (Fig. 2.26a), which has been utilized in light sensitive biosensors[145]. The use of PAZO[146] allowed for the fabrication of deltamethrin sensors with a detection limit below 0.1 nM. Moreover, PAZO is an effective polymer film material for holographic surface patterning[147].

## References

- [1] H.E. Becker, LOW VOLTAGE ELECTROLYTIC CAPACITOR, in: U.S Patent, 2 800 616, 1957.
- [2] D.L. BOOS, ELECTROLYTIC CAPACITOR HAVING CARBON PASTE ELECTRODES, in: U.S Patent, 3 536 963, 1970.
- [3] T.C. Murphy, R.B. Wright, R.A. Sutula, Electrochemical Capacitors II, Proceedings, The Electrochemical Society, Pennington, NJ, 96-25 (1997) 258.
- [4] R.K.t. a, M. Carlen, Principles and applications of electrochemical capacitors, *Electrochimica Acta*, 45 (2000) 2483-2498.
- [5] G. Wang, L. Zhang, J. Zhang, A review of electrode materials for electrochemical supercapacitors, *Chemical Society Reviews*, 41 (2012) 797-828.
- [6] L.L. Zhang, X.S. Zhao, Carbon-based materials as supercapacitor electrodes, *Chemical Society Reviews*, 38 (2009) 2520-2531.
- [7] Y. Zhu, S. Murali, M.D. Stoller, K.J. Ganesh, W. Cai, P.J. Ferreira, A. Pirkle, R.M. Wallace, K.A. Cychoz, M. Thommes, D. Su, E.A. Stach, R.S. Ruoff, Carbon-based supercapacitors produced by activation of graphene, *Science*, 332 (2011) 1537-1541.
- [8] P. SIMON, Y. GOGOTSI, Materials for electrochemical capacitors, *Nature materials*, 7 (2008) 845-853.
- [9] E. Frackowiak, Carbon materials for supercapacitor application, *Physical chemistry chemical physics : PCCP*, 9 (2007) 1774-1785.
- [10] J.H. J. P. Zheng, and T. R. Jowt, The Limitations of Energy Density for Electrochemical Capacitors, *Journal of The Electrochemical Society.*, 144 (1997) 2026-

2031.

[11] Y.M. Vol', fkovich, T.M. Serdyuk, Electrochemical Capacitors, Russian Journal of Electrochemistry, 38 (2002) 935-958.

[12] W. Kim, M.Y. Kang, J.B. Joo, N.D. Kim, I.K. Song, P. Kim, J.R. Yoon, J. Yi, Preparation of ordered mesoporous carbon nanopipes with controlled nitrogen species for application in electrical double-layer capacitors, Journal of Power Sources, 195 (2010) 2125-2129.

[13] L. Hao, B. Luo, X. Li, M. Jin, Y. Fang, Z. Tang, Y. Jia, M. Liang, A. Thomas, J. Yang, L. Zhi, Terephthalonitrile-derived nitrogen-rich networks for high performance supercapacitors, Energy & Environmental Science, 5 (2012) 9747-9751.

[14] B.E. Conway, Electrochemical Supercapacitors: Scientific Fundamentals and Technological Applications, Kluwer Academic/ Plenum Publisher, New York, 1999.

[15] R. Parsons, The electrical double layer: recent experimental and theoretical developments, Chemical Reviews, 90 (1990) 813-826.

[16] B.E. Conway, Transition from "Supercapacitor" to "Battery" Behavior in Electrochemical Energy Storage, Journal of The Electrochemical Society, 138 (1991) 1539-1548.

[17] L.G. Gouy, Sur la constitution de la charge électrique à la surface d'un electrolyte, C. R. Acad. Sci. III, 149 (1909) 457-468.

[18] D.L. Chapman, A Contribution to the Theory of Electrocapillarity, Philosophical Magazine Series, 148 (1913) 475-481.

[19] P.D.a.E. Hückel, The theory of electrolytes. I. Lowering of freezing point and related

phenomena, *Physikalische Zeitschrift*, 24 (1923) 185-206.

[20] O. Stern, The theory of the electrolytic double-layer, *Zeitschrift fuer Elektrochemie und Angewandte Physikalische Chemie*, 30 (1924) 508-516.

[21] D.C. Grahame, The Electrical Double Layer and the Theory of Electrocapillarity, *Chemical Reviews*, 41 (1947) 441-501.

[22] V. Augustyn, P. Simon, B. Dunn, Pseudocapacitive oxide materials for high-rate electrochemical energy storage, *Energy & Environmental Science*, 7 (2014) 1597-1614.

[23] H.D.H. W. J. Lorenz, N. Wüthrich and F. Hilbert, The Formation of Monolayer Metal Films on Electrodes, *Journal of The Electrochemical Society*, 121 (1974) 1167-1171.

[24] C.L.G., A. Kucernak, Determination of the Platinum and Ruthenium Surface Areas in Platinum–Ruthenium Alloy Electrocatalysts by Underpotential Deposition of Copper. I. Unsupported Catalysts, *the Journal of Physical Chemistry B*, 106 (2002) 1036-1047.

[25] G. Kokkinidis, Underpotential deposition and electrocatalysis, *Journal of Electroanalytical Chemistry and Interfacial Electrochemistry*, 201 (1986) 217-236.

[26] L.J.B. Enrique Herrero, He´ctor D. Abrun, Underpotential Deposition at Single Crystal Surfaces of Au, Pt, Ag and Other materials, *Chemical Reviews*, 101 (2001) 1897-1930.

[27] X. Dong, W. Shen, J. Gu, L. Xiong, Y. Zhu, H. Li, J. Shi, MnO<sub>2</sub>-Embedded-in-Mesoporous-Carbon-Wall Structure for Use as Electrochemical, *Journal of Physical Chemistry B*, 110 (2006) 6015-6019.

[28] W. Sugimoto, H. Iwata, Y. Murakami, Y. Takasu, Electrochemical Capacitor

Behavior of Layered Ruthenic Acid Hydrate, *Journal of The Electrochemical Society*, 151 (2004) A1181-A1187.

[29] M.S. Wu, P.C. Julia Chiang, Fabrication of Nanostructured Manganese Oxide Electrodes for Electrochemical Capacitors, *Electrochemical and Solid-State Letters*, 7 (2004) A123-A126.

[30] Y. Zhang, H. Feng, X. Wu, L. Wang, A. Zhang, T. Xia, H. Dong, X. Li, L. Zhang, Progress of electrochemical capacitor electrode materials: A review, *International Journal of Hydrogen Energy*, 34 (2009) 4889-4899.

[31] C. Hu, K. Chang, M. Lin, Y. Wu, Design and Tailoring of the Nanotubular Arrayed Architecture of Hydrated RuO<sub>2</sub> for Next Generation Supercapacitors, *Nano Letters*, 6 (2006) 2690–2695.

[32] M.a.J, B.E.Conway, Surface and bulk processes at oxidized iridium electrodes—I. Monolayer stage and transition to reversible multilayer oxide film behaviour, *Electrochimica Acta*, 28 (1983) 1-8.

[33] K.-W. Nam, K.-B. Kim, A Study of the Preparation of NiO<sub>x</sub> Electrode via Electrochemical Route for Supercapacitor Applications and Their Charge Storage Mechanism, *Journal of The Electrochemical Society*, 149 (2002) A346-A354.

[34] X.-C. Dong, H. Xu, X.-W. Wang, Y.-X. Huang, M.B. Chan-Park, H. Zhang, L.-H. Wang, W. Huang, P. Chen, 3D Graphene–Cobalt Oxide Electrode for High-Performance Supercapacitor and Enzymeless Glucose Detection, *ACS Nano*, 6 (2012) 3206-3213.

[35] T. Cottineau, M. Toupin, T. Delahaye, T. Brousse, D. Bélanger, Nanostructured transition metal oxides for aqueous hybrid electrochemical supercapacitors, *Applied*

Physics A, 82 (2005) 599-606.

[36] S. Biswas, L.T. Drzal, Multilayered Nanoarchitecture of Graphene Nanosheets and Polypyrrole Nanowires for High Performance Supercapacitor Electrodes, *Chemistry of Materials*, 22 (2010) 5667-5671.

[37] S. Ma, K. Nam, W. Yoon, X. Yang, K. Ahn, K. Oh, K. Kim, A novel concept of hybrid capacitor based on manganese oxide materials, *Electrochemistry Communications*, 9 (2007) 2807-2811.

[38] X. Li, B. Wei, Supercapacitors based on nanostructured carbon, *Nano Energy*, 2 (2013) 159-173.

[39] Y. Su, I. Zhitomirsky, Electrophoretic Nanotechnology of Composite Electrodes for Electrochemical Supercapacitors, *The Journal of Physical Chemistry B*, 117 (2013) 1563-1570.

[40] Sheng Chen, Junwu Zhu, Xiaodong Wu, Qiaofeng Han, a.X. Wang, Graphene Oxide MnO<sub>2</sub> Nanocomposites for Supercapacitors, *ACS Nano*, 4 (2010) 2822–2830.

[41] Y. Han, M. Shen, X. Lin, B. Ding, L. Zhang, H. Tong, X. Zhang, Ternary phase interfacial polymerization of polypyrrole/MWCNT nanocomposites with core-shell structure, *Synthetic Metals*, 162 (2012) 753-758.

[42] T. Brousse, P.-L. Taberna, O. Crosnier, R. Dugas, P. Guillemet, Y. Scudeller, Y. Zhou, F. Favier, D. Bélanger, P. Simon, Long-term cycling behavior of asymmetric activated carbon/MnO<sub>2</sub> aqueous electrochemical supercapacitor, *Journal of Power Sources*, 173 (2007) 633-641.

[43] K. Shi, I. Zhitomirsky, Polypyrrole nanofiber-carbon nanotube electrodes for

supercapacitors with high mass loading obtained using an organic dye as a co-dispersant, *Journal of Materials Chemistry A*, 1 (2013) 11614-11622.

[44] Y. He, W. Chen, C. Gao, J. Zhou, X. Li, E. Xie, An overview of carbon materials for flexible electrochemical capacitors, *Nanoscale*, 5 (2013) 8799-8820.

[45] F. Meng, Y. Ding, Sub-micrometer-thick all-solid-state supercapacitors with high power and energy densities, *Advanced materials*, 23 (2011) 4098-4102.

[46] G. Lota, T.A. Centeno, E. Frackowiak, F. Stoeckli, Improvement of the structural and chemical properties of a commercial activated carbon for its application in electrochemical capacitors, *Electrochimica Acta*, 53 (2008) 2210-2216.

[47] V. Khomenko, E. Raymundo-Piñero, E. Frackowiak, F. Béguin, High-voltage asymmetric supercapacitors operating in aqueous electrolyte, *Applied Physics. A*, 82 (2006) 567-573.

[48] M. Hong S.H. Lee, S.W. Kim., Use of KCl Aqueous Electrolyte for 2 V Manganese Oxide/Activated Carbon Hybrid Capacitor, *Electrochemical and Solid-State Letters*, 5 (2002) A227-A230.

[49] V. Khomenko, E. Raymundo-Piñero, F. Béguin, Optimisation of an asymmetric manganese oxide/activated carbon capacitor working at 2V in aqueous medium, *Journal of Power Sources*, 153 (2006) 183-190.

[50] M. Zhi, C. Xiang, J. Li, M. Li, N. Wu, Nanostructured carbon-metal oxide composite electrodes for supercapacitors: a review, *Nanoscale*, 5 (2013) 72-88.

[51] J. Li, X. Wang, Q. Huang, S. Gamboa, P.J. Sebastian, Studies on preparation and performances of carbon aerogel electrodes for the application of supercapacitor, *Journal*

of Power Sources, 158 (2006) 784-788.

[52] Z. Niu, L. Zhang, L. Liu, B. Zhu, H. Dong, X. Chen, All-solid-state flexible ultrathin micro-supercapacitors based on graphene, *Advanced materials*, 25 (2013) 4035-4042.

[53] Y. Jin, H. Chen, M. Chen, N. Liu, Q. Li, Graphene-patched CNT/MnO<sub>2</sub> nanocomposite papers for the electrode of high-performance flexible asymmetric supercapacitors, *ACS applied materials & interfaces*, 5 (2013) 3408-3416.

[54] Z. Tian, C. Xu, J. Li, G. Zhu, Z. Shi, Y. Lin, Self-assembled free-standing graphene oxide fibers, *ACS applied materials & interfaces*, 5 (2013) 1489-1493.

[55] J.-G. Wang, Y. Yang, Z.-H. Huang, F. Kang, Coaxial carbon nanofibers/MnO<sub>2</sub> nanocomposites as freestanding electrodes for high-performance electrochemical capacitors, *Electrochimica Acta*, 56 (2011) 9240-9247.

[56] S. Cheng, L. Yang, Y. Liu, W. Lin, L. Huang, D. Chen, C.P. Wong, M. Liu, Carbon fiber paper supported hybrid nanonet/nanoflower nickel oxide electrodes for high-performance pseudo-capacitors, *Journal of Materials Chemistry A*, 1 (2013) 7709-7716.

[57] V.T. Le, H. Kim, A. Ghosh, J. Kim, J. Chang, Q.A. Vu, D.T. Pham, J.H. Lee, S.W. Kim, Y.H. Lee, Coaxial fiber supercapacitor using all-carbon material electrodes, *ACS Nano*, 7 (2013) 5940-5947.

[58] M. Ghosh, S.K. Sonkar, M. Saxena, S. Sarkar, Carbon nano-onions for imaging the life cycle of *Drosophila melanogaster*, *Small*, 7 (2011) 3170-3177.

[59] D. Qu, H. Shi, Studies of activated carbons used in double-layer capacitors, *Journal of Power Sources*, 74 (1998) 99-107.

[60] M. Endo, T. Maeda, T. Takeda, Y. J. Kim, K. Koshiba, H. Hara and M. S.

Dresselhaus, Capacitance and Pore-Size Distribution in Aqueous and Nonaqueous Electrolytes Using Various Activated Carbon Electrodes, *Journal of The Electrochemical Society*, 148 (2001) A910-A914.

[61] E. Raymundo-Piñero, K. Kierzek, J. Machnikowski, F. Béguin, Relationship between the nanoporous texture of activated carbons and their capacitance properties in different electrolytes, *Carbon* 44 (2006) 2498-2507.

[62] J.W. Long, K. E. Swider, C. I. Merzbacher, D. R. Rolison, Voltammetric Characterization of Ruthenium Oxide-Based Aerogels and Other RuO<sub>2</sub> Solids: The Nature of Capacitance in Nanostructured Materials, *Langmuir*, 15 (1999) 780-785.

[63] G. Salitra, A. Soffer, L. Eliad, Y. Cohen, D. Aurbach, Carbon Electrodes for Double-Layer Capacitors I. Relations Between Ion and Pore Dimensions, *Journal of The Electrochemical Society*, 147 (2000) 2486-2493.

[64] J.Y. Chmiola, G. Gogotsi, Y. Portet, C. Simon, P. Taberna, P. L., Anomalous increase in carbon capacitance at pore sizes less than 1 nanometer, *Science*, 313 (2006) 1760-1763.

[65] C. Largeot, C. Portet, J. Chmiola, P. Taberna, Y. Gogotsi, P. Simon, Relation between the Ion Size and Pore Size for an Electric Double-Layer Capacitor, *Journal of American Chemical Society*, 130 (2008) 2730-2731.

[66] P.R. Bandaru, Electrical Properties and Applications of Carbon Nanotube Structures, *Journal of Nanoscience and Nanotechnology*, 7 (2007) 1239-1267.

[67] E. Raymundo-Piñero, V. Khomenko, E. Frackowiak, F. Béguina, Performance of Manganese Oxide/CNTs Composites as Electrode Materials for Electrochemical

Capacitors, *Journal of The Electrochemical Society*, 152 (2005) A229-A235.

[68] R. Jiang, T. Huang, Y. Tang, J. Liu, L. Xue, J. Zhuang, A. Yu, Factors influencing MnO<sub>2</sub>/multi-walled carbon nanotubes composite's electrochemical performance as supercapacitor electrode, *Electrochimica Acta*, 54 (2009) 7173-7179.

[69] J. Yan, Z. Fan, T. Wei, J. Cheng, B. Shao, K. Wang, L. Song, M. Zhang, Carbon nanotube/MnO<sub>2</sub> composites synthesized by microwave-assisted method for supercapacitors with high power and energy densities, *Journal of Power Sources*, 194 (2009) 1202-1207.

[70] J.-G. Wang, Y. Yang, Z.-H. Huang, F. Kang, Effect of temperature on the pseudocapacitive behavior of freestanding MnO<sub>2</sub>@carbon nanofibers composites electrodes in mild electrolyte, *Journal of Power Sources*, 224 (2013) 86-92.

[71] S. Hassan, M. Suzuki, S. Mori, A.A. El-Moneim, MnO<sub>2</sub>/carbon nanowall electrode for future energy storage application: effect of carbon nanowall growth period and MnO<sub>2</sub> mass loading, *RSC Advances*, 4 (2014) 20479-20488.

[72] Y. Gao, Y.S. Zhou, M. Qian, H.M. Li, J. Redepenning, L.S. Fan, X.N. He, W. Xiong, X. Huang, M. Majhour-Samani, L. Jiang, Y.F. Lu, High-performance flexible solid-state supercapacitors based on MnO<sub>2</sub>-decorated nanocarbon electrodes, *RSC Advances*, 3 (2013) 20613-20618.

[73] H. Xia, Y. Wang, J. Lin, L. Lu, Hydrothermal synthesis of MnO<sub>2</sub>/CNT nanocomposite with a CNT core/porous MnO<sub>2</sub> sheath hierarchy architecture for supercapacitors, *Nanoscale Research Letters*, 7 (2012) 1-10.

[74] H. Xia, M. Lai, L. Lu, Nanoflaky MnO<sub>2</sub>/carbon nanotube nanocomposites as anode

materials for lithium-ion batteries, *Journal of Materials Chemistry*, 20 (2010) 6896-6902.

[75] S.-B. Yoon, J.-P. Jegal, K.C. Roh, K.-B. Kim, Electrochemical Impedance Spectroscopic Investigation of Sodium Ion Diffusion in MnO<sub>2</sub> Using a Constant Phase Element Active in Desired Frequency Ranges, *Journal of The Electrochemical Society*, 161 (2014) H207-H213.

[76] W. Jiang, K. Zhang, L. Wei, D. Yu, J. Wei, Y. Chen, Hybrid ternary rice paper-manganese oxide-carbon nanotube nanocomposites for flexible supercapacitors, *Nanoscale*, 5 (2013) 11108-11117.

[77] C.-W. Lee, S.-B. Yoon, S.-M. Bak, J. Han, K.C. Roh, K.-B. Kim, Soft templated mesoporous manganese oxide/carbon nanotube composites via interfacial surfactant assembly, *Journal of Materials Chemistry A*, 2 (2014) 3641-3647.

[78] Y. Wang, H. Liu, X. Sun, I. Zhitomirsky, Manganese dioxide-carbon nanotube nanocomposites for electrodes of electrochemical supercapacitors, *Scripta Materialia*, 61 (2009) 1079-1082.

[79] V. Khomenko, E. Raymundo-Piñero, F. Béguin, Optimisation of an asymmetric manganese oxide/activated carbon capacitor working at 2 V in aqueous medium, *Journal of Power Sources*, 153 (2006) 183-190.

[80] F. Wang, S. Xiao, Y. Hou, C. Hu, L. Liu, Y. Wu, Electrode materials for aqueous asymmetric supercapacitors, *RSC Advances*, 3 (2013) 13059-13084.

[81] G.A. Snook, P. Kao, A.S. Best, Conducting-polymer-based supercapacitor devices and electrodes, *Journal of Power Sources*, 196 (2011) 1-12.

[82] K. Lota, V. Khomenko, E. Frackowiak, Capacitance properties of poly(3,4-

ethylenedioxythiophene)/carbon nanotubes composites, *Journal of Physics and Chemistry of Solids*, 65 (2004) 295-301.

[83] C. Meng, C. Liu, L. Chen, C. Hu, S. Fan, Highly flexible and all-solid-state paperlike polymer supercapacitors, *Nano letters*, 10 (2010) 4025-4031.

[84] X. Zhang, R. Bi, Surface Electric Properties of Polypyrrole in Aqueous Solutions, *Langmuir*, 19 (2003) 10703–10709.

[85] K. Shi, I. Zhitomirsky, Influence of current collector on capacitive behavior and cycling stability of Tiron doped polypyrrole electrodes, *Journal of Power Sources*, 240 (2013) 42-49.

[86] D.-D. Zhao, S.-J. Bao, W.-J. Zhou, H.-L. Li, Preparation of hexagonal nanoporous nickel hydroxide film and its application for electrochemical capacitor, *Electrochemistry Communications*, 9 (2007) 869-874.

[87] Mathieu Toupin, Thierry Brousse, D. Be' langer, Charge Storage Mechanism of MnO<sub>2</sub> Electrode Used in Aqueous Electrochemical Capacitor, *Chemistry of Materials*, 16 (2004) 3184-3190.

[88] W. Wei, X. Cui, W. Chen, D.G. Ivey, Manganese oxide-based materials as electrochemical supercapacitor electrodes, *Chemical Society reviews*, 40 (2011) 1697-1721.

[89] T.P. Gujar, V.R. Shinde, C.D. Lokhande, S.-H. Han, Electrosynthesis of Bi<sub>2</sub>O<sub>3</sub> thin films and their use in electrochemical supercapacitors, *Journal of Power Sources*, 161 (2006) 1479-1485.

[90] H.-W. Wang, Z.-A. Hu, Y.-Q. Chang, Y.-L. Chen, Z.-Q. Lei, Z.-Y. Zhang, Y.-Y.

Yang, Facile solvothermal synthesis of a graphene nanosheet - bismuth oxide composite and its electrochemical characteristics, *Electrochimica Acta*, 55 (2010) 8974-8980.

[91] K. Gopalsamy, Z. Xu, B. Zheng, T. Huang, L. Kou, X. Zhao, C. Gao, Bismuth oxide nanotubes-graphene fiber-based flexible supercapacitors, *Nanoscale*, 6 (2014) 8595-8600.

[92] S.X. Wang, C.C. Jin, W.J. Qian, Bi<sub>2</sub>O<sub>3</sub> with activated carbon composite as a supercapacitor electrode, *Journal of Alloys and Compounds*, 615 (2014) 12-17.

[93] F.-L. Zheng, G.-R. Li, Y.-N. Ou, Z.-L. Wang, C.-Y. Su, Y.-X. Tong, Synthesis of hierarchical rippled Bi<sub>2</sub>O<sub>3</sub> nanobelts for supercapacitor applications, *Chemical Communications*, 46 (2010) 5021-5023.

[94] D. Qu, L. Wang, D. Zheng, L. Xiao, B. Deng, D. Qu, An asymmetric supercapacitor with highly dispersed nano-Bi<sub>2</sub>O<sub>3</sub> and active carbon electrodes, *Journal of Power Sources*, 269 (2014) 129-135.

[95] S.T. Senthilkumar, R.K. Selvan, M. Ulaganathan, J.S. Melo, Fabrication of Bi<sub>2</sub>O<sub>3</sub>-AC asymmetric supercapacitor with redox additive aqueous electrolyte and its improved electrochemical performances, *Electrochimica Acta*, 115 (2014) 518-524.

[96] H. Xu, X. Hu, H. Yang, Y. Sun, C. Hu, Y. Huang, Flexible Asymmetric Micro-Supercapacitors Based on Bi<sub>2</sub>O<sub>3</sub> and MnO<sub>2</sub> Nanoflowers: Larger Areal Mass Promises Higher Energy Density, *Advanced Energy Materials*, (2014) DOI: 10.1002/aenm.201401882

[97] Q. Chu, W. Wang, X. Wang, B. Yang, X. Liu, J. Chen, Hierarchical NiCo<sub>2</sub>O<sub>4</sub>@nickel-sulfide nanoplate arrays for high-performance supercapacitors, *Journal of Power Sources*, 276 (2015) 19-25.

- [98] W. Hong, J. Wang, P. Gong, J. Sun, L. Niu, Z. Yang, Z. Wang, S. Yang, Rational construction of three dimensional hybrid  $\text{Co}_3\text{O}_4@\text{NiMoO}_4$  nanosheets array for energy storage application, *Journal of Power Sources*, 270 (2014) 516-525.
- [99] Y. Zhu, X. Ji, Z. Wu, W. Song, H. Hou, Z. Wu, X. He, Q. Chen, C.E. Banks, Spinel  $\text{NiCo}_2\text{O}_4$  for use as a high-performance supercapacitor electrode material: Understanding of its electrochemical properties, *Journal of Power Sources*, 267 (2014) 888-900.
- [100] Y.N. Venevtsev, V. Gagulin, I. Zhitomirsky, Material science aspects of seignette-magnetism problem, *Ferroelectrics*, 73 (1987) 221-248.
- [101] E. Bertaut, G. Buisson, S. Quezel-Ambrunaz, G. Quezel, Structure magnetique et proprietes magnetiques de  $\text{BiMn}_2\text{O}_5$ , *Solid State Communications*, 5 (1967) 25-30.
- [102] Q. Liu, D. Sallagoity, M. Josse, O. Toulemonde, On the Anomalous Magnetic Behavior and the Multiferroic Properties in  $\text{BiMn}_2\text{O}_5$ , *Inorganic Chemistry*, 52 (2013) 7853-7861.
- [103] J.W. Kim, S. Haam, Y. Oh, S. Park, S.-W. Cheong, P. Sharma, M. Jaime, N. Harrison, J.H. Han, G.-S. Jeon, Observation of a multiferroic critical end point, *Proceedings of the National Academy of Sciences*, 106 (2009) 15573-15576.
- [104] I. Zhitomirsky, N. Skorokhodov, A. Bush, O. Chechernikova, V. Chuprakov, Y.N. Venevtsev, Dielectric, pyroelectric and magnetic properties of  $\text{BiMn}_2\text{O}_5$  crystals, *Sov. Phys. Solid State*, 25 (1983) 550-552.
- [105] I. Fier, L. Walmsley, J. Souza, Relaxor behavior in multiferroic  $\text{BiMn}_2\text{O}_5$  ceramics, *Journal of Applied Physics*, 110 (2011) 084101.
- [106] I. Fier, D. Chinaglia, L. Walmsley, E. Pereira, A. Rabelo, R. Freitas, Contribution

of an extrinsic mechanism for the electrical polarization in BiMn<sub>2</sub>O<sub>5</sub> ceramics, AIP ADVANCES, 2 (2012) 42165.

[107] Y.Q. Lin, Y.J. Wu, X.M. Chen, S.P. Gu, J. Tong, S. Guan, Dielectric relaxation mechanisms of BiMn<sub>2</sub>O<sub>5</sub> ceramics, Journal of Applied Physics, 105 (2009) 54109.

[108] D. Shukla, R. Kumar, S. Mollah, R. Choudhary, P. Thakur, S. Sharma, N. Brookes, M. Knobel, Swift heavy ion irradiation induced magnetism in magnetically frustrated BiMn<sub>2</sub>O<sub>5</sub> thin films, Physical Review B, 82 (2010) 174432.

[109] I. Zhitomirsky, Cathodic Electrodeposition of Ceramic and Organoceramic Materials. Fundamental Aspects, Advances in Colloid and Interface Science, 97 (2002) 277-315.

[110] H. Zecha, Stabilization of colloidal dispersions by polymer adsorption., Acta Polym., 32 (1980) doi: 10.1002/actp.1981.010320915.

[111] D.H. Napper, Polymeric stabilization of colloidal dispersions, *Academic Pr.*, New York, 1983.

[112] E. B. Zhulina, O.V. Borisov, V. A. Priamitsyn, Theory of steric stabilization of colloid dispersions by grafted polymers, Journal of Colloid Interface Science, 137 (1990) 495-511.

[113] O.O. Van der Biest, L.J. Vandeperre, Electrophoretic deposition of materials, Annual Review of Materials Science, 29 (1999) 327-352.

[114] B. Ferrari, R. Moreno, EPD kinetics: A review, Journal of the European Ceramic Society, 30 (2010) 1069-1078.

[115] M. Ata, Y. Liu, I. Zhitomirsky, A review of new methods of surface chemical

modification, dispersion and electrophoretic deposition of metal oxide particles, *RSC Advances*, 4 (2014) 22716-22732.

[116] S.A. Hasan, D.W. Kavich, S.V. Mahajan, J.H. Dickerson, Electrophoretic deposition of CdSe nanocrystal films onto dielectric polymer thin films, *Thin Solid Films*, 517 (2009) 2665-2669.

[117] L.-Q. Wu, A.P. Gadre, H. Yi, M.J. Kastantin, G.W. Rubloff, W.E. Bentley, G.F. Payne, R. Ghodssi, Voltage-dependent assembly of the polysaccharide chitosan onto an electrode surface, *Langmuir*, 18 (2002) 8620-8625.

[118] S. Somarajan, S.A. Hasan, C.T. Adkins, E. Harth, J.H. Dickerson, Controlled electrophoretic deposition of uniquely nanostructured star polymer films, *Journal of Physical Chemistry B*, 112 (2008) 23-28.

[119] E.A. Olevsky, X. Wang, A. Maximenko, M.A. Meyers, Fabrication of net-shape functionally graded composites by electrophoretic deposition and sintering: Modeling and experimentation, *Journal of the American Ceramic Society*, 90 (2007) 3047-3056.

[120] H. Mazor, D. Golodnitsky, L. Burstein, A. Gladkich, E. Peled, Electrophoretic deposition of lithium iron phosphate cathode for thin-film 3D-microbatteries, *Journal of Power Sources*, 198 (2012) 264-272.

[121] I. Zhitomirsky, A. Petric, Electrophoretic deposition of ceramic materials for fuel cell applications, *Journal of the European Ceramic Society*, 20 (2000) 2055-2061.

[122] I. Zhitomirsky, A. Petric, Electrophoretic deposition of electrolyte materials for solid oxide fuel cells, *Journal of Materials Science*, 39 (2004) 825-831.

[123] Y. Su, I. Zhitomirsky, Electrophoretic deposition of graphene, carbon nanotubes

and composite films using methyl violet dye as a dispersing agent, *Colloids and Surfaces A: Physicochemical and Engineering Aspects*, 436 (2013) 97-103.

[124] H. Lee, S.M. Dellatore, W.M. Miller, P.B. Messersmith, Mussel-Inspired Surface Chemistry for Multifunctional Coatings, *Science*, 318 (2007) 426-430.

[125] J.H. Waite, Surface chemistry: Mussel power, *Nature Materials*, 7 (2008) 8-9.

[126] H. Lee, B.P. Lee, P.B. Messersmith, A reversible wet/dry adhesive inspired by mussels and geckos, *Nature*, 448 (2007) 338-341.

[127] B.P. Lee, P.B. Messersmith, J.N. Israelachvili, J.H. Waite, Mussel-inspired adhesives and coatings, *Annual review of materials research*, 41 (2011) 99-132.

[128] G.-L. Wang, J.-J. Xu, H.-Y. Chen, Dopamine sensitized nanoporous TiO<sub>2</sub> film on electrodes: Photoelectrochemical sensing of NADH under visible irradiation, *Biosensors and Bioelectronics*, 24 (2009) 2494-2498.

[129] S. Varaganti, G. Ramakrishna, Dynamics of Interfacial Charge Transfer Emission in Small Molecule Sensitized TiO<sub>2</sub> Nanoparticles: Is It Localized or Delocalized?, *The Journal of Physical Chemistry C*, 114 (2010) 13917-13925.

[130] T. Rajh, L.X. Chen, K. Lukas, T. Liu, M.C. Thurnauer, D.M. Tiede, Surface Restructuring of Nanoparticles: An Efficient Route for Ligand -Metal Oxide Crosstalk, *The Journal of Physical Chemistry B*, 106 (2002) 10543-10552.

[131] D.K. Nagesha, B.D. Plouffe, M. Phan, L.H. Lewis, S. Sridhar, S.K. Murthy, Functionalization-induced improvement in magnetic properties of Fe<sub>3</sub>O<sub>4</sub> nanoparticles for biomedical applications, *Journal of Applied Physics*, 105 (2009) 07B317.

[132] K.V. Korpany, F. Habib, M. Murugesu, A.S. Blum, Stable water-soluble iron oxide

nanoparticles using Tiron, *Materials Chemistry and Physics*, 138 (2013) 29-37.

[133] A.S. Goldmann, C. Schödel, A. Walther, J. Yuan, K. Loos, A.H.E. Müller, Biomimetic Mussel Adhesive Inspired Clickable Anchors Applied to the Functionalization of Fe<sub>3</sub>O<sub>4</sub> Nanoparticles, *Macromolecular Rapid Communications*, 31 (2010) 1608-1615.

[134] B.M. Rabatic, N.M. Dimitrijevic, R.E. Cook, Z.V. Saponjic, T. Rajh, Spatially Confined Corner Defects Induce Chemical Functionality of TiO<sub>2</sub> Nanorods, *Advanced Materials*, 18 (2006) 1033-1037.

[135] L. De la Garza, Z.V. Saponjic, N.M. Dimitrijevic, M.C. Thurnauer, T. Rajh, Surface States of Titanium Dioxide Nanoparticles Modified with Eneiol Ligands, *The Journal of Physical Chemistry B*, 110 (2005) 680-686.

[136] D. Gutiérrez-Tauste, X. Domènech, C. Domingo, J.A. Ayllón, Dopamine/TiO<sub>2</sub> hybrid thin films prepared by the liquid phase deposition method, *Thin Solid Films*, 516 (2008) 3831-3835.

[137] W. Huang, P. Jiang, C. Wei, D. Zhuang, J. Shi, Low-temperature one-step synthesis of covalently chelated ZnO/dopamine hybrid nanoparticles and their optical properties, *Journal of Materials Research*, 23 (2008) 1946-1952.

[138] K. Wu, I. Zhitomirsky, Electrophoretic deposition of ceramic nanoparticles, *International Journal of Applied Ceramic Technology*, 8 (2011) 920-927.

[139] Y. Wang, I. Zhitomirsky, Electrophoretic deposition of manganese dioxide - Multiwalled carbon nanotube composites for electrochemical supercapacitors, *Langmuir*, 25 (2009) 9684-9689.

- [140] K. Wu, P. Imin, A. Adronov, I. Zhitomirsky, Electrophoretic deposition of poly[3-(3-N,N-diethylaminopropoxy)thiophene] and composite films, *Materials Chemistry and Physics*, 125 (2011) 210-218.
- [141] C. Madruga, P.A. Filho, M.M. Andrade, M. Goncalves, M. Raposo, P.A. Ribeiro, Birefringence dynamics of poly{1-[4-(3-carboxy-4-hydroxyphenylazo)benzenesulfonamido]-1,2-ethanediyl, sodium salt} cast films, *Thin Solid Films*, 519 (2011) 8191-8196.
- [142] Q. Ferreira, P.J. Gomes, M. Raposo, J. Giacometti, O.N. Oliveira, P.A. Ribeiro, Influence of ionic interactions on the photoinduced birefringence of Poly [1-[4-(3-Carboxy-4 Hydroxyphenylazo) benzene sulfonamido]-1, 2-ethanediyl, sodium salt] films, *Journal of Nanoscience and Nanotechnology*, 7 (2007) 2659-2666.
- [143] N.S. Yadavalli, S. Santer, In-situ atomic force microscopy study of the mechanism of surface relief grating formation in photosensitive polymer films, *Journal of Applied Physics*, 113 (2013) 1-11.
- [144] N.S. Yadavalli, F. Linde, A. Kopyshv, S. Santer, Soft matter beats hard matter: Rupturing of thin metallic films induced by mass transport in photosensitive polymer films, *ACS Applied Materials & Interfaces*, 5 (2013) 7743-7747.
- [145] S.A. Maaland, R. Cai, T. Fulghum, R.C. Advincula, Adsorption of Fabrication on Polyonic Azobenzene Layer-by-Layer Film using Photoisomerization, *Polymer Preprints*, 49 (2008) 990-991.
- [146] L.M.G. Abegao, J.H.F. Ribeiro, P.A. Ribeiro, M. Raposo, Nano-Molar Deltamethrin Sensor Based on Electrical Impedance of PAH/PAZO Layer-by-Layer

Sensing Films, *Sensors*, 13 (2013) 10167-10176.

[147] L.M. Goldenberg, O. Kulikovska, J. Stumpe, Thermally stable holographic surface relief gratings and switchable optical anisotropy in films of an azobenzene-containing polyelectrolyte, *Langmuir*, 21 (2005) 4794-4796.

## **Chapter 3 Problem statements and objectives**

### **3.1 Dispersion of carbon nanotubes and MnO<sub>2</sub>**

As elaborated in literature review, CNTs possess good conductivity as well as high specific surface area but with drawback of low capacitance as EDLC electrode material, while, MnO<sub>2</sub> can provide much higher capacitance (theoretically 1370 F g<sup>-1</sup>) but with lower conductivity. The combination of MnO<sub>2</sub> and CNTs can not only excavate whole potential of MnO<sub>2</sub>, but also provides more flexible options to fabricate diverse nanostructured electrodes. Many works have been reported on well performed MnO<sub>2</sub>-CNTs composite electrodes[1-5].

#### 3.1.1 Challenges on dispersion of CNTs

Fabrication of homogenous MnO<sub>2</sub>-CNTs composite is critical for achieving excellent electrochemical performance, however, carbon nanotubes are bundled and self-aggregated naturally[6-8], and MnO<sub>2</sub> powder are also easy to agglomerate spontaneously [9, 10]. The nature of dispersion problem for CNTs is rather different from other materials, such as spherical particles and carbon fibers, because CNTs are characteristic of small diameter in nanometer scale with high aspect ratio (>1000) and thus extremely large surface area. In addition, the commercialized CNTs are supplied in the form of heavily entangled bundles, resulting in inherent difficulties in dispersion.

Many efforts have been putted into dispersion of CNTs, the main way is using surfactant [11-13]. However, many dispersants such as polymers may cause polymer wrapping. As

shown in Fig. 3.1 A[14], the CNTs are entwined by the rope-like long chain polymers, as a consequence, it greatly decreases the crucial intrinsic properties of CNTs such as conductivity, high specific surface areas due to the coverage by insulating polymers. Since the surfactant itself has no contribution to conductivity or capacitance, the whole electrochemical performance of CNTs is greatly restrained due to the existence of surfactants, thus the amount of dispersant should be limited in use.

Many studies disperse CNT by their oxidation in strong acids[15-17]. The treatment in hot acids resulted in the formation of carboxylic and other oxygen-containing groups on the CNT surface. These acidic groups electrostatically stabilized CNT in the suspensions. The dispersion of CNT can also be achieved by covalent functionalization methods[18]. It is important to note that the oxidation and functionalization strategies introduce defects and reduce the electronic conductivity and mechanical properties of CNT. Moreover, the acidic treatment is known to cut long CNT into smaller fragments with lower aspect ratio. Different from the traditional dispersing method, our new approach avoids the oxidation and functionalization of CNT, and the whole procedure is operated in safe and clean ethanol suspension instead of dealing with strong acid.

Another problem caused by some dispersants is chemical functionalization. As showing in Fig. 3.1 B[14], some surfactants would have chemical reaction and create covalent bond with CNTs. In this case, the structural integrity of CNTs would be destroyed by the new bonds. The electronic band structure of a nanotube can be described by considering the bonding of the carbon atoms arranged in a hexagonal lattice. Each carbon atom ( $Z=6$ ) is covalently bonded to three neighbor carbons via  $sp^2$  molecular orbitals. The fourth

valence electron, in the  $p_z$  orbital, hybridizes with all the other  $p_z$  orbitals to form a delocalized  $\pi$ - band. As the unit cell of graphene has two carbon atoms an even number of electrons are contained in the basic nanotube structure, which consequently can be metallic/semiconducting[19]. Thus the electrical conductivity of CNTs greatly depends on its structural integrity, and chemical functionalization should be avoided.



Fig 3.1. A. Polymer wrapping on surface of CNTs, B. covalent sidewall functionalization on CNTs[14]

### 3.1.2 Difficulties in fabrication of $\text{MnO}_2$ -CNT composite

The efficient dispersion of CNT and oxide nanoparticles in nanocomposites is of special interest for application in electrodes of ECs. The interest in  $\text{MnO}_2$ -CNT electrodes is attributed to high specific capacitance[20-22] of  $\text{MnO}_2$ . However, the electronic conductivity of  $\text{MnO}_2$  is low. The addition of CNT allows improved electronic conductivity of the composites[23, 24]. It is important to note that the CNT content in the composites must be minimized due to low specific capacitance of CNT and relatively high cost of this material. Moreover, the agglomeration of CNT and  $\text{MnO}_2$  nanoparticles in the composites must be avoided. Therefore, the efficient dispersion of  $\text{MnO}_2$  and CNT is necessary for the development of advanced  $\text{MnO}_2$ -CNT supercapacitors.

MnO<sub>2</sub>-CNT composites were obtained using redox reactions of KMnO<sub>4</sub> and CNTs. In this approach, the reduction of Mn<sup>7+</sup> species resulted in the oxidation of carbon to form carbonates in the solution. It should be noted that the oxidation of CNTs results in reduced conductivity. Moreover, the variation of the MnO<sub>2</sub> content in the composites presented difficulties, because the redox reaction was terminated when the available surfaces of CNTs were fully covered by MnO<sub>2</sub>[25].

As only the surface is involved in the pseudocapacitive behavior of manganese oxides, the key to obtain excellent capacitive properties is to improve their electronic conductivity and to increase usable specific surface area. Therefore, high dispersion of MnO<sub>2</sub> and conductive additives with excellent electronically conductivity and high specific surface area should be a promising way to improve the capacitive properties of MnO<sub>2</sub>. One of the most important conductive materials for this application is carbon materials, such as carbon nanotubes[10].

Moreover, there also have been reported that manganese oxides dispersed on the tangled carbon nanotubes by mechanical mixing and electrochemical deposition method were used as electrode materials for ECs[26-28]. Although the specific capacitance based on MnO<sub>2</sub> and MWCNT composite was higher than that of pure MnO<sub>2</sub>, the values were still low. The possible reasons is that the specific surface areas and dispersibility of MnO<sub>2</sub> prepared by these methods are still low. Therefore, it is very important to develop a effective way to achieve high usability and dispersibility of manganese oxides.

### **3.2 Low voltage window for symmetric supercapacitor**

Energy density is the main limitation and barrier for ES compared with batteries. Some achievements have improved energy density of ES in organic electrolyte. However, most organic electrolytes are relatively toxic, flammable, environmentally unfriendly, and expensive, so they are not suitable for utilization in ES.

It's urgent and necessary to develop ES with higher energy density in aqueous electrolyte. It was found that  $\text{MnO}_2$  and  $\text{MnO}_2$ -CNT composite electrodes show good capacitive behavior in a voltage window of 1V in aqueous electrolytes. It should be noted that the voltage windows of symmetric capacitors, containing two similar  $\text{MnO}_2$  based electrodes in aqueous electrolyte is smaller than the voltage windows of symmetric  $\text{RuO}_2/\text{RuO}_2$  devices [22, 29]. This is caused by the decomposition of aqueous solution when voltage window is beyond 1V, which will result a hydrogen evolution and an irreversible oxidation (polarized) process for  $\text{MnO}_2$  electrode (asymmetric CV curve). The development of asymmetric cells[22, 29], containing  $\text{MnO}_2$  positive electrodes and activated carbon (AC) negative electrodes, allowed enlarged voltage window and improved power-energy characteristics of the ES devices because of overpotential by introducing a carbon counter electrode.

### **3.3 Low mass loading of $\text{MnO}_2$ -CNTs electrode**

Recent studies highlighted the importance of the fabrication of efficient ES electrodes with high active mass loading and high active material to current collector mass ratio[30]. It is challenging to achieve high capacitance, good capacitance retention at high charge-discharge rates and cyclic stability for electrodes with mass loadings of 10-20  $\text{mg cm}^{-2}$ ,

which are required for many practical applications[30, 31]. The use of composites, prepared by mixing of MnO<sub>2</sub> nanofibers and multiwalled CNT (MWCNT) allowed[32] the fabrication of electrodes with mass loading of 40 mg cm<sup>-2</sup>. However, due to the poor dispersion of the individual components, the electrodes showed low capacitance retention at high charge-discharge rates. The need in improved dispersion of MnO<sub>2</sub> and CNT has generated interest in the development of new colloidal methods for the fabrication of MnO<sub>2</sub>-CNT composites. Additionally, our novel approach based on BiMn<sub>2</sub>O<sub>5</sub> as electrode materials paved the way for ultra-high mass loading.

### **3.4 Objectives**

As elaborated above, our main objective is to fabricate a hybrid supercapacitor which is composed of well dispersed MnO<sub>2</sub>-CNT composites as positive electrode and activated carbon-carbon black as negative electrode. The device has an enlarged voltage window in order to achieve a high energy density and power density.

Based on the problems stated above, our objectives are:

- (i) Development of new methods for the fabrication of MnO<sub>2</sub>-CNT composites with good dispersion of individual components;
- (ii) Fabrication of MnO<sub>2</sub>-CNT and activated carbon-carbon black electrodes with high active mass loading and high capacitance;
- (iii) Fabrication and testing of hybrid MnO<sub>2</sub>-CNTs/activated carbon-carbon black devices;
- (iv) Investigations on new capacitive materials BiMn<sub>2</sub>O<sub>5</sub> for higher areal and volumetric capacitance;

(v) Development of new dispersants for diverse materials dispersion and their applications in ECs and optical nanotechnology.

## References

- [1] S. Ma, K. Nam, W. Yoon, X. Yang, K. Ahn, K. Oh, K. Kim, A novel concept of hybrid capacitor based on manganese oxide materials, *Electrochemistry Communications*, 9 (2007) 2807-2811.
- [2] P. Yang, Y. Ding, Z. Lin, Z. Chen, Y. Li, P. Qiang, M. Ebrahimi, W. Mai, C.P. Wong, Z.L. Wang, Low-Cost High-Performance Solid-State Asymmetric Supercapacitors Based on MnO<sub>2</sub> Nanowires and Fe<sub>2</sub>O<sub>3</sub> Nanotubes, *Nano letters*, 14 (2014) 731-736.
- [3] Y. Hou, Y. Cheng, T. Hobson, J. Liu, Design and synthesis of hierarchical MnO<sub>2</sub> nanospheres/carbon nanotubes/conducting polymer ternary composite for high performance electrochemical electrodes, *Nano letters*, 10 (2010) 2727-2733.
- [4] Y. Wang, H. Liu, X. Sun, I. Zhitomirsky, Manganese dioxide-carbon nanotube nanocomposites for electrodes of electrochemical supercapacitors, *Scripta Materialia*, 61 (2009) 1079-1082.
- [5] Y. Wang, I. Zhitomirsky, Electrophoretic deposition of manganese dioxide-multiwalled carbon nanotube composites for electrochemical supercapacitors, *Langmuir*, 25 (2009) 9684-9689.
- [6] M. Zheng, A. Jagota, E.D. Semke, B.A. Diner, R.S. McLean, S.R. Lustig, R.E. Richardson, N.G. Tassi, DNA-assisted dispersion and separation of carbon nanotubes, *Nature Materials*, 2 (2003) 338-342.
- [7] P.C. Ma, N.A. Siddiqui, G. Marom, J.K. Kim, Dispersion and functionalization of carbon nanotubes for polymer-based nanocomposites: A review, *Compos Part a-Appl S*, 41 (2010) 1345-1367.

- [8] J. Sandlera, M.S.P. Shaffera, T. Prasseb, W. Bauhoferb, K. Schulte, A.H. Windle, Development of a dispersion process for carbon nanotubes in an epoxy matrix and the resulting electrical properties, *Polymer*, 40 (1999) 5967–5971.
- [9] J.J. Morgan, W. Stumm, Colloid-Chemical Properties of Manganese Dioxide, *Journal of Colloid Science*, 19 (1964) 347-359.
- [10] Z. Fan, J. Chen, B. Zhang, B. Liu, X. Zhong, Y. Kuang, High dispersion of  $\gamma$ -MnO<sub>2</sub> on well-aligned carbon nanotube arrays and its application in supercapacitors, *Diamond and Related Materials*, 17 (2008) 1943-1948.
- [11] Y. Sun, Y. Wang, I. Zhitomirsky, Dispersing agents for electrophoretic deposition of TiO<sub>2</sub> and TiO<sub>2</sub>-carbon nanotube composites, *Colloids and Surfaces A: Physicochemical and Engineering Aspects*, 418 (2013) 131-138.
- [12] X. Pang, P. Imin, I. Zhitomirsky, A. Adronov, Amperometric Detection of Glucose Using a Conjugated Polyelectrolyte Complex with Single-Walled Carbon Nanotubes, *Macromolecules*, 43 (2010) 10376-10381.
- [13] T. Casagrande, P. Imin, F. Cheng, G.A. Botton, I. Zhitomirsky, A. Adronov, Synthesis and Electrophoretic Deposition of Single-Walled Carbon Nanotube Complexes with a Conjugated Polyelectrolyte, *Chemistry of Materials*, 22 (2010) 2741-2749.
- [14] V. GmbH, Functionalization of Single-Walled Carbon Nanotubes, *Angew. Chem. Int. Ed.*, 41 (2002) 1853-1859.
- [15] Y. Han, M. Shen, X. Lin, B. Ding, L. Zhang, H. Tong, X. Zhang, Ternary phase interfacial polymerization of polypyrrole/MWCNT nanocomposites with core-shell structure, *Synthetic Metals*, 162 (2012) 753-758.

- [16] N.G. Sahoo, Y.C. Jung, H.H. So, J.W. Cho, Polypyrrole coated carbon nanotubes: Synthesis, characterization, and enhanced electrical properties, *Synthetic Metals*, 157 (2007) 374-379.
- [17] K. Esumi, M. Ishigami, A. Nakajima, K. Sawada, H. Honda, Chemical treatment of carbon nanotubes, *Carbon*, 34 (1996) 279-281.
- [18] T. Casagrande, G. Lawson, H. Li, J. Wei, A. Adronov, I. Zhitomirsky, Electrodeposition of composite materials containing functionalized carbon nanotubes, *Materials Chemistry and Physics*, 111 (2008) 42-49.
- [19] P.R. Bandaru, Electrical Properties and Applications of Carbon Nanotube Structures, *Journal of Nanoscience and Nanotechnology*, 7 (2007) 1239-1267.
- [20] L. Athouel, F. Moser, R. Dugas, O. Crosnier, D. Belanger, T. Brousse, Variation of the MnO<sub>2</sub> Birnessite Structure upon Charge/Discharge in an Electrochemical Supercapacitor Electrode in Aqueous Na<sub>2</sub>SO<sub>4</sub> Electrolyte, *The Journal of Physical Chemistry C*, 112 (2008) 7270-7277.
- [21] T. Brousse, P.-L. Taberna, O. Crosnier, R. Dugas, P. Guillemet, Y. Scudeller, Y. Zhou, F. Favier, D. Bélanger, P. Simon, Long-term cycling behavior of asymmetric activated carbon/MnO<sub>2</sub> aqueous electrochemical supercapacitor, *Journal of Power Sources*, 173 (2007) 633-641.
- [22] V. Khomenko, E. Raymundo-Piñero, F. Béguin, Optimisation of an asymmetric manganese oxide/activated carbon capacitor working at 2 V in aqueous medium, *Journal of Power Sources*, 153 (2006) 183-190.
- [23] R. Jiang, T. Huang, Y. Tang, J. Liu, L. Xue, J. Zhuang, A. Yu, Factors influencing

MnO<sub>2</sub>/multi-walled carbon nanotubes composite's electrochemical performance as supercapacitor electrode, *Electrochimica Acta*, 54 (2009) 7173-7179.

[24] J. Yan, Z. Fan, T. Wei, J. Cheng, B. Shao, K. Wang, L. Song, M. Zhang, Carbon nanotube/MnO<sub>2</sub> composites synthesized by microwave-assisted method for supercapacitors with high power and energy densities, *Journal of Power Sources*, 194 (2009) 1202-1207.

[25] Y. Wang, Y. Liu, I. Zhitomirsky, Surface modification of MnO<sub>2</sub> and carbon nanotubes using organic dyes for nanotechnology of electrochemical supercapacitors, *Journal of Materials Chemistry A*, 1 (2013) 12519.

[26] E. Raymundo-Piñero, V. Khomenko, E. Frackowiak, F. Béguin, Performance of Manganese Oxide/CNTs Composites as Electrode Materials for Electrochemical Capacitors, *Journal of The Electrochemical Society*, 152 (2005) A229-A235.

[27] C.Y. Lee, H.M. Tsai, H.J. Chuang, S.Y. Li, P. Lin, T.Y. Tseng, Characteristics and Electrochemical Performance of Supercapacitors with Manganese Oxide-Carbon Nanotube Nanocomposite Electrodes, *Journal of The Electrochemical Society*, 152 (2005) A716-A720.

[28] Y.-T. Wu, C.-C. Hu, Effects of Electrochemical Activation and Multiwall Carbon Nanotubes on the Capacitive Characteristics of Thick MnO<sub>2</sub> Deposits, *Journal of The Electrochemical Society*, 151 (2004) A2060-A2066.

[29] F. Wang, S. Xiao, Y. Hou, C. Hu, L. Liu, Y. Wu, Electrode materials for aqueous asymmetric supercapacitors, *RSC Advances*, 3 (2013) 13059-13084.

[30] Y. Gogotsi, P. Simon, True Performance Metrics in Electrochemical Energy Storage,

Science, 334 (2011) 917-918.

[31] L. Wei, G. Yushin, Nanostructured activated carbons from natural precursors for electrical double layer capacitors, *Nano Energy*, 1 (2012) 552-565.

[32] J. Li, Q.M. Yang, I. Zhitomirsky, Nickel foam-based manganese dioxide-carbon nanotube composite electrodes for electrochemical supercapacitors, *Journal of Power Sources*, 185 (2008) 1569-1574.

## Chapter 4 Experimental procedures

### 4.1 Materials synthesis

#### (i) MnO<sub>2</sub> particles

MnO<sub>2</sub> nanoparticles were prepared by reduction of KMnO<sub>4</sub> using ethanol (Eq.4.1).



KMnO<sub>4</sub> used in this dissertation were purchased from Aldrich Company. 50 mL dehydrated ethanol was added into 100 mL 0.21 M KMnO<sub>4</sub> solution under vigorous stirring for 24 hours. The black precipitation was collected using filtration and washed using 2 L water and 0.5 L dehydrated ethanol to remove ions and organics. The final powder was further dried in air for 48 hours and stored in desiccator. The full process is schematically shown in Fig.4.1. The MnO<sub>2</sub> nanoparticles obtained using this method had an diameters varying from 30 to 60 nm[1].

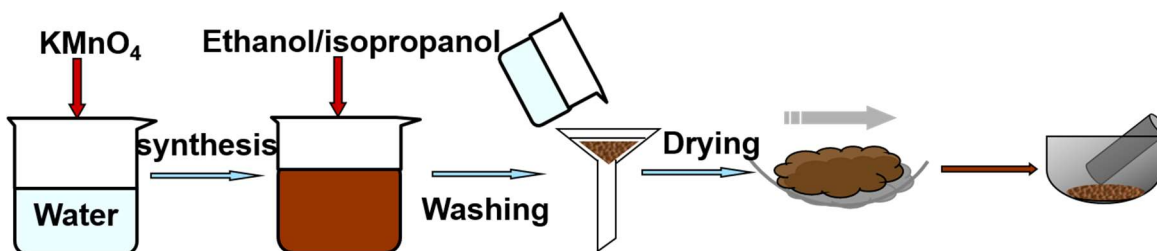


Fig. 4.1 Schematic of MnO<sub>2</sub> particles synthesis procedure

#### (ii) MnO<sub>2</sub> fibers

For the preparation of MnO<sub>2</sub> fibers, the aqueous 0.1 M KMnO<sub>4</sub> solution (50 mL) was

mixed with 0.2 M oxalic acid solution (50 mL). The volume of the mixed aqueous solution was increased to 250 mL. The reaction was performed at 100°C during 7 h. The obtained precipitate was washed with 2 L of deionized water and 1 L of ethanol, and then it was dried in air for 12 h. The product was annealed in furnace at 300°C for 3 h[2].

(iii) BiMn<sub>2</sub>O<sub>5</sub> nanocrystals

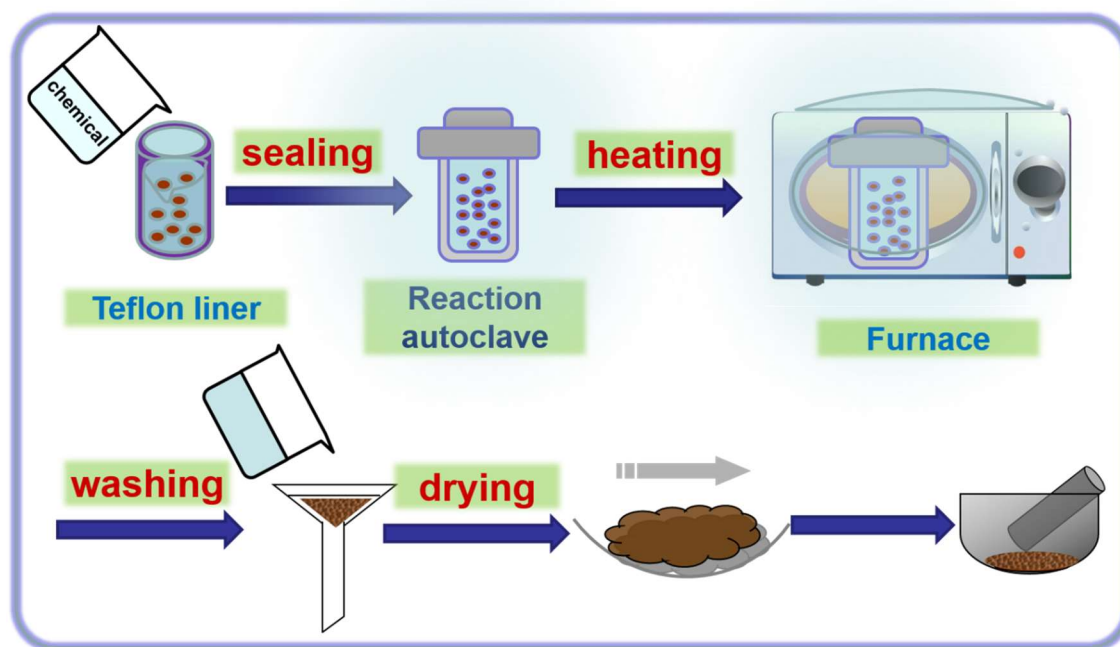


Fig. 4.2. Hydrothermal process for producing BiMn<sub>2</sub>O<sub>5</sub> nanocrystals

Bi(NO<sub>3</sub>)<sub>3</sub>, KMnO<sub>4</sub>, MnCl<sub>2</sub>·4H<sub>2</sub>O, KOH, Na<sub>2</sub>SO<sub>4</sub> were purchased from Aldrich Company. For synthesis of BiMn<sub>2</sub>O<sub>5</sub> particles, as Fig. 4.2 shows, 0.6 mmol of Bi(NO<sub>3</sub>)<sub>3</sub> was dissolved in 40 ml of deionized water, and then 0.8 mmol of MnCl<sub>2</sub>·4H<sub>2</sub>O and 0.4 mmol of KMnO<sub>4</sub> were added. Stirring of the solution was performed for 10 min and then 5 mmol of KOH was added, then stirring was continued for 10 min. The solution was

transferred to a stainless steel autoclave with a capacity of 50 ml. The autoclave was sealed and heated to 180 °C at a heating rate of 3 °C min<sup>-1</sup>. The synthesis of BiMn<sub>2</sub>O<sub>5</sub> was performed at 180 °C during 18 h. The obtained black powder was washed by deionised water and ethanol and then dried at 60 °C for 12 h[3].

(iv) MnO<sub>2</sub> tubes

Tube-like MnO<sub>2</sub> was prepared under a hydrothermal procedure: 0.3214 g of KMnO<sub>4</sub> was firstly dissolved in 29.3 mL of deionized water, followed by adding 0.7 mL of HCl aqueous solution (37 wt%). After vigorous stirring for 0.5 h, the mixed solution was transferred to a 50-mL autoclave for thermal treatment at 120 °C for 12 h. The powder were collected and washed with deionized water and ethanol for several times and then they were dried in oven at 60°C overnight.

(v) Fe<sub>2</sub>O<sub>3</sub> tubes

FeCl<sub>3</sub> and NH<sub>4</sub>H<sub>2</sub>PO<sub>4</sub> were purchased from Aldrich Company. Fe<sub>2</sub>O<sub>3</sub> nanotubes were synthesized by hydrothermal treatment. The procedure started with mixing 1.60 mL of aqueous FeCl<sub>3</sub> solution (0.5m) and 1.44 mL of aqueous NH<sub>4</sub>H<sub>2</sub>PO<sub>4</sub> solution (0.02m) with vigorous stirring. Deionized water was then added to a final volume of 40 mL. After stirring for 20 minutes, the mixture was transferred into a Teflon-lined stainless-steel autoclave with a capacity of 50 mL for hydrothermal treatment at 220°C for 48 h. The powders were collected and washed with deionized water and ethanol for several times, and dried in oven over at 60°C for overnight.

(vi) Reduced-Graphene Oxide (rGO):

Graphene oxide (GO) was synthesized from graphite powder based on modified Hummer's method. In details, 1 g of graphite powder was mixed with 0.5 g  $\text{NaNO}_3$  and 23 mL  $\text{H}_2\text{SO}_4$  (98%), the mixture was cooled to 0 °C. Then, 3 g  $\text{KMnO}_4$  was added slowly to keep the temperature of the suspension lower than 5 °C and magnetic stirred for 1h. Successively, the reaction system was transferred to 35 °C water bath and stirred for about 2h, forming a thick paste. Then, 46 mL distilled water was added slowly to the solution, and the solution was stirred for 30 min at 95 °C. The mixture was further diluted with 140 mL distilled water, treated with 10 mL  $\text{H}_2\text{O}_2$  (30%), washed with 50 mL HCl (1:10) and distilled water 2–3 times and then resuspended in distilled water. The solution was centrifuged in 12000rpm for 5 times and the precipitation was dried in 50°C. GO was reduced to rGO by a hydrothermal method. In a typical procedure, 4mL of ammonia solution (28 wt%) was added to 18 mL of aqueous GO dispersion (2.5 mg/mL), then the mixture was sealed in a Teflon-lined stainless-steel autoclave. Black hydrogels were formed after the mixture was heated at 180°C for 12 h. After washing 3-5 times by distilled water, NGHs were obtained after freeze-drying at -20°C for 12h.

(vii) PPy and PPy-MWCNTs synthesis procedure

MWCNTs in this dissertation were purchased from Bayer Inc., Germany. Pyrrole (Py) monomers, oxalic acid, bromothymol blue sodium salt (BT), and ammonium persulfate ( $(\text{NH}_4)_2\text{S}_2\text{O}_8$ ) (APS) were purchased from Sigma-Aldrich. PPy was prepared by adding 30 mM APS solution (50 mL) to 10 mM Py solution (50 mL), containing 1 mM BT. The reaction was performed at 4 °C for 5 h. A similar procedure was used for the fabrication of PPy-MWCNT composite. In this procedure, the BT dopant was used as dispersant for

MWCNTs. Stable MWCNT suspensions, containing 1 mM BT, were prepared and added to 10 mM Py solution in order to obtain composites with a PPy :MWCNT mass ratio of 7 : 3. Ultrasonic agitation was used prior to the addition of APS in order to achieve homogeneous dispersion of MWCNTs. The PPy and composite PPy - MWCNT powders were washed with 2L of deionized water and dried in air at 60 °C for 24 h[4, 5].

#### 4.2 Electrophoretic deposition and adhesion characterization

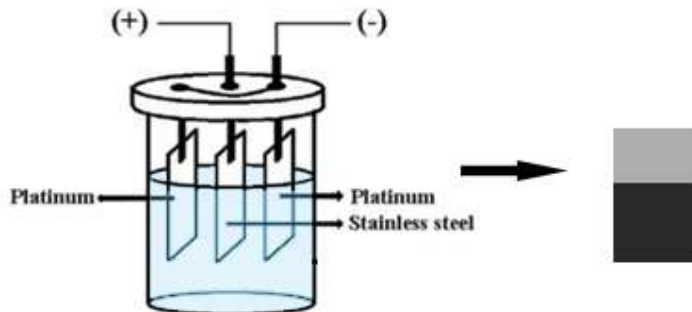


Fig. 4.3. Schematic procedure of electrophoretic deposition

EPD were performed using a constant current/constant voltage power supply (EPS 2A200, Amersham Biosciences). The EPD cell included a substrate and two Pt counter electrodes showing in Fig. 4.3. Stainless steel foils (2.5×5 cm) and Ni plaque (1×3 cm) were used as substrates. The distance between the substrate and counter electrodes was 15 mm. The deposition voltage was varied in the range of 5–150 V. The deposition time was varied in the range of 1–10 min. The deposition yield was studied for the films deposited on stainless steel substrates. A minimum of three samples were prepared in each deposition experiment. All the deposits were obtained using fresh solutions. The deposition yield measurements were repeatable, and the error was less than 5%. Adsorption mechanism

and deposition kinetics were studied by measuring the deposited film mass under different conditions. After deposition, the films were rinsed with de-ionized water and then dried in air.

### **4.3 Materials characterization techniques**

#### **(i) Phase characterization**

X-ray diffraction (XRD) studies were performed using powder diffractometer (Nicolet I2, monochromatized  $\text{CuK}\alpha$  radiation) at a scanning speed of  $0.5^\circ \text{ min}^{-1}$ .

#### **(ii) Morphology characterization**

Electron microscopy studies were performed using JEOL JSM-7000F scanning electron microscope (SEM) and FEI Tecnai Osiris transmission electron microscope (TEM) equipped with super X field emission gun (X-FEG) and ChemiSTEM™ X-ray detection system for energy-dispersive X-ray (EDX) spectroscopy. High angle annular dark field (HAADF) method in the STEM mode was used to form images and perform EDX analysis. The Esprit software was used for elemental mapping.

#### **(ii) Composition characterization**

Fourier transform infrared spectroscopy (FTIR) studies were performed on Bio-Rad FTS-40 instrument. The Ultraviolet-Visible (UV-vis) spectra were obtained using a Cary-50 UV-Vis spectrophotometer.

#### **(iv) In-situ deposit characterization**

Quartz crystal microbalance (QCM922, Princeton Applied Research, USA) method was

used for the in-situ investigation of the deposition yield. The mass  $\Delta m$  of deposited material was calculated using Sauerbrey's equation[6]:

$$-\Delta F = \frac{2F_0^2}{A\sqrt{\rho_q\mu_q}} \times \Delta m \quad (\text{eq.4.2})$$

where  $\Delta F$  is frequency decrease of the QCM,  $F_0$  is the parent frequency of QCM (9 MHz),  $A$  is the area of gold electrode ( $0.2 \text{ cm}^2$ ),  $\rho_q$  is the density of the quartz and  $\mu_q$  is the shear modulus of quartz.

#### 4.4 Electrode fabrication procedure

##### 4.4.1 Electrode fabrication using EPD

###### (i) Celestine blue as dispersant for fabrication of different electrodes

Celestine blue (CB) were purchased from Aldrich Company. The concentration of the ceramic powders in the suspensions in ethanol was  $4 \text{ g L}^{-1}$ . The concentration of CB was varied in the range of  $0-0.5 \text{ g L}^{-1}$ . Before the deposition, the suspensions were ultrasonicated for 30 min to achieve a homogeneous dispersion of the oxide particles. EPD was performed at a deposition voltage of 20 V, the deposition time was varied in the range of 1-8 min. After deposition, the deposits were dried in air for 48 h.

###### (ii) PAZO as co-dispersant for $\text{MnO}_2$ fibers-MWCNTs and ppy-MWCNTs

Poly[1-[4-(3-carboxy-4-hydroxyphenylazo)benzenesulfonamido]-1,2-ethanediyl, sodium salt] (PAZO) were purchased from Aldrich Company. For fabrication of  $\text{MnO}_2$ -MWCNTs composite electrode, concentration of  $\text{MnO}_2$ , MWCNTs and PAZO is kept at constant ratio of 4:1:1. The general procedure starts with dissolving certain amount of

PAZO into a mixture of 75% of ethanol and 25% of deionized water. After ultrasounication for 20 mins, a orange transparent solution was obtained. Then MnO<sub>2</sub> and MWCNTs were added following the rigid ratio mentioned before. After another 20 mins ultrasounication, an uniform and homogenous suspension was obtained. During EPD process, a clean and smooth Ni plaque was used as substrate and current collector for deposition. After deposition with variation of time and voltages, different MnO<sub>2</sub>-MWCNTs composite electrodes were obtained. This method was also employed for fabrication of PPy and MWCNT@PPy electrodes fabrication.

#### 4.4.2 Electrodes fabrication based on heterocoagulation

##### (i) PE and PS as dispersants for fabrication of MnO<sub>2</sub>-MWCNTs composite electrode

Phosphate ester (PE) was purchased from Richard E. Mistler Company. Poly(vinyl butyral-co-vinyl alcohol-co-vinyl acetate) (PVB, average Mw = 50,000–80,000), m-cresolsulfonphthalein sodium salt (CS) and KMnO<sub>4</sub> were purchased from Aldrich company. Ni foams with a porosity of 95% were supplied by Vale Company. The MnO<sub>2</sub> suspensions, containing PE dispersant, and MWCNT suspensions, containing CS dispersant, were mixed and the obtained precipitates were washed with ethanol (Fig. 4.4). For comparison, MnO<sub>2</sub> and MWCNT were mixed without dispersing agents and obtained precipitate was washed by the same method. The mixtures were used for the fabrication of slurries in ethanol, containing MnO<sub>2</sub> and MWCNT with total concentration of 10 g L<sup>-1</sup> and 0.2 g L<sup>-1</sup> of PVB binder. The slurries were used for the impregnation of Ni foam current collectors. The impregnated current collectors were dried in air and then pressed to 30% of original thickness. The mass of the impregnated material was 40 mg cm<sup>-2</sup>

(based on projected area)

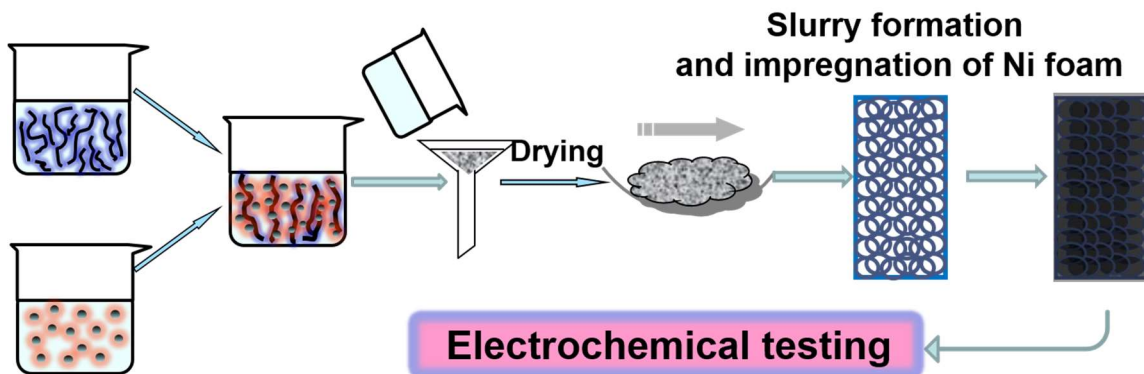


Fig. 4.4 Schematic of MnO<sub>2</sub>-MWCNTs composite electrode fabrication based on hercoagulation

(ii) BAC and CA as dispersants for fabrication of MnO<sub>2</sub>-MWCNTs composite electrode

Benzyldimethylhexadecylammonium chloride (BAC), hexa-decyltrimethylammonium bromide (CTAB), caffeic acid (CA), trans-cinnamic acid (TCA), p-coumaric acid (PCA), and 2,4-dihydroxycinnamic acid (DCA) were purchased from Aldrich company. The MnO<sub>2</sub> suspensions, containing CA dispersant, and MWCNT suspensions, containing BAC dispersant, were mixed, filtered, washed with water and dried. For comparison, MnO<sub>2</sub> and MWCNT mixtures were prepared using the same procedure without dispersing agents. The MnO<sub>2</sub>-MWCNT mixtures, containing 5% PVB binder, were impregnated into Ni foam current collectors and then pressed. The mass of the impregnated material was 40 mg cm<sup>-2</sup> (based on projected area).

#### 4.4.3 Electrodes fabrication based on colloidal route and slurry

(i) Fabrication of BiMn<sub>2</sub>O<sub>5</sub>-MWCNTs composite

CB was used as a co-dispersant for the dispersion of  $\text{BiMn}_2\text{O}_5$  and MWCNT in ethanol. The powders, containing 85 mass %  $\text{BiMn}_2\text{O}_5$  and 15 mass % MWCNT, were dispersed in ethanol and ultrasonically agitated during 30 min. PVB binder was dissolved in ethanol and added to the suspensions; the mass ratio PVB/( $\text{BiMn}_2\text{O}_5$  - MWCNT) was 0.05. The  $\text{BiMn}_2\text{O}_5$ -MWCNTs suspensions, containing PVB, were impregnated onto Ni foam current collectors, which were pressed by rolling machine to 20% of original (1.5 mm) thickness of the Ni foam. This procedure allowed improved contact of  $\text{BiMn}_2\text{O}_5$ , MWCNT and current collector. The mass loading of the active material was  $80 \text{ mg cm}^{-2}$ . In this case, the active material to current collector mass ratio was 1:1.

#### 4.4.4 Fabrication of activated carbon-carbon black for negative electrode

Activated carbon (AC) (PICACTIF, PICA) with specific area of  $2300 \text{ m}^2 \text{ g}^{-1}$  and carbon black (CB) (Cabot) were used for the fabrication of electrodes. Poly(vinylidene fluoride) (PVDF) binder and 1-Methyl-2-pyrrolidinone (MP) solvent were purchased from Alfa Aesar. Ni foams (95% porosity, Vale) were used as current collectors. The Ni foams were impregnated using slurries, containing AC, CB and PVDF in MP, and then dried at  $70^\circ\text{C}$  in air for 4 h.

### 4.5 Cell fabrication

#### (i) Coin cell fabrication

Composite  $\text{MnO}_2(\text{BiMn}_2\text{O}_5)$ -MWCNTs electrodes and activated carbon-carbon black electrodes (described previously), separated by a porous polyethylene membrane (mean pore size 0.4  $\mu\text{m}$ , Vale, Canada) were combined for the fabrication of coin cells (CR2032

type, MTI corporation, USA), which were sealed using a hydraulic crimping machine (MSK-110, MTI Corporation, USA). The general process is demonstrated in Fig. 4.5.

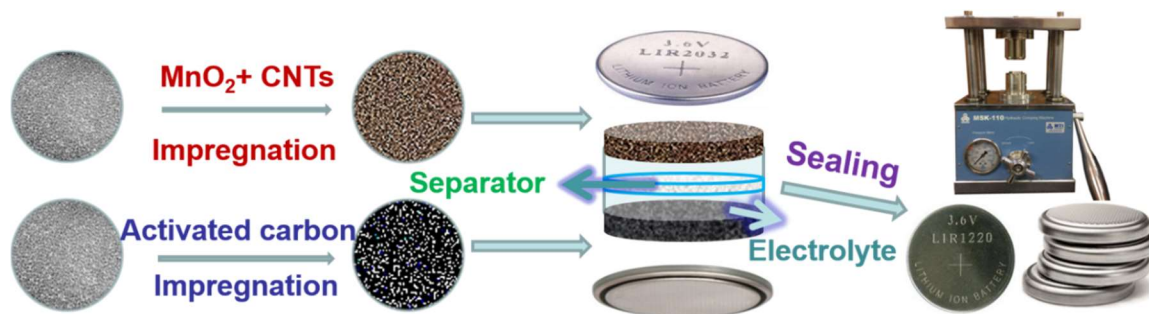


Fig. 4.5 Schematic of coin cell fabrication procedure

#### (ii) Membrane cell fabrication

Envelope cells contained two electrodes with an area of  $6 \text{ cm}^2$ , separated by a porous membrane, and aqueous  $0.5 \text{ M Na}_2\text{SO}_4$  solution as an electrolyte in a sealed plastic envelope.

### 4.6 Electrochemical characterization

The electrochemical characterization of electrode was carried out by a standard three electrode system using a potentiostat (PARSTAT 2273, Princeton Applied Research) as shown in Fig. 4.6. Surface area of the working electrode was  $1 \text{ cm}^2$ . The counter electrode was a platinum gauze, and the reference electrode was a standard calomel electrode (SCE). The characterization was in  $0.5 \text{ M Na}_2\text{SO}_4$  aqueous solutions using (i) Cyclic Voltammetry (CV), (ii) Electrochemical Impedance spectroscopy (EIS) and (iii) Galvanostatic charge–discharge studies. CV and charge-discharge studies were performed within a potential range of  $-0.9$  to  $0 \text{ V}$  versus SCE for AC-CB electrode and  $0$  to  $0.9 \text{ V}$

versus SCE for MnO<sub>2</sub>-MWCNT electrode.

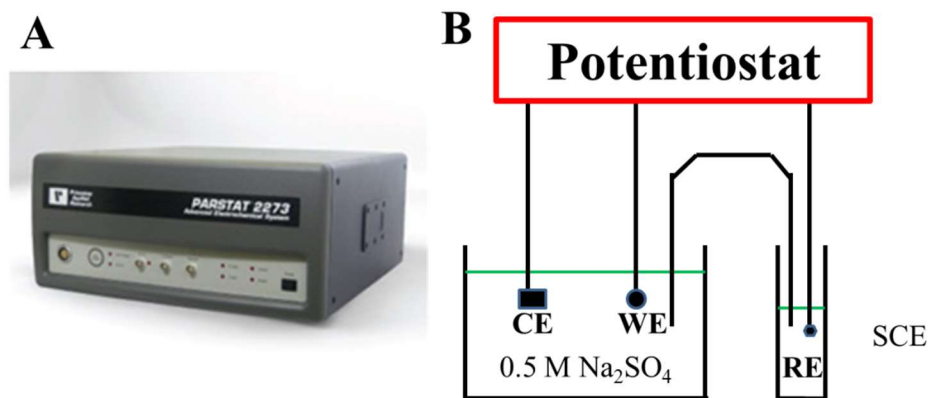


Fig. 4.6 38 PARSTAT 2273 Potentiostat (A) and three-electrodes testing system (B)

#### 4.6.1 Cyclic voltammetry

In this study, CV was performed using potentiostat. The data was recorded by PowerSuite electrochemical software. The total capacitance could be calculated using half the integrated area of the CV curve to obtain the charge (Q), and subsequently dividing by the width of the potential window ( $\Delta V$ ). The mass-normalized specific capacitance could be calculated from

$$C_m = \frac{Q}{m \times \Delta V}, \quad (\text{eq.4.3})$$

where 'm' denotes for mass loading of the electrode. If 'm' in the above equation is replaced by the area (S) of the electrode, capacitance per unit area is obtained ( $\text{F cm}^{-2}$ ), expressed as

$$C_s = \frac{Q}{S \times \Delta V}. \quad (\text{eq.4.4})$$

#### 4.6.2 Electrochemical Impedance Spectroscopy

EIS is a powerful method of evaluating a component's capacitive performance in the frequency domain. It requires to apply a small AC voltage and measure the changes in magnitude and phase over a range of frequencies. In this study, EIS were conducted using potentiostat in the frequency range of 10 mHz-100 kHz and the amplitude of AC signal of 5mV.

The impedance frequency behavior of electrode was studied using the complex mode of the capacitance. The impedance of a ES electrode can be expressed as

$$Z = \frac{1}{j\omega C} \quad (\text{eq.4.5})$$

Here C is the total capacitance,  $\omega$  is frequency, the equation then yields

$$C = \frac{1}{j\omega Z} = \frac{z''}{\omega|Z|^2} - \frac{jz'}{\omega|Z|^2} \quad (\text{eq.4.6})$$

Therefore, the total capacitance of the electrode can be written as

$$C = C' - jC'' \quad (\text{eq.4.7})$$

where  $C' = z''/\omega|Z|^2$ ,  $C'' = z'/\omega|Z|^2$ . The real part of total capacitance,  $C'$ , indicates the effective capacitance that could be utilized for energy delivery. On the other hand, the imaginary part of total capacitance,  $C''$ , reflects the irreversible loss of energy delivery.  $C''$  reaches a maximum value at a frequency of  $f_0$ , which defines as a time constant as  $\tau = 1/f_0$ . This time constant is described as a relaxation time, reflecting the rate capability of the electrode. Previous research results suggested that high power density ES generally retain

capacitance behavior over a large frequency range and has small  $\tau$ .

#### 4.6.3 Galvanostatic charge–discharge

Further evaluation of electrode's performance is accomplished by galvanostatic charge–discharge. In these experiments, a constant current density is applied and the potential vs. time response is recorded. The specific capacitance is evaluated using the equation

$$C = \frac{I \times \Delta t}{m \times \Delta V} \quad (\text{eq.4.8})$$

The energy density is evaluated employing the following equation:

$$S_E = \frac{I \Delta t (V_{\max} - V_{\min})}{2m}, \quad (\text{eq.4.9})$$

And the power density is calculated following the below equation:

$$S_P = \frac{I \Delta (V_{\max} - V_{\min})}{2m} \quad (\text{eq.4.10})$$

Where I indicated the current,  $\Delta t$  denotes the discharge time,  $\Delta V$  is the potential range, m being the mass of the active material.

Each sample runs 20 cycles before data collection, and the results for cyclic voltammetry, impedance spectroscopy, charge-discharge and capacitance retentions are repeatable and experimental errors for the results are 9%-10%.

## References

- [1] Y. Liu, K. Shi, I. Zhitomirsky, New colloidal route for electrostatic assembly of oxide nanoparticle – carbon nanotube composites, 446 (2014) 15-22.
- [2] Y. Liu, K. Shi, I. Zhitomirsky, Azopolymer triggered electrophoretic deposition of MnO<sub>2</sub>-carbon nanotube composites and polypyrrole coated carbon nanotubes for supercapacitors, journal of Materials Chemistry A, 3 (2015) 16486-16494.
- [3] Y. Liu, I. Zhitomirsky, Electrochemical supercapacitor based on multiferroic BiMn<sub>2</sub>O<sub>5</sub>, Journal of Power Sources, 284 (2015) 377-382.
- [4] K. Shi, I. Zhitomirsky, Electrophoretic nanotechnology of graphene-carbon nanotube and graphene-polypyrrole nanofiber composites for electrochemical supercapacitors, Journal of Colloid and Interface Science, 407 (2013) 474-481.
- [5] Y. Zhu, K. Shi, I. Zhitomirsky, Polypyrrole coated carbon nanotubes for supercapacitor devices with enhanced electrochemical performance, Journal of Power Sources, 268 (2014) 233-239.
- [6] M.R. Deakin, D.A. Buttry, Electrochemical applications of the quartz crystal microbalance, Analytical Chemistry, 61 (1989) 1147A-1154A.

## Chapter 5. Colloidal route for electrostatic assembly of MnO<sub>2</sub>-MWCNTs composites for supercapacitors

### 5.1 Proposed approach based on electrostatic heterocoagulation in ethanol

Carbon nanotube (CNT) - metal oxide nanocomposites are currently under development for electrochemical ECs[1] and batteries[2]. Colloidal methods are of special interest for the fabrication of nanocomposites with advanced microstructure and properties.

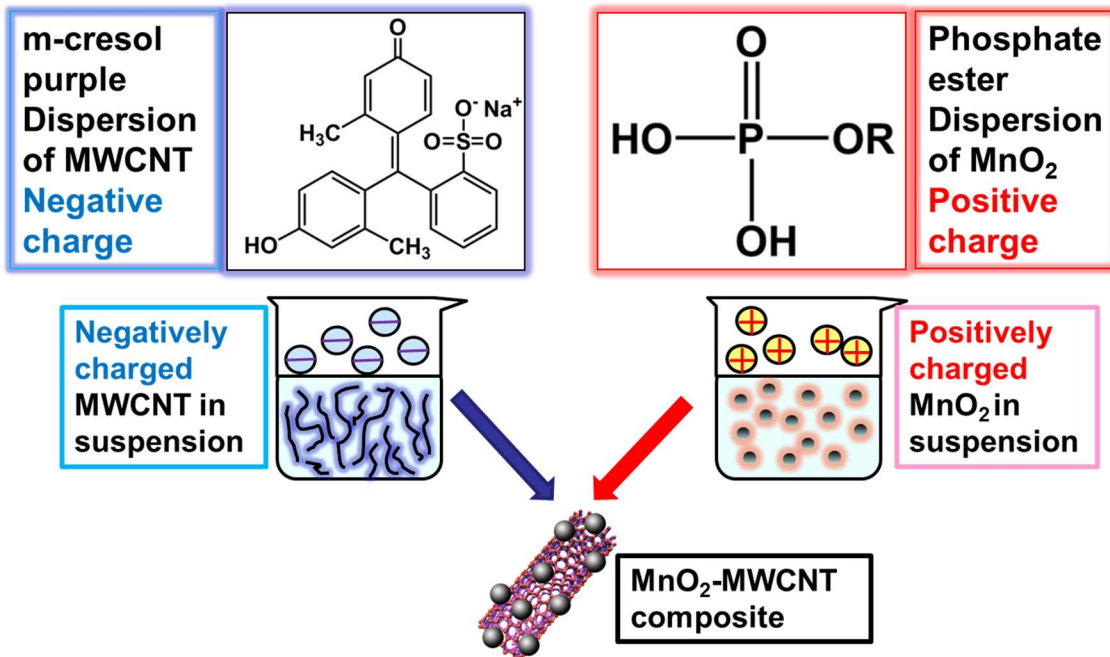


Fig. 5.1 Schematic configuration of colloidal route for fabrication of MnO<sub>2</sub>-CNT composite electrode in ethanol

The goal of this investigation was the development of a new strategy for the fabrication of metal oxide – multiwalled carbon nanotubes (MWCNT) composites. The approach is

based on the dispersion of oxide nanoparticles using phosphate ester and dispersion of MWCNT using an organic dye (Fig 5.1). The method allowed the formation of positively charged oxide nanoparticles and negatively charged MWCNT. The electrostatic heterocoagulation resulted in the fabrication of composites with uniform distribution of MWCNT and oxide particles. The results presented below indicated that this method can be used for the fabrication of advanced MnO<sub>2</sub>-MWCNT electrodes for ECs with enhanced electrochemical performance. Moreover, it was found that this method can be used for the fabrication of other nanocomposites.

## 5.2 Charging and dispersion of MWCNTs

### 5.2.1 Adsorption mechanism, involving $\pi$ - $\pi$ interaction

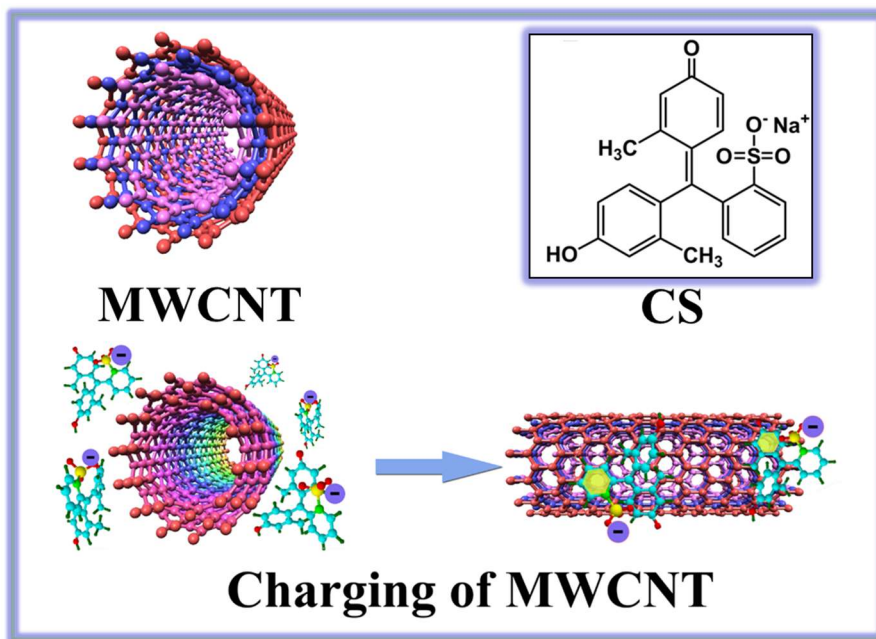


Fig 5.2 Mechanism of CS charging and dispersing MWCNTs in ethanol suspension

In the proposed approach, organic dye named m-cresol purple sodium salt (CS)

containing three aromatic rings is used to charge and disperse MWCNTs in ethanol suspension. The mechanism of CS charging and dispersing CNTs is based on  $\pi$ - $\pi$  stacking adsorption, which can be illustrated as following (Fig. 5.2). The structure of MWCNT shows the bonding of the carbon atoms arranged in a hexagonal lattice. Each carbon atom ( $Z = 6$ ) is covalently bonded to three neighbor carbons via  $sp^2$  molecular orbitals. The CS structure possesses three aromatic rings inside. The anionic properties of CS are attributed to the dissociation of  $SO_3Na$  group. Once CS is dissolved in ethanol, the sodium cations are separated from molecules, leaving the anions possessing three aromatic rings, which are adsorbed on MWCNTs due to the  $\pi$ - $\pi$  stacking effect, which has been described in many investigations. Since this  $\pi$ - $\pi$  stacking is physical adsorption and the dispersant is small molecule, it avoids the MWCNT integrity destruction and formation of thick insulating layer at the MWCNT surface, thus MWCNT can be negatively charged and efficiently dispersed stably in suspension.

### 5.2.2 EPD and characterization of MWCNTs with CS

The investigations of MWCNT suspensions in ethanol, containing CS showed that the increase in the CS concentration in the range of 0.1–1.0 g L<sup>-1</sup> resulted in improved suspension stability and increased anodic deposition rate. The amount of the deposited material increased with increasing deposition time (Fig. 5.3 A). Relatively uniform deposits were obtained (Fig. 5.3 A, inset). The results indicated that CS adsorbed on MWCNT and imparted a negative charge. SEM image of the deposit film (Fig 5.3 B) shows deposited MWCNT, which formed a porous microstructure.

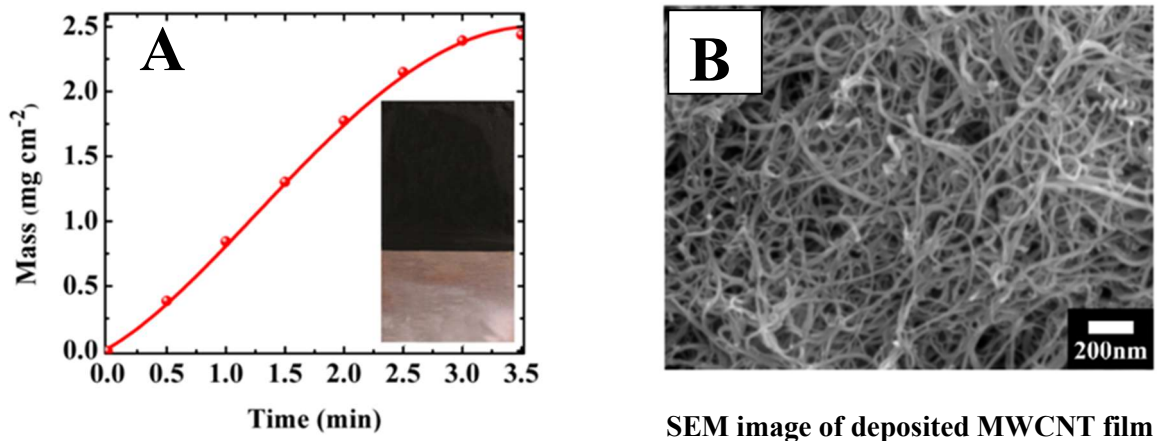


Fig. 5.3 A deposit mass versus deposition time at CS concentration of  $1 \text{ g L}^{-1}$  for  $1 \text{ g L}^{-1}$  MWCNT suspension in ethanol at a deposition voltage of 100 V; (B) SEM image of deposited MWCNT film.

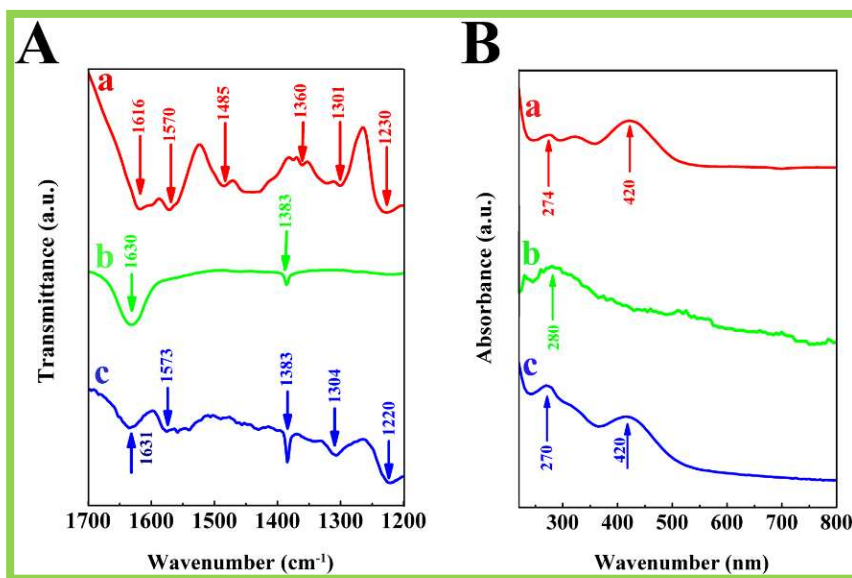


Fig. 5.4 (A) FTIR and (B) UV-vis spectra for (a) as-received CS, (b) as-received MWCNT and (c) deposited MWCNT.

The CS adsorption was confirmed by FTIR and UV-Vis studies of MWCNT removed

from the substrates. The FTIR spectrum of CS (Fig. 5.4A(a)) showed absorptions at 1616, 1571, 1485 and 1301  $\text{cm}^{-1}$ , attributed to  $\nu(\text{C}-\text{C})/\nu(\text{C}=\text{C})$  stretching vibrations of aromatic rings[3]. The absorptions at 1360 and 1224 were related to stretching  $\nu(\text{C}=\text{O})$  and  $\nu(\text{C}-\text{OH})$  vibrations, respectively[3-5]. The stretching vibrations  $\nu(\text{SO}_3^-)$  resulted in peaks at 1161, 1138 and 1019  $\text{cm}^{-1}$ [3, 6]. Bending  $\delta(\text{C}-\text{H})$  vibrations[4, 7, 8] contributed to absorptions at 1086 and 1043  $\text{cm}^{-1}$ . The FTIR spectrum of as-received MWCNT (Fig. 5.4A (b)) showed absorptions at 1630 and 1383  $\text{cm}^{-1}$ , related to stretching  $\nu(\text{C}-\text{C})$  vibrations and stretching vibration of surface  $\text{COO}^-$  groups, respectively[3, 9]. In comparison with the spectra of as-received MWCNT, the spectra of deposited MWCNT (Fig. 5.4(c)) showed additional adsorptions at 1572, 1303, 1223, 1161, 1137, 1084 and 1018  $\text{cm}^{-1}$ . Similar absorptions were observed in the spectrum of CS. Therefore, the FTIR data indicated that deposited MWCNT contained adsorbed CS. The UV-Vis studies provided further evidence of CS adsorption. The UV-Vis spectrum of CS (Fig. 5.4B(a)) showed absorptions at 274 and 420 nm. Such adsorptions were not observed in the spectrum of MWCNT(Fig. 5.4B(b)). Taking into account that similar absorptions at 270 and 420 nm were observed (Fig. 5.4B(c)) in the spectrum of deposited MWCNT it was concluded that deposited MWCNT contained adsorbed CS.

### **5.3 Charging and dispersion of $\text{MnO}_2$**

#### **5.3.1 Mechanism for charging and dispersion of $\text{MnO}_2$**

Another promising dispersant named phosphate ester (PE) is applied to charge and disperse  $\text{MnO}_2$ . The phosphate ester is an effective electrostatic stabilizer, which charges

the particles positively in organic liquids by donating protons to the surface. Moreover, phosphate ester acts as a steric dispersant by anchoring the long-chain molecules to the particle surfaces. According to the manufacturer, PE contains a mixture of long-chain phosphate esters of ethoxylated alcohols. Fig. 5.5 shows the structures of the mono- and diesters [10]. The PE used in this investigation (Emphos PS 21-A) is an equal mixture of mono and dialkyl phosphate esters, containing alkoxy functional groups  $R = (\text{CH}_2\text{CH}_2\text{O})_7(\text{CH}_2)_9\text{CH}_3$ .

Important factors to consider when selecting a binder-dispersant-solvent system are: chemical compatibility of components; solubility of binder and additives; particle charge; viscosity; and electric resistivity of the suspension. It was demonstrated that ethyl alcohol-

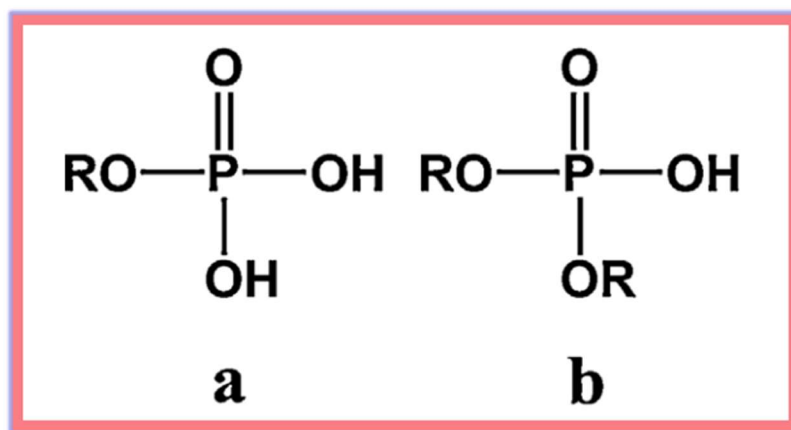


Fig. 5.5 Chemical structures of (a) mono- and (b) di-alkyl phosphate esters

-hol-phosphate ester-polyvinyl butyral system is an effective solvent-dispersant-binder system for electrophoretic deposition of various ceramic materials and ceramic laminates.

Mechanism of PE charging and dispersing  $\text{MnO}_2$  is illustrated by Fig 5.6. When PE is added (A) to ethanol suspension, only a very small amount of PE is ionized; then after

introducing  $\text{MnO}_2$  (B), PE adsorbs as neutral molecules on the surface of  $\text{MnO}_2$  particles;

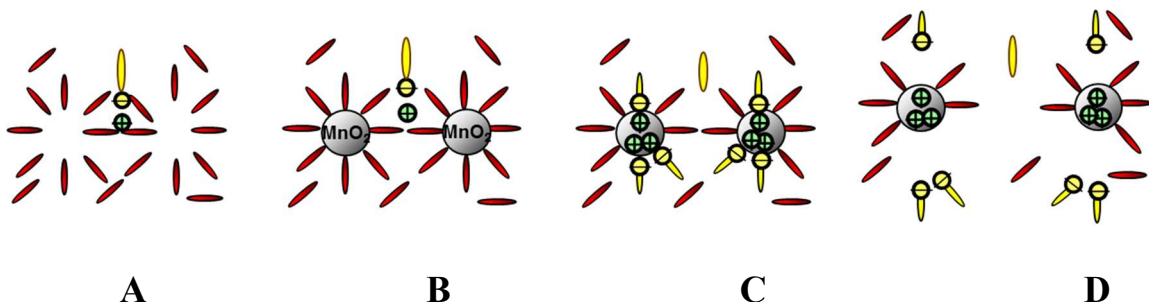


Fig. 5.6 Mechanism of PE charging and dispersing  $\text{MnO}_2$

a large portion of PE donate their protons to the surface of  $\text{MnO}_2$  particles, since the protons have positive charges,  $\text{MnO}_2$  can be highly charged (C); finally (D), the dissociated PE separate from  $\text{MnO}_2$  and leave protons on the surface of particle, thus  $\text{MnO}_2$  can be positively charged and dispersed, avoiding agglomeration.

### 5.3.2 EPD and characterization of $\text{MnO}_2$ with PE

Cathodic deposits were obtained from pure  $\text{MnO}_2$  suspensions in ethanol without PE. However, the deposits were highly agglomerated and non-uniform. The positive charge of  $\text{MnO}_2$  can be attributed to adsorbed  $\text{H}^+$ , originated from ethanol dissociation, as described in the literature[11]. The addition of PE resulted in increased deposition yield with increasing PE concentration in the range of 0-0.5 g L<sup>-1</sup>, as shown in Fig. 5.7 A. The deposition rate can be varied by variation of deposition time (Fig. 5.7 B) or voltage (Fig. 5.7 C). The addition of PE resulted in reduced agglomeration and allowed the formation of relatively uniform deposits (Fig. 5.7 B, inset). The low current in pure PE solutions is in agreement with the literature and indicates low PE dissociation degree in the bulk of the suspension [12]. The PE adsorption on particle surface and dissociation resulted in

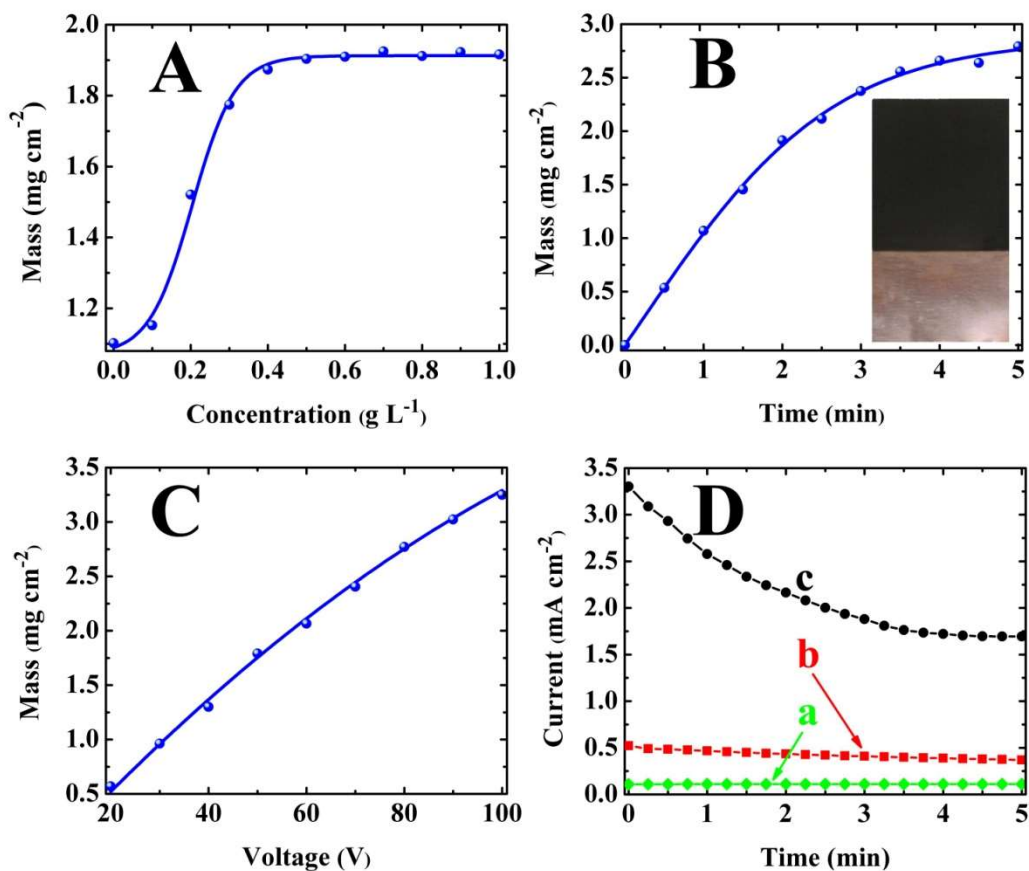


Fig. 5.7 (A,B,C) Deposit mass of MnO<sub>2</sub> from 10 g L<sup>-1</sup> MnO<sub>2</sub> suspensions versus (A) PE concentration in the suspensions at a deposition voltage of 40 V and deposition time of 2 min, (B) deposition time at a deposition voltage of 40V and PE concentration of 1 g L<sup>-1</sup>, inset shows MnO<sub>2</sub> deposit on a stainless steel foil, (C) deposition voltage at PE concentration of 1 g L<sup>-1</sup> and deposition time of 1 min and (D) current versus time dependence at a voltage of 100 V for (a) 1 g L<sup>-1</sup> PE solution (b) 10g L<sup>-1</sup> MnO<sub>2</sub> suspension (c) 10g L<sup>-1</sup> MnO<sub>2</sub> suspension, containing 1g L<sup>-1</sup> PE.

H<sup>+</sup> transfer to the surface and particle charging[12]. This dispersion and charging method offers important advantages, because efficient dispersion can be achieved at relatively

low ionic strength[12]. It is important to note that the chemical structure of PE, used in our investigation, was similar to that, used in the reference[12]. The comparison with other literature data, described above [13, 14], indicated that the chemical structure and composition of PE dispersant play an important role in its functionality.

In the previous investigations, PE was used for the dispersion of inorganic materials. It was found that PE strongly adsorbed on various inorganic materials [15-17]. PE was used a dispersant for tape casting of silicon nitride [18], titanium dioxide[19], lanthanum chromite[20] and barium titanate[21]. PEs of mono-alkyl, di-alkyl and ethoxy alkyl type imparted a negative charge to  $\text{BaTiO}_3$  particles in organic solvents, providing their dispersion[13]. In contrast, in another investigation it was found that  $\text{BaTiO}_3$  particles in the presence of PE were positively charged in non-aqueous suspensions and negatively charged in aqueous suspensions [12]. PE imparted a positive charge to complex oxides[22-24] in organic solvents. The suggested charging mechanism in non-aqueous suspensions involved adsorption of electrically neutral PE molecules on the particle surface, dissociation of PE, proton transfer to the particle surface and desorption of anionic PE species[12]. However, in another investigation it was suggested that PE dissociated in the bulk of the solutions and then released protons adsorbed on ceramic particles, imparting a positive charge[14]. The investigations of  $\text{BaTiO}_3$ , dispersed in a mixed ethanol-acetone solvent without PE, showed a high positive charge, which decreased with increasing PE addition[25]. It was found that the stability of  $\text{BaTiO}_3$  suspensions increased with the addition of PE in spite of the surface charge decrease. These studies showed a competitive adsorption of a solvent and PE molecules [25].

## 5.4 Fabrication and characterization of MnO<sub>2</sub>-MWCNTs composite electrodes

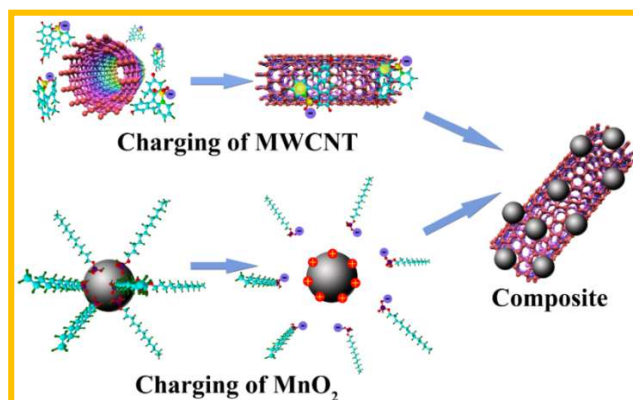


Fig. 5.8 Fabrication of MnO<sub>2</sub>-MWCNT composite by mixing of MnO<sub>2</sub> suspension, containing PE dispersant, and MWCNT suspension, containing CS dispersant.

The use of CS for the dispersion and charging of MWCNT opened a new strategy for the fabrication of composites. In this new strategy, the suspensions of negatively charged MWCNT, dispersed using CS, and the suspensions of positively charged MnO<sub>2</sub> nanoparticles, dispersed using PE, were mixed for the formation of composites, as it is shown in Fig. 5.8.

### 5.4.1 Morphology characterization

Fig. 5.9 shows SEM images of MnO<sub>2</sub>, MWCNT and MnO<sub>2</sub>-MWCNT composites, obtained after filtration, washing with ethanol and drying of corresponding suspensions. The comparison of the SEM images of MnO<sub>2</sub> nanoparticles (Fig.5A) and fibrous network, formed by MWCNT (Fig. 5B) with SEM images of the composite (Fig. 5C,D) indicated that the method developed in this investigation allowed relatively uniform distribution of

individual components. The SEM images indicated that MWCNT were well dispersed and formed a 3-D network in the MnO<sub>2</sub> matrix.

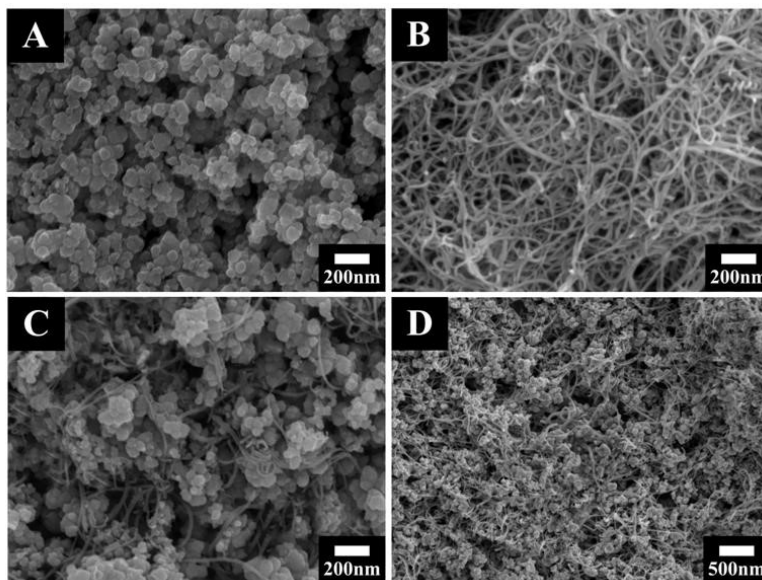


Fig. 5.9 SEM images of (A) MnO<sub>2</sub>, (B) MWCNT and (C,D) composite MnO<sub>2</sub>-MWCNT composite, prepared using PE and CS, at different magnifications.

#### 5.4.2 Electrochemical characterization for single electrode

The MnO<sub>2</sub>-MWCNT composites, prepared using PE and CS, were investigated for application in ECs. Fig.5.10 shows CVs for the electrodes, prepared using PE and CS dispersants, and without dispersants. The electrodes, prepared with dispersants showed box shape CVs at different scan rates, indicating good capacitive behavior. In contrast, the electrodes, prepared without dispersants showed tilted CVs of lower area, indicating lower capacitance and higher resistance.

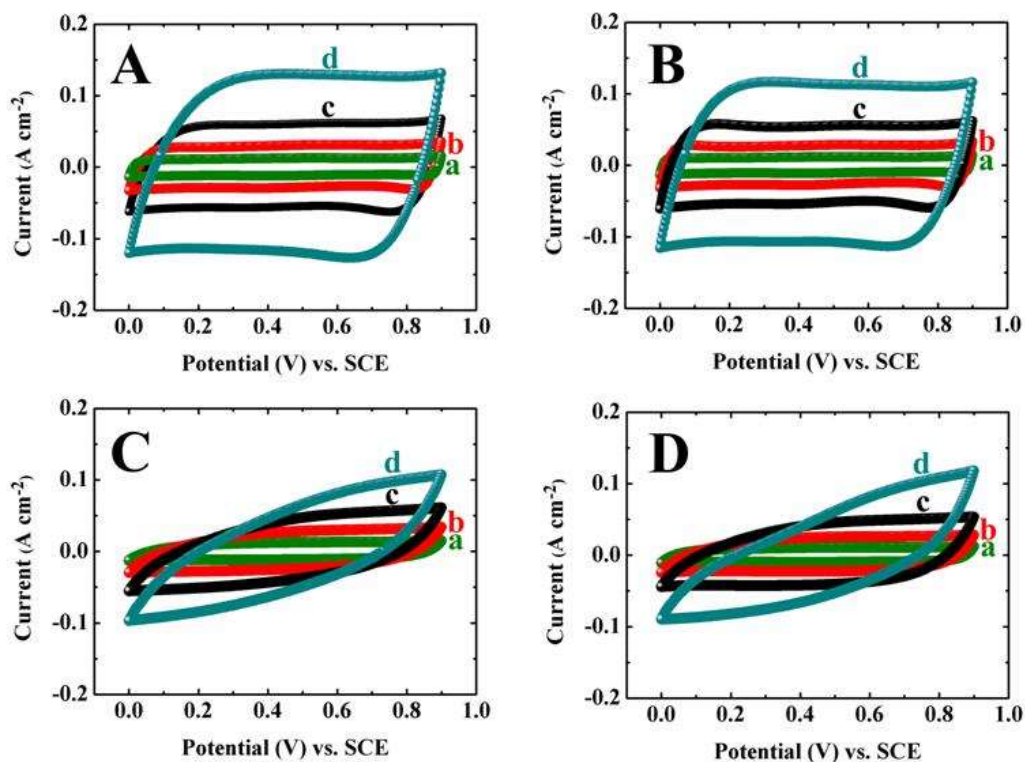


Fig. 5.10 CVs for electrodes with mass loading of  $40 \text{ mg cm}^{-2}$ , prepared (A,B) using PE and CS dispersants and (C,D) without dispersants, containing (A,C) 83%  $\text{MnO}_2$ , 15% MWCNT and 2% PVB and (B,D) 78%  $\text{MnO}_2$ , 20% MWCNT and 2% PVB at scan rates of (a) 2, (b) 5, (c) 10 and (d)  $20 \text{ mV s}^{-1}$ .

Fig. 5.11 A shows capacitances  $C_s$  and  $C_m$ , calculated from the CV data, for electrodes, prepared with PE and CS dispersants and without dispersants. The  $\text{MnO}_2$ -MWCNT electrodes, prepared using the dispersants, showed significantly higher capacitance, compared to the  $\text{MnO}_2$ -MWCNT electrodes, prepared by mixing of the individual components without dispersants. The difference is especially evident at scan rates above  $20 \text{ mV s}^{-1}$ , where the electrodes, prepared using dispersants, showed 2-3 times higher

capacitance.

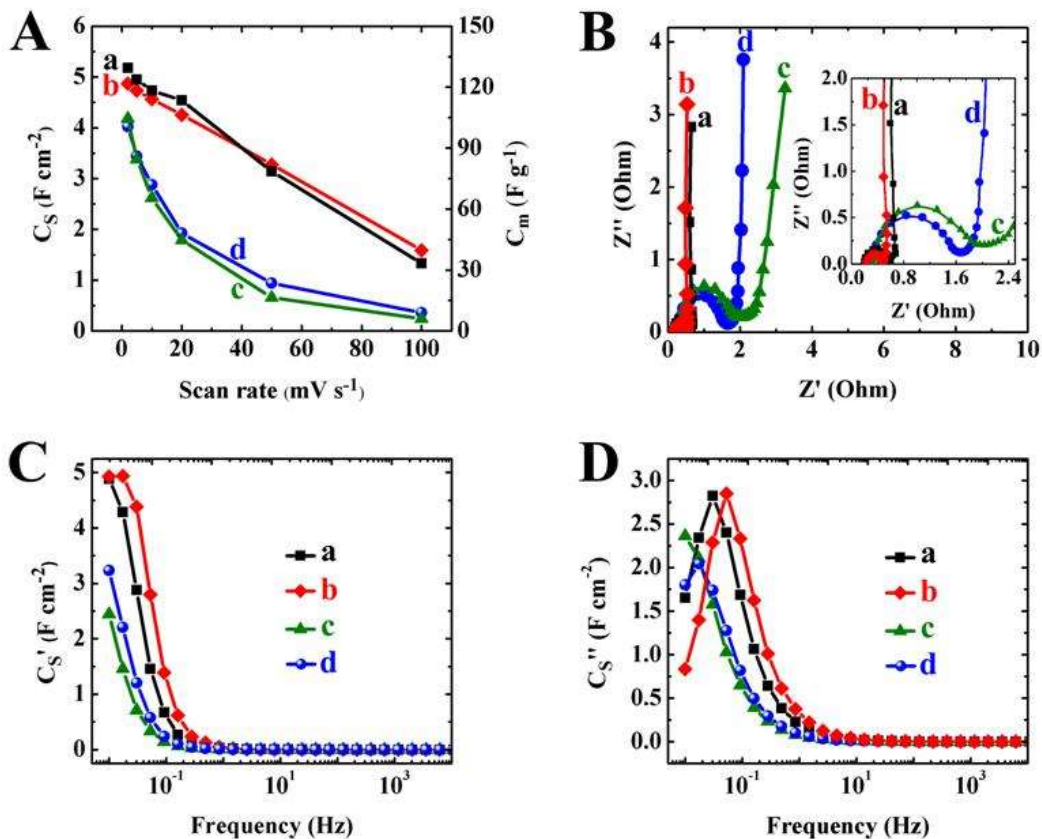


Fig. 5.11 (A)  $C_s$  and  $C_m$ , calculated from the CV data, (B) Nyquist plot of complex impedance and components of complex capacitance (C)  $C_s'$  and (D)  $C_s''$  versus frequency for electrodes with mass loading of  $40\ mg\ cm^{-2}$ , prepared (a,b) using PE and CS dispersants and (c,d) without dispersants, containing (a,c) 83%  $MnO_2$ , 15% MWCNT and 2% PVB and (b,d) 78%  $MnO_2$ , 20% MWCNT and 2% PVB.

The electrochemical testing results indicated that good dispersion of  $MnO_2$  and MWCNT and improved contact between  $MnO_2$  and MWCNT allowed enhanced electrochemical performance. The charge-discharge mechanism of  $MnO_2$  is described by the following

reaction[26]:



where  $\text{A}^+ = \text{Li}^+, \text{Na}^+, \text{K}^+, \text{H}^+$ . Equation (5.1) indicates that high electronic and ionic conductivities are necessary in order to utilize capacitive properties of  $\text{MnO}_2$  in ES electrodes. The good dispersion of  $\text{MnO}_2$  was beneficial for access of electrolyte ions to this material. MWCNT improved electronic conductivity of the composite. However, as pointed out above, the amount of MWCNT in the composite must be minimized due to low specific capacitance of MWCNT.

Therefore, good dispersion of MWCNT is of critical importance for the fabrication of efficient capacitive electrodes. Good contact of  $\text{MnO}_2$  and MWCNT is important in order to supply electrons for the charge-discharge reactions of  $\text{MnO}_2$ . The approach developed in this investigation allowed improved contact of MWCNT and  $\text{MnO}_2$ , which was achieved by heterocoagulation of well dispersed positively charged  $\text{MnO}_2$  and negatively charged MWCNT in the suspensions.

The comparison of the data for electrodes, prepared using dispersants, showed that the electrode, containing 15% MWCNT, exhibited higher capacitance at low scan rates, compared to the electrode, containing 20% MWCNT Fig 5.11 A(a,b). The difference can be attributed to lower specific capacitance of MWCNT, compared to that of  $\text{MnO}_2$ . However, the high conductivity of MWCNT was beneficial at high scan rates and allowed slightly higher capacitance of the electrode, containing 20% MWCNT. The highest capacitance of  $5.3 \text{ F cm}^{-2}$  was achieved at a scan rate of  $2 \text{ mV s}^{-1}$  for the electrode,

containing 15 % MWCNT.

The enhanced electrochemical performance of the composites, prepared using dispersants, was confirmed by the impedance spectroscopy data, presented in Fig. 5.11 (B). The electrodes, prepared using dispersants showed lower resistance  $R=Z'$ . The capacitances, calculated from the impedance data, showed typical relaxation type dispersions[27], as indicated by the reduction of  $C'$  with frequency and corresponding relaxation maxima in the frequency dependences of  $C''$  (Fig. 5.11C,D). The electrodes, prepared using PE and CS, showed relaxation type dispersion at higher frequencies, as illustrated by the reduction in  $C'$  at higher frequencies and corresponding shift of relaxation maxima of  $C''$ . This result is in agreement with the data, presenting in Fig.5.11(A), which indicated improved capacitance retention at high scan rates for the electrodes, prepared in the presence of dispersants.

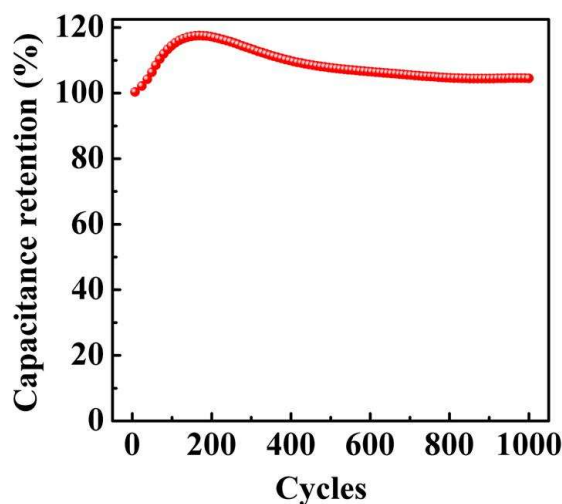


Fig. 5.12 Capacitance retention of  $\text{MnO}_2$ -MWCNT composite electrode, containing 15% MWCNT, prepared using PE and CS dispersants at a scan rate of  $50 \text{ mV s}^{-1}$  in 0.5 M

Na<sub>2</sub>SO<sub>4</sub> electrolyte.

The investigation of cycling behavior of the electrodes showed good cycling stability. The capacitance increased with increasing cycle number during the first 200 cycles and then decreased (Fig. 5.12). The capacitance retention after 1000 cycles was found to be 104%. The variations of capacitance during cycling can be attributed to different factors, described in the literature, such as oxidation[28] of non-stoichiometric MnO<sub>2</sub> or changes in the electrode microstructure[27].

#### 5.4.3 Electrochemical characterization for device

The composite MnO<sub>2</sub>-MWCNT electrodes were used for the fabrication of hybrid devices with an additional electrode, containing activated carbon as a capacitive material. The hybrid cells offer an advantage of larger voltage window[29-31], compared to the symmetrical devices, containing two similar MnO<sub>2</sub>-MWCNT electrodes.

The charge-discharge behavior of the hybrid 2-electrode coin cells was studied by chronopotentiometry. The galvanostatic charge-discharge curves were analyzed at different current densities (Fig. 5.13A) and using multiple charge-discharge cycling (Fig. 5.13B) in a voltage window of 1.6 V. Fig.5.13 indicates that prepared coin cells showed linear charge-discharge behavior at different current densities and during multiple cycling. The coin cells can be used for powering of 20 mA light emitting devices (Fig. 5.13 A inset).

It was found that the approach developed in this investigation can be used for the fabrication of other nanocomposites, containing MWCNT and nanoparticles of various

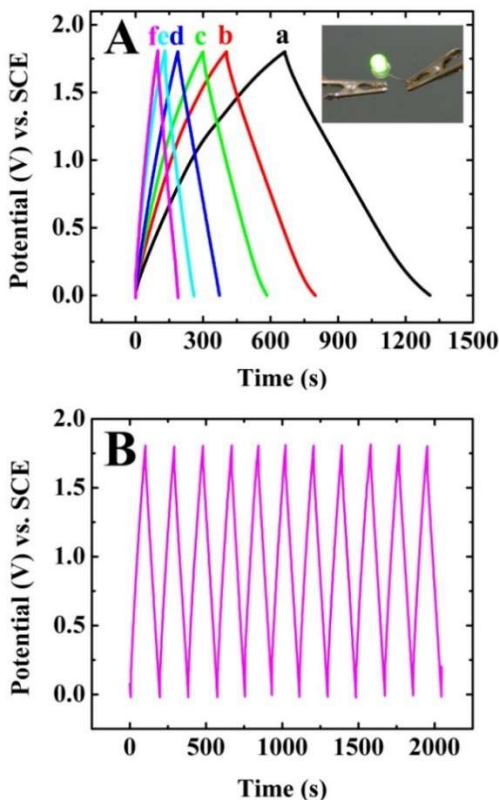


Fig. 5.13. Galvanostatic charge-discharge behavior of a hybrid coin cell (A) at current densities of (a) 2, (b) 3, (c) 4, (d) 7 and (e) 10 mA cm<sup>-2</sup> and (B) multiple cycling at 10 mA cm<sup>-2</sup>, inset shows a bulb powered by a coin cell.

oxide materials, which can be positively charged and dispersed using PE, such as BaTiO<sub>3</sub>, Gd<sub>2</sub>O<sub>3</sub>, Y<sub>2</sub>O<sub>3</sub>, Mn<sub>3</sub>O<sub>4</sub> and other oxides[32].

## 5.5 Conclusions

PE dispersant allowed the formation of stable suspension of positively charged oxide nanoparticles in ethanol. The charging mechanism involved the dissociation of PE, catalyzed by oxide particles, and H<sup>+</sup> transfer to the particle surface. CS dispersant allowed the formation of stable suspensions of negatively charged MWCNT in ethanol. It was

found that MnO<sub>2</sub>-MWCNT composites with uniform distribution of individual components can be obtained by heterocoagulation of positively charged MnO<sub>2</sub> and negatively charged MWCNT. Electrochemical testing results demonstrated that efficient dispersion of individual components is of critical importance for the fabrication of advanced composites with improved electrochemical performance. The MnO<sub>2</sub>-MWCNT composites are promising materials for application in electrodes of ECs. The method, developed in this investigation can be used for the fabrication of other nanocomposites, containing oxide nanoparticles and MWCNT.

Yangshuai Liu has the major contribution to this work, Dr. Igor Zhitomirsky also contributes to this work, and Kaiyuan Shi has contribution on SEM characterization to this work.

## References

- [1] Y. Su, I. Zhitomirsky, Electrophoretic Assembly of Organic Molecules and Composites for Electrochemical Supercapacitors, *J. Colloid Interface Sci.*, 392 (2013) 247-255.
- [2] A.C. Marschilok, C.P. Schaffer, K.J. Takeuchi, E.S. Takeuchi, Carbon nanotube-metal oxide composite electrodes for secondary lithium-based batteries, *Journal of Composite Materials*, 47 (2013) 41-49.
- [3] Y. Sun, Y. Wang, I. Zhitomirsky, Dispersing Agents for Electrophoretic Deposition of TiO<sub>2</sub> and TiO<sub>2</sub>-Carbon Nanotube Composites, *Colloids Surf., A*, 418 (2013) 131-138.
- [4] I.A. Jankovic, Z.V. Saponjic, M.I. Comor, J.M. Nedeljkovic, Surface Modification of Colloidal TiO<sub>2</sub> Nanoparticles with Bidentate Benzene Derivatives, *The Journal of Physical Chemistry C*, 113 (2009) 12645-12652.
- [5] I. Mohammed-Ziegler, F. Billes, Vibrational spectroscopic calculations on pyrogallol and gallic acid, *Journal of Molecular Structure: THEOCHEM*, 618 (2002) 259-265.
- [6] S. Li, F. Zheng, X. Liu, F. Wu, N. Deng, J. Yang, Photocatalytic degradation of p-nitrophenol on nanometer size titanium dioxide surface modified with 5-sulfosalicylic acid, *Chemosphere*, 61 (2005) 589-594.
- [7] K.D. Dobson, A.J. McQuillan, In situ infrared spectroscopic analysis of the adsorption of aromatic carboxylic acids to TiO<sub>2</sub>, ZrO<sub>2</sub>, Al<sub>2</sub>O<sub>3</sub>, and Ta<sub>2</sub>O<sub>5</sub> from aqueous solutions, *Spectrochimica Acta A*, 56 (2000) 557-565.
- [8] H. Gulley-Stahl, P.A. Hogan, W.L. Schmidt, S.J. Wall, A. Buhrlage, H.A. Bullen, Surface Complexation of Catechol to Metal Oxides: An ATR-FTIR, Adsorption, and

Dissolution Study, *Environmental Science & Technology*, 44 (2010) 4116-4121.

[9] K. Shi, I. Zhitomirsky, Electrophoretic nanotechnology of graphene-carbon nanotube and graphene-polypyrrole nanofiber composites for electrochemical supercapacitors, *Journal of Colloid and Interface Science*, 407 (2013) 474-481.

[10] Cathodic electrodeposition of ceramic and organoceramic materials. Fundamental aspects, *Advances in Colloid and Interface Science*, 97 (2002) 279-317.

[11] R. Damodaran, B.M. Moudgil, Electrophoretic deposition of calcium phosphates from non-aqueous media, *Colloids and Surfaces A: Physicochemical and Engineering Aspects*, 80 (1993) 191-195.

[12] K.R. Mikeska, W.R. Cannon, Non-aqueous dispersion properties of pure barium titanate for tape casting, *Colloids and Surfaces*, 29 (1988) 305-321.

[13] L.W. Chu, K.N. Prakash, M.-T. Tsai, I.N. Lin, Dispersion of nano-sized BaTiO<sub>3</sub> powders in nonaqueous suspension with phosphate ester and their applications for MLCC, *Journal of the European Ceramic Society*, 28 (2008) 1205-1212.

[14] T. Uchikoshi, Y. Sakka, Phosphate esters as dispersants for the cathodic electrophoretic deposition of alumina suspensions, *Journal of the American Ceramic Society*, 91 (2008) 1923-1926.

[15] G.F. Hudson, M.C.A. Mathur, S. Raghavan, Interaction of barium ferrite particles with phosphate ester dispersants, *IEEE Transactions on Magnetics*, 27 (1991) 4663-4665.

[16] H.B. Abderrahmen, H. Said, S. Partyka, R. Denoyel, Ester phosphate adsorption on calcium carbonate, *Journal de Chimie Physique et de Physico-Chimie Biologique*, 94 (1997) 750-750.

- [17] C.-J. Chung, J.-H. Jean, Dispersion of titania powder in an electronic ink for electrophoretic display, *Journal of the American Ceramic Society*, 90 (2007) 3490-3495.
- [18] C.A. Gutierrez, R. Moreno, Tape casting of non-aqueous silicon nitride slips, *Journal of the European Ceramic Society*, 20 (2000) 1527-1537.
- [19] Z. Jingxian, J. Dongliang, L. Weisensel, P. Greil, Deflocculants for tape casting of TiO<sub>2</sub> slurries, *Journal of the European Ceramic Society*, 24 (2004) 2259-2265.
- [20] M.W. Murphy, T.R. Armstrong, P.A. Smith, Tape casting of lanthanum chromite, *Journal of the American Ceramic Society*, 80 (1997) 165-170.
- [21] T. Chartier, E. Jorge, P. Boch, Dispersion properties of BaTiO<sub>3</sub> tape-casting slurries, *Journal of the European Ceramic Society*, 11 (1993) 387-393.
- [22] G.F. Hudson, M.M. Andrews, S. Raghavan, Interaction of phosphate ester dispersants with calcined alumina, *Colloid and Polymer Science*, 271 (1993) 56-62.
- [23] I. Zhitomirsky, A. Petric, Electrophoretic deposition of ceramic materials for fuel cell applications, *Journal of the European Ceramic Society*, 20 (2000) 2055-2061.
- [24] I. Zhitomirsky, A. Petric, Electrophoretic deposition of electrolyte materials for solid oxide fuel cells, *Journal of Materials Science*, 39 (2004) 825-831.
- [25] U. Paik, V.A. Hackley, S.-C. Choi, Y.-G. Jung, The effect of electrostatic repulsive forces on the stability of BaTiO<sub>3</sub> particles suspended in non-aqueous media, *Colloids and Surfaces A: Physicochemical and Engineering Aspects*, 135 (1998) 77-88.
- [26] S. Devaraj, N. Munichandraiah, High Capacitance of Electrodeposited MnO<sub>2</sub> by the Effect of a Surface-Active Agent, *Electrochemical and Solid-State Letters*, 8 (2005) A373-A377.

- [27] K. Shi, I. Zhitomirsky, Influence of current collector on capacitive behavior and cycling stability of Tiron doped polypyrrole electrodes, *Journal of Power Sources*, 240 (2013) 42-49.
- [28] N. Nagarajan, M. Cheong, I. Zhitomirsky, Electrochemical capacitance of MnOx films, *Materials Chemistry and Physics*, 103 (2007) 47-53.
- [29] T. Brousse, P.-L. Taberna, O. Crosnier, R. Dugas, P. Guillemet, Y. Scudeller, Y. Zhou, F. Favier, D. Bélanger, P. Simon, Long-term cycling behavior of asymmetric activated carbon/MnO<sub>2</sub> aqueous electrochemical supercapacitor, *Journal of Power Sources*, 173 (2007) 633-641.
- [30] T. Brousse, M. Toupin, D. Belanger, A Hybrid Activated Carbon-Manganese Dioxide Capacitor using a Mild Aqueous Electrolyte, *Journal of The Electrochemical Society*, 151 (2004) 614-622.
- [31] V. Khomenko, E. Raymundo-Piñero, F. Béguin, Optimisation of an asymmetric manganese oxide/activated carbon capacitor working at 2 V in aqueous medium, *Journal of Power Sources*, 153 (2006) 183-190.
- [32] Y. Liu, K. Shi, I. Zhitomirsky, New colloidal route for electrostatic assembly of oxide nanoparticle-carbon nanotube composites, *Colloids and Surfaces A*, 446 (2014) 15–22.

## **Chapter 6 Aqueous electrostatic dispersion and heterocoagulation of MnO<sub>2</sub>-MWCNTs composite for supercapacitor**

### **6.1 New approach based on electrostatic heterocoagulation in aqueous suspension**

Two promising dispersants were used to charge and disperse MnO<sub>2</sub> and MWCNT in aqueous condition. The goal of this investigation was the development of composite MnO<sub>2</sub>-MWCNT electrodes by a new aqueous colloidal method, based on the electrostatic heterocoagulation of negatively charged MnO<sub>2</sub> nanoparticles and positively charged MWCNT. New strategy involved the use of anionic and cationic dispersants, which selectively adsorbed on MnO<sub>2</sub> and MWCNT, respectively. Proof-of-concept studies resulted in the formation of MnO<sub>2</sub>-MWCNT composites with high active mass loadings, which showed significant improvement in capacitance at high charge-discharge rates. The use of colloidal methods for the fabrication of MnO<sub>2</sub>-MWCNT nanocomposites offers advantages, because the problem of MWCNT degradation can be avoided. The results presented below indicated that the method allowed the fabrication of efficient asymmetric capacitors with a voltage window of 1.8 V and good electrochemical performance. In this case, as shown in Fig 6.1, caffeic acid (CA) is used to negatively charge and disperse MnO<sub>2</sub> powder, meanwhile, BAC is used to positively charge and

disperse MWCNT in aqueous suspension. By simply mixing, due to the electrostatic attractive force, the composite with uniform distribution of the individual components, can be obtained for application in ES.

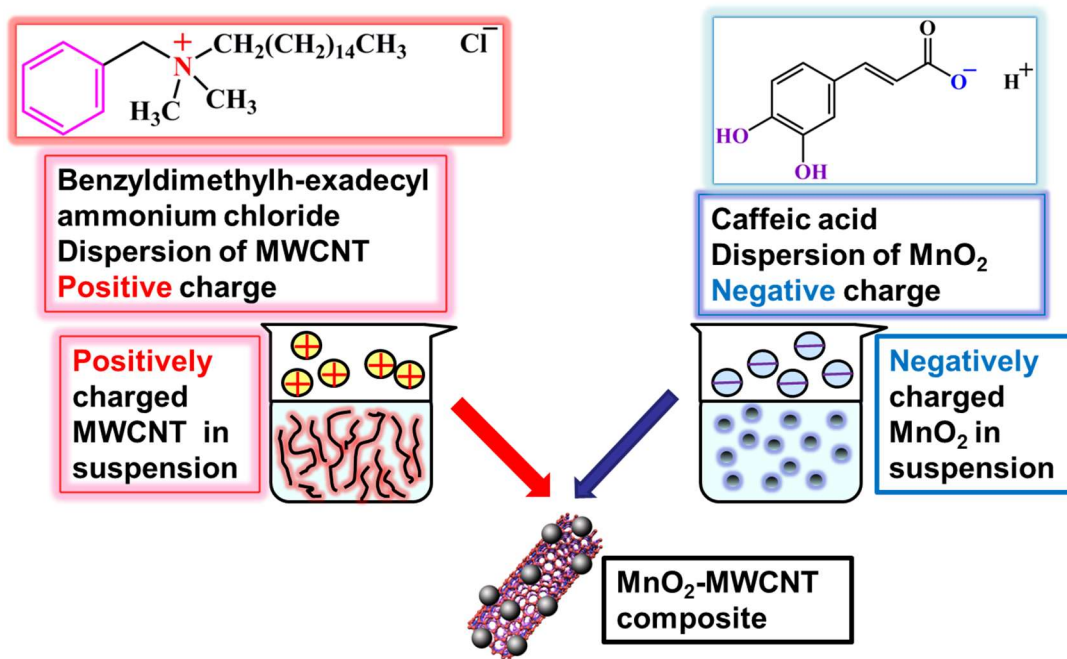


Fig 6.1. Procedure of fabrication of MnO<sub>2</sub>-MWCNT composite using CA and BAC as dispersants, for MnO<sub>2</sub> and MWCNT, respectively

## 6.2 Molecular structure comparison of BAC and CTAB

In our investigation, BAC was used as a new dispersing agent for MWCNT. BAC is a long chain cationic surfactant (Fig. 6.1A), containing an alkyl chain, a charged group and a benzene ring moiety. The sedimentation test results showed that BAC provided efficient dispersion of MWCNT in water. EPD experiments indicated that MWCNT were positively charged in the suspensions, containing BAC, and formed films on the cathodic substrates.

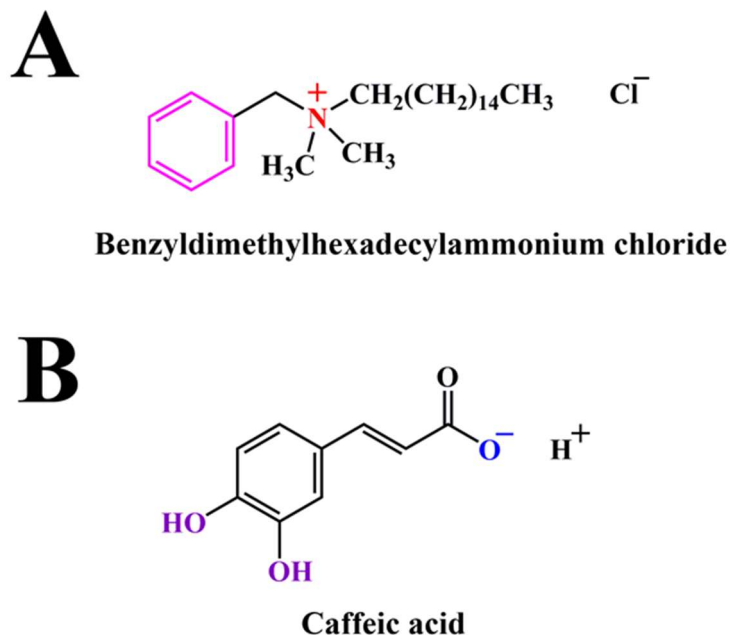
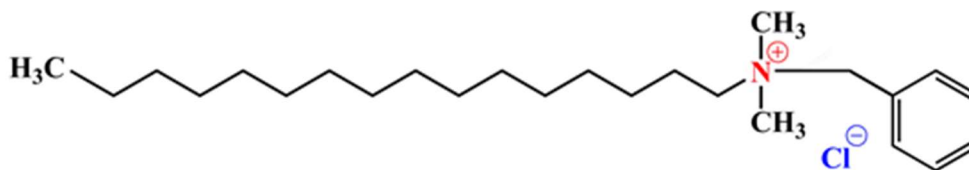


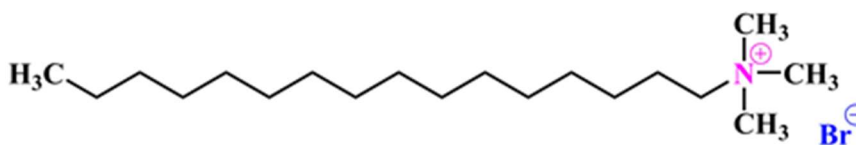
Fig. 6.2. Molecular structures of (A) BAC and (B) caffeic acid (CA).

Recent studies of anionic surfactants[1] showed that the benzene ring of sodium dodecylbenzenesulfonate (NaDDBS) is one of the main reasons of superior performance of this material, compared to other anionic surfactants, such as sodium dodecylsulfate (SDS). The NaDDBS, consisting of a benzene ring moiety, enhanced the stability of CNTs in water by a factor on the order of 10 to 100 compared to other commonly employed surfactants and polymers[2].

In our investigation we compared cationic BAC, containing a benzene ring, with CTAB, which is another cationic surfactant with a similar structure, but without a benzene ring (Fig.6.2). CTAB is commonly used for the dispersion of CNT in water. Our sedimentation test for 1 g L<sup>-1</sup> MWCNT suspensions, containing 0.25 -1.0 gL<sup>-1</sup> BAC or CTAB showed that the use of BAC as a dispersant allowed improved suspension stability.



**Benzyltrimethylhexadecylammonium chloride (BAC)**



**Hexadecyltrimethylammonium bromide (CTAB)**

Fig. 6.3. Comparison of chemical structures of (BAC) and hexadecyltrimethylammonium CTAB.

### 6.3 Adsorption mechanism of BAC on MWCNT

The deposit mass increased with increasing BAC concentration in the suspension and deposition time (Fig. 6.3). It is suggested that BAC adsorbed on the MWCNT surface and imparted a positive charge to MWCNT. The increase in BAC concentration in the suspension resulted in increasing BAC adsorption on MWCNT, which in turn resulted in increasing charge and deposition yield (Fig. 6.3). It is known[3] that surfactants disperse CNT in water mainly through hydrophobic/hydrophilic interactions, in which the alkyl chain of the surfactant molecule adsorbs on the CNT surface, while the hydrophilic head associates with water and promotes dispersion. Other investigations indicated that dispersion efficiency increased with increasing length of the alkyl chains and it is energetically favorable for the chains to lie along the length of the nanotubes[2].

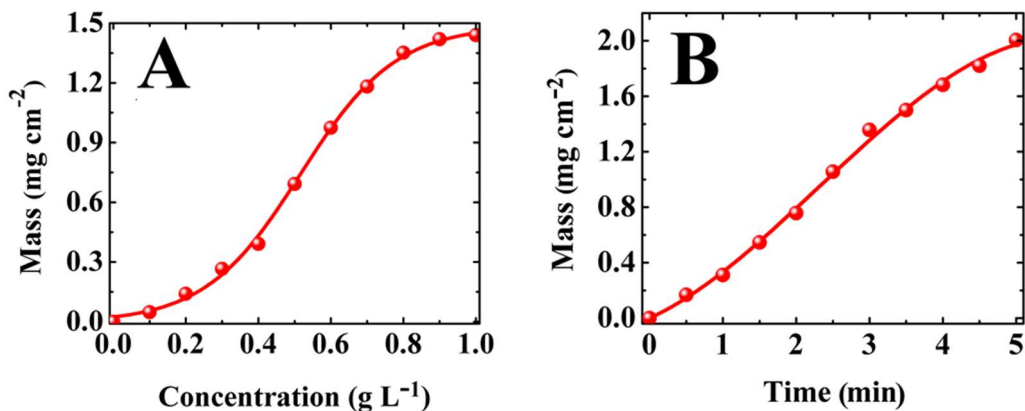


Fig. 6.4. Deposit mass for 1 g L<sup>-1</sup> MWCNT suspension in water at a deposition voltage of 20 V: (A) versus BAC concentration at a deposition time of 3 min and (B) versus deposition time at BAC concentration of 1 g L<sup>-1</sup>.

The comparison of the deposition yield data (Fig. 6.4) showed that BAC allowed significantly higher deposition yield of MWCNT, compared to the deposition yield of MWCNT, achieved using CTAB dispersant at similar deposition conditions. The difference can be attributed to improved adsorption of charged BAC on MWCNT, which resulted in improved dispersion and higher charge of MWCNT. The results obtained for cationic BAC, containing a benzene ring, correlate with literature data, comparing dispersion efficiency of the anionic NaDDBS with other anionic surfactants without a benzene ring[2]. The influence of the benzene ring on surfactant adsorption is not well understood[4]. We suggest that electrostatic repulsion of charged groups of the surfactants, exposed to the aqueous phase[5], is detrimental for the adsorption. Such repulsions can be partially reduced by the  $\pi$ - $\pi$  attractive interactions of the benzene rings of adjacent surfactant molecules, adsorbed on the MWCNT surface.

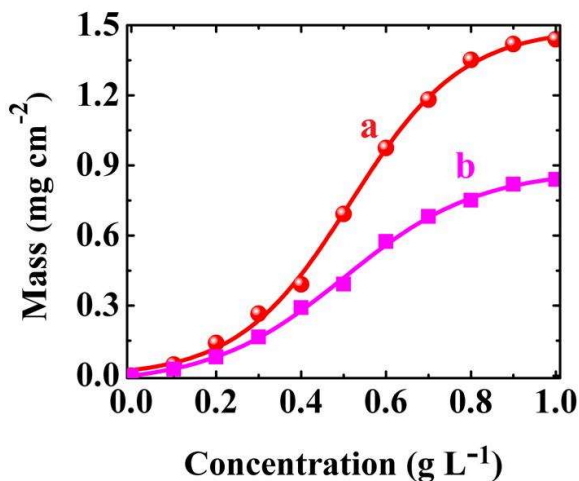


Fig. 6.5 Comparison of the deposition yield obtained from 1 g L<sup>-1</sup> MWCNT suspension in water at a deposition voltage of 20 V and deposition time of 3 min: (a) versus BAC concentration and (b) versus CTAB concentration.

#### 6.4 Adsorption mechanism of CA on MnO<sub>2</sub> particles

Our results indicated that BAC can be used for the efficient dispersion of MWCNT in water; however, the dispersion of MnO<sub>2</sub> presents difficulties. We have found a solution of this problem by utilizing important properties of surfactants, which were not paid enough attention earlier. It is known that cationic surfactants form ion-pairs with tungstosilicic acid[6], anionic dyes[7-9], caffeic acid[10] and other ion-pairing agents[11]. The electrostatic ion-pair interactions between cationic surfactants and anionic organic molecules are involved in many self-organized systems and biological systems[12]. Of special interest are the investigations of the formation of ion-pairs between surfactants and chelating agents[8, 11], which were utilized for the extraction of ions, surface modification of inorganic particles, modification of absorption properties of organic dyes

and other applications, utilizing fascinating properties of the ion-pair assemblies. The interaction of cationic surfactants with caffeic acid (CA)[10] is of special interest for nanotechnology of composites.

CA belongs to the catechol family of materials (Fig.6.1B). The anionic properties of CA are attributed to the carboxylic group. It is known that materials from the catechol family show strong adsorption to different inorganic surfaces[13]. The growing interest in the catecholate type adsorption is motivated by recent advances in the investigation of the mechanism of mussel adhesion to metal and mineral surfaces in water, which showed that strong adhesion is attributed to the chelation of natural catecholic amino acid, L-3,4-dihydroxyphenylalanine (DOPA)[14-16]. CA is a closest molecular analogue of DOPA. Similar to DOPA, the chelating properties of CA are attributed to OH groups, bonded to the adjacent carbon atoms of the aromatic ring (Fig.1B). Previous investigations showed strong adsorption of CA on MnO<sub>2</sub> in ethanol[17]. It should be noted that the adsorption of organic molecules on inorganic particles is influenced by particle–solvent interactions, solvation effects and dielectric constant of the solvent[18]. It is known that water and other liquids with high dielectric constants lead to the deterioration of performance of various adhesives[18]. In this investigation we analysed the adsorption of CA on MnO<sub>2</sub> in water. It was found that CA additive improved MnO<sub>2</sub> dispersion in water.

The EPD experiments showed that MnO<sub>2</sub> particles were negatively charged in water. The natural negative charge of MnO<sub>2</sub> particle in the solutions without CA can result from preferred adsorption of OH<sup>-</sup> ions[19]. However, the deposition rate of MnO<sub>2</sub> was relatively low (Fig. 6.5A). The addition of CA resulted in significant increase of the depo-

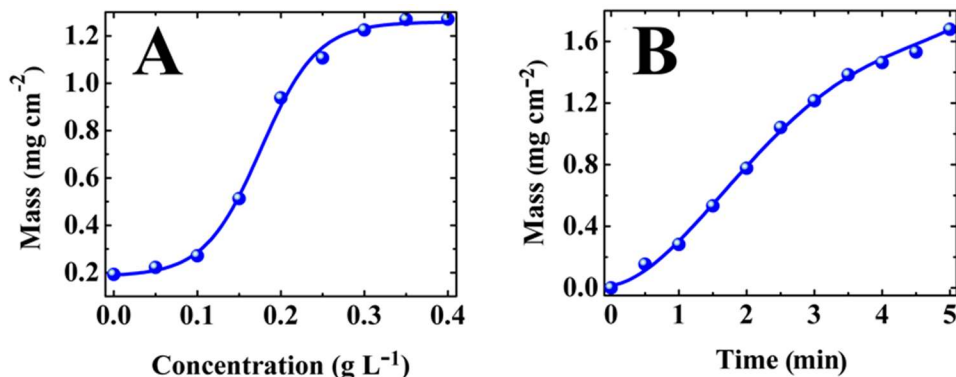


Fig. 6.6 Deposit mass for 4 g L<sup>-1</sup> MnO<sub>2</sub> suspension in water at a deposition voltage of 20 V: (A) versus CA concentration at a deposition time of 3 min and (B) versus deposition time for CA concentration of 0.4 g L<sup>-1</sup>.

-osition yield. The deposit mass increased with increasing deposition time, indicating film growth.

### 6.5 Formation of MnO<sub>2</sub>-MWCNT composite and morphology studies

The possibility of dispersion of MWCNT using cationic BAC and dispersion of MnO<sub>2</sub> using anionic CA paved the way for the formation of composite materials (Fig.6.6). This approach is based on the ion-pairing of BAC and CA, which resulted in attraction of positively charged MWCNT and negatively charged MnO<sub>2</sub>. It is known that ion-pair assemblies of aromatic ion-pairing agents and surfactants, containing a benzene ring, are governed by the electrostatic interactions and  $\pi$ - $\pi$  interactions[20]. The attraction of MWCNT and CA allowed the formation of a composite with improved mixing of the individual components.

SEM observation of the composite material showed MnO<sub>2</sub> nanoparticles attached to the non-agglomerated MWCNT (Fig. 6.7 A), which formed a 3-D conductive network. In co-

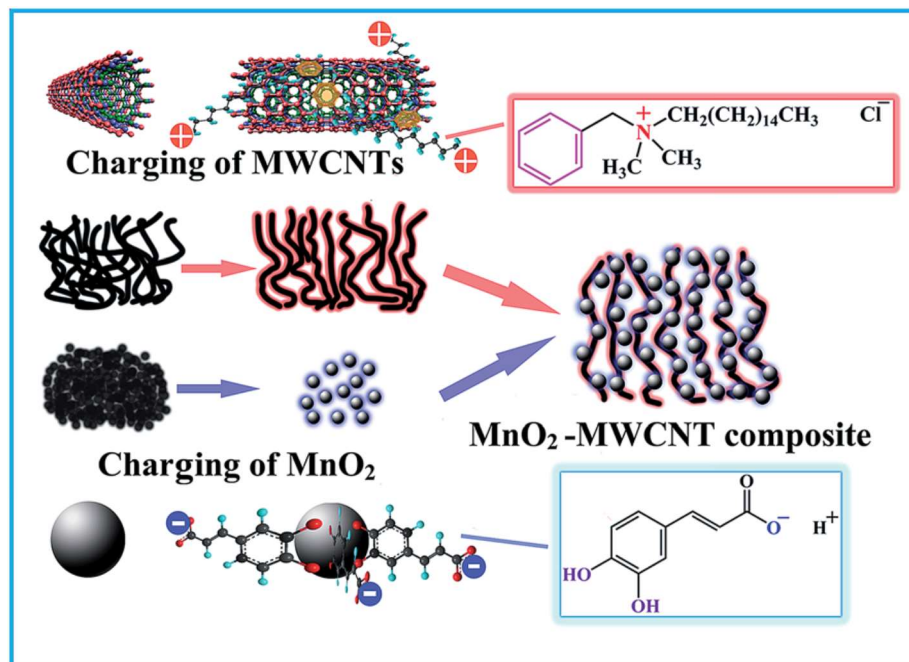


Fig. 6.7 Fabrication of MnO<sub>2</sub>-MWCNT composite by dispersion of MWCNT using cationic BAC, dispersion of MnO<sub>2</sub> using anionic CA and electrostatic heterocoagulation.

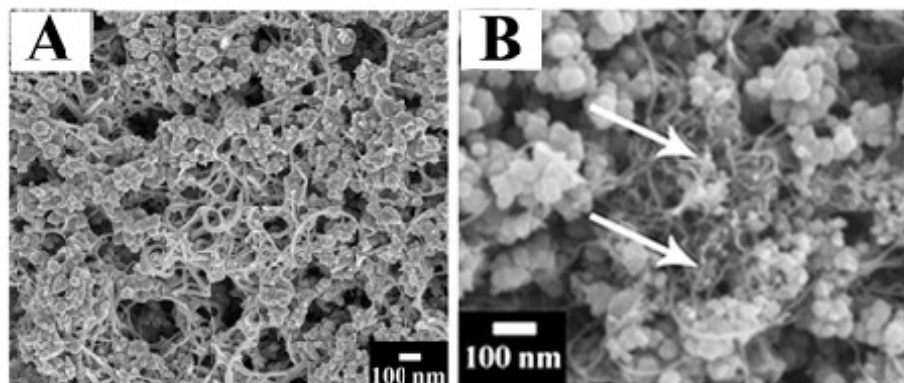


Fig. 6.8 SEM images of MnO<sub>2</sub>-MWCNT composite, prepared with (A) and without (B) CA and BAC

In contrast, the composites, prepared without dispersants, showed large agglomerates of MWCNT and MnO<sub>2</sub> (Fig. 6.7 B).

## 6.6 Electrochemical characterization of composite electrode

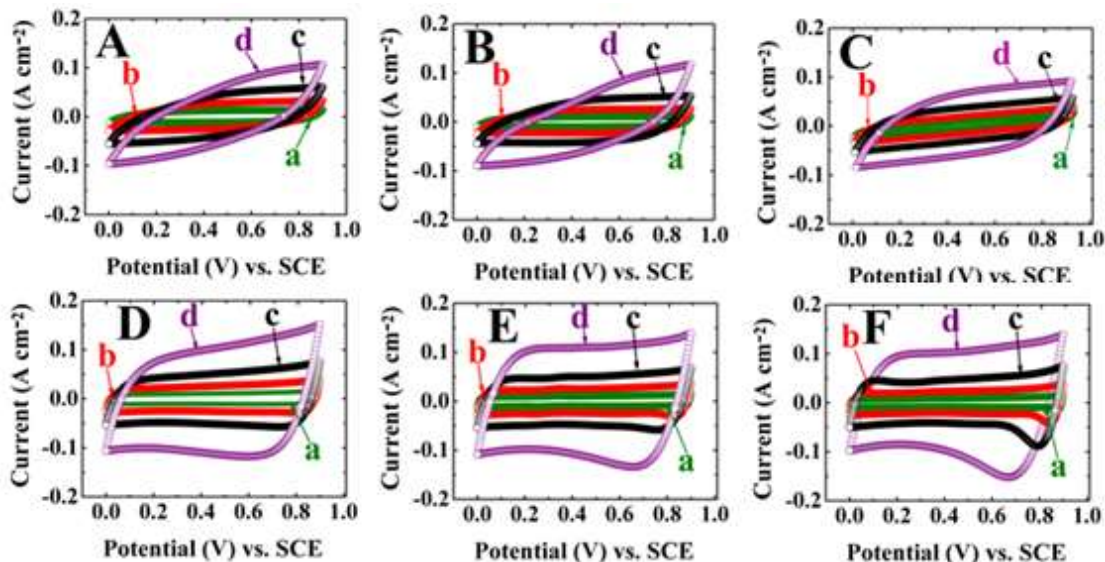


Fig. 6.9 CVs for electrodes with mass loading of  $40 \text{ mg cm}^{-2}$ , prepared (A, B and C) without CA and BAC dispersants and (D, E and F) with dispersants, containing (A and D) 85%  $\text{MnO}_2$ , 15% MWCNT, (B and E) 80%  $\text{MnO}_2$ , 20% MWCNT and (C and F) 75%  $\text{MnO}_2$ , 25% MWCNT at scan rates of (a) 2, (b) 5, (c) 10 and (d)  $20 \text{ mV s}^{-1}$  in 0.5 M aqueous  $\text{Na}_2\text{SO}_4$  electrolyte.

The improved mixing of  $\text{MnO}_2$  and MWCNT allowed improved electrochemical performance of the composite electrodes. Fig.6.8 compares CVs at different scan rates for electrodes with different MWCNT contents, prepared without and with dispersing agents. The electrodes, prepared without dispersants showed tilted CVs with low area, indicating poor electrochemical performance. The electrodes, prepared using BAC and CA, showed significantly larger CV areas, indicating higher capacitance. The electrodes, prepared using 20 % MWCNT showed nearly ideal box shape CVs. The CV areas increased with

increasing scan rate, indicating good capacitance retention. It is important to note that good capacitive behavior was achieved at active mass loadings of  $40 \text{ mg cm}^{-2}$ , which meet requirements[21, 22] for practical applications in electrodes of ES.

The specific capacitances, calculated from the CV data are presented in Fig. 6.9. Pure Mn

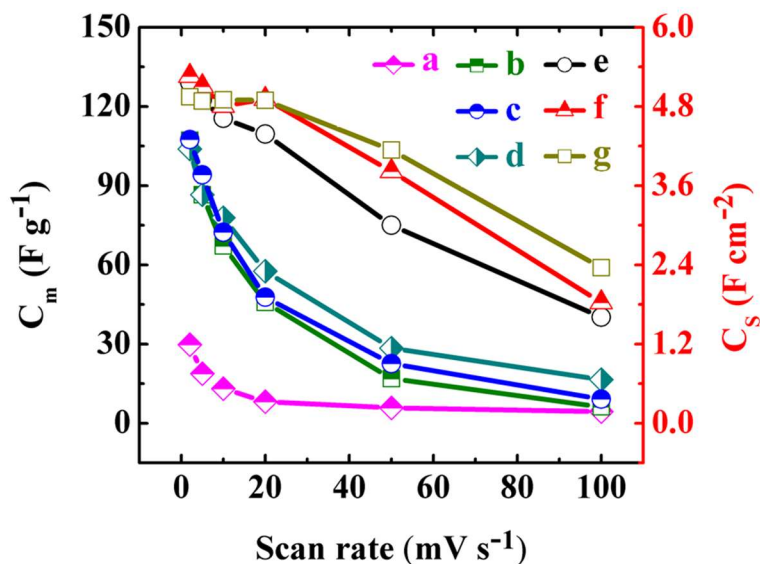


Fig. 6.10  $C_s$  and  $C_m$ , calculated from the CV data, for different electrodes with mass loading of  $40 \text{ mg cm}^{-2}$ : (a) pure  $\text{MnO}_2$  and (b-g) different composite electrodes, prepared (b, c and d) without dispersants, (e, f and g) using BAC and CA dispersants, containing (b and e) 85%  $\text{MnO}_2$  and 15% MWCNT, (c and f) 80%  $\text{MnO}_2$  and 20% MWCNT and (d and g) 75%  $\text{MnO}_2$  and 25% MWCNT.

$\text{O}_2$  electrodes, prepared without MWCNT showed a specific capacitance of  $1.19 \text{ F cm}^{-2}$  ( $29.8 \text{ F g}^{-1}$ ) at a scan rate of  $2 \text{ mV s}^{-1}$ . The capacitance decreased with increasing scan rate. The composite electrodes, prepared without BAC and CA showed capacitances of  $4.29 \text{ F cm}^{-2}$  ( $107.2 \text{ F g}^{-1}$ ),  $4.30 \text{ F cm}^{-2}$  ( $107.5 \text{ F g}^{-1}$ ),  $3.98 \text{ F cm}^{-2}$  ( $99.5 \text{ F g}^{-1}$ ) for MWCNT content

of 15, 20 and 25%, respectively, at a scan rate of  $2 \text{ mV s}^{-1}$ . However, the capacitance decreased rapidly with increasing scan rate. The electrodes, prepared using BAC and CA showed specific capacitances of  $5.16 \text{ F cm}^{-2}$  ( $129.1 \text{ F g}^{-1}$ ),  $5.26 \text{ F cm}^{-2}$  ( $131.6 \text{ F g}^{-1}$ ),  $4.95 \text{ F cm}^{-2}$  ( $123.7 \text{ F g}^{-1}$ ) for MWCNT content of 15, 20 and 25%, respectively at a scan rate of  $2 \text{ mV s}^{-1}$ . It is important to note that the addition of MWCNT results in improved electronic conductivity of the composite and higher capacitance (Eq.(1)). However the specific capacitance of MWCNT is significantly lower than that of  $\text{MnO}_2$ . The increase in MWCNT content in the composite above the optimum amount can result in decreasing capacitance. Therefore, the lower capacitance of the electrode, containing 25% MWCNT, compared to the capacitance of the electrode, containing 20% MWCNT, can be attributed to lower capacitance of MWCNT. The composite electrodes, prepared using BAC and CA showed capacitance retention of 31.2, 34.8 and 47.8, for MWCNT content of 15, 20 and 25%, respectively, at a scan rate of  $100 \text{ mV s}^{-1}$ . It is important to note that at scan rates above  $20 \text{ mV s}^{-1}$  the composite electrodes, prepared using BAC and CA showed 2-3 times higher capacitance, compared to the capacitance of the electrodes prepared without dispersants.

The analysis of the impedance data (Fig. 6.10 (A,B)) indicated that the addition of MWCNT to  $\text{MnO}_2$  resulted in reduced resistance  $R=Z'$ . The electrodes prepared using BAC and CA (Fig. 6.10 B, e-g) showed lower resistance, compared to the electrodes prepared without dispersants (Fig. 6.10 B, b-c). The difference can be attributed to better mixing of the components in the composite materials. Figs. 6.10 C,D show frequency dependencies of the components of complex capacitance  $C^*=C'-iC''$ , calculated from the

impedance data. The composite MnO<sub>2</sub> – MWCNT electrodes showed significantly higher capacitance C', compared to the capacitance of pure MnO<sub>2</sub> at low frequencies. The frequency dependences of capacitances for composite electrodes showed typical relaxation type dispersions[23], as indicated by the reduction of C' with increasing frequency and corresponding maxima in the frequency dependencies of C''.

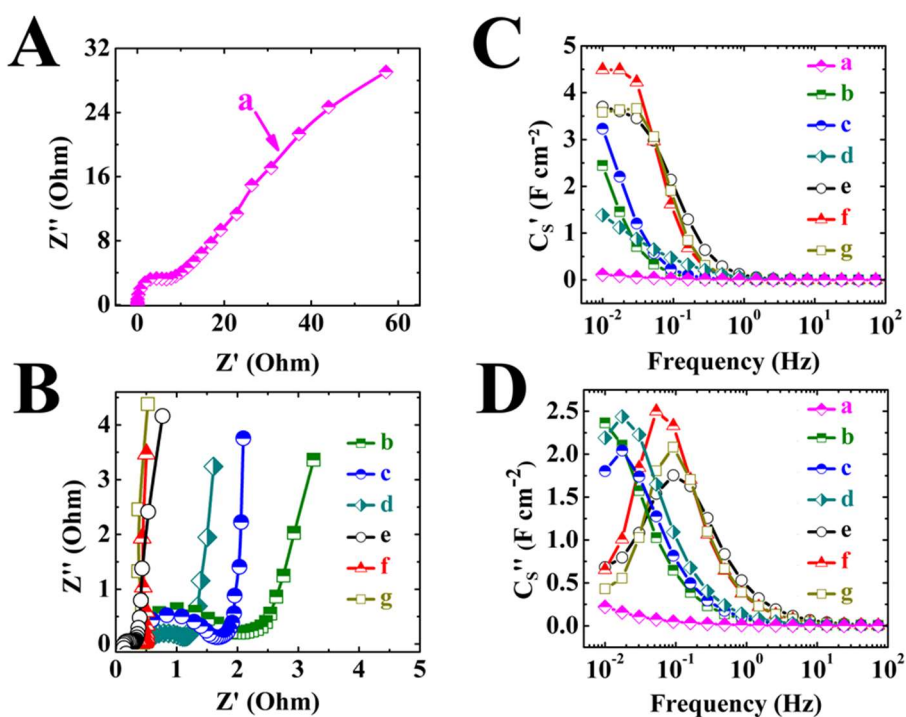


Fig. 6.11 Nyquist plot of complex impedance and components of complex capacitance of (A) pure MnO<sub>2</sub> and (B) different composite electrodes, (C) C<sub>s</sub>' and (D) C<sub>s</sub>'' versus frequency for electrodes with mass loading of 40 mg cm<sup>-2</sup>, prepared (a) pure MnO<sub>2</sub>, (b, c and d) without dispersants, (e, f and g) using CA and BAC dispersants and containing (b and e)85% MnO<sub>2</sub>, 15% MWCNT,(c and f) 80% MnO<sub>2</sub>, 20% MWCNT and (d and g) 75% MnO<sub>2</sub>, 25% MWCNT.

The electrodes, prepared using BAC and CA, showed relaxation type dispersion at higher frequencies, as illustrated by the reduction in  $C'$  at higher frequencies and corresponding shift of relaxation maxima of  $C''$ . This result is in agreement with the data, presented in Fig. 6.9, which indicated improved capacitance retention at high scan rates for the electrodes, prepared in the presence of dispersants.

### 6.7 Electrochemical characterization for device

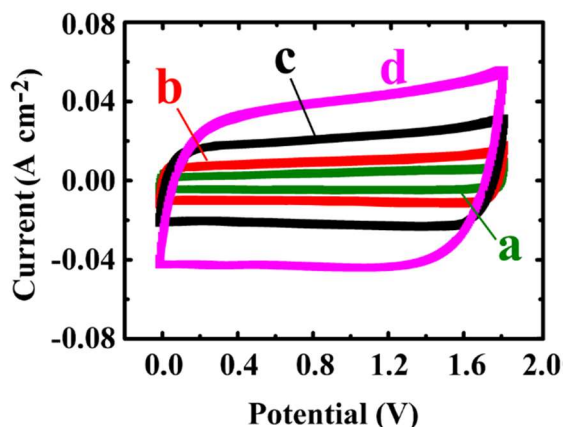


Fig. 6.12 CVs for two-electrode, which is composed by a  $\text{MnO}_2$ -MWCNT electrode, containing 80%  $\text{MnO}_2$  and 20% MWCNT and a AC-CB electrode with 85% PICA and 10% CB (5% binder). Scan rate are  $2\text{ mV s}^{-1}$  (a),  $5\text{ mV s}^{-1}$  (b),  $10\text{ mV s}^{-1}$  (c), and  $20\text{ mV s}^{-1}$  (d) in  $0.5\text{ M Na}_2\text{SO}_4$  electrolyte.

The composite  $\text{MnO}_2$ -MWCNT positive electrodes, containing 20% MWCNT, and activated carbon-carbon black (AC-CB, 10% CB) negative electrodes were used for the fabrication of asymmetric devices. The asymmetric device showed a box shape CV (Fig. 6.11) in a voltage window of 1.8 V. The increase in scan rate resulted in increasing current, indicating good capacitive behavior. The capacitance of the asymmetric cells,

calculated from the CV data decreased from 2.3 to 0.9 F cm<sup>-2</sup> with increasing scan rate from 2 to 100 mV s<sup>-1</sup>. Such decrease can be attributed to electrolyte diffusion limitations in pores of individual electrodes.

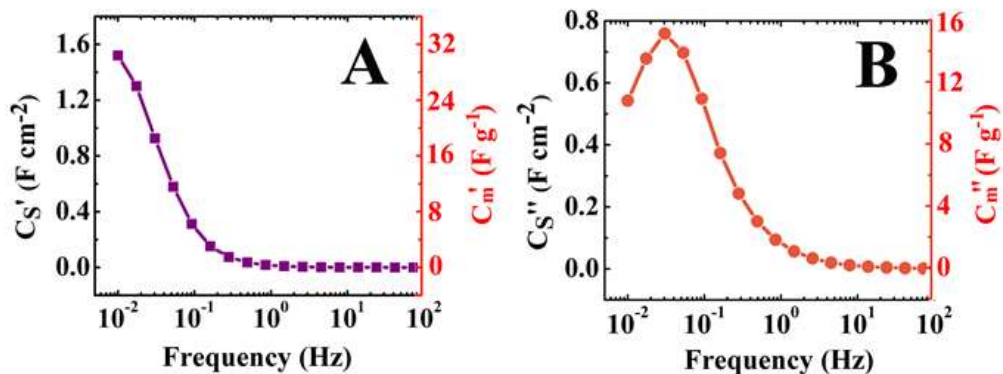


Fig. 6.13 Frequency dependencies of components of complex capacitance (A)  $C_s'$ ,  $C_m'$  and (B)  $C_s''$ ,  $C_m''$ , calculated from the impedance data for the two electrode asymmetric cell, containing a positive MnO<sub>2</sub>-MWCNT electrode (80% MnO<sub>2</sub> and 20% MWCNT) and a negative AC-CB electrode (90 % AC and 10% CB).

The components of complex AC capacitance of the asymmetric devices were calculated from the impedance data at different frequencies (Fig. 6.12). The capacitance  $C'$  of 1.6 F cm<sup>-2</sup> was obtained at a frequency of 10 mHz. The frequency dependence of capacitance showed typical relaxation type dispersion, as indicated by decrease in  $C'$  with increasing frequency and corresponding maximum in the frequency dependence of  $C''$ . It is important to note that capacitance, calculated from the CV data depends on scan rate, whereas AC capacitance depends on frequency. The specific capacitance was also calculated from the chronopotentiometry data.

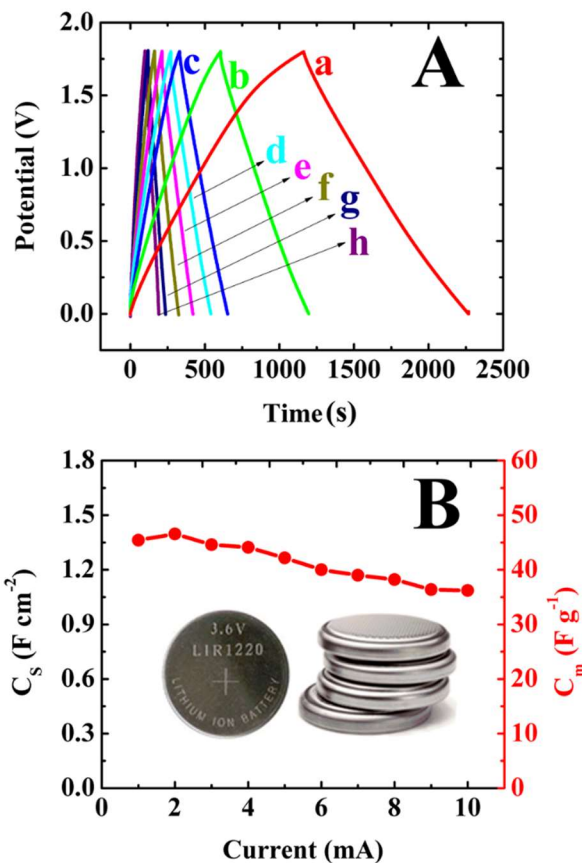


Fig. 6.14 (A) Galvanostatic charge–discharge behavior of an asymmetric coin cell at currents of (a) 1, (b) 2, (c) 3, (d) 4, (e) 5, (f) 6, (g) 8, and (h) 10 mA, (B) cell capacitance  $C_s$  and  $C_m$  versus current, inset shows coin cells.

Fig. 6.13 shows typical charge-discharge curves for the asymmetric coin cells. The charge discharge curves at different current densities were of symmetric triangular shape, indicating good Coulombic efficiency. The capacitance calculated from chronopotentiometry data decreased from 1.36 to 1.09  $F\ cm^{-2}$  with increasing discharge current in the range of 1-10 mA (Fig. 6.13).

Fig.6.14 A shows Ragone plot for the coin cell asymmetric device. The maximum energy

density of  $10.2 \text{ Wh kg}^{-1}$  and power density of  $2.67 \text{ kW kg}^{-1}$  were achieved. The investigation of the cyclic stability of the coin cells showed capacitance retention of 95.1%

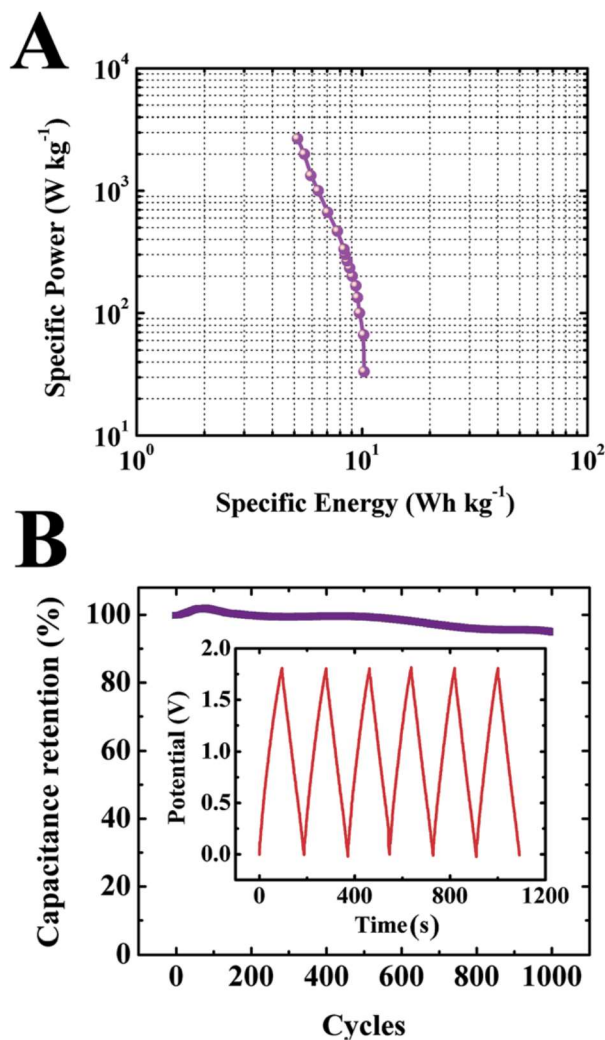


Fig. 6.15 (A) Ragone plot and (B) capacitance retention versus cycle number for an asymmetric coin cell, inset shows multiple charge-discharge cycles at a constant current of 10 mA.

after 1000 cycles (Fig. 6.14B). The method, developed in this investigation was used for the fabrication of larger envelope cells with area of  $6 \text{ cm}^2$ . Two envelope cells were used

for powering of 19 LED bulbs with a nominal current of 20 mA (Fig. 6.15). The results indicated that the asymmetric ES cells, developed in this investigation, are promising for practical applications[24].



Fig. 6.16 Two envelope asymmetric cells power 19 LED bulbs with a nominal current of  $20 \text{ mA cm}^{-2}$  for each bulb.

## 6.8 Conclusions

The adsorption of BAC on MWCNT in water allowed efficient dispersion of MWCNT, imparted a positive charge, which was confirmed by EPD of MWCNT films. The adsorption of CA on MWCNT in water allowed efficient dispersion of  $\text{MnO}_2$ , imparted a negative charge, which was confirmed by anodic EPD of  $\text{MnO}_2$  films. Composite  $\text{MnO}_2$ -MWCNT electrodes can be obtained by heterocoagulation based on ion-pairing assembly of BAC and CA. The method allowed improved mixing of the individual components, which resulted in superior electrochemical performance of the  $\text{MnO}_2$ -MWCNT electrodes.

High capacitance and good capacitance retention can be achieved at high active mass loadings. The asymmetric devices, based on MnO<sub>2</sub>-MWCNT positive electrode and AC-CB negative electrode showed good capacitive behavior in a voltage window of 1.8V. The specific power of 2.67 kW kg<sup>-1</sup> and specific energy 10.2 Wh kg<sup>-1</sup> were achieved. The devices showed good capacitance retention at high charge-discharge rates and good cyclic stability. The ES devices are promising for practical applications.

Yangshuai Liu has the major contribution to this work, and Dr. Igor Zhitomirsky also contributes to this work.

## References

- [1] V. Datsyuk, P.r. Landois, J. Fitremann, A. Peigney, A.M. Galibert, B. Soula, E. Flahaut, Double-walled carbon nanotube dispersion via surfactant substitution, *Journal of Materials Chemistry*, 19 (2009) 2729-2736.
- [2] M. Islam, E. Rojas, D. Bergey, A. Johnson, A. Yodh, High weight fraction surfactant solubilization of single-wall carbon nanotubes in water, *Nano Letters*, 3 (2003) 269-273.
- [3] H. Wang, Dispersing carbon nanotubes using surfactants, *Current Opinion in Colloid & Interface Science*, 14 (2009) 364-371.
- [4] O. Matarredona, H. Rhoads, Z. Li, J.H. Harwell, L. Balzano, D.E. Resasco, Dispersion of single-walled carbon nanotubes in aqueous solutions of the anionic surfactant NaDDBS, *The Journal of Physical Chemistry B*, 107 (2003) 13357-13367.
- [5] Q. Wang, Y. Han, Y. Wang, Y. Qin, Z.-X. Guo, Effect of surfactant structure on the stability of carbon nanotubes in aqueous solution, *The Journal of Physical Chemistry B*, 112 (2008) 7227-7233.
- [6] R. Hosseinzadeh, R. Tahmasebi, K. Farhadi, A.A. Moosavi-Movahedi, A. Jouyban, J. Badraghi, Novel cationic surfactant ion pair based solid phase microextraction fiber for nano-level analysis of BTEX, *Colloids and Surfaces B: Biointerfaces*, 84 (2011) 13-17.
- [7] H. Akbas, T. Taner, Spectroscopic studies of interactions between C.I. Reactive Orange 16 with alkyltrimethylammonium bromide surfactants, *Spectrochimica Acta - Part A: Molecular and Biomolecular Spectroscopy*, 73 (2009) 150-153.
- [8] A.C.R. Gomes, L.D.F. Cafer, P. Homem-de-Mello, M.D. Coutinho-Neto, I. Gaubeur, The interaction of an azo compound with a surfactant and ion pair adsorption to solid

phases, *Journal of Colloid and Interface Science*, 367 (2012) 370-377.

[9] A. Ali, S. Uzair, N.A. Malik, M. Ali, Study of interaction between cationic surfactants and cresol red dye by electrical conductivity and spectroscopy methods, *Journal of Molecular Liquids*, 196 (2014) 395-403.

[10] S. Rudiuk, M. Delample, S. Franceschi-Messant, N. Chouini-Lalanne, E. Perez, J.-C. Garrigues, I. Rico-Lattes, Spontaneous vesicle formation by caffeate ion-pair surfactants: Antioxidant properties and application to dna protection, *Journal of Dispersion Science and Technology*, 31 (2010) 384-391.

[11] S.R. Yousefi, E. Zolfonoun, M.R. Pourjavid, S.J. Ahmadi, On-line surfactant-based extraction using ion-pair microparticles combined with ICP-OES for simultaneous preconcentration and determination of rare earth elements in aqueous samples, *Analytical Methods*, 6 (2014) 3694-3699.

[12] E.L. Tan, J.-C. Liu, Y.W. Chien, Characterization of ion-pair formation between ionized indomethacin and cationic surfactants, *Journal of Dispersion Science and Technology*, 14 (1993) 609-624.

[13] M. Ata, Y. Liu, I. Zhitomirsky, A review of new methods of surface chemical modification, dispersion and electrophoretic deposition of metal oxide particles, *RSC Advances*, 4 (2014) 22716-22732.

[14] J.H. Waite, Surface chemistry: Mussel power, *Nature Materials*, 7 (2008) 8-9.

[15] L. Haeshin, S.M. Dellatore, W.M. Miller, P.B. Messersmith, Mussel-inspired surface chemistry for multifunctional coatings, *Science*, 318 (2007) 426-430.

[16] X. Fan, L. Lin, P.B. Messersmith, Surface-initiated polymerization from TiO<sub>2</sub>

nanoparticle surfaces through a biomimetic initiator: A new route toward polymer-matrix nanocomposites, *Composites Science and Technology*, 66 (2006) 1198-1204.

[17] Y. Wang, I. Zhitomirsky, Bio-Inspired Catechol Chemistry for Electrophoretic Nanotechnology of Oxide Films, *J. Colloid Interface Sci.*, 380 (2012) 8-15.

[18] B.P. Lee, P.B. Messersmith, J.N. Israelachvili, J.H. Waite, Mussel-Inspired Adhesives and Coatings, *Annual Review of Materials Research*, 41 (2011) 99-132.

[19] I. Zhitomirsky, Cathodic Electrodeposition of Ceramic and Organoceramic Materials. Fundamental Aspects, *Adv. Colloid Interface Sci.*, 97 (2002) 277-315.

[20] A.A. Shahir, M. Rashidi-Alavijeh, S. Javadian, J. Kakemam, A. Yousefi, Molecular interaction of Congo Red with conventional and cationic gemini surfactants, *Fluid Phase Equilibria*, 305 (2011) 219-226.

[21] Y. Gogotsi, P. Simon, True Performance Metrics in Electrochemical Energy Storage, *Science*, 334 (2011) 917-918.

[22] L. Wei, G. Yushin, Nanostructured activated carbons from natural precursors for electrical double layer capacitors, *Nano Energy*, 1 (2012) 552-565.

[23] K. Shi, I. Zhitomirsky, Polypyrrole nanofiber-carbon nanotube electrodes for supercapacitors with high mass loading obtained using an organic dye as a co-dispersant, *Journal of Materials Chemistry A*, 1 (2013) 11614-11622.

[24] Y. Liu, Igor Zhitomirsky, Aqueous electrostatic dispersion and heterocoagulation of multiwalled carbon nanotubes and manganese dioxide for the fabrication of supercapacitor electrodes and devices, *RSC Adv.* 4 (2014), 45481-45489.

## Chapter 7. BiMn<sub>2</sub>O<sub>5</sub>-MWCNTs composite for supercapacitor

### 7.1 BiMn<sub>2</sub>O<sub>5</sub> as a capacitive material

Although MnO<sub>2</sub> has been studied for its highly theoretical capacitance, the conductivity of MnO<sub>2</sub> is low, it limits the applications of MnO<sub>2</sub> and it is important to develop new capacitive materials with improved performance. Oxides of Bi and Mn are of special interest for application in ES due to the multiple valence states of Bi and Mn. Many investigations were focused on the analysis of capacitive behavior of MnO<sub>2</sub> for application in positive electrodes of aqueous ES[1-4]. The charge storage mechanism of MnO<sub>2</sub> is pseudocapacitive, it can be described by the following reaction[5]:



where  $\text{A}^+ = \text{Li}^+, \text{Na}^+, \text{K}^+, \text{H}^+$ . Equation (7.1) indicates that high electronic and ionic conductivities are necessary[6-8] in order to utilize capacitive properties of MnO<sub>2</sub> in ES electrodes.

The goal of our investigation was the fabrication and testing of BiMn<sub>2</sub>O<sub>5</sub> based electrodes and devices. The approach was based on the use of hydrothermal synthesis for the fabrication of submicrometre BiMn<sub>2</sub>O<sub>5</sub> particles. An important finding was the possibility of the fabrication of BiMn<sub>2</sub>O<sub>5</sub>-MWCNT composite electrodes using Celestine blue dye as a co-dispersant for BiMn<sub>2</sub>O<sub>5</sub> and MWCNT. The results presented below showed excellent

capacitive performance of  $\text{BiMn}_2\text{O}_5$ -MWCNT electrodes, which exhibited high capacitance at low scan rates and outstanding capacitance retention at high scan rates and high active mass loadings. These results paved the way to the fabrication of ES devices with high power-energy characteristics, based on the  $\text{BiMn}_2\text{O}_5$ -MWCNT electrodes. Moving toward this goal we fabricated and tested asymmetric ES, containing  $\text{BiMn}_2\text{O}_5$ -MWCNT positive electrodes and AC-CB negative electrodes, which showed excellent performance in a voltage window of 1.8 V in an aqueous electrolyte.

## 7.2 Phase and morphology characterization of $\text{BiMn}_2\text{O}_5$

XRD studies of as-prepared material confirmed the formation of  $\text{BiMn}_2\text{O}_5$ . The diffraction pattern presented in the Fig. 7.1 is in agreement with the JCPDS file 027-0048 of  $\text{BiMn}_2\text{O}_5$ . The SEM images of the  $\text{BiMn}_2\text{O}_5$  powder at different magnifications are presented in Fig. 7.2(A,B). The SEM image at low magnification (Fig. 7.2A) indicated low agglomeration of the powder. The analysis of the image (Fig. 7.2B) at higher magnification indicated the formation of submicrometre particles. The diameter of the particles varied from 100 to 600 nm.

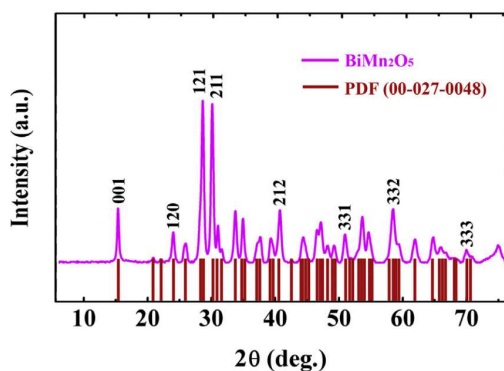


Fig. 7.1 X-ray diffraction pattern of as-prepared  $\text{BiMn}_2\text{O}_5$  powder and corresponding

JCPDS file.

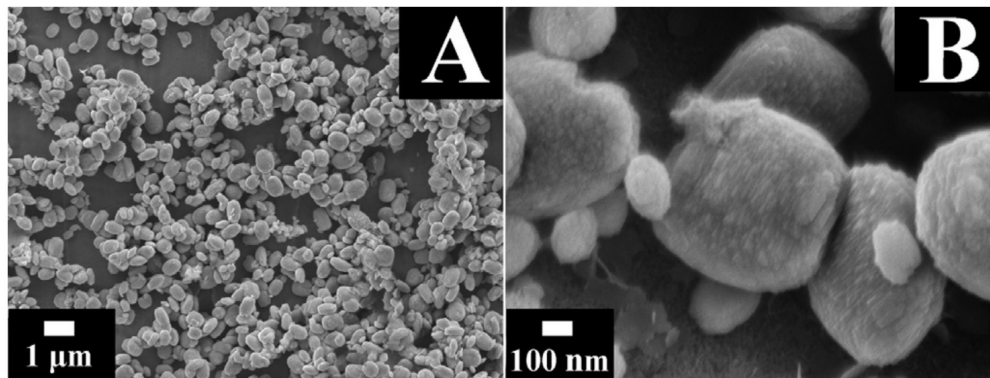


Fig. 7.2 (A,B) SEM images of as-prepared BiMn<sub>2</sub>O<sub>5</sub> powder at different magnifications

### 7.3 Celestine blue as dispersing agent

Previous investigations[9, 10] showed that the conductivity of BiMn<sub>2</sub>O<sub>5</sub> is higher than that of MnO<sub>2</sub>. The higher conductivity of BiMn<sub>2</sub>O<sub>5</sub> is attributed to the hopping[9] of charge between Mn<sup>3+</sup> and Mn<sup>4+</sup>. However, it is critical to use conductive additives, such as MWCNT, in order to reduce resistance and increase capacitance of the BiMn<sub>2</sub>O<sub>5</sub> electrodes. It is known that good dispersion of individual components is of paramount importance for the fabrication of efficient composite electrodes for ES[11]. It was found that significant improvement in capacitance retention at high scan rates can be achieved by the use of new dispersants and advanced dispersion methods[11, 12]. Especially attractive is approach, based on the use of polyaromatic charged dispersants from the catechol family[13]. Such dispersants show good adsorption on MWCNT due to the  $\pi$ - $\pi$  interactions and allow electrosteric dispersion[13, 14]. On the other hand, the catechol ligands of such dispersants provide their strong adsorption on metal oxide nanoparticles due to the complex formation between the catechol ligand of the dispersant and metal

atoms on the particle surface[14, 15]. Recent review[15] described fundamental aspects of the adsorption of different dispersants from the catechol family. It was found that polyaromatic Celestine blue[15] dye is a versatile dispersion agent, suitable for efficient colloidal processing of carbon nanotubes and various oxide materials. As an extension of previous investigation, we found that Celestine blue allowed efficient dispersion of  $\text{BiMn}_2\text{O}_5$ . Electrophoretic deposition experiments showed the possibility of the formation of cathodic  $\text{BiMn}_2\text{O}_5$  films from stable suspensions, indicating that cationic Celestine blue was adsorbed on  $\text{BiMn}_2\text{O}_5$  particles and imparted a positive charge to  $\text{BiMn}_2\text{O}_5$ . The adsorbed Celestine blue provided electrosteric dispersion of  $\text{BiMn}_2\text{O}_5$  particles in the suspensions. The formation of stable suspensions of  $\text{BiMn}_2\text{O}_5$  and MWCNT using Celestine blue as a co-dispersant was an important step in the formation of composite electrodes from the colloidal suspensions.

#### **7.4 Electrochemical characterization for composite electrodes**

The composite  $\text{BiMn}_2\text{O}_5$  – MWCNT electrodes showed capacitive behavior in a voltage window of 0-0.9V versus SCE (Fig. 7.3A). Nearly box shape CVs were recorded at scan rates as high as  $200 \text{ mV s}^{-1}$ . In contrast,  $\text{MnO}_2$  –MWCNT electrodes[14] showed poor capacitive behavior even at lower scan rates, such as  $100 \text{ mV s}^{-1}$ . The increase in scan rate resulted in increasing current, indicating good capacitive behavior (Fig. 7.3A). The charge–discharge currents at a scan rate of  $200 \text{ mV s}^{-1}$  were about  $1 \text{ A cm}^{-2}$ . The electrodes showed (Fig. 7.3B) a capacitance of  $6.0 \text{ F cm}^{-2}$  ( $540 \text{ F cm}^{-3}$ ) at a scan rate of  $2 \text{ mV s}^{-1}$ , which is higher than that achieved for  $\text{MnO}_2$ -MWCNT electrodes, using the same current collectors[14]. The  $\text{BiMn}_2\text{O}_5$  – MWCNT electrodes showed excellent

performance at higher scan rates. A remarkably high capacitance of  $4.5 \text{ F cm}^{-2}$  was achieved at a scan rate of  $100 \text{ mV s}^{-1}$ , which was much superior, compared to that, achieved for  $\text{MnO}_2$ -MWCNT composites ( $1.1 \text{ F cm}^{-2}$ )[14].

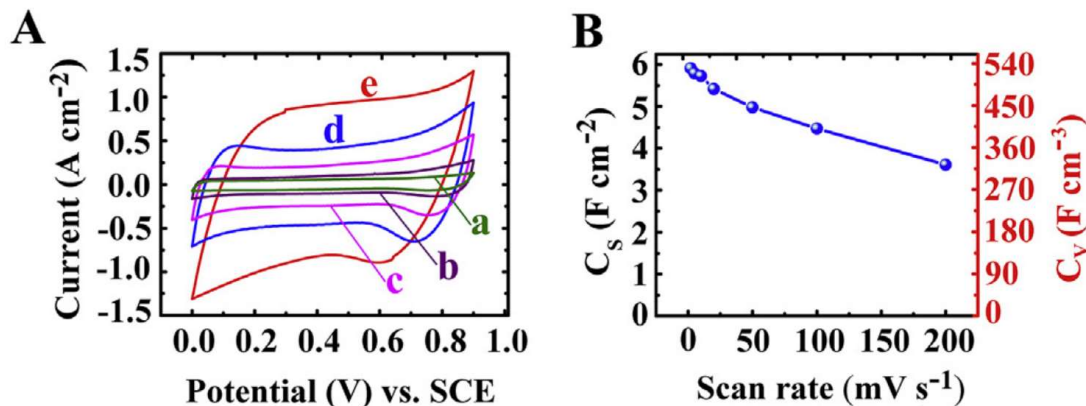


Fig. 7.3 (A) CVs for  $\text{BiMn}_2\text{O}_5$  - MWCNT electrode at scan rates of (a) 10, (b) 20, (c) 50, (d) 100, and (e)  $200 \text{ mV s}^{-1}$  in  $0.5 \text{ M}$  aqueous  $\text{Na}_2\text{SO}_4$  electrolyte, (B)  $C_s$  and  $C_v$ , calculated from the CV data at different scan rates.

The  $\text{BiMn}_2\text{O}_5$  - MWCNT electrodes showed capacitance of  $3.5 \text{ F cm}^{-2}$  at  $200 \text{ mV s}^{-1}$ . The capacitance retention was found to be 75 and 58% at scan rates of 100 and  $200 \text{ mV s}^{-1}$ , respectively (Fig. 7.3B). It is suggested that lower resistivity of  $\text{BiMn}_2\text{O}_5$ , compared to that of  $\text{MnO}_2$ , is one of the important factors, contributing to good electrochemical performance of the  $\text{BiMn}_2\text{O}_5$  based electrodes. Another important factor is remarkably high dielectric constant[9] of  $\text{BiMn}_2\text{O}_5$  which can result in reduced voltage drop in the bulk of the  $\text{BiMn}_2\text{O}_5$  particles and enhanced charge accumulation on the surface. The following charging mechanism can be suggested for the  $\text{BiMn}_2\text{O}_5$  electrodes:



The combination of Bi and Mn species is of significant interest for electrodes of electrochemical energy storage devices. Fundamental investigations in the battery technology showed that Bi modified manganese dioxide exhibited improved cycling characteristics with a two-electron capacity in rechargeable alkaline cells[16]. Significant research efforts were focused on the analysis of influence of  $\text{Bi}^{3+}$  ions in the redox properties of manganese oxides[16-19]. It was concluded that deeper discharge of  $\text{MnO}_2$  can be achieved in the presence of  $\text{Bi}^{3+}$  ions[20, 21].

The analysis of complex AC impedance data, presented in the Nyquist plot (Fig. 7.4 A), showed relatively low resistance  $R=Z'$  of the  $\text{BiMn}_2\text{O}_5 - \text{MWCNT}$  electrodes (Fig. 7.4). The slope of  $Z''$  versus  $Z'$  curve at low frequencies was close to  $90^\circ$ , indicating good capacitive behavior. At higher frequencies (Fig. 7.4A, inset) a semicircle was observed, which can be associated with charge transfer resistance. The impedance data were used for the calculation of complex capacitance. It is important to note that cyclic voltammetry data provides integral capacitance in the tested voltage window, whereas impedance data divides differential capacitance at low voltage.

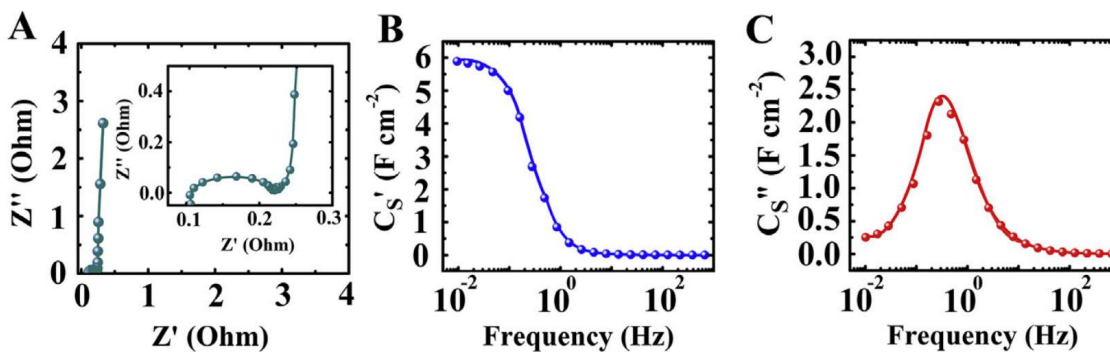


Fig. 7.4 (A) Nyquist plot of complex impedance, inset shows high frequency range, (B)

$C_s'$  and ( $C$ )  $C_s''$  components of complex capacitance versus frequency for  $\text{BiMn}_2\text{O}_5$ -MWCNT electrode.

The differential capacitance  $C_s'$  (Fig.7.4 B), measured at low frequencies, was comparable with the integral capacitance, measured at low scan rates (Fig. 7.3 B). The frequency dependence of differential capacitance showed relaxation type[22] dispersion, as indicated by the reduction in  $C_s'$  with increasing frequency and corresponding maximum at 0.4 Hz in the frequency dependence of  $C_s''$  (Fig. 7.4 C).

## 7.5 Electrochemical characterization of a device

Asymmetric devices, containing  $\text{BiMn}_2\text{O}_5$  – MWCNT positive electrodes and AC-CB negative electrodes were fabricated and tested, the configuration is shown in Fig. 7.5. It was found that good electrochemical performance can be achieved in a voltage window of 1.8 V.

The analysis of CV data showed that nearly box shape CVs were obtained (Fig. 7.6A). The current increased with increasing scan rate indicated good capacitive behavior. The capacitance of the asymmetric cells at a scan rate of  $2 \text{ mV s}^{-1}$  was found to be  $3.5 \text{ F cm}^{-2}$ , the capacitance retention at  $100 \text{ mV s}^{-1}$  was 34% (Fig.7.6B). The impedance data presented in the Nyquist plot (Fig.7.7A) showed that the slope of the  $Z''$  versus  $Z'$  curve at low frequencies was close to  $90^\circ$ , the semicircle at lower frequencies is related to charge transfer resistance (Fig.7.7A, inset). The resistance  $R=Z'$  of the device was higher than that of the individual  $\text{BiMn}_2\text{O}_5$  – MWCNT electrodes. As a result, the relaxation type[22] dispersion shifted to lower frequencies (Fig.7.7 B,C). The relaxation frequency,

corresponding to the maximum in the frequency dependence of imaginary part of  $C''$  was found to be 0.05 Hz. The  $C_s'$  value at low frequency (Fig. 7.7 B) is comparable with  $C_s$ , calculated from CV data at low scan rates (Fig.7.7 B).

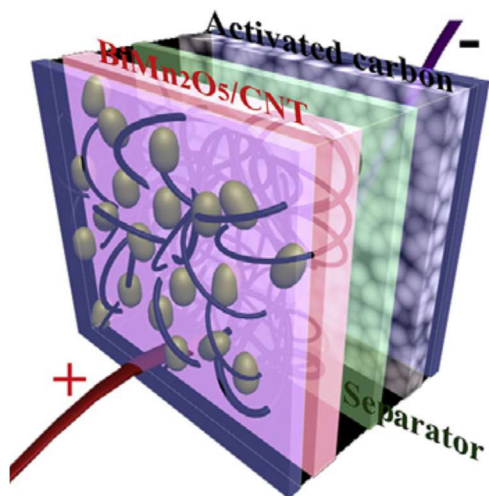


Fig. 7.5 Schematic of BiMn<sub>2</sub>O<sub>5</sub>-MWCNTs/activated carbon-carbon black hybrid device

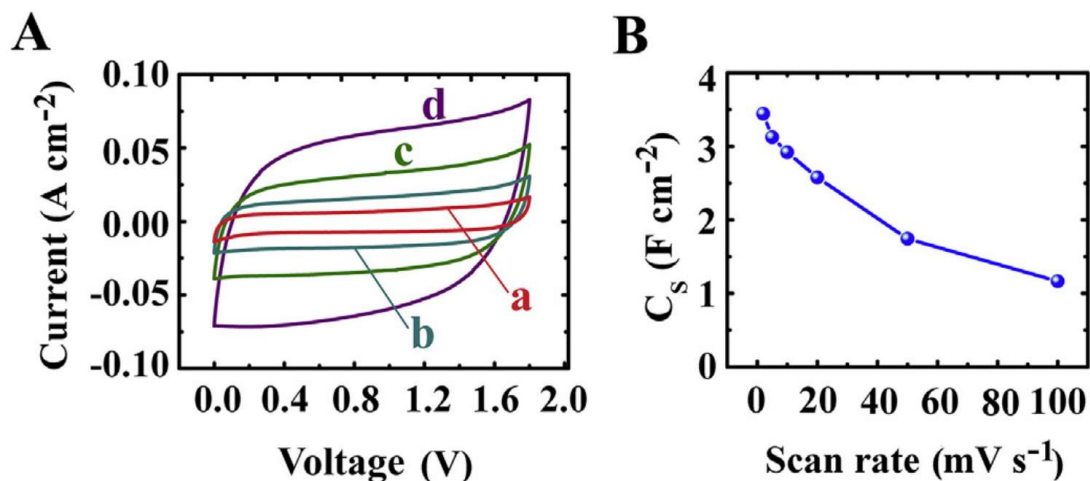


Fig. 7.6 CVs for the two electrode asymmetric cell, containing a positive BiMn<sub>2</sub>O<sub>5</sub>-MWCNT electrode and a negative AC-CB electrode at scan rates of (a) 2 (b) 5 (b), (c)10 and (d) 20 mV s<sup>-1</sup> in 0.5 M Na<sub>2</sub>SO<sub>4</sub> electrolyte, (B) Cs calculated from the CV data at

different scan rates.

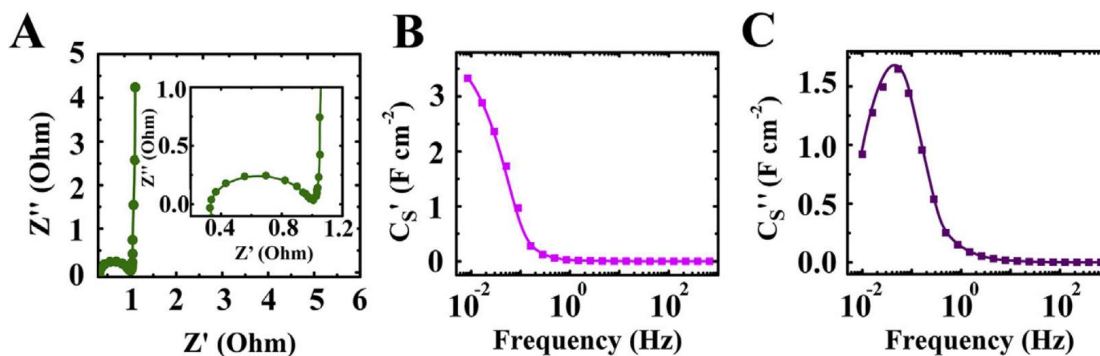


Fig. 7.7 (A) Nyquist plots of complex impedance, inset shows high frequency range and (B)  $C_s'$  and (C)  $C_s''$  components of complex capacitance versus frequency for two electrode asymmetric cell, containing a positive  $\text{BiMn}_2\text{O}_5$ -MWCNT electrode and a negative AC-CB electrode

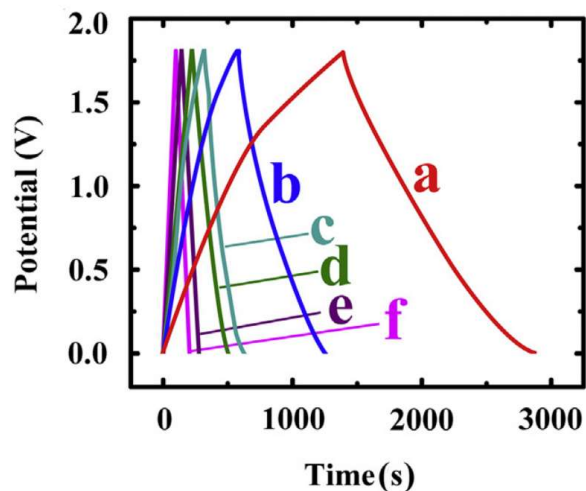


Fig. 7.8 Galvanostatic charge-discharge behavior of an asymmetric cell at currents of (a) 1, (b) 2, (c) 4, (d) 5, (e) 8 and (f)  $10 \text{ mA cm}^{-2}$

Fig. 7.8 shows galvanostatic charge-discharge data at different current densities. The discharge current was nearly linear. The charge-discharge curves in the voltage window

of 1.8 V were of nearly symmetrical triangular shape. Fig. 7.9 shows cyclic behavior of a coin cell. The capacitance decreased during the first 200 cycles and then remained nearly constant. The capacitance retention after 1000 cycles was 90.0%. The inset in Fig.7.9 shows multiple cycles in a voltage window of 1.8 V, which indicates that the shape of the charge-discharge curves remained unchanged during cycling.

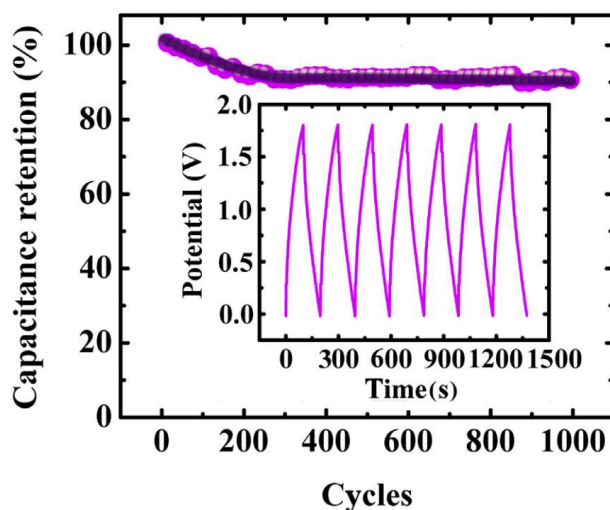


Fig. 7.9. Capacitance retention versus cycle number for an asymmetric cell, inset shows multiple charge-discharge cycles at a constant current of  $10 \text{ mA cm}^{-2}$ .

Fig. 7.10 shows a Ragone plot for the asymmetric cells (Fig.7.9, inset). The analysis of power-energy characteristics indicates that maximum energy density of  $13.0 \text{ Wh L}^{-1}$  ( $9.0 \text{ Wh kg}^{-1}$ ) and maximum power density  $3.6 \text{ kW L}^{-1}$  ( $2.5 \text{ kW kg}^{-1}$ ) can be achieved (Fig.7.10). The power-energy characteristics of the coin cells reported in this preliminary investigation are comparable with literature data for other advanced ES devices[23]. However, in many cases the direct comparison presents difficulties due to the lack[23] of standard techniques for comparison of performance of supercapacitive materials and

devices. The results of our investigation indicated that  $\text{BiMn}_2\text{O}_5$  is a promising material for ES applications. The results of our investigation indicated that good electrochemical performance can be achieved at high mass loadings, high active material to current collector mass ratio and high charge – discharge rates. We expect that in further investigations, currently under way, the performance of the  $\text{BiMn}_2\text{O}_5$  will be improved by the reduction of particle size and optimization of electrode and device composition and design.

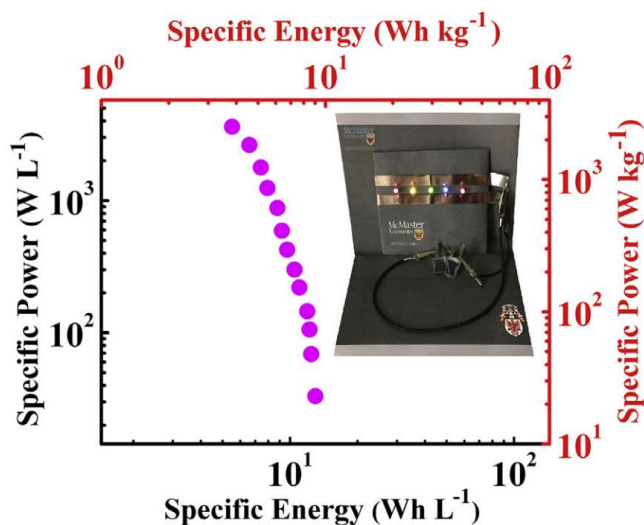


Fig 7.10. Ragone plot for an asymmetric cell, inset shows five LED bulbs powered by two asymmetric cells in series.

The important task is to scale up the procedure and fabricate larger ES devices. As a step in this direction we prepared larger envelope cells, which were used for powering of LED bulbs with nominal current of 20 mA (Fig.7.10). It is expected that the investigation of various oxides with similar structure will result in the development of new pseudocapacitive materials, combining unique capacitive, magnetic, ferroelectric and

other functional properties[24].

## 7.6 Conclusions

Submicrometre particles of multiferroic  $\text{BiMn}_2\text{O}_5$  were prepared by a hydrothermal method. It was demonstrated for the first time that  $\text{BiMn}_2\text{O}_5$  – multiwalled carbon nanotube (MWCNT) composite can be used as a new active material for positive electrodes of ES. It was found that Celestine blue dye can be used as a co-dispersant for  $\text{BiMn}_2\text{O}_5$  and MWCNT for the formation of  $\text{BiMn}_2\text{O}_5$  –MWCNT composites from colloidal suspensions. The composite  $\text{BiMn}_2\text{O}_5$  – MWCNT electrodes with high mass loading and high active material to current collector mass ratio showed a capacitance of  $6.0 \text{ F cm}^{-2}$  ( $540 \text{ F cm}^{-3}$ ) at a scan rate of  $2 \text{ mV s}^{-1}$  and excellent capacitive behavior at high scan rates. The capacitance retention was found to be 75 and 58 % at scan rates of 100 and  $200 \text{ mV s}^{-1}$ , respectively. Testing results indicated that relatively high conductivity and high dielectric constant of  $\text{BiMn}_2\text{O}_5$  was beneficial for good capacitive behavior, especially at high scan rates. Asymmetric devices, containing  $\text{BiMn}_2\text{O}_5$  –MWCNT positive electrodes and AC-CB negative electrodes were fabricated and tested. The asymmetric devices showed good capacitive behavior and good cyclic stability in a voltage window of 1.8 V. The analysis of power-energy characteristics indicated that maximum energy density of  $13.0 \text{ Wh L}^{-1}$  ( $9.0 \text{ Wh kg}^{-1}$ ) and maximum power density  $3.6 \text{ kW L}^{-1}$  ( $2.5 \text{ kW kg}^{-1}$ ) can be achieved.

Yangshuai Liu has the major contribution to this work, and Dr. Igor Zhitomirsky also contributes to this work.

## References

- [1] D. Bélanger, T. Brousse, J.W. Long, Manganese oxides: Battery materials make the leap to electrochemical capacitors, *Electrochemical Society Interface*, 17 (2008) 49-52.
- [2] T. Brousse, P.-L. Taberna, O. Crosnier, R. Dugas, P. Guillemet, Y. Scudeller, Y. Zhou, F. Favier, D. Bélanger, P. Simon, Long-term cycling behavior of asymmetric activated carbon/MnO<sub>2</sub> aqueous electrochemical supercapacitor, *Journal of Power Sources*, 173 (2007) 633-641.
- [3] T. Brousse, M. Toupin, D. Bélanger, A Hybrid Activated Carbon-Manganese Dioxide Capacitor using a Mild Aqueous Electrolyte, *Journal of The Electrochemical Society*, 151 (2004) A614-A622.
- [4] L. Athouel, F. Moser, R. Dugas, O. Crosnier, D. Bélanger, T. Brousse, Variation of the MnO<sub>2</sub> Birnessite Structure upon Charge/Discharge in an Electrochemical Supercapacitor Electrode in Aqueous Na<sub>2</sub>SO<sub>4</sub> Electrolyte, *The Journal of Physical Chemistry C*, 112 (2008) 7270-7277.
- [5] S. Devaraj, N. Munichandraiah, High Capacitance of Electrodeposited MnO<sub>2</sub> by the Effect of a Surface-Active Agent, *Electrochemical and Solid-State Letters*, 8 (2005) A373-A377.
- [6] Y. Li, G. Wang, K. Ye, K. Cheng, Y. Pan, P. Yan, J. Yin, D. Cao, Facile preparation of three-dimensional multilayer porous MnO<sub>2</sub>/reduced graphene oxide composite and its supercapacitive performance, *Journal of Power Sources*, 271 (2014) 582-588.
- [7] J.-J. Zhu, L.-L. Yu, J.-T. Zhao, 3D network mesoporous beta-manganese dioxide: Template-free synthesis and supercapacitive performance, *Journal of Power Sources*, 270

(2014) 411-417.

[8] S. Jiang, T. Shi, D. Liu, H. Long, S. Xi, F. Wu, X. Li, Q. Xia, Z. Tang, Integration of  $\text{MnO}_2$  thin film and carbon nanotubes to three-dimensional carbon microelectrodes for electrochemical microcapacitors, *Journal of Power Sources*, 262 (2014) 494-500.

[9] Y.Q. Lin, Y.J. Wu, X.M. Chen, S.P. Gu, J. Tong, S. Guan, Dielectric relaxation mechanisms of  $\text{BiMn}_2\text{O}_5$  ceramics, *Journal of Applied Physics*, 105 (2009) 54109.

[10] I. Zhitomirsky, N. Skorokhodov, A. Bush, O. Chechernikova, V. Chuprakov, Y.N. Venevtsev, Dielectric, pyroelectric and magnetic properties of  $\text{BiMn}_2\text{O}_5$  crystals, *Sov. Phys. Solid State*, 25 (1983) 550-552.

[11] Y. Liu, K. Shi, I. Zhitomirsky, New colloidal route for electrostatic assembly of oxide nanoparticle-carbon nanotube composites, *Colloids and Surfaces A: Physicochemical and Engineering Aspects*, 446 (2014) 15-22.

[12] Y. Liu, I. Zhitomirsky, Aqueous electrostatic dispersion and heterocoagulation of multiwalled carbon nanotubes and manganese dioxide for the fabrication of supercapacitor electrodes and devices, *RSC Advances*, 4 (2014) 45481-45489.

[13] X. Li, I. Zhitomirsky, Electrodeposition of polypyrrole-carbon nanotube composites for electrochemical supercapacitors, *Journal of Power Sources*, 221 (2013) 49-56.

[14] Y. Wang, Y. Liu, I. Zhitomirsky, Surface modification of  $\text{MnO}_2$  and carbon nanotubes using organic dyes for nanotechnology of electrochemical supercapacitors, *Journal of Materials Chemistry A*, 1 (2013) 12519-12526.

[15] M. Ata, Y. Liu, I. Zhitomirsky, A review of new methods of surface chemical modification, dispersion and electrophoretic deposition of metal oxide particles, *RSC*

Advances, 4 (2014) 22716-22732.

[16] A. Kannan, S. Bhavaraju, F. Prado, M.M. Raja, A. Manthiram, Characterization of the Bismuth-modified manganese dioxide cathodes in rechargeable alkaline cells, *Journal of The Electrochemical Society*, 149 (2002) A483-A492.

[17] H.S. Wroblowa, N. Gupta, Rechargeable manganese oxide electrodes: Part II. physically modified materials, *Journal of Electroanalytical Chemistry and Interfacial Electrochemistry*, 238 (1987) 93-102.

[18] C.G. Castledine, B.E. Conway, Effects of electrochemically incorporated bismuth on the discharge and recharge of electrodeposited manganese dioxide films in 9m aqueous KOH, *Journal of Applied Electrochemistry*, 25 (1995) 707-715.

[19] K.S. Abou-El-Sherbini, M. Askar, R. Schollhorn, Hydrated layered manganese dioxide:: III. Role of bismuth oxide on the redox behaviour of hydrated layered manganese dioxides, *Solid State Ionics*, 139 (2001) 121-133.

[20] S.W. Donne, G.A. Lawrance, D.A.J. Swinkels, Redox Processes at the Manganese Dioxide Electrode: I. Constant Current Intermittent Discharge, *Journal of The Electrochemical Society*, 144 (1997) 2949-2953.

[21] S.W. Donne, G.A. Lawrance, D.A.J. Swinkels, Redox Processes at the Manganese Dioxide Electrode: II. Slow Scan Cyclic Voltammetry, *Journal of The Electrochemical Society*, 144 (1997) 2954-2961.

[22] Y. Zhu, K. Shi, I. Zhitomirsky, Polypyrrole coated carbon nanotubes for supercapacitor devices with enhanced electrochemical performance, *Journal of Power Sources*, 268 (2014) 233-239.

[23] Y. Gogotsi, P. Simon, True Performance Metrics in Electrochemical Energy Storage, *Science*, 334 (2011) 917-918.

[24] Y. Liu, D. Luo, M. S. Ata, I. Zhitomirsky, Electrochemical supercapacitor based on multiferroic  $\text{BiMn}_2\text{O}_5$ , *J. Power Sources*, 284 (2015), 377-382

# **Chapter 8 Azopolymer triggered electrophoretic deposition of MnO<sub>2</sub>-MWCNTs composites for supercapacitors**

## **8.1 Motivation and origin**

The goal of our investigation was the use of poly[1-[4-(3-carboxy-4-hydroxyphenylazo)benzenesulfonamido]-1,2-ethanediyl, sodium salt] (PAZO) polymer for the fabrication of nanocomposite electrodes from colloidal suspensions for applications in ECs. The unique feature of the PAZO structure, is that it includes diaromatic monomers with salicylate ligands. Such monomers can provide multiple adsorption sites for efficient adsorption on particles of various materials and impart electrical charges to the particles. Therefore, the use of PAZO can overcome the limitations of small organic molecules. Moreover, the use of PAZO polymer offers the advantages of improved steric stabilization. Proof of concept studies involved the fabrication of composites, containing advanced materials for ECs, such as MnO<sub>2</sub> nanofibers, multiwalled carbon nanotubes (MWCNT), polypyrrole (PPy) and PPy coated multiwalled carbon nanotubes (MWCNT). Moving toward our goal we developed a new method for the fabrication of PPy coated MWCNT.

In addition to these efforts aimed at the development of ES electrodes we demonstrate additional promising benefits of the EPD method. A conceptually new approach

developed in this investigation for the EPD of materials opens up a new and promising strategy for the fabrication of composite materials, utilizing physical properties of PAZO and various functional materials. It is in this regard that PAZO exhibits a unique set of properties, making this polymer an advanced functional material for many applications in photonics, optoelectronics, memory devices and sensors[1-3]. Of particular interest is a photo-induced birefringence in PAZO[1], resulting from reversible *trans-cis-trans* photoisomerization of azo groups, optical storage and photochromic properties, surface-relief grating[4, 5]. We propose a deposition mechanism of PAZO and describe advantages of EPD compared to other film deposition methods.

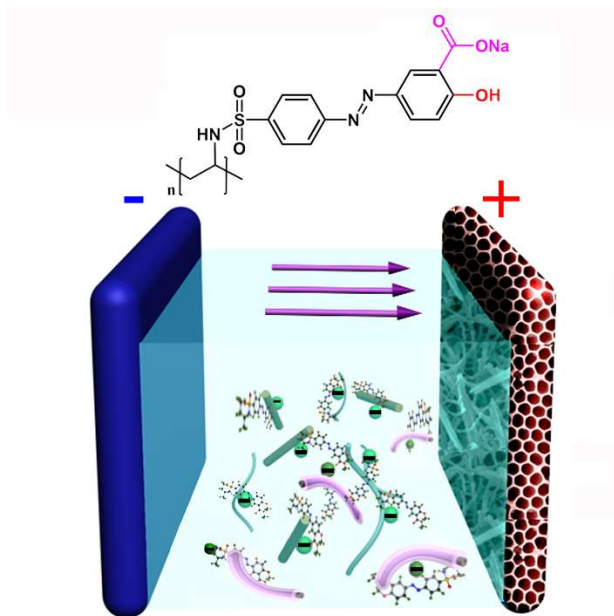


Fig. 8.1 Schematic of PAZO as dispersant for charging and EPD of MnO<sub>2</sub> and PPy fibers

## 8.2 Materials synthesis and morphology characterization

In this investigation, MnO<sub>2</sub> nanofibers, PPy and PPy coated MWCNT were prepared for application in electrodes of ECs. Fig. 8.2(A-C) shows SEM and TEM data for the MnO<sub>2</sub>

nanofibers. The SEM and TEM images indicated that the diameter of the nanofibers was varied in the range of 10-30 nm. The electron diffraction pattern (Fig. 8.2B, inset) and HRTEM image (Fig. 8.2C) showed that the nanofibers were crystalline. The crystallinity of the nanofibers was confirmed by the XRD data presented in the Fig. 8.2 D. The X-ray diffraction pattern shows peaks, corresponding to the JCPDS file 24-0735 for MnO<sub>2</sub>.

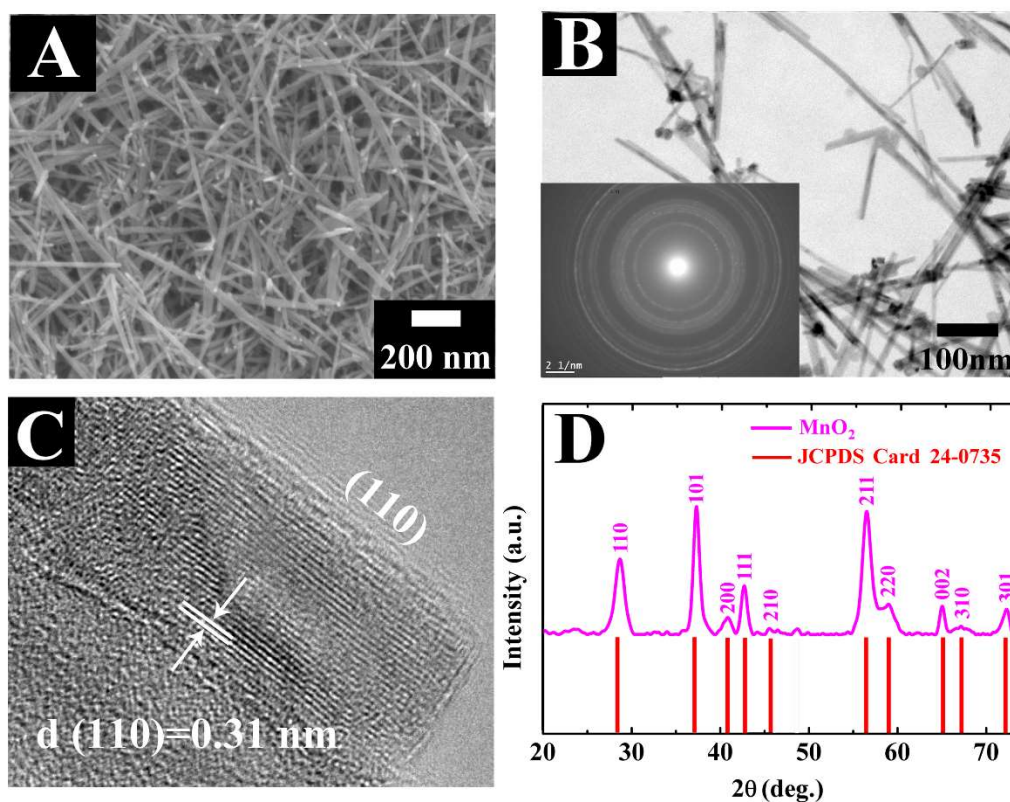


Fig. 8.2 (A) SEM image, (B) TEM image, inset shows electron diffraction pattern, (C) high resolution TEM image and (D) X-ray diffraction pattern of MnO<sub>2</sub> nanofibers

Fig. 8.3(A) shows a chemical structure of BT used in this investigation. BT is a polyaromatic molecule, containing an anionic SO<sub>3</sub><sup>-</sup> group. It was found that PPy powders can be prepared by chemical polymerization, using BT as an anionic dopant. Another im-

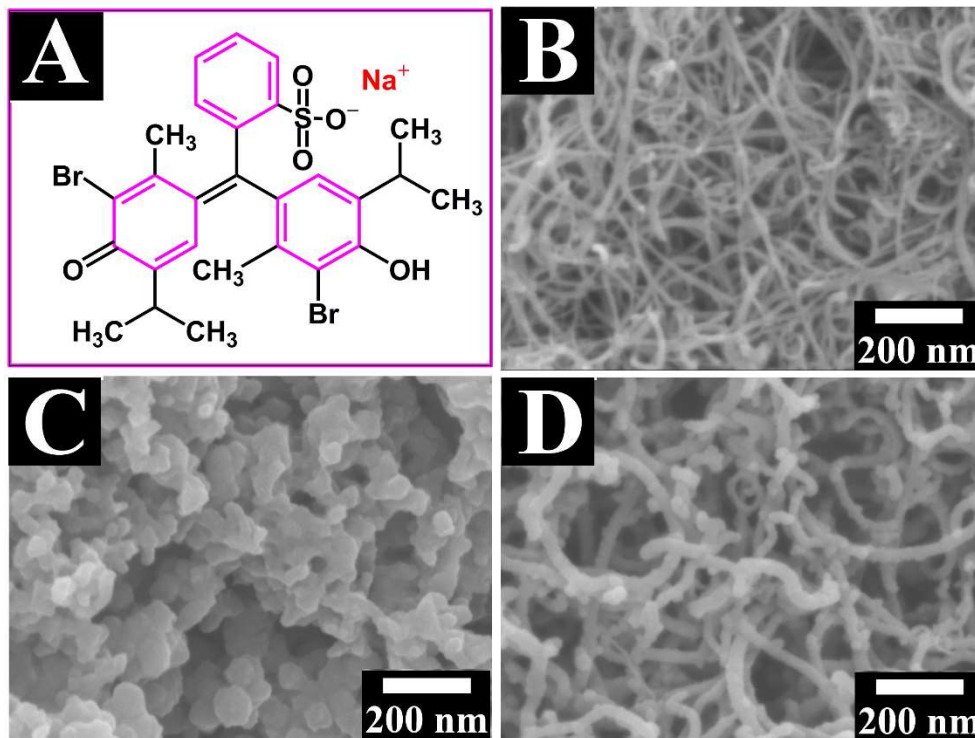


Fig. 8.3 (A) Chemical structure of BT dopant, (B) SEM image of pristine MWCNT, (C) SEM image of PPy particles prepared using BT dopant, (D) SEM image of PPy coated MWCNT, prepared using BT as a dopant for PPy and dispersant for MWCNT.

-portant finding was the possibility of fabrication of stable suspension of MWCNT in water using BT as a dispersant. Fig 8.3(B) shows an SEM image of the MWCNT used in this investigation. The  $1 \text{ g L}^{-1}$  MWCNT suspensions, containing  $1 \text{ g L}^{-1}$  BT, were stable for one month. The PPy powders, prepared using BT as a dopant, contained agglomerates of primary particles of nearly spherical shape with particle size of about 50 nm (Fig. 8.3C). The SEM images of PPy, synthesized in the presence of MWCNT and BT, showed a fibrous morphology of the prepared composite material (Fig. 8.3D). The comparison of the images shown in Fig. 8.3B and Fig. 8.3D indicated that the fibers, shown in the Fig.

8.3D have larger diameters. Moreover, spherical PPy particles or agglomerates, similar to those shown in Fig. 8.3C, were not observed in Fig. 8.3D. Therefore, the method resulted in the formation of PPy coated MWCNT. The formation of PPy coated MWCNT was confirmed by the results of TEM investigations.

TEM images of the PPy coated MWCNT at different magnifications are shown in Fig. 8.4 (A, B). The images showed relatively uniform PPy coatings with typical thickness of 10 nm (Fig. 8.4B).

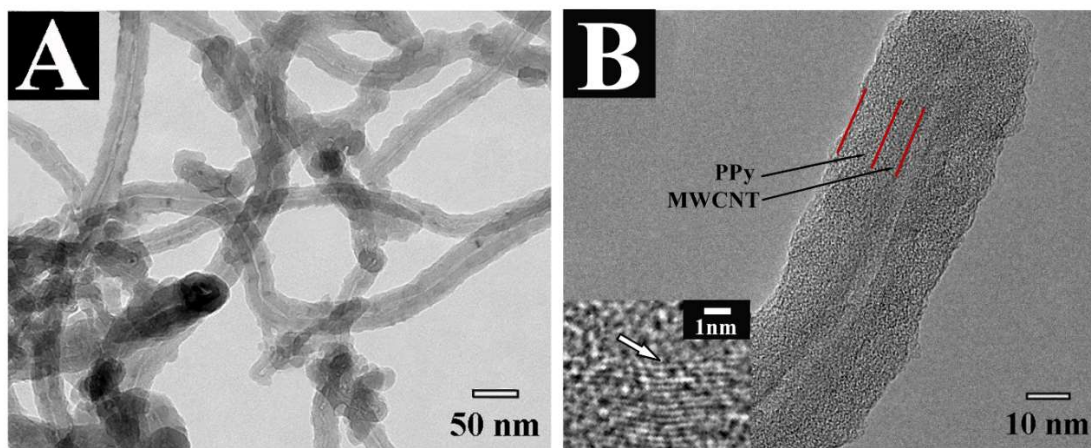


Fig. 8.4 TEM images (A and B) at different magnifications of the PPy coated MWCNT, prepared using BT as a dopant for PPy and dispersant for MWCNT, inset in (B) shows interface of PPy coating and MWCNT.

### 8.3 Dispersion mechanism and stability characterization

The method, developed in this investigation, provides an efficient and simple technique for fabricating PPy coated MWCNT. It is suggested that  $\pi$ - $\pi$  interactions of polyaromatic BT and MWCNT resulted in BT adsorption on MWCNT. The adsorbed BT provided suspension stability and promoted PPy polymerization on the surface of well dispersed

MWCNT. As a result, PPy coated MWCNT were prepared by simple one-step procedure. The method is suitable for mass production of PPy coated MWCNT.

The MnO<sub>2</sub> nanofibers, MWCNT, PPy and PPy coated MWCNT were used for the fabrication of electrodes of ECs by EPD. Fig. 8.5A shows a chemical structure of PAZO, used as a charging and dispersing agent for EPD. The salicylate ligands of the PAZO monomers are powerful complexing agents, which promoted PAZO adsorption on the surface of MnO<sub>2</sub> nanofibers (Fig. 8.5B).

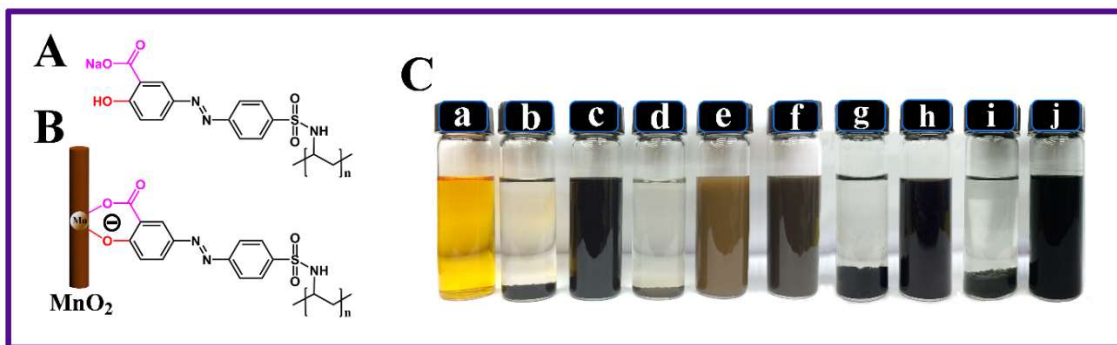


Fig. 8.5(A) Molecular structure of PAZO, (B) schematic of adsorption of PAZO on MnO<sub>2</sub> nanofiber, involving the complexation of a Mn atom with a salicylate ligand of a PAZO monomer; (C) (a) PAZO solution, and suspensions of (b) 1 g L<sup>-1</sup> MWCNTs, (c) 1 g L<sup>-1</sup> MWCNTs and 1 g L<sup>-1</sup> PAZO, (d) 1 g L<sup>-1</sup> MnO<sub>2</sub>, (e) 1 g L<sup>-1</sup> MnO<sub>2</sub> and 1 g L<sup>-1</sup> PAZO, (f) 1 g L<sup>-1</sup> MnO<sub>2</sub>, 1 g L<sup>-1</sup> MWCNTs and 1 g L<sup>-1</sup> PAZO, (g) 1 g L<sup>-1</sup> PPy, (h) 1 g L<sup>-1</sup> PPy and 1 g L<sup>-1</sup> PAZO, (i) 1 g L<sup>-1</sup> PPy coated MWCNTs, (j) 1 g L<sup>-1</sup> PPy coated MWCNTs and 1 g L<sup>-1</sup> PAZO in an ethanol–water solvent.

The PAZO monomers provided multiple adsorption sites and offered advantages of stronger adsorption, compared to small molecules from the salicylate family[6],

containing single salicylate ligands. The diaromatic structure of individual monomers and long hydrocarbon chain of PAZO (Fig. 8.5A), allowed for strong PAZO adsorption on MWCNT, PPy and PPy coated MWCNT due to  $\pi$ - $\pi$  and hydrophobic interactions. The adsorbed PAZO macromolecules, containing monomers with anionic  $\text{COO}^-$  groups, allowed for efficient electrostatic dispersion of  $\text{MnO}_2$ , MWCNT, PPy, PPy coated MWCNT and their mixtures. The sedimentation tests showed excellent stability (Fig. 8.5C) of suspensions, containing PAZO.

The stability of the suspensions was an important factor for film formation by EPD. In the EPD process, the particles must be well dispersed and charged in the bulk of the suspensions. An applied electric field provides electrophoretic motion of the particles to the electrode and their accumulation at the electrode surface. However, it is known[7] that the strong mutual repulsion of the particles at the electrode surface can prevent deposition. In order to achieve deposition of materials using PAZO as a charging and dispersing agent, we utilized other important properties of PAZO, which have not been paid enough attention to in the literature.

The salt form of PAZO, used in this investigation (PAZO-Na), is well soluble in water. However it is known from the available literature[1] that PAZO precipitates at low pH as an insoluble acidic form of this polymer (PAZO-H), containing protonated carboxylic groups ( $\text{COOH}$ ). Such properties can be utilized for film formation by EPD. In aqueous solutions, the electrochemical decomposition of water results in a pH decrease at the anode surface:



The charge neutralization of carboxylic groups of PAZO at the anode surface



and formation of insoluble PAZO-H promoted deposit formation.

#### **8.4 EPD and adsorption characterization**

The proof-of-concept studies involved EPD of films from pure PAZO solutions. It was found that anodic films can be obtained from aqueous solutions or solutions in a mixed ethanol-water solvent. The deposition process was investigated in-situ by QCM in dilute solutions. The QCM data showed that the mass gain increased with increasing deposition time, indicating continuous film growth. Higher deposition yield was obtained from solutions in water, compared to the solutions in ethanol-water solvent. However, the use of mixed ethanol water solvent offered the advantage of reduced gas evolution. The film mass increased with increasing PAZO concentration in the solutions (Fig. 8.6A). The non-linear increase in the deposit mass can result from continuous displacement of film-solution interface during the film growth [8], influence of polymer concentration at electrode surface on deposit formation [7] and other factors, discussed in the literature [7]. The analysis of deposition yield data at different deposition durations at PAZO concentrations of  $1 \text{ g L}^{-1}$  indicated that relatively high deposition yield can be achieved (Fig. 8.6C). The deposition yield data presented in Fig. 8.6A-C indicated that the deposition yield of PAZO can be varied by the variation of PAZO concentration and deposition time. The SEM studies of the films prepared from aqueous solutions showed significant surface roughness (Fig. 8.6D). The surface roughness can result from gas evolution during deposition. The use of ethanol-water solvent allowed the formation of

relatively uniform films (Fig. 8.6E,F). Small pin holes can result from the solvent evaporation (Fig. 8.6E). Fig.8.5F shows typical film cross section. The analysis of film cross sections for films prepared at different deposition durations showed that relatively thick films with film thickness of 0.1-2  $\mu\text{m}$  can be obtained. Thick films were removed from the substrates and studied by FTIR.

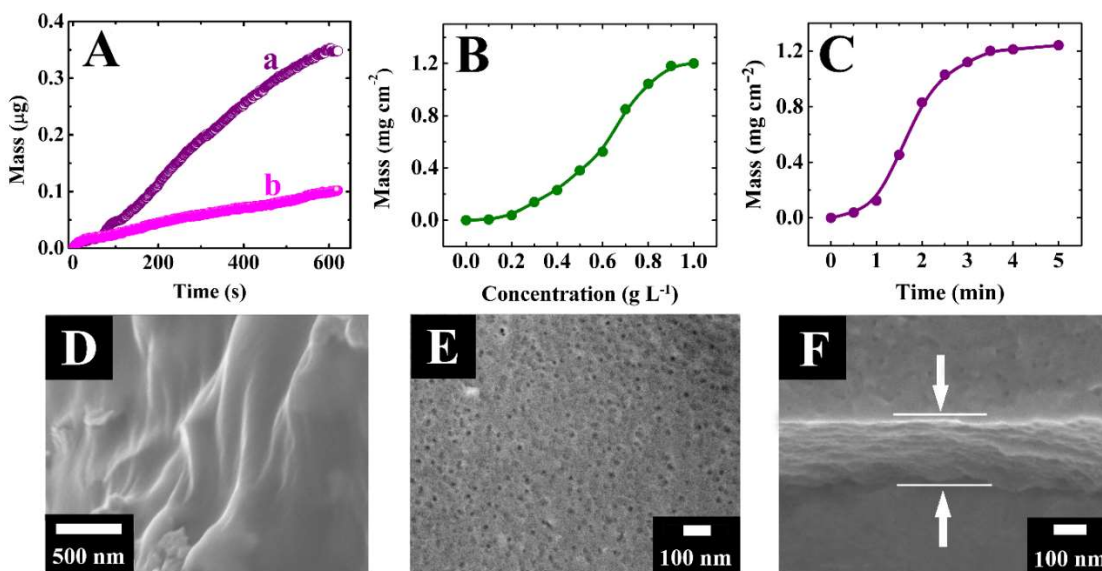


Fig. 8.6 (A–C) Deposit mass at a deposition voltage of 5 V: (A) versus deposition time in 0.1  $\text{g L}^{-1}$  PAZO solutions in (a) water, (b) ethanol–water solvent, measured by QCM; (B) versus PAZO concentration in ethanol–water solvent at a deposition time of 5 min; (C) versus time for 1  $\text{g L}^{-1}$  PAZO solution in ethanol–water solvent, (D–F) SEM images of films prepared from 1  $\text{g L}^{-1}$  PAZO solutions in (D) water and (E and F) ethanol–water solvent, (E) surface, (F) cross section.

Fig. 8.7(a,b) shows FTIR spectra of as-received and deposited PAZO. The absorptions at 1325 and 1326  $\text{cm}^{-1}$  resulted from stretching S=O vibrations[9]. The adsorptions at 1396

and  $1481\text{ cm}^{-1}$  were related to aromatic C—C/C=C vibrations[10]. N=N stretching[9] contributed to the absorptions at  $1427\text{ cm}^{-1}$ . The spectra (Fig.6(a,b)) showed significant difference in the range of  $1500\text{-}1700\text{ cm}^{-1}$ . The as-received PAZO showed broad absorptions at  $1583$  and  $1635\text{ cm}^{-1}$ , which can be assigned to stretching C=O and  $\text{COO}^-$  vibrations, respectively[5, 9]. The peaks at  $1673$  and  $1619\text{ cm}^{-1}$  were attributed to stretching vibrations of the protonated COOH groups[5, 9]. The spectrum of the deposited PAZO is similar to that of the protonated form of PAZO, prepared in acidic conditions[5, 9]. Therefore, the FTIR data confirm the suggested deposition mechanism, which resulted in the deposition of acidic form of PAZO.

EPD offers significant advantages for the fabrication of PAZO films, compared to layer-by-layer (LbL) self-assembly technique, which involves multiple and time consuming steps of multilayer deposition of PAZO and cationic polyelectrolytes[9, 11-13]. EPD is a simple technique, which allows deposition of thin and thick films of pure PAZO polymer at high deposition rate. It is expected that further development of this method will result in fabrication of advanced devices, utilizing important properties of PAZO, such as photo-induced birefringence, photonic, optoelectronic and optical memory properties[1-3], photochromism and surface-relief grating[4, 5]. The film forming and binding properties of PAZO offered additional benefits for EPD of crack free and adherent films of MWCNT,  $\text{MnO}_2$  nanofibers, PPy and PPy coated MWCNT.

The FTIR spectrum of deposited  $\text{MnO}_2$  nanofibers showed absorption peaks, similar to the peaks of deposited PAZO (Fig. 8.7c). Such peaks were also observed in the FTIR spectrum of deposited MWCNT (Fig. 8.7d). The broad peak at  $\sim 1644\text{ cm}^{-1}$  represents a

combination of absorptions related to protonated COOH groups[5, 9] and aromatic vibrations of MWCNT[14]. Therefore, the FTIR data confirmed co-deposition of protonated form of PAZO with MnO<sub>2</sub> nanofibers and MWCNT.

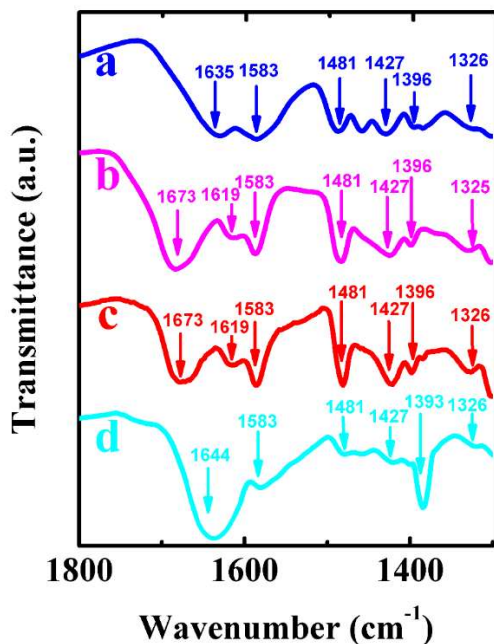


Fig. 8.7 FTIR spectra of (a) as-received PAZO and deposits, prepared from (b) 1 g L<sup>-1</sup> PAZO, (c) 4 g L<sup>-1</sup> MnO<sub>2</sub> and 1 g L<sup>-1</sup> PAZO, (d) 1 g L<sup>-1</sup> MWCNT and 1 g L<sup>-1</sup> PAZO in a mixed ethanol–water solvent

The use of PAZO as a dispersing, charging and film forming agent allowed the EPD of MWCNT, MnO<sub>2</sub> nanofibers, PPy and PPy coated MWCNT. The deposition yield increased with increasing PAZO concentration in suspensions (Fig. 8.8A) and with increasing deposition time at a constant PAZO concentration.

The increase in the deposit mass with increasing PAZO concentration (Fig. 8.8A) was attributed to increased adsorption of PAZO on particle surface and increased particle cha-

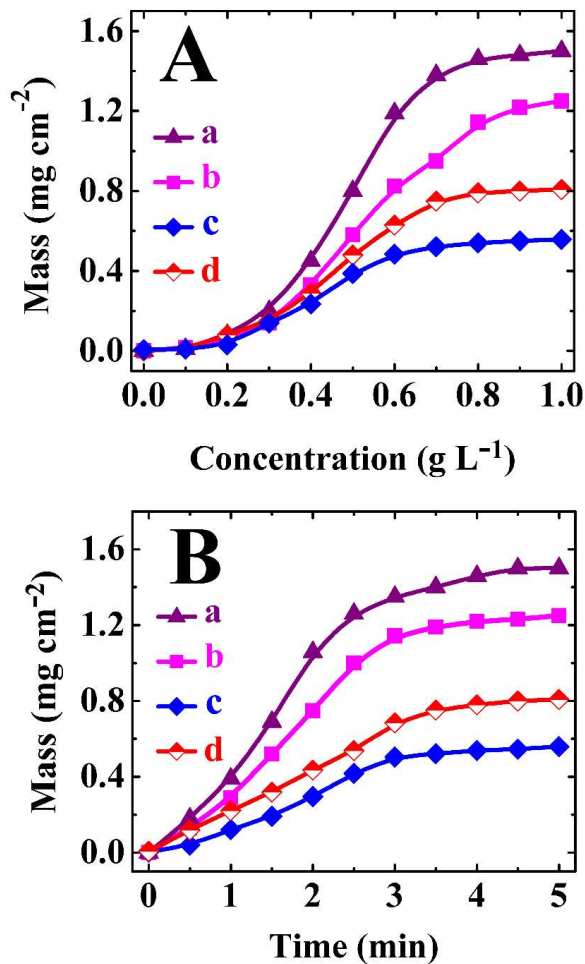


Fig. 8.8 Deposit mass versus (A) PAZO concentration at a deposition time of 5 min and (B) time at PAZO concentration of 1 g L<sup>-1</sup> for suspensions of (a) 2 g L<sup>-1</sup> MnO<sub>2</sub> nanofibers, (b) 1 g L<sup>-1</sup> MWCNT, (c) 1 g L<sup>-1</sup> PPy powder, (d) 1 g L<sup>-1</sup> PPy coated MWCNT in a mixed ethanol– water solvent

-rge. The results presented in Fig. 8.8 indicate that MWCNT, MnO<sub>2</sub> nanofibers, PPy and PPy coated MWCNT can be deposited at high deposition rate and deposit mass can be varied. The use of PAZO as a co-dispersant for MWCNT and MnO<sub>2</sub> allowed the fabrication of composites.

### 8.4 Electrode fabrication and morphology characterization

The good dispersion and fibrous microstructure of MnO<sub>2</sub> nanofibers and MWCNT allowed for the fabrication of free-standing flexible composites (Fig. 8.8D).

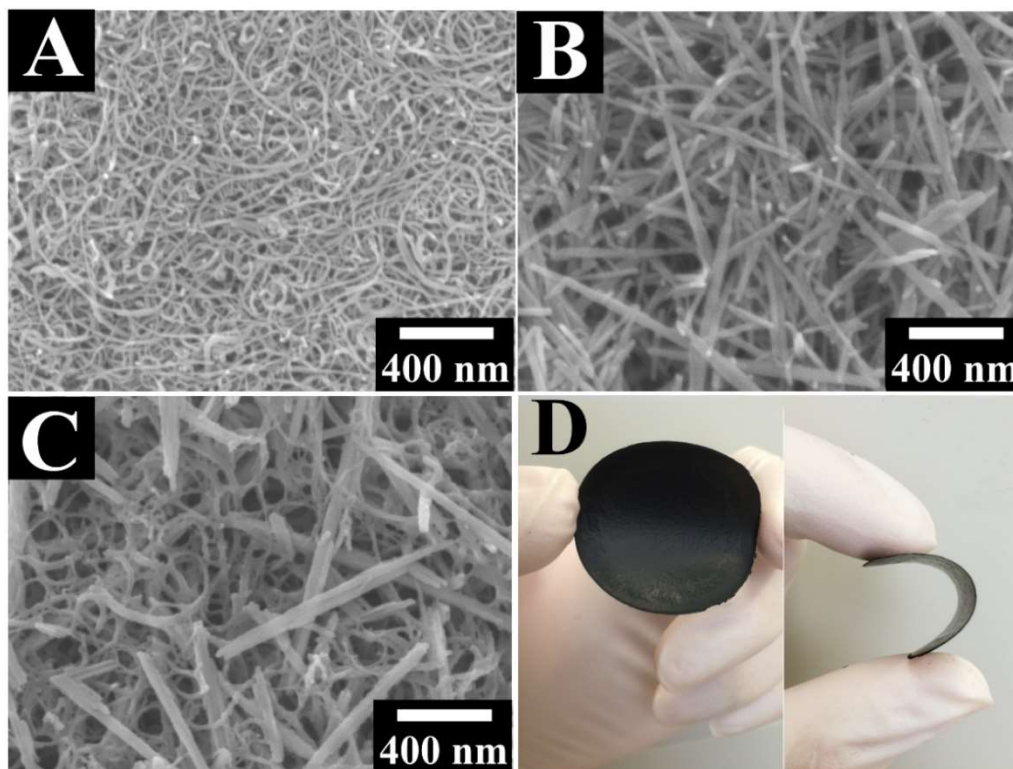


Fig. 8.9 (A–C) SEM images of deposits, prepared at a deposition voltage of 100 V from suspensions of (A) 1 g L<sup>-1</sup> MWCNT and 1 g L<sup>-1</sup> PAZO, (B) 4 g L<sup>-1</sup> MnO<sub>2</sub> nanofiber and 1 g L<sup>-1</sup> PAZO (C) 4 g L<sup>-1</sup> MnO<sub>2</sub> nanofiber, 1 g L<sup>-1</sup> MWCNT and 1 g L<sup>-1</sup> PAZO, (D) composite, prepared by filtration of 4 g L<sup>-1</sup> MnO<sub>2</sub> nanofiber and 1 g L<sup>-1</sup> MWCNT suspension, dispersed using 1 g L<sup>-1</sup> PAZO in ethanol–water solvent.

Fig. 8.9(A-C) compares SEM images of MWCNT, MnO<sub>2</sub> nanofibers and a composite, containing both materials. The EPD method allowed the fabrication of continuous, crack free deposits, containing non-agglomerated MWCNT and MnO<sub>2</sub> nanofibers. The deposits

were porous with typical pore size below 100 nm.

The SEM images of PPy and PPy coated MWCNT are shown in the Fig. 8.10. The EPD method allowed for the fabrication of porous deposits. The SEM image of PPy coated MWCNT indicated the formation of fibrous porous network, containing non-agglomerated fibers. The porosity of the films shown in Fig. 8.9, and 8.10 was beneficial for their application in electrodes of ECs. The film porosity allows electrolyte access to the surface of electrochemically active materials.

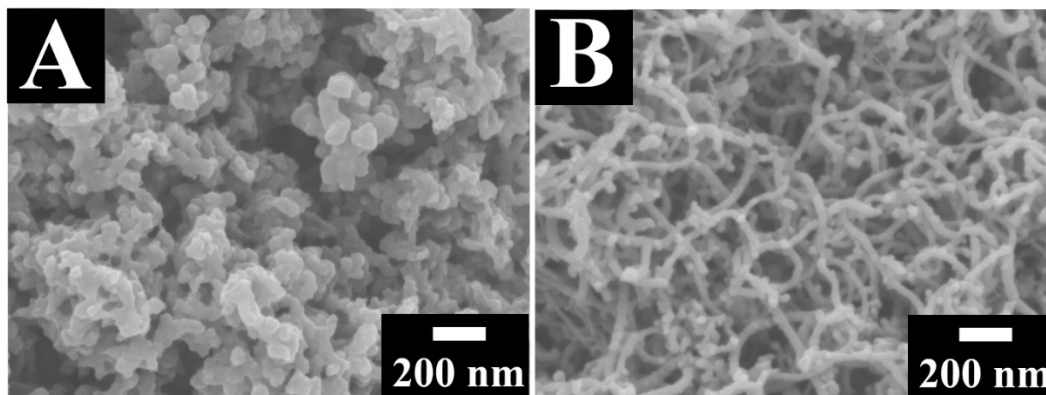


Fig. 8.10 SEM images of deposits prepared from 4 g L<sup>-1</sup> suspensions of (A) PPy and (B) PPy coated MWCNT, containing 1 g L<sup>-1</sup> PAZO in ethanol–water solvent at a deposition voltage of 100 V.

### 8.5 Electrochemical characterization

The MnO<sub>2</sub> nanofiber-MWCNT composites and PPy coated MWCNT were investigated for the application in electrodes of ECs. Fig. 8.11 (A-C) compares CVs at different scan rates for electrodes, prepared using Ni plaque current collectors and different active materials, such as MnO<sub>2</sub> nanofibers, deposited by EPD using PAZO, MnO<sub>2</sub> nanofiber-

MWCNT impregnated into the current collectors from slurries, prepared without PAZO, and MnO<sub>2</sub> nanofiber-MWCNT composites prepared by EPD using PAZO. The integral capacitances in the voltage window of 0-0.9 V were calculated from the CV data at different scan rates and presented in Fig. 8.11D. The composite electrodes, containing MWCNT, showed larger CV areas (Fig. 8.11B,C) and higher capacitances (Fig. 8.11D(b,c)), compared to the MnO<sub>2</sub> electrodes (Fig. 8.11A and Fig. 8.11D (a)). The difference is attributed to higher conductivity of the electrodes, containing MWCNT. The MnO<sub>2</sub> nanofiber-MWCNT electrodes, prepared by EPD using PAZO, showed improved capacitive behavior, compared to the MnO<sub>2</sub> nanofiber-MWCNT electrodes, prepared without PAZO. The MnO<sub>2</sub> nanofiber-MWCNT electrodes, prepared using PAZO, showed nearly box shape CVs, even at relatively high scan rates (Fig. 8.11C). The highest capacitance of 140 F g<sup>-1</sup> was obtained at a scan rate of 2 mV s<sup>-1</sup> (Fig. 8.11D(c)). The impedance data for the electrodes, presented in the Nyquist plot (Fig. 8.12A), indicated that the electrodes, prepared by co-deposition of MnO<sub>2</sub> nanofibers and MWCNT in the presence of PAZO showed lower resistance  $R=Z'$ , compared to the MnO<sub>2</sub> nanofibers electrodes without MWCNT. The lower resistance of the composite electrodes, prepared using PAZO (Fig. 8.12A(c)), compared to the composites formed without PAZO (Fig. 8.12A(b)), resulted from improved dispersion of MWCNT. Figs. 8.12B,C show frequency dependencies of the components of differential capacitance, obtained from the impedance data. The MnO<sub>2</sub> nanofiber - MWCNT electrodes, prepared by EPD using PAZO, showed the highest differential AC capacitance at low frequency in agreement with the data for integral capacitances.

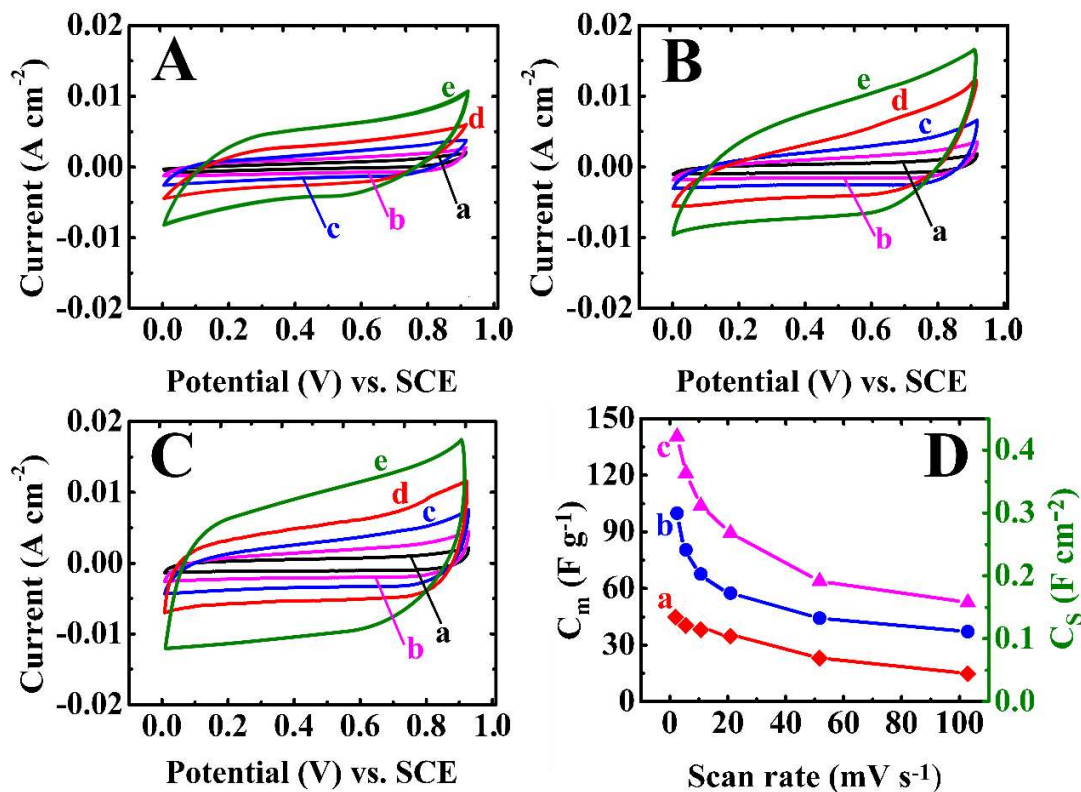


Fig. 8.11 (A–C) CVs for 3 mg cm<sup>-2</sup> electrodes of (A) of pure MnO<sub>2</sub> prepared by EPD using PAZO, (B) MnO<sub>2</sub>-MWCNT, prepared by slurry impregnation method without PAZO, (C) MnO<sub>2</sub>-MWCNT, prepared by EPD using PAZO at scan rates of (a) 2, (b) 5, (c) 10, (d) 20, and (e) 50 mV s<sup>-1</sup>, the mass ratio of MWCNT : MnO<sub>2</sub> in the suspensions (B and C) was 1 : 4, (D) C<sub>s</sub> and C<sub>m</sub> versus scan rate, calculated from the CV data, for (a) pure MnO<sub>2</sub>, prepared by EPD using PAZO (b) MnO<sub>2</sub>-MWCNT, prepared by slurry impregnation (c) MnO<sub>2</sub>-MWCNT, prepared by EPD using PAZO.

The use of PAZO allowed for the EPD of electrically neutral PPy and PPy coated MWCNT. The capacitive behavior of the electrodes, prepared by EPD was investigated by cyclic voltammetry and impedance spectroscopy (Fig. 8.12). The CV data showed capacitive behavior of the electrodes (Fig. 8.13A,B). The PPy coated MWCNT electrodes

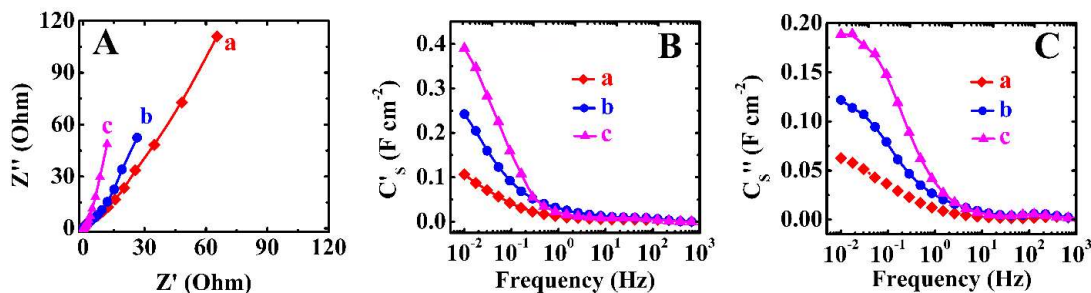


Fig. 8.12 (A) Nyquist plot of complex impedance for  $3 \text{ mg cm}^{-2}$  electrodes and (B and C) components of complex capacitance, calculated the impedance data versus frequency, for (a) of pure  $\text{MnO}_2$  prepared by EPD using PAZO, (b)  $\text{MnO}_2\text{-MWCNT}$ , prepared by slurry impregnation method without PAZO (c)  $\text{MnO}_2\text{-MWCNT}$ , prepared by EPD using PAZO, the mass ratio of  $\text{MWCNT} : \text{MnO}_2$  in the suspensions (b and c) was 1 : 4.

showed larger areas of CVs and higher capacitance, compared to pure PPy (Fig. 8.13A-C).

The highest capacitance of  $155 \text{ F g}^{-1}$  was obtained for the PPy coated MWCNT at a scan

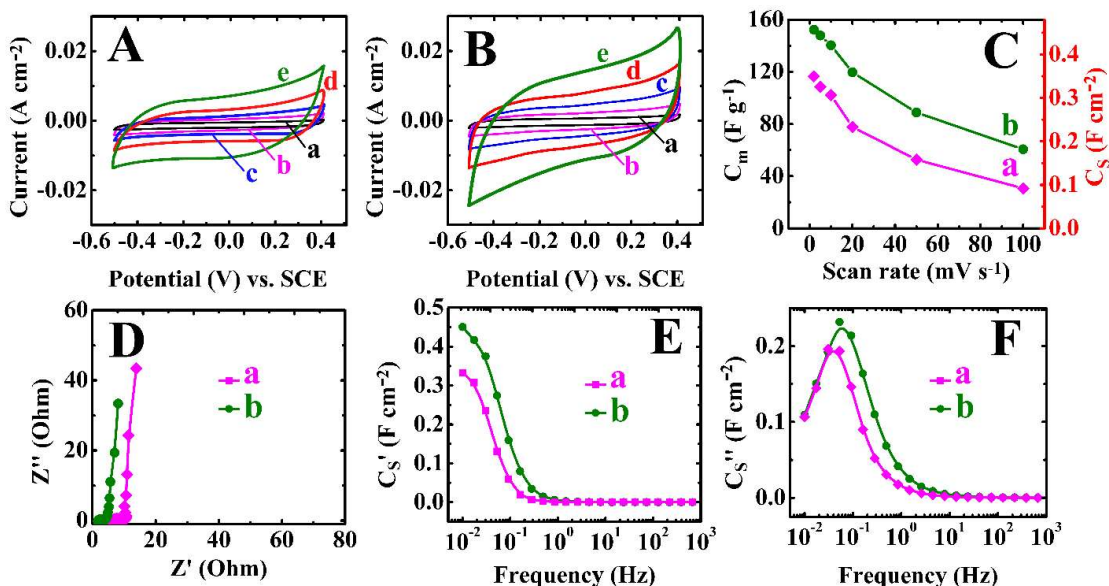


Fig 8.13. Electrochemical testing data for  $3 \text{ mg cm}^{-2}$  electrodes prepared by EPD using PAZO: (A and B) CVs for (A) PPy and (B) PPy coated MWCNT at scan rates of (a) 2, (b)

5, (c) 10, (d) 20, and (e) 50  $\text{mV s}^{-1}$ , (C)  $C_s$  and  $C_m$ , calculated from the CVs for (a) PPy and (b) PPy coated MWCNT, (D–F) impedance data for (a) PPy and (b) PPy coated MWCNT: (D) Nyquist plot of complex impedance and (E and F) components of complex capacitance, calculated from the impedance data versus frequency.

rate of 2  $\text{mV s}^{-1}$ .

The results of impedance spectroscopy analysis are presented in Fig. 8.13 (D-F). The PPy coated MWCNT showed lower resistance and increased real component of complex differential capacitance at low scan rates.

Fig. 8.14 shows capacitance retention versus cycle number dependences for  $\text{MnO}_2$  nanofiber-MWCNT composites and PPy coated MWCNT. The capacitance retention after 1000 cycles was found to be 93% and 91% for  $\text{MnO}_2$  nanofiber-MWCNT composites and PPy coated MWCNT, respectively. The results of this investigation indicate that PAZO can be used for EPD of advanced materials for ECs, such as  $\text{MnO}_2$  nanofibers, MWCNT, PPy and PPy coated MWCNT. The use of PAZO as a co-dispersant allows for the results

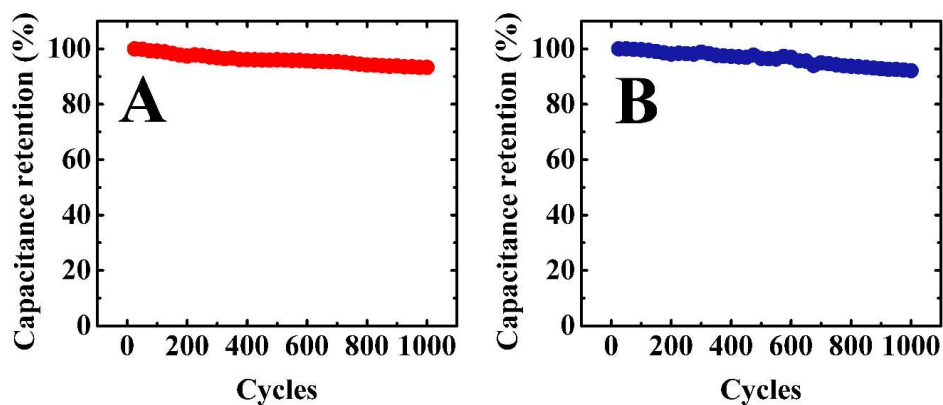


Fig. 8.14 Capacitance retention versus cycle number for (A)  $\text{MnO}_2$ - MWCNT and (B) PPy coated MWCNT electrodes, prepared by EPD using PAZO.

in enhanced properties. It is expected that PAZO can be used for EPD of other materials and fabrication of novel composites, utilizing functional properties of different materials and unique physical properties of PAZO[15].

## **8.6. Conclusions**

Films of PAZO have been deposited by anodic EPD. The deposition mechanism involved electrophoresis of anionic PAZO macromolecules, pH decrease at the anode due to the electrode reactions, protonation of carboxylic groups of PAZO and precipitation of insoluble acidic form of PAZO at the electrode surface. The deposition rate and film thickness can be varied. The EPD method offers advantages for the deposition of PAZO films due to the simple deposition procedure, high deposition rate, possibility of deposition of thin and thick films. Moreover, EPD allows for the deposition of pure PAZO films as well as composites at controlled deposition rate. MnO<sub>2</sub> nanofibers, PPy and PPy coated MWCNT have been prepared for application in electrodes of ECs. BT has been used as a new dopant for chemical polymerization of PPy and new dispersant for MWCNT. The use of BT as a dopant and dispersant allowed for the fabrication of PPy coated MWCNT by a simple on-step chemical method. PAZO exhibits unique adsorption on different materials due to the unique structure of this polymer. The aromatic anionic PAZO monomers, containing chelating salicylate ligands provided multiple adsorption sites for PAZO adsorption on MnO<sub>2</sub> nanofibers, PPy, MWCNT and PPy coated MWCNT and allowed for their efficient electrosteric dispersion and EPD. Composite films have been prepared by EPD using PAZO as a co-dispersant for different materials. MnO<sub>2</sub> nanofibers, MWCNT, PPy nanoparticles, PPy coated MWCNT and composites, deposited

by EPD have been utilized for energy storage in electrodes of ECs. Testing results showed beneficial effect of PAZO for the dispersion and EPD of advanced ES materials. The results of this investigation paved the way for EPD of other composites utilizing properties of different functional materials and unique physical properties of PAZO.

Yangshuai Liu has the major contribution to this work, Dr. Igor Zhitomirsky also contributes to this work, and Kaiyuan Shi has contribution on TEM characterization to this work.

## References

- [1] L.M. Goldenberg, V. Lisinetskii, A. Ryabchun, A. Bobrovsky, S. Schrader, Influence of the cation type on the DFB lasing performance of dye-doped azobenzene-containing polyelectrolytes, *Journal of Materials Chemistry C*, 2 (2014) 8546-8553.
- [2] S.A. Maaland, R. Cai, T. Fulghum, R.C. Advincula, Adsorption of Fabrication Azobenzene Layer-by-Layer Film using Photoisomerization, *Polymer Preprints*, 49 (2008) 990.
- [3] N. Li, J. Lu, H. Li, E.-T. Kang, Nonlinear optical properties and memory effects of the azo polymers carrying different substituents, *Dyes and Pigments*, 88 (2011) 18-24.
- [4] C. Madruga, P.A. Filho, M.M. Andrade, M. Goncalves, M. Raposo, P.A. Ribeiro, Birefringence dynamics of poly{1-[4-(3-carboxy-4-hydroxyphenylazo)benzenesulfonamido]-1,2-ethanediyl, sodium salt} cast films, *Thin Solid Films*, 519 (2011) 8191-8196.
- [5] Q. Ferreira, P.J. Gomes, M. Raposo, J. Giacometti, O.N. Oliveira, P.A. Ribeiro, Influence of ionic interactions on the photoinduced birefringence of Poly [1-[4-(3-Carboxy-4 Hydroxyphenylazo) benzene sulfonamido]-1, 2-ethanediyl, sodium salt] films, *Journal of Nanoscience and Nanotechnology*, 7 (2007) 2659-2666.
- [6] M.S. Ata, Y. Liu, I. Zhitomirsky, A review of new methods of surface chemical modification, dispersion and electrophoretic deposition of metal oxide particles, *RSC Advances*, 4 (2014) 22716-22732.
- [7] I. Zhitomirsky, Cathodic electrodeposition of ceramic and organoceramic materials. Fundamental aspects, *Advances in Colloid and Interface Science*, 97 (2002) 277-315.

- [8] X. Pang, T. Casagrande, I. Zhitomirsky, Electrophoretic deposition of hydroxyapatite-CaSiO<sub>3</sub>-chitosan composite coatings, *Journal of Colloid and Interface Science*, 330 (2009) 323-329.
- [9] Q. Ferreira, P.A. Ribeiro, O.N. Oliveira Jr, M. Raposo, Long-term stability at high temperatures for birefringence in PAZO/PAH Layer-by-Layer films, *ACS applied materials & interfaces*, 4 (2012) 1470-1477.
- [10] I.A. Jankovic, Z.V. Saponjic, M.I. Comor, J.M. Nedeljkovic, Surface Modification of Colloidal TiO<sub>2</sub> Nanoparticles with Bidentate Benzene Derivatives, *The Journal of Physical Chemistry C*, 113 (2009) 12645-12652.
- [11] H.-J. Kim, K. Lee, S. Kumar, J. Kim, Dynamic sequential layer-by-layer deposition method for fast and region-selective multilayer thin film fabrication, *Langmuir*, 21 (2005) 8532-8538.
- [12] T.J. Lane, W.R. Fletcher, M.V. Gormally, M.S. Johal, Dual-beam polarization interferometry resolves mechanistic aspects of polyelectrolyte adsorption, *Langmuir*, 24 (2008) 10633-10636.
- [13] P.J. Kett, M.T. Casford, A.Y. Yang, T.J. Lane, M.S. Johal, P.B. Davies, Structural changes in a polyelectrolyte multilayer assembly investigated by reflection absorption infrared spectroscopy and sum frequency generation spectroscopy, *The Journal of Physical Chemistry B*, 113 (2009) 1559-1568.
- [14] K. Shi, I. Zhitomirsky, Electrophoretic nanotechnology of graphene-carbon nanotube and graphene-polypyrrole nanofiber composites for electrochemical supercapacitors, *Journal of Colloid and Interface Science*, 407 (2013) 474-481.

[15] Y. Liu, K. Shi, I. Zhitomirsky, Azopolymer triggered electrophoretic deposition of MnO<sub>2</sub>-carbon nanotube composites and polypyrrole coated carbon nanotubes for supercapacitors, *Journal of Materials Chemistry A*, 3 (2015) 16486-16494.

# Chapter 9 Fabrication and testing of asymmetric devices based on manganese dioxide positive electrode and iron oxide negative electrode formed by EPD on rGO

## 9.1 Synthesis of materials and current collectors

EPD method has been utilized for the fabrication of asymmetric devices, containing manganese dioxide positive electrode and iron oxide negative electrode. It is known from the literature that EPD method offers many processing advantages for the fabrication of films at high deposition rate[1-7]. The method allows for uniform deposition on high surface area substrates. Fig.9.1 shows a schematic of the device, containing individual electrodes, which were prepared by EPD on rGO and separated by a porous membrane.

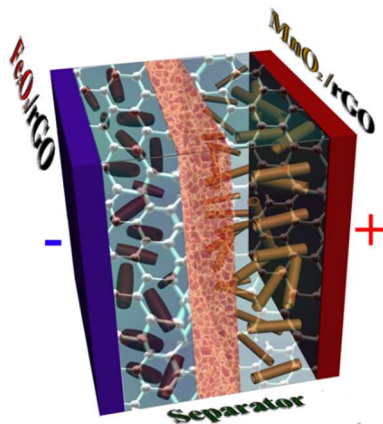


Fig. 9.1 Schematic of asymmetric supercapacitor composed by a  $\text{MnO}_2$ -rGO positive electrode and a  $\text{Fe}_2\text{O}_3$ -rGO negative electrode

Fig.9.2A. shows X-ray diffraction pattern of MnO<sub>2</sub>, prepared by the hydrothermal synthesis method. The X-ray diffraction pattern exhibits peaks, corresponding to JCPDS file 44-01041 of MnO<sub>2</sub>. The SEM image in Fig.9.2B shows that MnO<sub>2</sub> formed hollow nanotubes with typical diameters 70-150 nm. The fibrous structure of MnO<sub>2</sub> nanotubes was also confirmed by TEM studies (Fig.9.2C,D).

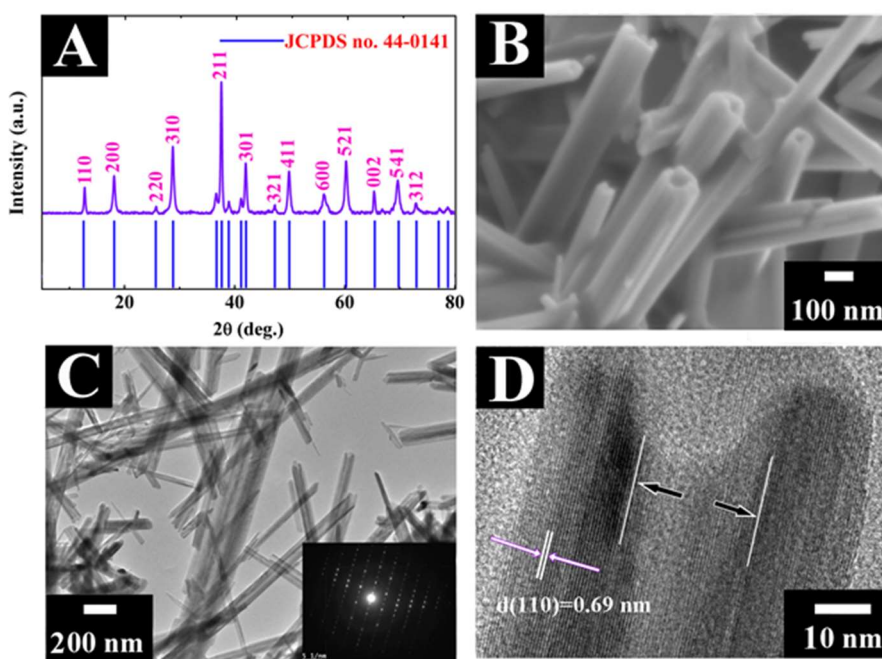


Fig. 9.2 (A) X-ray diffraction pattern, (B) SEM image, (C) TEM image, inset shows electron diffraction pattern and (D) high resolution TEM image of MnO<sub>2</sub> nanotubes, arrows show inner diameter.

The selected area electron diffraction pattern (Fig.9.2C, inset ) and high resolution TEM image (Fig.9.2D) confirmed crystallinity of the MnO<sub>2</sub> nanotubes, which had typical inner diameter of 25-50 nm (Fig.9.2D).

The XRD studies of iron oxide powders, prepared by the hydrothermal method, showed diffraction peaks, corresponding to the JCPDS file 33-0664 (Fig.9.3A) of  $\text{Fe}_2\text{O}_3$ . The SEM studies showed that  $\text{Fe}_2\text{O}_3$  particles exhibited a nanotube morphology with typical diameter lower than 100nm.

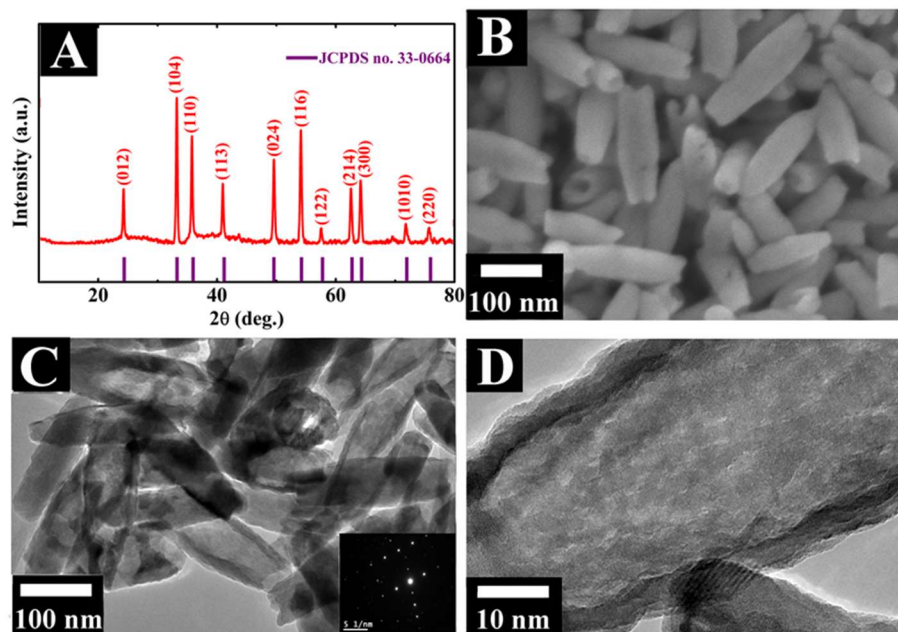


Fig. 9.3 (A) X-ray diffraction pattern, (B) SEM image, (C) TEM image, inset shows electron diffraction pattern and (D) high resolution TEM image of  $\text{Fe}_2\text{O}_3$  nanotubes.

The  $\text{Fe}_2\text{O}_3$  nanotubes (Fig.9.3B) had a typical aspect ratio of 5-8, which was significantly lower, than that of  $\text{MnO}_2$  nanotubes (Fig.2B,C). The SEM and TEM images (Fig.9.3 B-D) showed that the nanotubes had a non-uniform diameter, which decreased from the middle part to the end of the nanotubes. The thickness of the walls of the nanotubes was about 4-5 nm. The selected area electron diffraction pattern (Fig.9.3C, inset) confirmed the crystallinity of the nanotubes.

The dispersion of  $\text{MnO}_2$  and  $\text{Fe}_2\text{O}_3$  nanotubes in a mixed water-ethanol (75%) ethanol solvent was achieved using PAZO, as a dispersant. The chemical structure of PAZO includes aromatic monomers, containing chelating salicylate ligands (Fig.9.4A). The chelating salicylate ligands provided multiple adsorption sites for adsorption of PAZO on nanotubes (Fig.9.4B,C). Moreover, the salicylate ligands imparted a charge for the electrosteric particle stabilization in the suspensions.

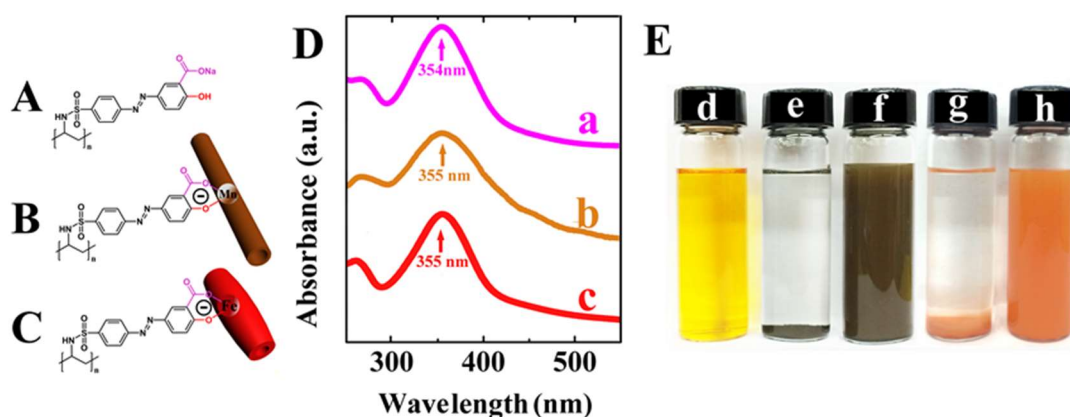


Fig. 9.4 (A) Molecular structure of PAZO, (B) and (C) schematic of adsorption of PAZO on  $\text{MnO}_2$  and  $\text{Fe}_2\text{O}_3$  nanotubes, respectively, involving the complexation of a Mn and Fe atoms with a salicylate ligand of a PAZO monomer; (D) UV-Vis data for (a) pure PAZO, and deposits prepared from  $2 \text{ g L}^{-1}$  suspensions of (b)  $\text{MnO}_2$ , (c)  $\text{Fe}_2\text{O}_3$ , containing  $0.5 \text{ g L}^{-1}$  PAZO at a deposition voltage of 20 V in 25% water and 75% ethanol; E(d)  $0.5 \text{ g L}^{-1}$  PAZO solution, and suspensions of (e)  $2 \text{ g L}^{-1}$   $\text{MnO}_2$ , (f)  $2 \text{ g L}^{-1}$   $\text{MnO}_2$  and  $0.5 \text{ g L}^{-1}$  PAZO, (g)  $2 \text{ g L}^{-1}$   $\text{Fe}_2\text{O}_3$  and (h)  $2 \text{ g L}^{-1}$   $\text{Fe}_2\text{O}_3$  and  $0.5 \text{ g L}^{-1}$  PAZO.

The adsorption of PAZO on  $\text{MnO}_2$  and  $\text{Fe}_2\text{O}_3$  nanotubes was confirmed in EPD experiments, which showed that adsorbed PAZO imparted charge and allowed for the

anodic deposition of the nanotubes. The comparison of the UV-Vis spectra for the pure PAZO and deposited materials confirmed the adsorption of PAZO on the nanotubes. The spectrum of pure PAZO showed absorption peak at 354 nm (Fig.9.4D). The similar absorptions were observed in the spectra of the deposited materials at 355 nm (Fig.9.4D). The adsorption of PAZO on the nanotubes allowed the formation of stable suspensions, as shown in Fig.9.4E. The EPD method allowed for the deposition on various conductive substrates, such as stainless steel, platinum, graphite. Of particular interest is the deposition of nanotubes on rGO, which offers benefits of high surface area and porosity. Fig.9.5 (A-E) shows images of rGO, prepared in this investigation. The prepared rGO aerogel showed a porous microstructure. The XRD analysis confirmed the formation of rGO from GO. The XRD patterns are in agreement with the literature data [8].

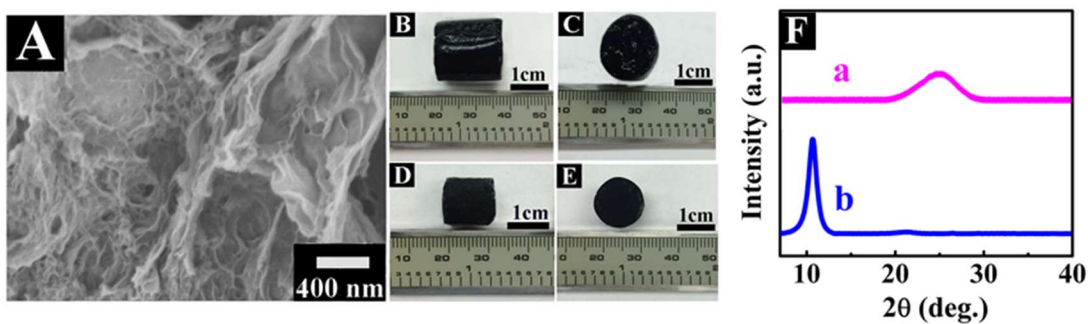


Fig. 9.5 (A) SEM image of rGO after freeze drying; (B), (C) are lateral and plan view of as-prepared rGO hydrogel before freeze drying; (D), (E) are lateral and plan view of rGO hydrogel after freeze drying; F(a) and (b) are X-ray diffraction pattern of as- prepared rGO and GO, respectively.

The thin ( $\sim 1$  mm) layers of rGO with mass of  $1 \text{ mg cm}^{-2}$  were used as substrates for EPD

of nanotubes.

## 9.2. Electrochemical testing of electrodes and devices

Fig.9.6 shows electrochemical testing results for the rGO before deposition. The rGO substrate showed capacitive behavior with nearly box shape CVs. The current increased with increasing scan rate indicating good capacitive behavior and good capacitance retention (Fig.9.6A). The highest capacitance of  $64 \text{ mF cm}^{-2}$  ( $64 \text{ F g}^{-1}$ ) was obtained at a scan rate of  $2 \text{ mV s}^{-1}$ . The capacitance decreased with increasing scan rate, showing good capacitance retention (Fig.9.6B). The capacitance, calculated from the impedance data (Fig.9.6C,D) showed relaxation type frequency dispersion, as indicated by the reduction in  $C'_s$  with frequency and a maximum in the frequency dependence of  $C''_s$ .

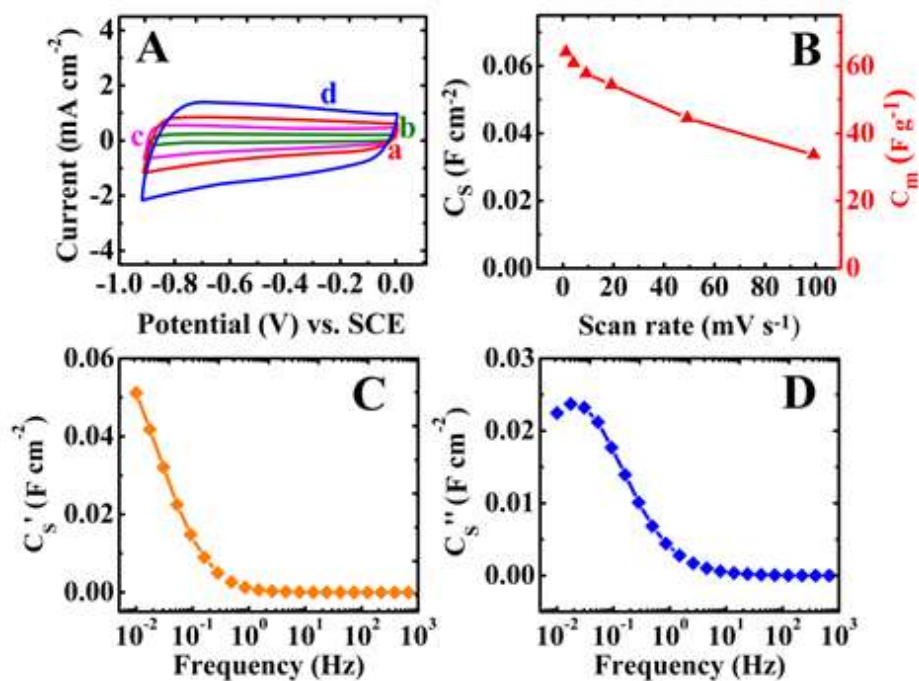


Fig. 9.6 (A) CVs for rGO electrode with mass loading of  $1 \text{ mg cm}^{-2}$ , at scan rates of (a) 2,

(b) 5, (c) 10 and (d) 20  $\text{mV s}^{-1}$  in 0.5 M aqueous  $\text{Na}_2\text{SO}_4$  electrolyte. (B)  $C_s$  and  $C_m$ , calculated from the CV data; (C)  $C'$  and (D)  $C''$  components of complex capacitance versus frequency.

Fig.9.7 compared SEM images of  $\text{MnO}_2$  deposits on stainless steel and rGO substrates. The SEM image of the deposit on stainless substrate shows a porous  $\text{MnO}_2$  network. The deposition on rGO resulted in impregnation of rGO with  $\text{MnO}_2$ .

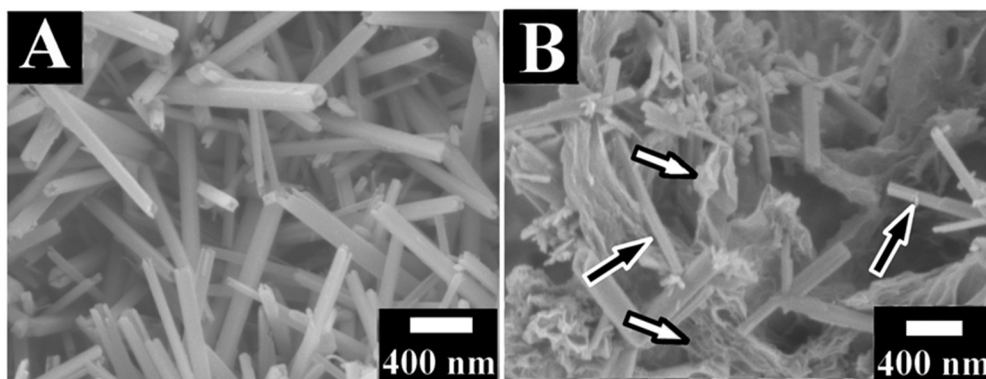


Fig. 9.7 SEM image of EPD of  $2 \text{ g L}^{-1} \text{ MnO}_2$  with  $0.5 \text{ g L}^{-1} \text{ PAZO}$  (A) onto stainless steel and (B) into rGO substrate (white arrows show rGO and black arrows show  $\text{MnO}_2$  tubes) under 10V for 5 min in 75% ethanol and 25% water.

The testing of the electrodes, formed on stainless steel by EPD showed box shape CVs, indicating nearly ideal capacitive behavior (Fig.9.8A). The highest capacitance of  $88 \text{ mFcm}^{-2}$  ( $88 \text{ F g}^{-1}$ ) was obtained (Fig.9.8B) at a scan rate of  $2 \text{ mVs}^{-1}$ . The capacitance decreased with increasing scan rate due to the diffusion limitation in pores. The analysis of the components of AC capacitance (Fig.9.8 C,D), derived from the impedance data, showed that real component of AC capacitance  $C'_s$  measured at low frequencies was

comparable with the capacitance, calculated from the CV data at low scan rates. The  $C'_s$  component decreased with frequency and  $C''_s$  showed a corresponding maximum, indicating a relaxation type dispersion.

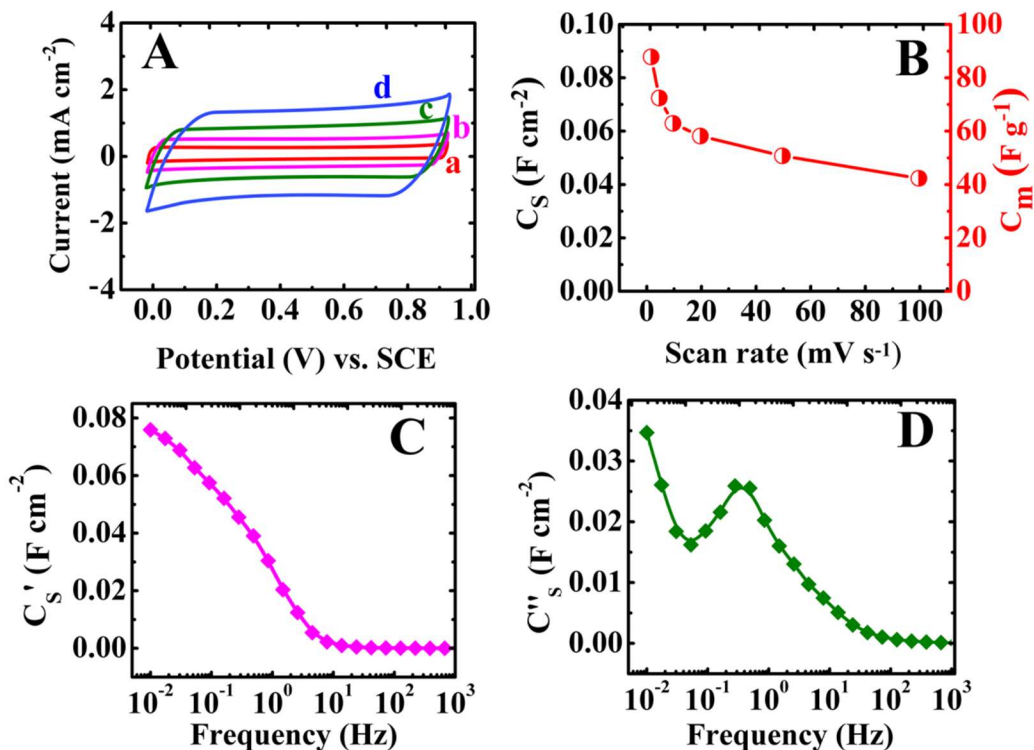


Fig. 9.8 (A) CVs for MnO<sub>2</sub> electrode prepared by EPD of 2 g L<sup>-1</sup> MnO<sub>2</sub> with 0.5 g L<sup>-1</sup> PAZO onto stainless steel with MnO<sub>2</sub> mass loading of 1 mg cm<sup>-2</sup>, at scan rates of (a) 2, (b) 5, (c) 10 and (d) 20 mV s<sup>-1</sup> in 0.5 M aqueous Na<sub>2</sub>SO<sub>4</sub> electrolyte. (B)  $C_s$  and  $C_m$ , calculated from the CV data; (C)  $C'_s$  and (D)  $C''_s$  components of complex capacitance versus frequency.

The use of rGO substrate allowed for significant improvement in capacitive behavior of the MnO<sub>2</sub> electrodes. The electrodes showed nearly ideal box shape CVs (Fig.9.9A) and a

significant current increase with increasing scan rate, indicating good capacitive behavior at high charge-discharge rates. The highest capacitance (Fig.9.9B) of  $274 \text{ mF cm}^{-2}$  ( $137 \text{ F g}^{-1}$ ) was achieved at a scan rate of  $2 \text{ mV s}^{-1}$ . The capacitance retention at  $100 \text{ mV s}^{-1}$  was

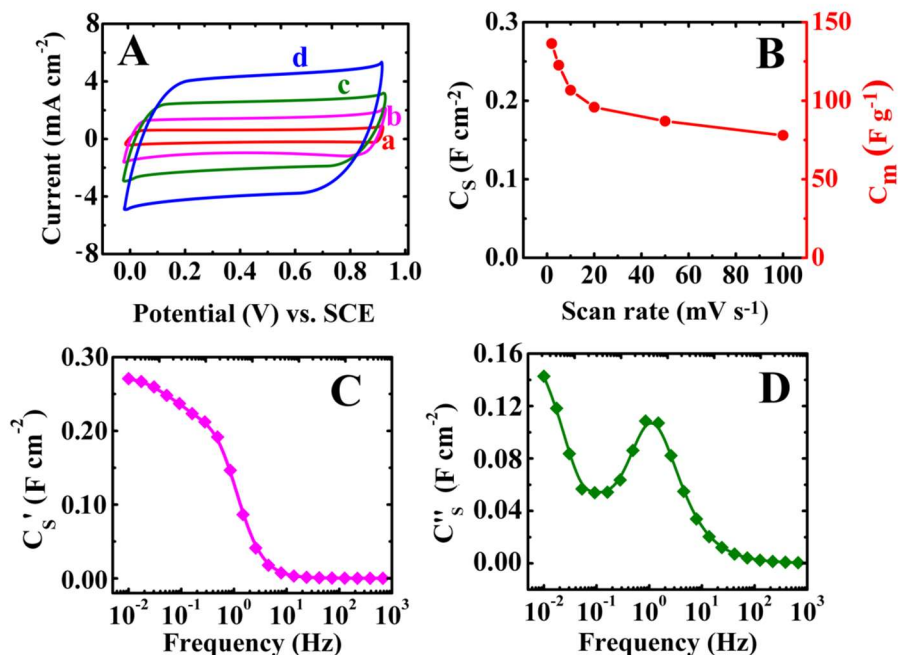


Fig. 9.9 (A) CVs for  $\text{MnO}_2$  electrode prepared by EPD of  $2 \text{ g L}^{-1}$   $\text{MnO}_2$  with  $0.5 \text{ g L}^{-1}$  PAZO into rGO with total mass loading of  $2 \text{ mg cm}^{-2}$ , at scan rates of (a) 2, (b) 5, (c) 10 and (d)  $20 \text{ mV s}^{-1}$  in  $0.5 \text{ M}$  aqueous  $\text{Na}_2\text{SO}_4$  electrolyte. (B)  $C_s$  and  $C_m$ , calculated from the CV data; (C)  $C'$  and (D)  $C''$  components of complex capacitance versus frequency.

above 50%. It is important to note that the capacitance of  $274 \text{ mF cm}^{-2}$  of  $1 \text{ mg cm}^{-2}$   $\text{MnO}_2$ , deposited on  $1 \text{ mg cm}^{-2}$  rGO is significantly higher than the sum of capacitances of  $1 \text{ mg cm}^{-2}$  rGO and  $1 \text{ mg cm}^{-2}$   $\text{MnO}_2$  deposited on stainless steel. Therefore, improved utilization of capacitive properties of  $\text{MnO}_2$  was achieved using rGO substrates. The gravimetric capacitance of the electrodes, normalized by the total mass of the active

material and substrate was found to be  $137 \text{ F g}^{-1}$ . This value is significantly higher than the gravimetric capacitance ( $88 \text{ F g}^{-1}$ ) of the  $\text{MnO}_2$  electrode formed on the stainless steel, calculated using mass of the active material only. Taking into account that the mass of stainless steel current collector is  $55.6 \text{ mg cm}^{-2}$ , the gravimetric capacitance of the  $\text{MnO}_2$  electrodes on stainless steel, normalized by the total mass of the active materials and current collector, is only  $1.55 \text{ F g}^{-1}$ .

The analysis of the frequency dependences of components of AC capacitance (Fig.9.9C,D) showed relatively high relaxation frequency, indicating good capacitance retention at high charge-discharge rates in agreement with the CV data (Fig.9.9 A,B).

Fig.9.10 shows SEM images of the  $\text{Fe}_2\text{O}_3$  particles deposited on stainless steel and rGO substrates. The  $\text{Fe}_2\text{O}_3$  particles formed a porous layer on the stainless steel, whereas the particles impregnated the rGO substrate.

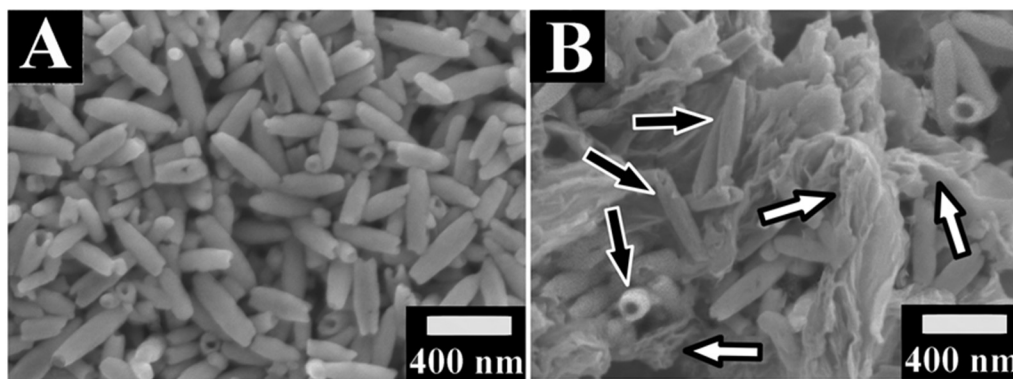


Fig. 9.10 SEM image of EPD of  $2 \text{ g L}^{-1} \text{ Fe}_2\text{O}_3$  with  $0.5 \text{ g L}^{-1} \text{ PAZO}$  (A) onto stainless steel and (B) into rGO substrate (white arrows show rGO and black arrows show  $\text{Fe}_2\text{O}_3$  tubes) under 10V for 5 min in 75% ethanol and 25% water.

Fig.9.11 shows testing results for the  $\text{Fe}_2\text{O}_3$  electrode on stainless steel current collector. The CVs (Fig.9.11 A) show good capacitive behavior in the negative potential range. The highest capacitance of  $89 \text{ mF cm}^{-2}$  was obtained at a scan rate of  $2 \text{ mV s}^{-1}$ . The gravimetric capacitances normalized by active material mass and total mass of active material and current collector were  $89 \text{ F g}^{-1}$  and  $1.57 \text{ F g}^{-1}$ , respectively.

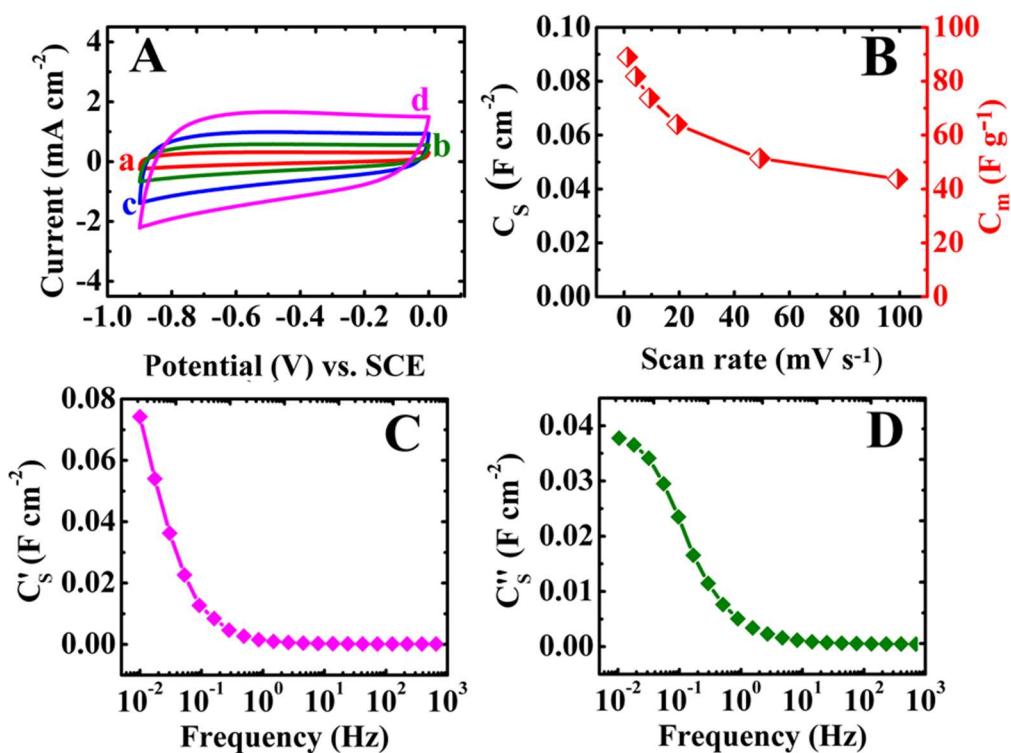


Fig. 9.11 (A) CVs for  $\text{Fe}_2\text{O}_3$  electrode prepared by EPD of  $2 \text{ g L}^{-1}$   $\text{Fe}_2\text{O}_3$  with  $0.5 \text{ g L}^{-1}$  PAZO onto stainless steel with  $\text{Fe}_2\text{O}_3$  mass loading of  $1 \text{ mg cm}^{-2}$ , at scan rates of (a) 2, (b) 5, (c) 10 and (d) 20  $\text{mV s}^{-1}$  in 0.5 M aqueous  $\text{Na}_2\text{SO}_4$  electrolyte. (B)  $C_s$  and  $C_m$ , calculated from the CV data; (C)  $C'$  and (D)  $C''$  components of complex capacitance versus frequency.

The capacitance decreased with increasing scan rate due to the diffusion limitation in pores (Fig.9.11B). The frequency dependencies showed relaxation type dispersion. The relaxation maximum was not observed at frequencies above 10 mHz, indicating poor capacitance retention with increasing frequency (Fig.9.11C,D).

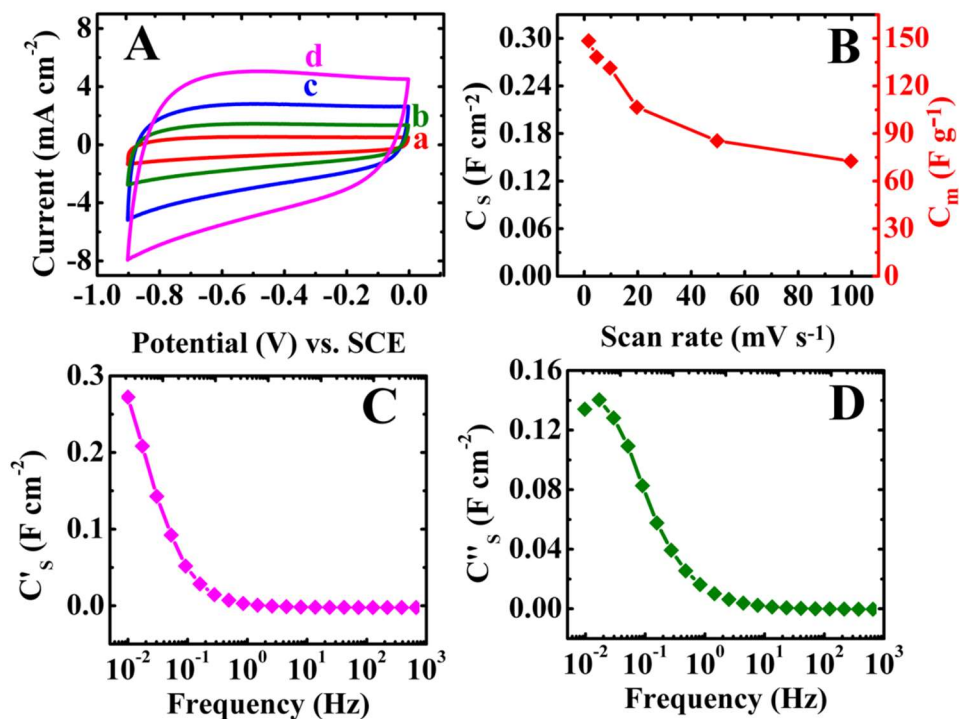


Fig. 9.12 (A) CVs for Fe<sub>2</sub>O<sub>3</sub> electrode prepared by EPD of 2 g L<sup>-1</sup> Fe<sub>2</sub>O<sub>3</sub> with 0.5 g L<sup>-1</sup> PAZO into rGO with total mass loading of 2 mg cm<sup>-2</sup>, at scan rates of (a) 2, (b) 5, (c) 10 and (d) 20 mV s<sup>-1</sup> in 0.5 M aqueous Na<sub>2</sub>SO<sub>4</sub> electrolyte. (B) C<sub>s</sub> and C<sub>m</sub>, calculated from the CV data; (C) C' and (D) C'' components of complex capacitance versus frequency.

The testing of the electrodes with a similar active mass loading, deposited on the rGO substrates showed significant increase in current and CV areas (Fig.9.12A). The specific capacitance of 286 mF cm<sup>-2</sup> was obtained at a scan rate of 2 mV s<sup>-1</sup>. The gravimetric

capacitance, normalized by the total mass of active material and current collector was found to be  $143 \text{ F g}^{-1}$ . Therefore, the use of rGO allows significant improvement of utilization of capacitive properties of the active material. Of particular importance is good capacitive performance achieved at low current collector mass and high mass ratio of active material to current collector. The capacitance retention of above 50% was obtained at a scan rate of  $100 \text{ mV s}^{-1}$ .

The frequency dependences of the components of complex AC capacitance (Fig.9.12 C,D) showed improvement in the capacitance retention with increasing frequency, compared to the electrodes formed using stainless steel current collector.

The  $\text{MnO}_2$  and  $\text{Fe}_2\text{O}_3$  electrodes formed on the rGO current collectors were used for the fabrication of asymmetric device. The asymmetric device showed box shape CVs in a voltage window of 1.8V (Fig.9.13A). The increase in scan rate resulted in increasing current, indicating good capacitive behavior. The device showed a capacitance of  $152 \text{ mF cm}^{-2}$  ( $38 \text{ F g}^{-1}$ ). The capacitance decreased with increasing scan rate due to the diffusion limitation in pores of electrodes and membrane (Fig.9.13B). The frequency dependence of the components of the complex capacitance (Fig.9.13C,D), calculated from the impedance data showed relaxation type dispersion, as indicated by the decrease in  $C'_s$  with frequency increase and corresponding maximum in the frequency dependence of  $C''_s$ . The relatively high relaxation frequency indicates good capacitance retention.

The impedance data for different electrodes are summarized in Nyquist plots, presented in Fig.9.14. It is seen that the deposits obtained on stainless steel substrates showed higher

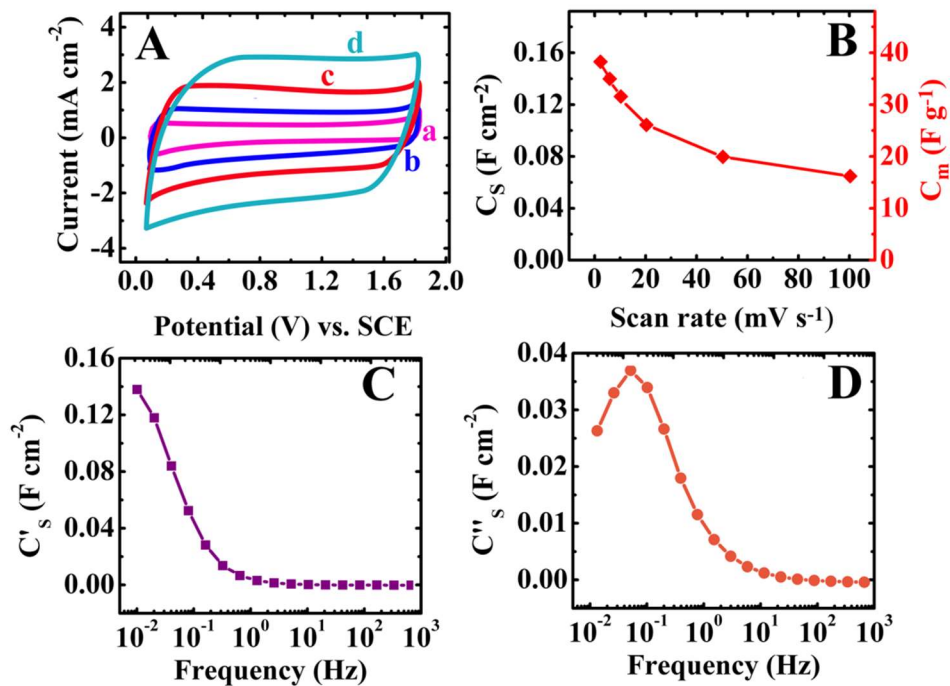


Fig. 9.13 (A) CVs for asymmetric device composed by EPD of 2 g L<sup>-1</sup> MnO<sub>2</sub> as positive electrode and Fe<sub>2</sub>O<sub>3</sub> as negative electrode with 0.5 g L<sup>-1</sup> PAZO into rGO with total mass loading of 4 mg cm<sup>-2</sup>, at scan rates of (a) 2, (b) 5, (c) 10 and (d) 20 mV s<sup>-1</sup> in 0.5 M aqueous Na<sub>2</sub>SO<sub>4</sub> electrolyte. (B) C<sub>s</sub> and C<sub>m</sub>, calculated from the CV data; (C) C' and (D) C'' components of complex capacitance versus frequency.

real component of impedance, compared to the deposits obtained on rGO. As a result the device showed relatively low real component of impedance.

Fig.9.15A shows charge-discharge behavior of the electrodes at different current densities. The charge-discharge curves were of nearly triangular shape, indicating good Coulombic efficiency. The analysis of cyclic stability (Fig.9.15B) showed 90% capacitance retention after 1000 cycles.

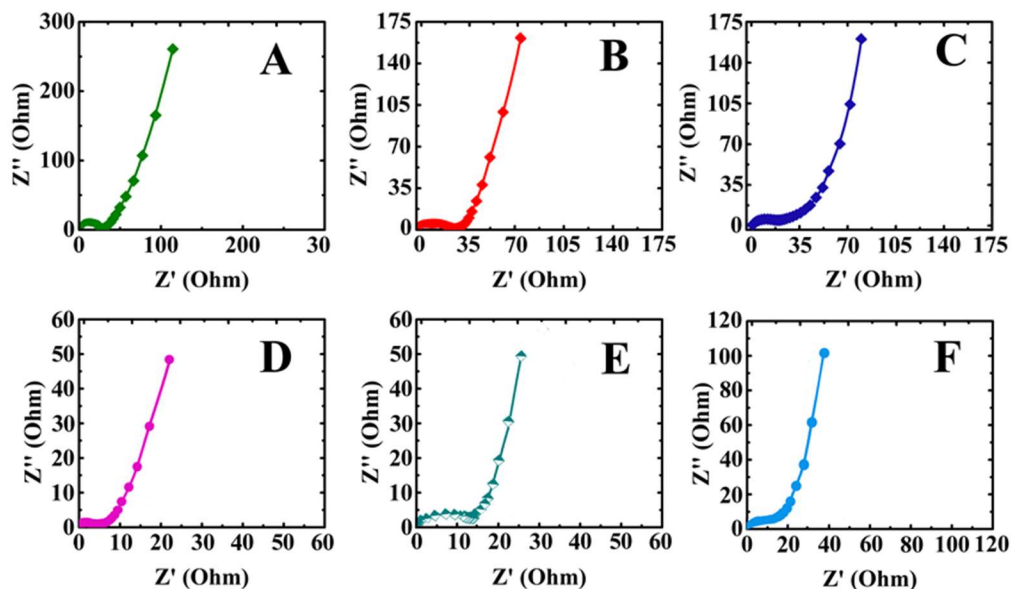


Fig. 9.14 Impedance data for (A) pure rGO, (B) pure MnO<sub>2</sub> nanotubes on stainless steel, (C) pure Fe<sub>2</sub>O<sub>3</sub> nanotubes on stainless steel, (D) MnO<sub>2</sub>- rGO, (E) Fe<sub>2</sub>O<sub>3</sub>-rGO and (F) asymmetric device.

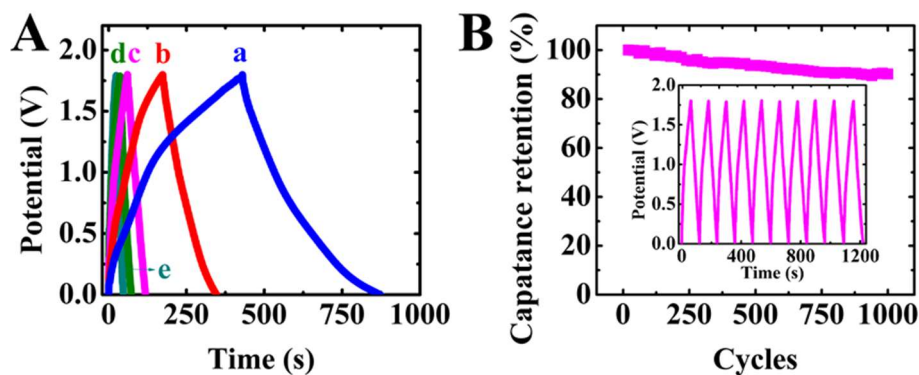


Fig. 9.15 (A) Galvanostatic charge-discharge behavior of an asymmetric coin cell at currents of (a) 0.5, (b) 1, (c) 3, (d) 4 and (e) 5 mA, (B) capacitance retention versus cycle number for an asymmetric coin cell, inset shows multiple charge-discharge cycles at a constant current of 3 mA.

### 9.3 Conclusions

MnO<sub>2</sub> and Fe<sub>2</sub>O<sub>3</sub> nanotubes were prepared by hydrothermal methods. The rGO aerogels were prepared and used as current collectors. The use of PAZO allowed excellent dispersion and anodic EPD of MnO<sub>2</sub> and Fe<sub>2</sub>O<sub>3</sub> nanotubes. The use of rGO aerogels allowed improved performance of the electrodes prepared by EPD. Good electrochemical performance was achieved at high active mass to current collector mass ratio. The asymmetric devices showed good electrochemical performance in a voltage window of 1.8 V and capacitance of 152 mF cm<sup>-2</sup>. The devices showed capacitance retention of 90 % after 1000 cycles.

Yangshuai Liu and Dan Luo have the major and equal contributions to this work, Dan Luo has contribution on rGO fabrication, Dr. Igor Zhitomirsky also contributes to this work, Kaiyuan Shi has contribution on TEM characterization and Tianshi Zhang has contribution on XRD characterization to this work.

## References

- [1] I. Zhitomirsky, Cathodic Electrodeposition of Ceramic and Organoceramic Materials. Fundamental Aspects, *Advances in Colloid and Interface Science*, 97 (2002) 277-315.
- [2] S.A. Hasan, D.W. Kavich, S.V. Mahajan, J.H. Dickerson, Electrophoretic deposition of CdSe nanocrystal films onto dielectric polymer thin films, *Thin Solid Films*, 517 (2009) 2665-2669.
- [3] S. Somarajan, S.A. Hasan, C.T. Adkins, E. Harth, J.H. Dickerson, Controlled electrophoretic deposition of uniquely nanostructured star polymer films, *Journal of Physical Chemistry B*, 112 (2008) 23-28.
- [4] E.A. Olevsky, X. Wang, A. Maximenko, M.A. Meyers, Fabrication of net-shape functionally graded composites by electrophoretic deposition and sintering: Modeling and experimentation, *Journal of the American Ceramic Society*, 90 (2007) 3047-3056.
- [5] H. Mazor, D. Golodnitsky, L. Burstein, A. Gladkich, E. Peled, Electrophoretic deposition of lithium iron phosphate cathode for thin-film 3D-microbatteries, *Journal of Power Sources*, 198 (2012) 264-272.
- [6] I. Zhitomirsky, A. Petric, Electrophoretic deposition of ceramic materials for fuel cell applications, *Journal of the European Ceramic Society*, 20 (2000) 2055-2061.
- [7] I. Zhitomirsky, A. Petric, Electrophoretic deposition of electrolyte materials for solid oxide fuel cells, *Journal of Materials Science*, 39 (2004) 825-831.
- [8] Z. Bo, X. Shuai, K. Cen, S. Mao, H. Yang, J. Qian, J. Chen, J. Yan, Green preparation of reduced graphene oxide for sensing and energy storage applications, *Scientific Reports*, 4 (2014), doi:10.1038/srep04684.

## Chapter 10 Functional properties of PAZO and fabrication of composites using PAZO as an universal dispersing agent

### 10.1 PAZO as universal dispersant for optics and supercapacitor application

In this investigation we demonstrate the possibility of EPD of PAZO films, and propose a deposition mechanism. The PAZO films, prepared by EPD, exhibited a photo-induced birefringence. The unique adsorption and film forming properties of PAZO allowed for the dispersion and EPD of various materials. Therefore, the use of PAZO allowed the fabrication of composites, combining capacitive properties of materials deposited using PAZO, and functional properties of PAZO and other co-deposited materials.

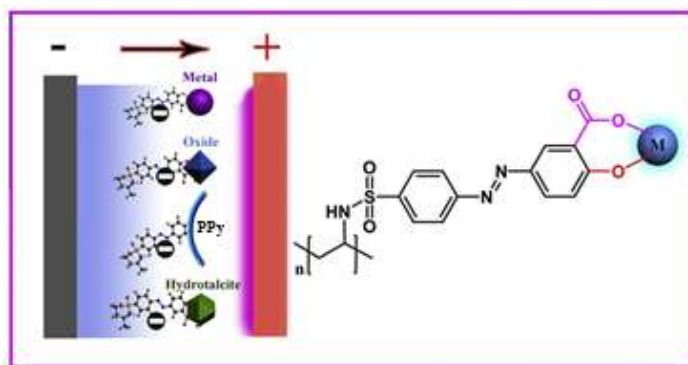


Fig. 10.1 Schematic of EPD for different materials using PAZO as dispersant

As Fig. 10.1 shows, we demonstrate that various functional materials of different types and composites can be deposited using PAZO as a dispersing, charging and film forming agent. This versatility is a unique feature of PAZO and addresses the limitation of other

common dispersing agents, that they are only capable of dispersing a few specific materials for EPD. The results of this investigation pave the way for the deposition of composite films utilizing the functional properties of different materials and PAZO. To this end, we investigated optical, charge storage, electrochemical and other properties of the composite films.

## 10.2 EPD of PAZO thin films from different solvents

In this investigation the EPD of PAZO films in different solvents has been compared. It was found that anodic films can be obtained from 0.05-1.0 g L<sup>-1</sup> PAZO solutions in methanol or ethanol-water solvent. The deposition mechanism involved the electrophoresis of negatively charged PAZO macromolecules, containing anionic COO<sup>-</sup> groups (Fig. 10.2 A(a)), toward the anode and their accumulation at the anode surface. The electrochemical decomposition of methanol[1] or water[2] in anodic reactions resulted in H<sup>+</sup> generation and a local pH decrease at the anode. The charge neutralization of COO<sup>-</sup> groups of PAZO:



at the anode surface promoted deposit formation. It is important to note that in this investigation a soluble salt of PAZO (PAZO-Na) was used for deposition. It is known[3] that the addition of acid to the PAZO-Na solutions results in the precipitation of the insoluble acidic form of this polymer (PAZO-H). Therefore, it is suggested that the low solubility of the acidic form of PAZO, which formed at the anode, was an important factor in the successful deposition of PAZO at the anode surface.

Fig. 10.2B shows QCM data for deposition yield measurements in dilute solutions. The deposit mass increased with increasing deposition time. Higher deposition yields were obtained from methanol solutions, compared to the deposition yields in ethanol-water solvent. The difference in the deposition yields can be attributed to different factors[2], such as electrode reactions, gas evolution at the electrode surface and dielectric constant of the solvent. Increasing the PAZO concentration in solution resulted in a significant increase in the deposition rate and allowed for the formation of relatively thick films. The films, prepared in different solvents showed photo-induced birefringence (Fig. 10.2C).

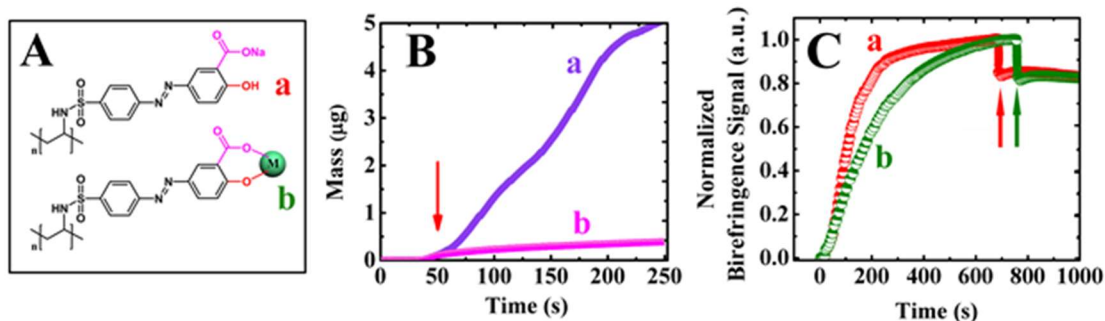


Fig. 10.2(A) (a) Structure of PAZO and (b) adsorption mechanism, involving complexation of salicylate ligands of PAZO with metal atom (M) on the particle surface, (B) time dependence of QCM mass gain during EPD from 0.1 g L<sup>-1</sup> PAZO solutions in (a) methanol and (b) ethanol-water solvent; arrow shows time, corresponding to application of cell voltage of 10V, (C) photoinduced birefringence for films prepared from 1 g L<sup>-1</sup> PAZO solutions in (a) methanol and (b) ethanol-water solvent, arrows show OFF times for writing laser.

The birefringence increased with time after application of the writing laser beam and then

showed saturation. The writing time[4], related to the birefringence buildup was comparable with that, reported for the PAZO films prepared in acidic conditions by LbL method[4]. It is known[4] that photoinduced birefringence of PAZO results from reversible *trans-cis-trans* photoisomerization of azo groups of this polymer and their orientation perpendicularly to the polarization direction of the writing beam. The films, prepared in methanol, showed lower writing time, compared to the films, prepared in a mixed water-ethanol solvent. The difference in the writing times can result from the difference in the microstructures of the films prepared in different conditions and other factors, discussed in the literature[4, 5]. The films showed residual birefringence after turning off the writing beam (Fig. 10.2C).

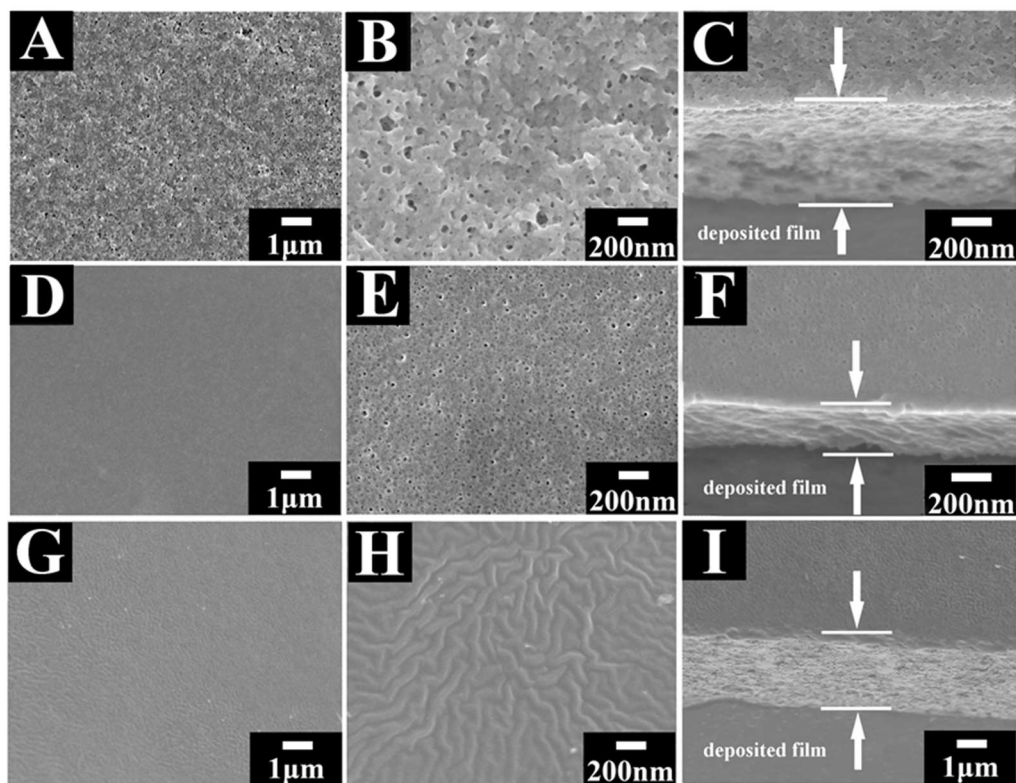


Fig. 10.3 SEM images of films, prepared from (A-F) 1 g L<sup>-1</sup> PAZO solutions and (G-I) 1

$\text{g L}^{-1}$  PAZO solutions, containing  $0.5 \text{ g L}^{-1}$  PVDM in (A-C) methanol and (D-I) ethanol-water solvent at a deposition voltage of 10 V and deposition time of 3 min, (A,B,D,E,G,H) – surfaces at different magnifications, (C,F,I) - cross sections.

Fig. 10.3(A-F) shows SEM images of the films prepared by EPD from  $1 \text{ g L}^{-1}$  PAZO solutions. The films were continuous and crack free. The film porosity can result from gas evolution during deposition or solvent evaporation during drying. The analysis of SEM images of films surfaces and cross sections (Fig. 10.3(A-F)) showed that films prepared from methanol exhibited larger porosity, compared to the films prepared using ethanol-water as the solvent.

EPD method overcomes the principal drawbacks of LbL assembly, where multiple time-consuming steps are required for the fabrication of relatively thin films, containing PAZO and, by necessity cationic polymers. In contrast, EPD allows for the fabrication of thin and thick films of pure PAZO at relatively high deposition rates. Fig. 10.3(A-F) indicates that the thick films were relatively uniform, because the uniformity of EPD films is controlled by the electric field[6]. A natural expansion of this work would be the application of EPD for the fabrication of thin film devices, utilizing photo-induced birefringence, optical memory, surface-relief grating, photochromic and other functional properties of PAZO.

The EPD method is not limited to the deposition of pure PAZO films. It was found that other polymers can be incorporated into the PAZO films. The addition of electrically neutral PVDM polymer to PAZO solutions resulted in co-deposition of both materials. The deposition yield from  $1 \text{ g L}^{-1}$  PAZO solutions, containing  $0.5 \text{ g L}^{-1}$  PVDM, was 4

times higher, compared to the deposition yield, obtained from pure  $1 \text{ g L}^{-1}$  PAZO solutions. SEM investigations showed that composite films were relatively dense, without porosity (Fig. 10.3G,H). The thickness of the composite films was significantly higher (Fig. 10.3I), compared to the films prepared from pure PAZO solutions (Fig.10.3C,F) at similar conditions, due to the higher deposition rate. It is important to note that no deposition was achieved from pure solutions of electrically neutral PVDM without PAZO. It is suggested that hydrophobic interactions of PVDM and PAZO in the solutions resulted in the formation of mixed charged polymer species and co-deposition of both polymers.

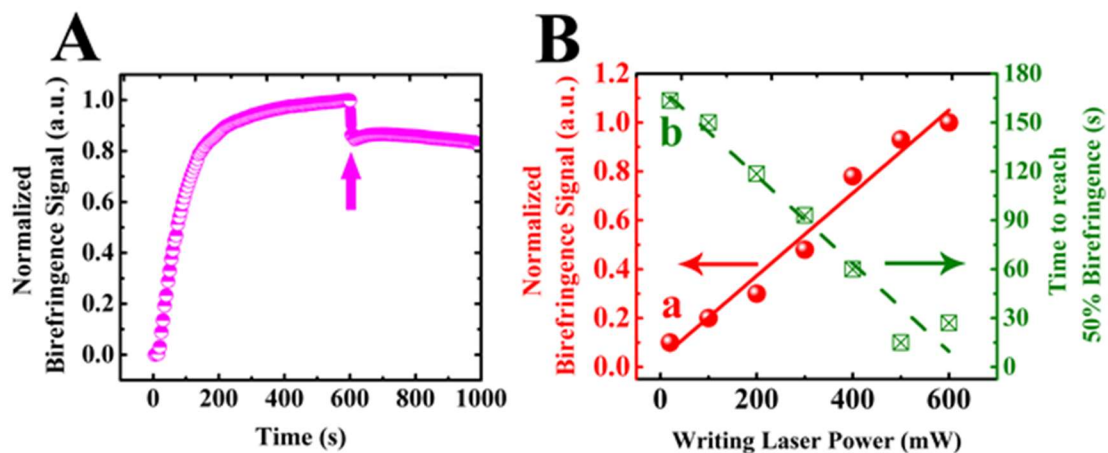


Fig. 10.4 (A) Photoinduced birefringence versus time, arrow shows OFF time for writing laser, (B) saturated birefringence and birefringence buildup time versus power of the writing laser for films, prepared from  $1 \text{ g L}^{-1}$  PAZO solutions in ethanol-water solvent, containing  $0.5 \text{ g L}^{-1}$  PVDM.

The composite films showed a photoinduced birefringence (Fig. 10.4). The birefringence

signal increased with time after application of writing laser beam and then the saturation was observed (Fig. 10.4A). The films showed a residual birefringence after the removal of the writing laser beam. Therefore, the birefringence properties of the composite films were similar to the properties of pure PAZO films. It is important to note that the birefringence behavior of pure PAZO and composite films was dependent on the writing laser power, as shown in the Fig. 10.4B. The birefringence signal increased and the time for birefringence buildup decreased with increasing laser power. A similar behavior was observed for the films, prepared by other methods[5].

### **10.3 Adsorption and phase characterization of different materials with PAZO**

The main challenge for the fabrication of composite deposits by EPD is charging and dispersion of particles. We found that PAZO exhibited remarkable adsorption on different materials and allowed for their dispersion, charging and EPD.

The pure PAZO and composite deposits were studied by FTIR and UV-Vis methods. Literature data[4] on FTIR studies of PAZO revealed differences in the spectra of the protonated and deprotonated forms of this polymer. The FTIR spectrum of the PAZO deposit, prepared by EPD (Fig. 10.5A(a)) was similar to the spectrum of the protonated form of PAZO[4]. The absorptions at 1680 and 1620  $\text{cm}^{-1}$  are attributed to the stretching vibrations[4, 7] of protonated COOH groups (Fig. 10.5A(a)). The adsorption at 1589  $\text{cm}^{-1}$  resulted from stretching C=O vibrations. Aromatic C—C/C=C vibrations[8] contributed to absorptions at 1488 and 1398  $\text{cm}^{-1}$ . The absorption at 1429  $\text{cm}^{-1}$  was attributed to N=N stretching[7]. The absorption at 1324  $\text{cm}^{-1}$  resulted from stretching S=O vibrations[7].

Similar adsorptions were observed in the FTIR spectra of composite deposits. Fig. 10.5(b-f) shows typical FTIR spectra of different materials, deposited by EPD, such as MnO<sub>2</sub>, aluminium hydroxide, Pd, PPy and MWCNT. The spectra contained peaks related to PAZO absorptions and indicated co-deposition of PAZO with materials of different types. The spectrum of MWCNT included a broad absorption centered at 1638 cm<sup>-1</sup>; this represents a combination of absorptions related to protonated COOH groups[4, 7] of PAZO and aromatic vibrations of MWCNT[8]. The UV-Vis spectrum of PAZO (Fig. 10.5B(a)) showed absorption at about 354 nm, which corresponds to the *trans*-azobenzene isomer  $\pi$ - $\pi^*$  and  $n$ - $\pi^*$  transitions associated with azo group[7, 9]. Similar absorptions were observed in the spectra of various deposited materials (Fig. 10.5B(b-f)). Therefore, the FTIR and UV spectra confirmed that the deposited materials contained adsorbed PAZO in acidic form, which is in agreement with the proposed deposition mechanism.

In addition to these efforts focused on EPD of inorganic materials, MWCNT and polymers we found that PAZO can be used for EPD of functional organic molecules. Fig. 10.5C shows UV-Vis spectrum of the deposit, which was prepared from PAZO solution, containing aurintricarboxylic acid ammonium salt (AT) dye. The broad absorption in the range of 300-380 nm represents a combination of absorption of AT dye at 310 nm[10] and PAZO absorption at ~354 nm, the additional absorption peak at ~ 530 nm was attributed to AT[10]. Therefore, the UV-Vis data confirmed co-deposition of PAZO and AT. It is expected that various dyes and other organic molecules can be incorporated into PAZO films by EPD. Recently PAZO films, containing various dyes were prepared by

the LbL method for application in light-sensitive and optical devices[11, 12]. However, there are difficulties in controlling the incorporation of the dyes into the multilayer structures, containing anionic PAZO and cationic polyelectrolytes. In contrast, EPD is a simple one-step technique, which allows for incorporation of dyes in the PAZO monolayers.

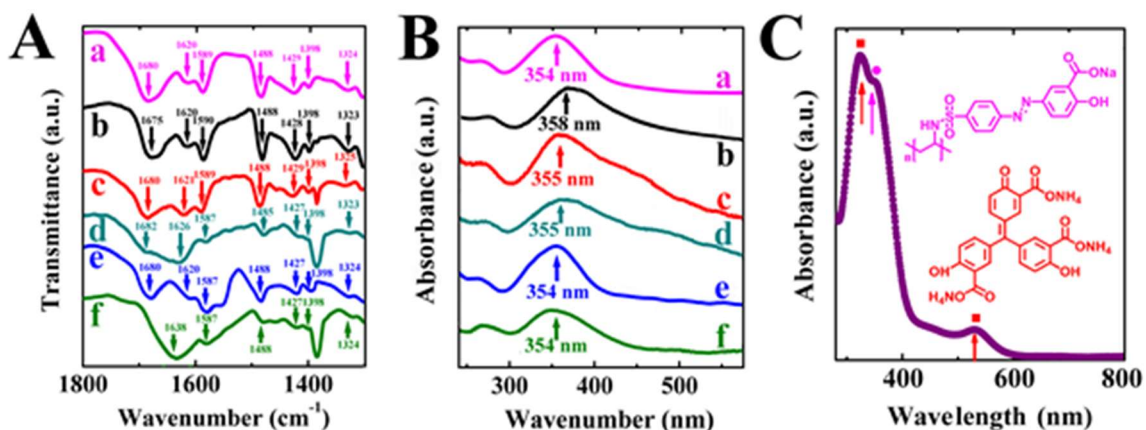


Fig. 10.5. (A) FTIR and (B) UV-Vis spectra for deposits, prepared from 1 g L<sup>-1</sup> PAZO solution in a mixed ethanol-water solvent: (a) without additives and containing 2 g L<sup>-1</sup> of (b) MnO<sub>2</sub>, (c) aluminium hydroxide, (d) Pd, (e) PPy nanofibers and (f) MWCNT, (C) UV-Vis spectrum of the deposit prepared from 1 g L<sup>-1</sup> PAZO solution, containing 1 g L<sup>-1</sup> AT dye (■ - absorption of AT, ● - absorption of PAZO).

The strong adsorption of PAZO on different materials offers exceptional benefits for EPD and other colloidal methods. The applications of other dispersing and charging agents are typically limited to a specific group of materials, such as oxides or carbon materials. Relatively little progress has been achieved in the EPD of metals and neutral polymers. It is suggested that the application of PAZO can address the limitations of other dispersants.

Moreover, in contrast to other dispersants, PAZO exhibits unique functional properties.

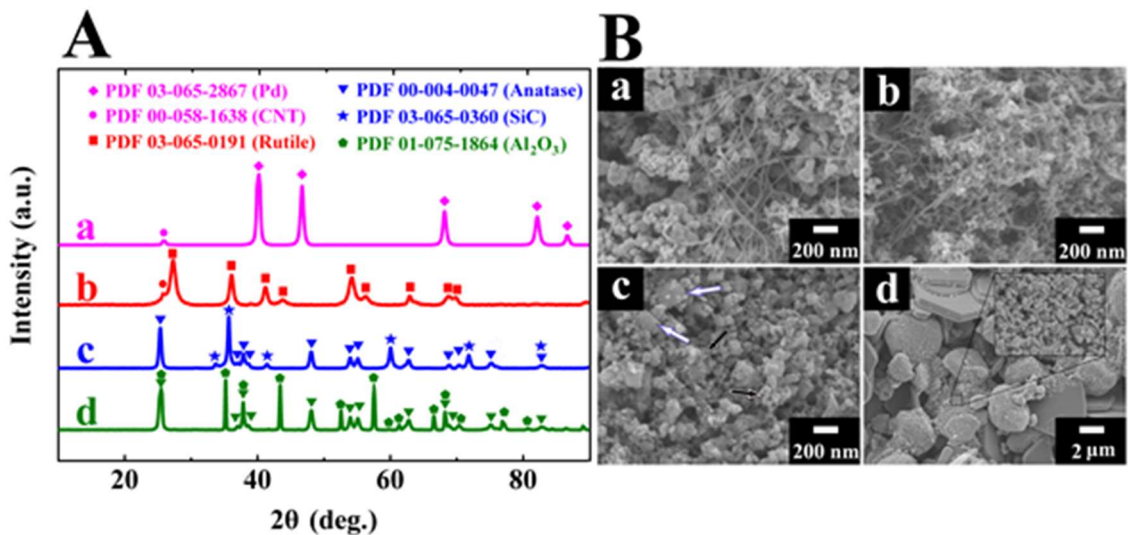


Fig. 10.6. (A) X-ray diffraction patterns and (B) corresponding SEM images of deposits, prepared from  $1 \text{ g L}^{-1}$  PAZO solution in a mixed ethanol-water solvent, containing (a)  $2 \text{ g L}^{-1}$  Pd and  $1 \text{ g L}^{-1}$  MWCNT, (b)  $2 \text{ g L}^{-1}$  TiO<sub>2</sub> rutile and  $1 \text{ g L}^{-1}$  MWCNT, (c)  $2 \text{ g L}^{-1}$  TiO<sub>2</sub> anatase and  $2 \text{ g L}^{-1}$  SiC, (d)  $2 \text{ g L}^{-1}$  TiO<sub>2</sub> anatase and  $2 \text{ g L}^{-1}$  alumina platelets, white arrows and black arrows in B(c) show SiC and TiO<sub>2</sub> anatase, respectively, inset in B(d) shows TiO<sub>2</sub> anatase.

The use of PAZO as a universal dispersing and charging agent opens the door to the fabrication of a large variety of composites. As a step in this direction we deposited composites, such as Pd - MWCNT, TiO<sub>2</sub> rutile - MWCNT, TiO<sub>2</sub> anatase - SiC, TiO<sub>2</sub> anatase - alumina platelets, using PAZO as a co-dispersant. The formation of composite materials was confirmed by X-ray diffraction analysis (Fig. 10.6A). The comparison of the X-ray diffraction patterns with the corresponding JCPDS files of the individual components showed the formation of composite films, containing two different materials.

Fig. 10.6B shows SEM images of the same composites, which contain two different types of materials in agreement with the XRD data. The SEM images presented in Fig. 10.6B(a,b) shows MWCNT and particles of (a) Pd metal and (b) Ti rutile. The SEM image in Fig. 10.6B(c) shows larger particles of SiC and smaller particles of TiO<sub>2</sub> anatase. The nanoparticles of TiO<sub>2</sub> anatase were accumulated in the voids between relatively large Al<sub>2</sub>O<sub>3</sub> platelets in Fig. 10.6B(d).

#### **10.4 Electrochemical characterization**

The deposited materials and composites can be used for many important applications. PAZO, metal oxides, SiC, MWCNT, Pd, PPy and aluminium hydroxide possess properties that makes them desirable materials for electronic, optical, catalytic, flame retardant, energy generation and storage applications. Composite films prepared by EPD can be used for energy storage in ECs. Fig. 10.7 compares the capacitive performance of pure PPy films and PPy-MWCNT composites. The composite PPy-MWCNT film showed larger CV area (Fig. 10.7A), when compared to the CV of pure PPy, indicating a higher capacitance. The integral capacitances were calculated from the CV data at different scan rates in the voltage window of 0.9 V. The results of these calculations are presented in Fig. 10.7B.

The composite material showed higher capacitance, compared to the capacitance of PPy. The analysis of the differential capacitance, measured at AC voltage of 5 mV at different frequencies (Fig.10.7 C,D), confirmed higher capacitance of the composite films. Therefore, PAZO can be used for the fabrication of composites with improved properties.

The possibility of co-deposition of capacitive and other functional materials can be used for the fabrication of multifunctional composites, utilizing functional properties of PAZO and c-deposited materials [13, 14].

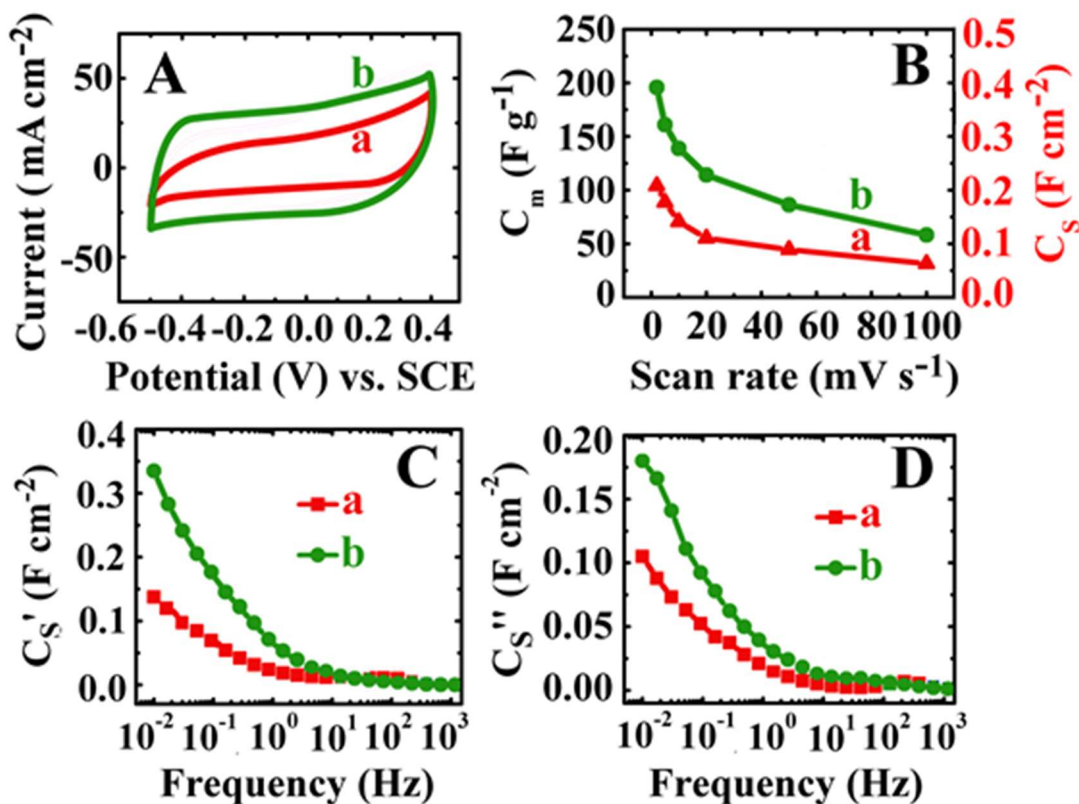


Fig. 10.7 (A) CVs at a scan rate of 20 mV s<sup>-1</sup>, (B) specific capacitance versus scan rate, (C) real and (D) imaginary components of AC capacitance, calculated from impedance data versus frequency for (a) PPy nanofibers and (b) PPy nanofibers(85%) – MWCNT(15%) composite deposits with active mass of 2 mg cm<sup>-2</sup>, prepared using PAZO.

### 10.5 Conclusion

PAZO films can be prepared from solutions in different solvents. The pure PAZO films and composite films showed photoinduced birefringence. It was found that PAZO can be

used as a universal charging, dispersing and film forming agent for EPD of a large variety of different materials, including individual and complex metal oxides, Pd metal, aluminium hydroxide, SiC, MWCNT, PPy and AT. PAZO showed superior performance compared to other dispersing agents for EPD technology, overcoming some of their limitations. It was found that the deposition rate, film microstructure and composition can be varied. The unique adsorption properties of PAZO allowed for EPD of composites, using PAZO as a co-dispersant for different materials. Testing results indicated that EPD methods can be used for the fabrication of films and coatings, utilizing the unique functional properties of PAZO and other functional materials.

Yangshuai Liu has the major contribution to this work, Dr. Igor Zhitomirsky also contributes to this work, Dan Luo and Tianshi Zhang have contribution on XRD characterization, Kaiyuan Shi, Patrick Wojtal and Cameron J. Wallar have contribution on SEM characterization, Qianli Ma, Eric Gusdave Daigle, Dr. Adrian Kitai and Changqing Xu have contribution on setting up the laser system for birefringence testing to this work.

## References

- [1] G. T. Burstein, C. J. Barnett, A. R. Kucernak, K. R. Williams, Aspects of the anodic oxidation of methanol, *Catalysis Today*, 38 (1997) 425-437.
- [2] I. Zhitomirsky, Cathodic electrodeposition of ceramic and organoceramic materials. fundamental aspects, *Advances in Colloid and Interface Science*, 97(2002) 277-315.
- [3] L. M. Goldenberg, V. Lisinetskii,; A. Ryabchun, A. Bobrovsky, S. Schrader, Influence of the cation type on the DFB lasing performance of dye-doped azobenzene-containing polyelectrolytes, *Journal of Materials Chemistry C*, 2 (2014) 8546-8553.
- [4] Q. Ferreira, P.J. Gomes, M. Raposo, J. Giacometti, O.N. Oliveira, P.A. Ribeiro, Influence of ionic interactions on the photoinduced birefringence of Poly [1-[4-(3-Carboxy-4 Hydroxyphenylazo) benzene sulfonamido]-1, 2-ethanediyl, sodium salt] films, *Journal of Nanoscience and Nanotechnology*, 7 (2007) 2659-2666.
- [5] C. Madruga, P.A. Filho, M.M. Andrade, M. Goncalves, M. Raposo, P.A. Ribeiro, Birefringence dynamics of poly{1-[4-(3-carboxy-4-hydroxyphenylazo)benzenesulfonamido]-1,2-ethanediyl, sodium salt} cast films, *Thin Solid Films*, 519 (2011) 8191-8196.
- [6] I. Zhitomirsky, Electrophoretic and electrolytic deposition of ceramic coatings on carbon fibers, *Journal of Europe Ceramic Society*, 18 (1998) 849-856.
- [7] Q. Ferreira, P.A. Ribeiro, O.N. Oliveira Jr, M. Raposo, Long-term stability at high temperatures for birefringence in PAZO/PAH Layer-by-Layer films, *ACS Applied Materials & Interface Sciences*, 4 (2012) 1470-1477.
- [8] K. Shi, I. Zhitomirsky, Electrophoretic nanotechnology of graphene-carbon

nanotube and graphene-polypyrrole nanofiber composites for electrochemical supercapacitors, *Journal of Colloid and interface Science*, 407 (2013) 474-481.

[9] Q. Ferreira, P.A. Ribeiro, M. Raposo, Villain's fractal growth of poly [1-[4-(3-carboxy-4-hydroxyphenylazo) benzenesulfonamido]-1, 2-ethanediyl, sodium salt] J-aggregates onto layer-by-layer films and its effect on film absorbance spectrum, *Journal of Applied Physics*, 113 (2013) 243-508.

[10] M. Mallah, M. Ghannadi Maragheh, A. Badiei, R. Habibzadeh Sbo, Novel functionalized mesopore of SBA-15 as prospective sorbent for praseodymium and lutetium, *Journal of Radioanal and Nuclear Chemistry*. 283 (2010) 597-601.

[11] R.C. Advincula, E. Fells, M.-k. Park, Molecularly ordered low molecular weight azobenzene dyes and polycation alternate multilayer films: Aggregation, layer order, and photoalignment, *Chemistry of Materials*, 13 (2001) 2870-2878.

[12] V.E. Campbell, P.A. Chiarelli, S. Kaur, M.S. Johal, Coadsorption of a polyanion and an azobenzene dye in self-assembled and spin-assembled polyelectrolyte multilayers, *Chemistry of Materials*, 17 (2005) 186-190.

[13] Y. Liu, D. Luo, T. Zhang, K. Shi, P. Wojtal, C. J. Wallar, Q. Ma, E. G. Daigle, A. Kitai, C.Xu, I. Zhitomirsky, Film deposition mechanisms and properties of optically active chelating polymer and composites, *Colloids and Surfaces A*, 487 (2015) 17-25.

[14] Y. Liu, D. Luo, M. S. Ata, T. Zhang, C.J. Wallar, I. Zhitomirsky, Universal dispersing agent for electrophoretic deposition of inorganic Materials with improved adsorption, triggered by chelating monomers, *Journal of Colloid and Interface Science*, 462 (2015) 1-8

# Chapter 11 Approach for dispersing MnO<sub>2</sub> using Celestine blue

## 11.1 Motivation of using Celestine blue

Celestine blue (CB) is a promising charging and dispersing agent for cathodic EPD of inorganic nanoparticles. Similar to DA, the structure of CB (Fig. 11.1) includes a catechol ligand, which can provide CB adsorption on inorganic nanoparticles. The relatively large size of the CB molecules, compared to that of DA, is beneficial for the electrosteric dispersion. The proof-of-concept results presented below indicated that particle charging can be achieved by the dissociation of CB in the solutions and adsorption of cationic CB on the particle surface. The difficulties related to the protonation of DA molecules or self-polymerization of DA can be avoided. Moreover, we demonstrate that CB can be used for the dispersion and EPD of various materials with advanced properties and fabrication of composites.

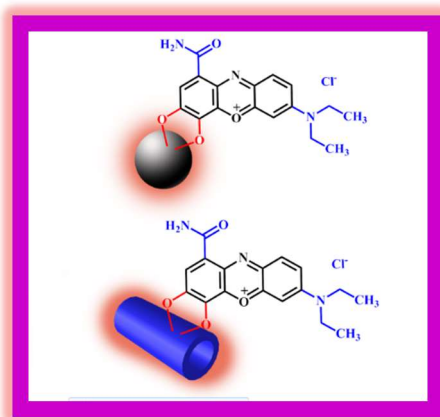


Fig. 11.1 Chemical structure of Celestine blue (adsorption on ceramic particles)

## 11.2 Materials synthesis & morphology characterization

The procedure for the fabrication of MnO<sub>2</sub> was based on that described in a previous investigation[1]. The MnO<sub>2</sub> powder, prepared by this method[1] contained mainly amorphous phase with a small amount of birnessite (JCPDS file 80-1098), which was converted to the cryptomelane (JCPDS file 44-1386) phase after annealing at 300°C during 2h. In contrast to the previous investigation, the solution was ultrasonicated during the reaction in order to avoid the agglomeration of MnO<sub>2</sub> particles. The formation of non-agglomerated particles was confirmed by transmission electron microscopy (TEM) investigations. Typical TEM images at different magnifications are shown in Fig. 11.2. The low magnification image indicated that ultrasonic agitation was beneficial in order to avoid particle agglomeration (Fig. 11.2A). This is in contrast to the results of the previous investigations[1], which showed agglomeration of the primary particles. The typical size of the primary particles (Fig. 11.2B) was in the range of 50-100 nm in agreement with the results of the previous investigation[1].

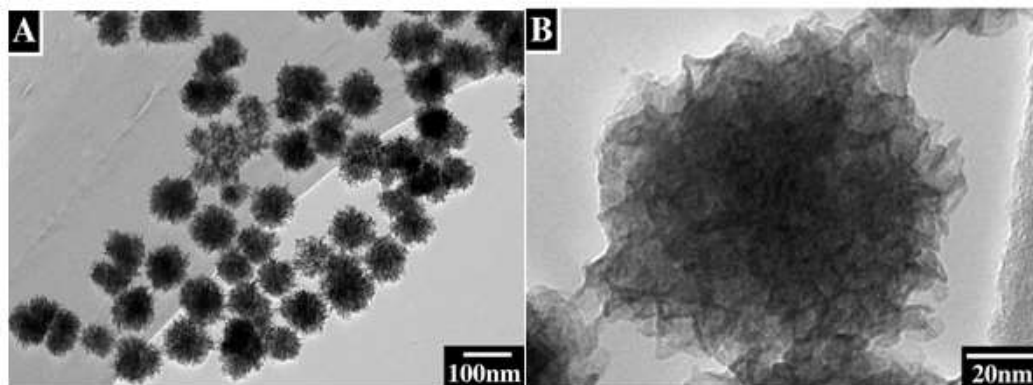


Fig. 11.2 (A,B) TEM images of MnO<sub>2</sub> particles at different magnifications

The procedure for the fabrication of  $\text{Mn}_3\text{O}_4$  nanoparticles involved slow addition of 15 ml of  $\text{NH}_4\text{OH}$  solution to 100 ml of aqueous 0.1M  $\text{Mn}(\text{NO}_3)_2$  solution at a temperature of  $60^\circ\text{C}$ . Then 1 mL of  $\text{H}_2\text{O}_2$  was added to the mixture and stirring was continued during 1h at  $60^\circ\text{C}$ . The precipitate was washed and dried at  $60^\circ\text{C}$ . The typical particle size was about 20-50 nm (Fig.11.3).

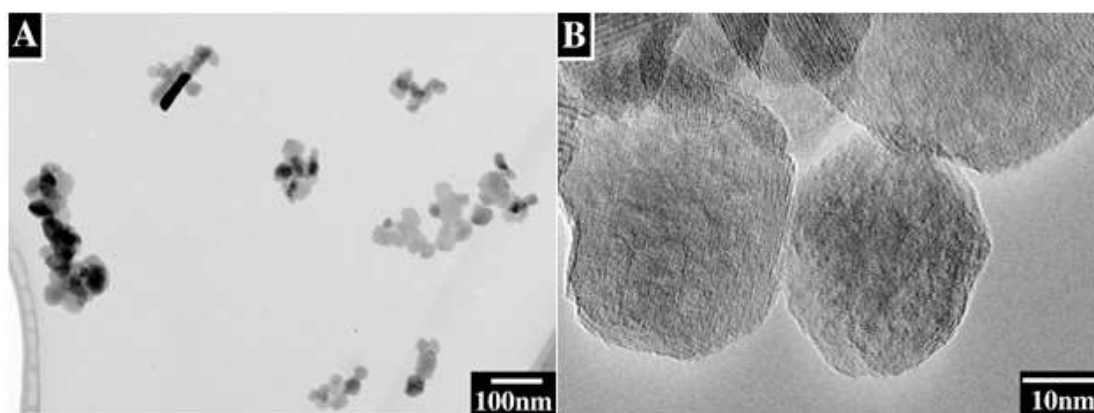


Fig. 11.3 (A,B) TEM images of  $\text{Mn}_3\text{O}_4$  particles at different magnifications

### 11.3 EPD and Adsorption mechanism

The suspensions of  $\text{MnO}_2$ ,  $\text{Mn}_3\text{O}_4$ ,  $\text{TiO}_2$  and  $\text{BaTiO}_3$  particles in ethanol were unstable and showed rapid sedimentation after the ultrasonic agitation. No EPD was achieved from such suspensions. In contrast, the addition of CB allowed the formation of stable suspensions and cathodic deposits were obtained at a deposition voltage of 20 V.

The influence of charging additives on the electrokinetic behavior of oxide particles is usually analyzed on the basis of zeta-potential measurements. However, the concept of zeta potential has been developed for rigid particles[2]. The use of this concept for the analysis of oxide particles, containing adsorbed large organic molecules, presents

difficulties[2, 3]. Therefore, in this investigation the influence of CB on the EPD of various oxide particles was analyzed on the basis of the deposition yield measurements.

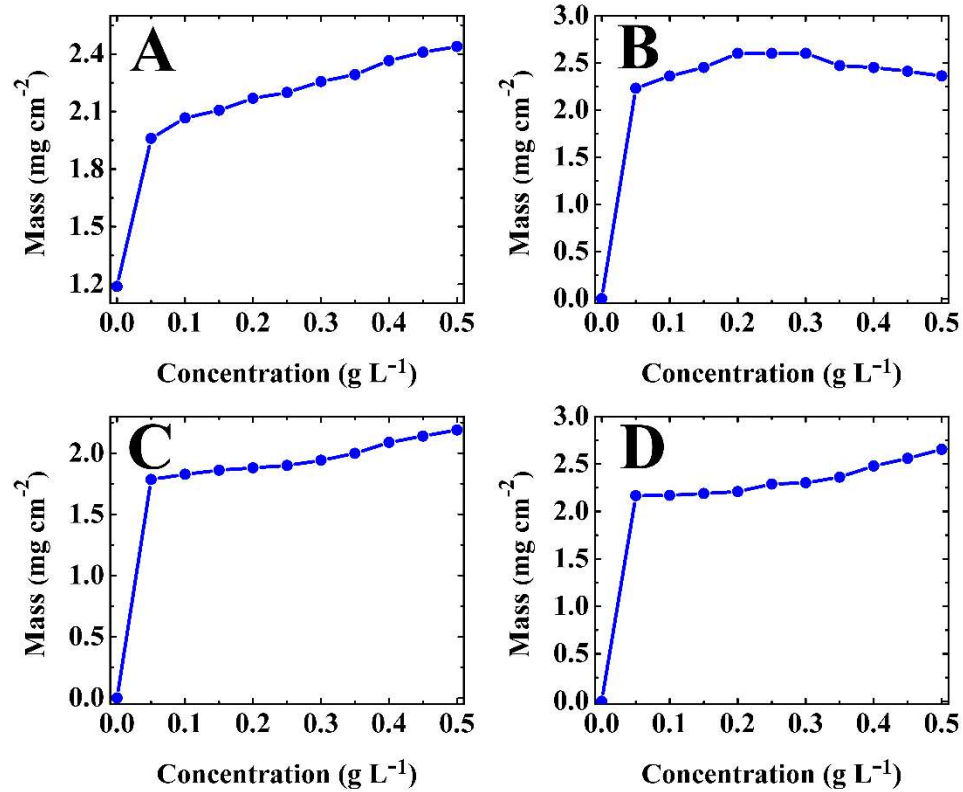


Fig.11.4 Deposit mass versus CB concentration in 4 g L<sup>-1</sup> suspensions of (A) MnO<sub>2</sub>, (B) Mn<sub>3</sub>O<sub>4</sub>, (C) TiO<sub>2</sub> and (D) BaTiO<sub>3</sub> at a deposition voltage of 20V and deposition time of 5 min.

Fig. 11.4 shows the influence of CB concentration on the deposition yield for MnO<sub>2</sub>, Mn<sub>3</sub>O<sub>4</sub>, TiO<sub>2</sub> and BaTiO<sub>3</sub> suspensions. Significant increase in the deposition yield was observed (Fig. 11.4) with increasing CB concentration in the range of 0-0.1 g L<sup>-1</sup> and then the deposition yield increased gradually at higher CB concentrations. It is suggested that the addition of CB to the solutions resulted in CB adsorption on the oxide particles.

Similar to other materials from the catechol family[4], the CB adsorption involves bidentate bridging bonding or bidentate chelating bonding. The adsorbed CB provided suspension stability and imparted a positive charge to the particles for cathodic EPD. However, we cannot exclude a possibility that the suspensions also included free, non-adsorbed CB. The high deposition rate obtained at low CB concentration indicated that CB efficiently adsorbed on the oxide particles and the amount of free CB in the suspensions was very low.

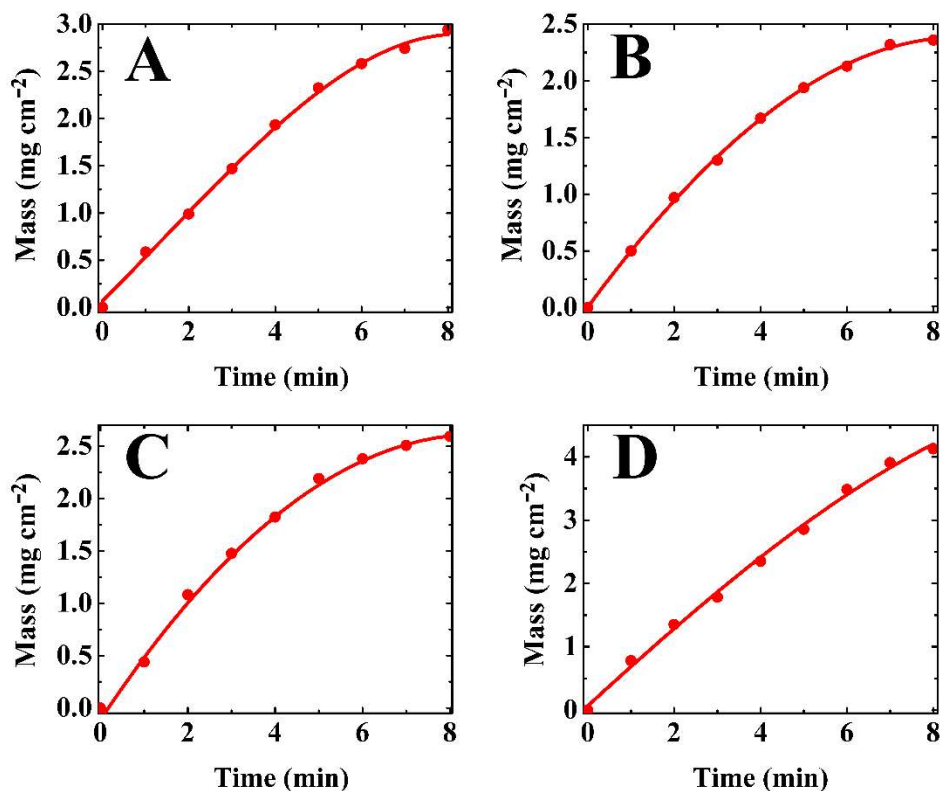


Fig. 11.5. Deposit mass versus deposition time for  $4 \text{ g L}^{-1}$  suspensions of (A)  $\text{MnO}_2$ , (B)  $\text{Mn}_3\text{O}_4$ , (C)  $\text{TiO}_2$  and (D)  $\text{BaTiO}_3$ , containing  $0.5 \text{ g L}^{-1}$  CB at a deposition voltage of 20V.

As pointed out above, non-adsorbed dispersing agent is detrimental for the suspension

stabilization. Moreover, non-adsorbed charged dispersant can be accumulated at the electrode surface during EPD due to electromigration. In this case, accumulated dispersant prevents deposit formation. The results indicated that CB is a promising charging agent for the EPD of materials. The deposition yield increased with increasing deposition time at a constant CB concentration and constant voltage (Fig.11.5). The decrease in the deposition rate with time is related to the decreasing electric field in the suspension due to the increasing voltage drop in the growing films.

#### 11.4 Morphology and adsorption characterization

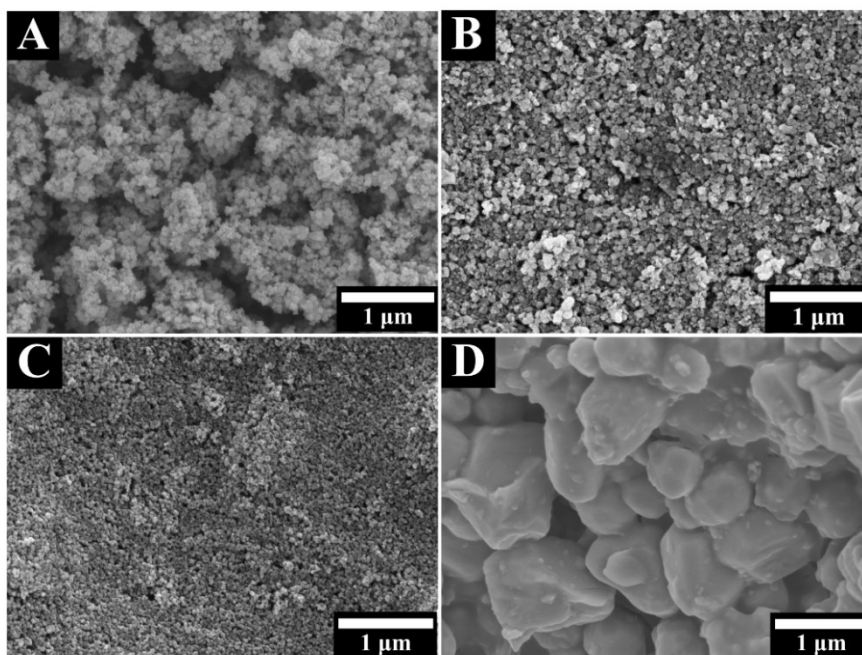


Fig. 11.6 SEM images of films, prepared from 4 g L<sup>-1</sup> suspensions of (A) MnO<sub>2</sub>, (B) Mn<sub>3</sub>O<sub>4</sub>, (C) TiO<sub>2</sub> and (D) BaTiO<sub>3</sub>, containing 0.5 g L<sup>-1</sup> CB at a deposition voltage of 20V.

Fig.11.6 shows typical SEM images of the films, prepared by EPD. The films of MnO<sub>2</sub>, Mn<sub>3</sub>O<sub>4</sub> and TiO<sub>2</sub> contained nanoparticles. The BaTiO<sub>3</sub> films contained larger particles in

agreement with the particle size data provided by the manufacturer. The porosity of the films can be attributed to gas evolution and packing of the particles. In order to confirm the CB adsorption on the particle surface, the deposits were removed from the substrates and investigated by FTIR and UV-Vis methods.

Fig.11.7A shows the FTIR spectra of the  $\text{MnO}_2$ ,  $\text{Mn}_3\text{O}_4$ ,  $\text{TiO}_2$  and  $\text{BaTiO}_3$  deposits. The absorptions in the range of  $1625\text{--}1627\text{ cm}^{-1}$ ,  $1567\text{--}1571\text{ cm}^{-1}$ ,  $1442\text{--}1443\text{ cm}^{-1}$  and  $1390\text{--}1400$  (Fig. 11.7A(a-d)) were attributed to stretching vibrations of the aromatic ring  $\nu(\text{C}\text{--}\text{C})$  and  $\nu(\text{C}=\text{C})$ [4-6] of adsorbed CB. The absorption in the range of  $1344\text{--}1346$  were attributed to stretching  $\nu(\text{C}\text{--}\text{N})$  and  $\nu(\text{C}=\text{N})$  vibrations[7] of CB. The broad absorptions in the UV-Vis spectra in the range of  $622\text{--}625\text{ nm}$  (Fig.11.7B(a-d)) were related to adsorbed CB[8]. Therefore, the FTIR and UV-Vis data confirmed that deposited ceramic particles contained adsorbed CB.

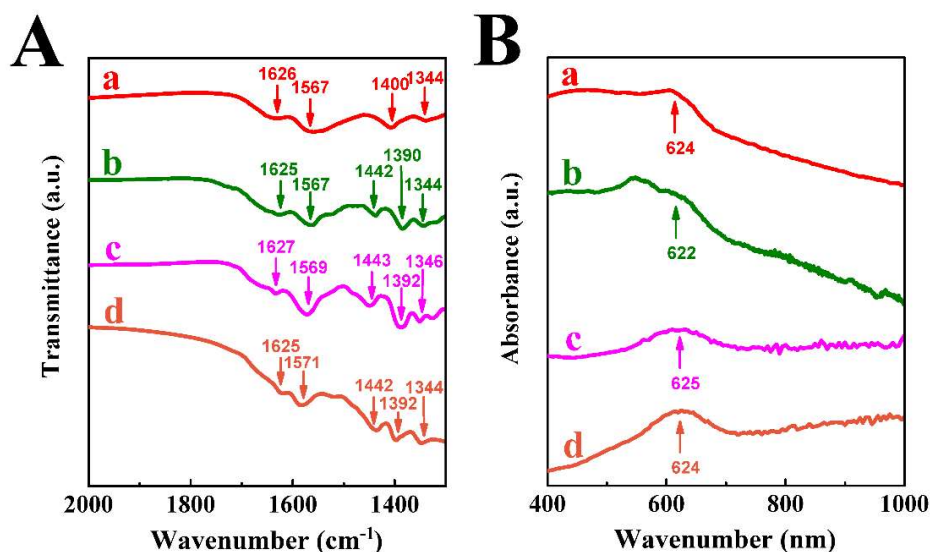


Figure. 11.7 (A) FTIR and (B)UV-Vis data for deposits, prepared from  $4\text{ g L}^{-1}$  suspensions of (a)  $\text{MnO}_2$ , (b)  $\text{Mn}_3\text{O}_4$ , (c)  $\text{TiO}_2$  and (d)  $\text{BaTiO}_3$ , containing  $0.5\text{ g L}^{-1}$  CB at

a deposition voltage of 20V.

The QCM data presented in Fig. 11.8 provide additional evidence of strong CB adsorption on  $\text{MnO}_2$ . The mass gain of gold coated quartz resonator, containing a  $\text{MnO}_2$  film, was observed after injection of CB into the solvent. The mass gain increased with time, showing a gradual decrease of the adsorption rate.

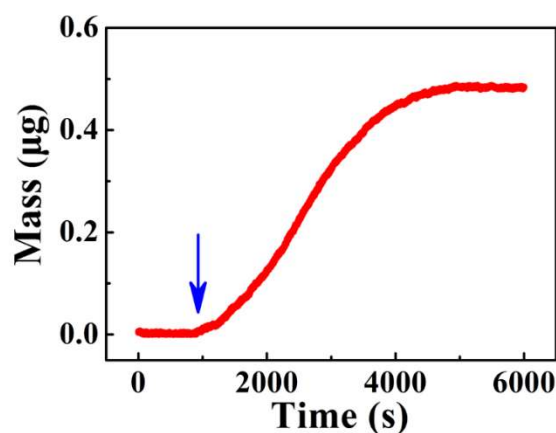


Fig. 11.8 Mass gain, measured using QCM for the  $\text{MnO}_2$  film deposited on a gold coated quartz crystal versus time after the injection of CB. Arrow shows injection time.

The possibility of EPD of different materials using CB as a charging and dispersing agent paved the way for the fabrication of composites. Fig. 11.9 shows SEM images and XRD patterns of the composites, prepared from the mixed suspensions, containing  $\text{TiO}_2$  and other materials, such as  $\text{MnO}_2$ , halloysite nanotubes and  $\text{BaTiO}_3$ . The  $\text{TiO}_2$ - $\text{MnO}_2$  composite contained nanoparticles of both materials (Fig. 11.9A), the corresponding XRD pattern (Fig. 11.9D(a)) showed peaks of  $\text{TiO}_2$  and  $\text{MnO}_2$  phases. The SEM image of  $\text{TiO}_2$ -HNT composite (Fig. 11.9B) showed nanoparticles of  $\text{TiO}_2$  and HNT, the corresponding XRD pattern (Fig. 11.9D(b)) included peaks of both phases. The SEM

image of TiO<sub>2</sub>-BaTiO<sub>3</sub> composite (Fig. 11.9C) showed nanoparticles of TiO<sub>2</sub> and larger BaTiO<sub>3</sub> particles, the XRD peaks of both materials were observed in the corresponding XRD pattern (Fig. 11. 9D(c)). Therefore, various composites can be obtained using CB as a co-dispersant for different materials.

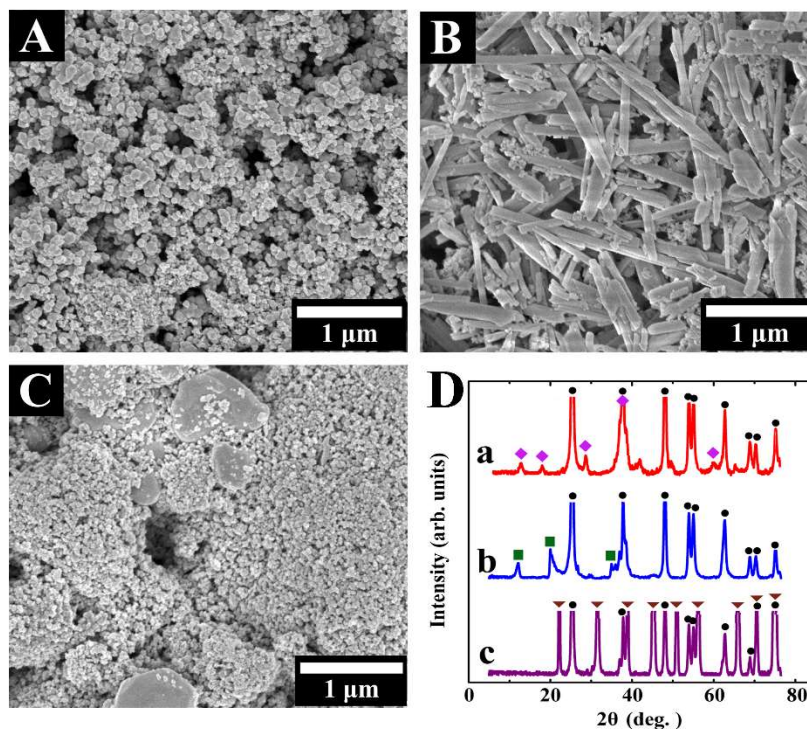


Fig. 11.9 (A,B,C) SEM images of films and (D) corresponding X-ray diffraction patterns for films, prepared from mixed suspensions, containing 2 g L<sup>-1</sup> TiO<sub>2</sub> and (A), (D (a)) 2 g L<sup>-1</sup> MnO<sub>2</sub>, (B), (D(b)) 2 g L<sup>-1</sup> halloysite and (C), (D(c)) BaTiO<sub>3</sub> at a deposition voltage of 20 V (●- JCPDS file 21-1272, ◆-JCPDS file 44-1386, ■-JCPDS file 29-1487, ▼-JCPDS file 5-0626)

The experimental results, discussed above indicated that the use of CB as a charging and dispersing agent allowed EPD of various materials and composites. In this approach,

many problems related to the application of EPD for nanotechnology can be addressed. It is known that the application of electric field to the suspensions of nanoparticles or stirring of the suspensions can result in the particle agglomeration and sedimentation[9]. Previous investigations showed that the fabrication of colloidal dispersions of MnO<sub>2</sub> nanoparticles with concentration above 1 mM presents difficulties[10] due to the high surface energy of the MnO<sub>2</sub> nanoparticles, which promotes their agglomeration and sedimentation. However, significantly higher concentrations of the nanoparticles are necessary for practical applications in EPD and other colloidal methods. Such problems can be successfully addressed by the use of CB. Nanoparticles of TiO<sub>2</sub>, MnO<sub>2</sub>, Mn<sub>3</sub>O<sub>4</sub> (Fig. 11.4-11.6) were successfully deposited by adding CB to the suspensions.

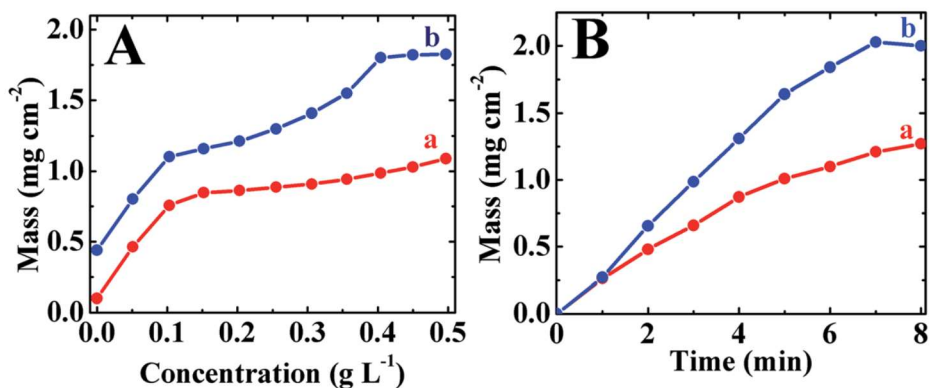


Fig. 11.10 Deposit mass versus (A) CB concentration in suspensions at a deposition time of 5 min and (B) versus deposition time for CB concentration of 0.5 g L<sup>-1</sup> for suspensions of (a) zirconia I and (b) zirconia II at a deposition voltage 20 V.

EPD of oxide nanoparticles can be used for many important applications, utilizing their functional properties. It is expected that similar to DA, the catechol type of CB bonding can result in modification of functional properties of nanomaterials. Moreover,

CB exhibits interesting properties for application in sensors and photovoltaic devices[8, 11]. The use of CB allows cathodic EPD of materials, which offers many processing advantages, compared to anodic EPD. It is in this regard that anodic EPD generates problems related to anodic dissolution of non-noble substrates and chemical instability of some materials in anodic conditions. It is important to note that cathodic electrodeposition is widely used for electroplating of metals, alloys, electrosynthesis of various oxides, quantum dots and other materials. Therefore, further development of cathodic EPD is important for the fabrication of composite materials by combined electrochemical methods. In contrast, anodic electrodeposition has limited utility due to the limited number of materials, which can be deposited using anodic techniques. Especially important is the possibility of cathodic EPD of materials on high surface area non-noble substrates for the development of advanced energy storage devices.

### **11.5 Electrochemical characterization**

Cathodic EPD was investigated for the deposition of  $\text{MnO}_2$  on high surface area Ni plaque substrates for application in electrodes of ECs.

Commercial Ni plaque current collectors, used in this investigation, were designed for high power battery applications[12-14]. In the battery technology, cathodic electrosynthesis is used for the electrochemical loading of the porous Ni plaques with  $\text{Ni(OH)}_2$  active material. However, the electrosynthesis of  $\text{MnO}_2$  for ES and battery applications is usually performed by anodic oxidation[15] of  $\text{Mn}^{2+}$  salts. In this case, difficulties are attributed to the use of high surface area porous Ni plaques, which show

significant dissolution in anodic conditions. This problem can be avoided by the use of cathodic EPD.

Fig. 11.11A shows CVs at different scan rates for the Ni-plaque based electrode prepared by cathodic EPD of MnO<sub>2</sub> nanoparticles (shown in Fig. 11.6). The nearly box shapes of the CVs indicated good capacitive behaviour. It is important to note that box shape CVs were obtained at scan rates as high as 100 mV s<sup>-1</sup>. The current increased with increasing scan rate, indicating good capacitance retention. It should be mentioned that in other investigations, significant deviations from the ideal box shape CVs and poor capacitance retention were observed at high scan rates[16].

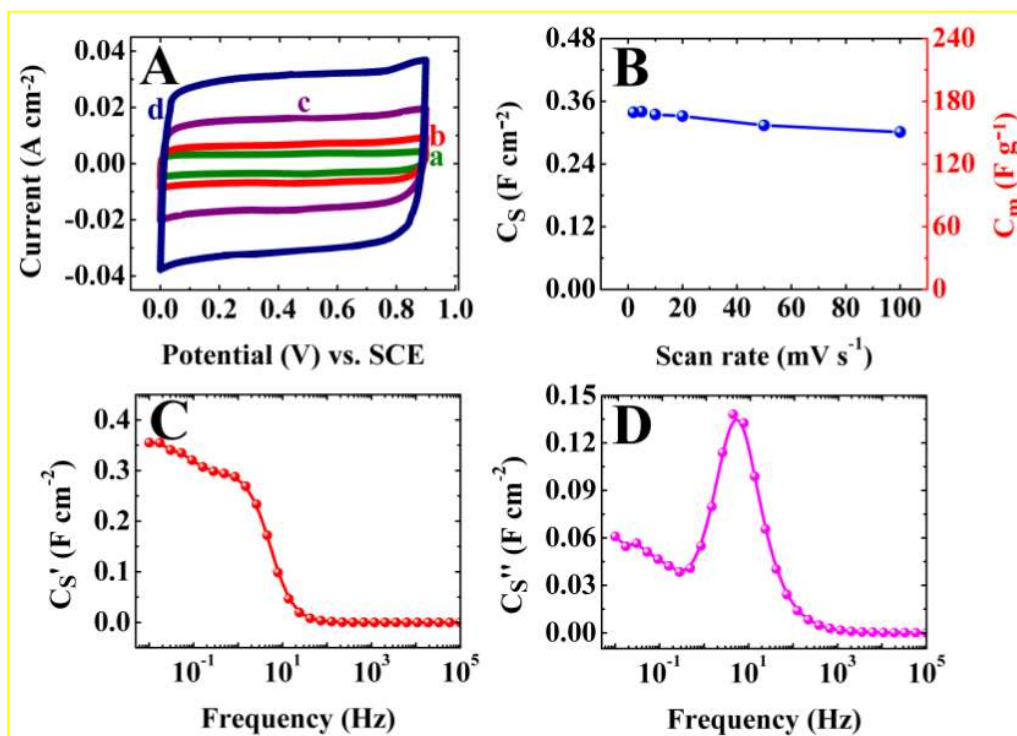


Fig. 11.11 Schematic mechanism of CB adsorption on MnO<sub>2</sub> and hollloysite nanotubes

The MnO<sub>2</sub> electrodes, prepared by cathodic EPD showed (Fig. 11.11B) specific

capacitances of 0.34 and 0.30 F cm<sup>-2</sup> at scan rates of 2 and 100 mV s<sup>-1</sup>, respectively, and excellent capacitance retention of 88.5% in the scan rate range of 2-100 mV s<sup>-1</sup>. For comparison, recent advances in the development of anodic electrodeposition of MnO<sub>2</sub> on 3D porous Ni electrodes showed the highest capacitance of 121.6 mF cm<sup>-2</sup>. The higher capacitance achieved in our investigation indicates that cathodic EPD is a promising technique for the fabrication of ES electrodes. It is important to note that the deposition rate of EPD is typically by 1-2 orders of magnitude higher, compared to the deposition rate of the electrodeposition process [9].

Fig. 11.11 C, D show frequency dependencies of the components of complex capacitance, calculated from the impedance data. The dependencies showed relaxation type dispersion[17], as indicated by the fast reduction in C' with frequency in the range of 0.7-10 Hz and related maximum in the frequency dependence of C'' at ~8 Hz. The relatively high relaxation frequency, corresponding to the C'' maximum (Fig. 11.11D) and good capacitance retention at high scan rates (Fig. 11.11B) indicated that the electrodes, prepared by cathodic EPD are promising for the development of high power ECs. The good electrochemical performance was achieved due to the use of cathodic EPD and good dispersion of MnO<sub>2</sub> nanoparticles, which allowed good electrolyte access to the MnO<sub>2</sub> surface. It is expected that CB can be efficiently used for the EPD of other functional materials for various applications.

Specific capacitance, C' and C'' in Fig. 11.11 B, C and D exhibit a good retention of the electrode and the lowest value can even be above 150 F g<sup>-1</sup>, indicating that the electrodes, prepared by cathodic EPD are promising for the development of high power ECs[18].

## 11.6 Conclusions

CB showed strong adsorption on surfaces of different materials. The adsorption mechanism involved the interactions of the OH groups of the catechol ligand of CB and metal atoms on the particle surface. The adsorbed CB allowed efficient particle dispersion and imparted a positive charge for cathodic EPD. The strong CB adsorption was critical for efficient dispersion, which was achieved at low CB concentrations. This new finding opens a new and promising strategy for EPD of various materials, such as TiO<sub>2</sub>, MnO<sub>2</sub>, Mn<sub>3</sub>O<sub>4</sub>, and other materials using CB as universal dispersing agent. The results indicated that CB can be used as a co-dispersant for the EPD of various materials and fabrication of composite films. CB can be used as efficient dispersing agent for synthesis of nanoparticles. The method developed in this investigation can be used for the EPD of nanoparticles on high surface area metallic substrates. EPD of MnO<sub>2</sub> nanoparticles on commercial Ni plaques allowed the fabrication of efficient electrodes for ECs, which showed high capacitance and excellent capacitance retention at high charge– discharge rates. The method, developed in this investigation can be used for the EPD of other functional nanomaterials and composites for advanced applications.

Yangshuai Liu has the major contribution to this work, Dr. Igor Zhitomirsky also contribute to this work, Mustafa Ata has contribution on providing Mn<sub>3</sub>O<sub>4</sub> nanoparticles, Kaiyuan Shi has contribution on SEM characterization, Dr. Guozhen Zhu and Dr. Gianluigi. A. Botton also have contribution on TEM characterization to this work.

## References

- [1] G.M. Jacob, Q.M. Yang, I. Zhitomirsky, Electrodes for Electrochemical Supercapacitors, *Materials and Manufacturing Processes*, 24 (2009) 1359-1364.
- [2] H. Ohshima, Dynamic electrophoretic mobility of a soft particle, *Journal of Colloid and Interface Science*, 233 (2001) 142-152.
- [3] K. Kimura, S. Takashima, H. Ohshima, Molecular Approach to the Surface Potential Estimate of Thiolate-Modified Gold Nanoparticles, *The Journal of Physical Chemistry B*, 106 (2002) 7260-7266.
- [4] I.A. Jankovic, Z.V. Saponjic, M.I. Comor, J.M. Nedeljkovic, Surface Modification of Colloidal TiO<sub>2</sub> Nanoparticles with Bidentate Benzene Derivatives, *The Journal of Physical Chemistry C*, 113 (2009) 12645-12652.
- [5] S. Tunesi, M.A. Anderson, Surface effects in photochemistry: an in situ cylindrical internal reflection-Fourier transform infrared investigation of the effect of ring substituents on chemisorption onto titania ceramic membranes, *Langmuir*, 8 (1992) 487-495.
- [6] I. Mohammed-Ziegler, F. Billes, Vibrational spectroscopic calculations on pyrogallol and gallic acid, *Journal of Molecular Structure: THEOCHEM*, 618 (2002) 259-265.
- [7] B. Catikkas, E. Aktan, Z. Seferoglu, DFT, FT-Raman, FTIR, NMR, and UV-Vis studies of a hetarylazo indole dye, *International Journal of Quantum Chemistry*, 113 (2013) 683-689.
- [8] S. Yadav, C. Lal, Optimization of performance characteristics of a mixed dye based photogalvanic cell for efficient solar energy conversion and storage, *Energy Conversion*

and Management, 66 (2013) 271-276.

[9] I. Zhitomirsky, Cathodic electrodeposition of ceramic and organoceramic materials. Fundamental aspects, *Advances in Colloid and Interface Science*, 97 (2002) 277-315.

[10] S.-F. Chin, S.-C. Pang, M.A. Anderson, Material and Electrochemical Characterization of Tetrapropylammonium Manganese Oxide Thin Films as Novel Electrode Materials for Electrochemical Capacitors, *Journal of the Electrochemical Society*, 149 (2002) A379-A384.

[11] A. Noorbakhsh, A. Salimi, Amperometric detection of hydrogen peroxide at nano-nickel oxide/thionine and celestine blue nanocomposite-modified glassy carbon electrodes, *Electrochimica Acta*, 54 (2009) 6312-6321.

[12] V.I. Chani, Q. Yang, D.S. Wilkinson, G.C. Weatherly, Effect of substrate pre-coating on adhesion of sintered nickel plaques for electrode application in rechargeable batteries, *Journal of Power Sources*, 142 (2005) 370-381.

[13] E. Cormier, E.B. Wasmund, L.V. Renny, Q.M. Yang, D. Charles, A new powder morphology for making high-porosity nickel structures, *Journal of Power Sources*, 171 (2007) 999-1009.

[14] A.Y. Zaitsev, D.S. Wilkinson, G.C. Weatherly, T.F. Stephenson, The preparation of highly porous structures from filamentary nickel powders, *Journal of Power Sources*, 123 (2003) 253-260.

[15] J. Xiao, S. Yang, L. Wan, F. Xiao, S. Wang, Electrodeposition of manganese oxide nanosheets on a continuous three-dimensional nickel porous scaffold for high performance electrochemical capacitors, *Journal of Power Sources*, 245 (2014) 1027-

1034.

[16] J. Li, Q.M. Yang, I. Zhitomirsky, Nickel foam-based manganese dioxide-carbon nanotube composite electrodes for electrochemical supercapacitors, *Journal of Power Sources*, 185 (2008) 1569-1574.

[17] R. Kötz, M. Carlen, Principles and applications of electrochemical capacitors, *Electrochimica Acta*, 45 (2000) 2483-2498.

[18] Y.Liu, M.S.Ata, K.Shi, G.-Z.Zhu, G.Botton and I.Zhitomirsky, Surface modification and cathodic electrophoretic deposition of ceramic materials and composites using Celestine blue dye, *RSC Adv*, 4 (2014) 29652-29659.

## Conclusions

This dissertation puts main efforts into fabrication of composite materials for ECs electrodes and devices. Many goals have been achieved. New strategies were developed based on electrostatic heterocoagulation in aqueous and non-aqueous suspensions. We demonstrated that PE dispersant can positively charge oxide nanoparticles in ethanol suspension. CS dispersant allowed the formation of stable suspensions of negatively charged MWCNT in ethanol. Well-dispersed MnO<sub>2</sub>-MWCNT composites were obtained by heterocoagulation of positively charged MnO<sub>2</sub> and negatively charged MWCNT. The as-obtained MnO<sub>2</sub>-MWCNT composites are promising materials for application in electrodes of ECs with significantly improved capacitive performance than that of MnO<sub>2</sub>-MWCNT, mixed without dispersants. This concept was also proved applicable in aqueous suspension by utilizing BAC positively charging MWCNT and CA negatively charging MnO<sub>2</sub> particles. The well-dispersed composite electrode exhibited high capacitance and good capacitance retention at high active mass loadings. The asymmetric devices, based on MnO<sub>2</sub>-MWCNT positive electrode and AC-CB negative electrode showed good capacitive behavior in a voltage window of 1.8V. The specific power of 2.67 kW kg<sup>-1</sup> and specific energy 10.2 Wh kg<sup>-1</sup> were achieved.

In this work, we firstly proposed and proved that BiMn<sub>2</sub>O<sub>5</sub> can be used as capacitive material for ES electrode fabrication. BiMn<sub>2</sub>O<sub>5</sub> nanocrystals were successfully prepared by a hydrothermal method. The as-prepared BiMn<sub>2</sub>O<sub>5</sub> – MWCNT composite using CB as dispersant showed very high areal and volumetric capacitance of 6.0 F cm<sup>-2</sup> (540 F cm<sup>-3</sup>)

with good capacitance retention of 75 and 58 % at scan rates of 100 and 200 mV s<sup>-1</sup>, respectively, which indicated that relatively high conductivity and high dielectric constant of BiMn<sub>2</sub>O<sub>5</sub> was beneficial for good capacitive behavior. Asymmetric devices showed maximum energy density of 13.0 Wh L<sup>-1</sup> (9.0 Wh kg<sup>-1</sup>) and maximum power density 3.6 kW L<sup>-1</sup> (2.5 kW kg<sup>-1</sup>) with voltage window of 1.8V.

We found that PAZO exhibits unique adsorption on different materials due to the unique structure of this polymer. The aromatic anionic PAZO monomers, containing chelating salicylate ligands provided multiple adsorption sites for PAZO adsorption on MnO<sub>2</sub> nanofibers, PPy, MWCNT and PPy coated MWCNT and allowed for their efficient electrosteric dispersion and EPD. Testing results showed beneficial effect of PAZO for the dispersion and EPD of advanced ES materials. The results of this investigation paved the way for EPD of other composites utilizing properties of different functional materials and unique physical properties of PAZO.

PAZO thin films prepared by EPD showed photo-induced birefringence by EPD of its thin film on ITO glass, resulting from reversible *trans-cis-trans* photoisomerization of azo groups. We found that PAZO can be used as universal dispersant for various materials such as individual and complex metal oxides, Pd metal, aluminium hydroxide, SiC, MWCNT, PPy and AT. PAZO showed superior performance compared to other dispersing agents for EPD technology, overcoming some of their limitations. It was found that the deposition rate, film microstructure and composition can be varied. The unique adsorption properties of PAZO allowed for EPD of composites, using PAZO as a co-dispersant for different materials. Testing results indicated that EPD methods can be

used for the fabrication of films and coatings, utilizing the unique functional properties of PAZO and other functional materials.

CB was proved as effective dispersant for various materials including  $\text{TiO}_2$ ,  $\text{MnO}_2$ ,  $\text{Mn}_3\text{O}_4$  through cathodic EPD. We found that the strong CB adsorption results from the interactions of the OH groups of the catechol ligand of CB and metal atoms on the particle surface. This adsorption is beneficial for efficient dispersion of oxide particles thus increase their surface area and improve capacitive performance. EPD of  $\text{MnO}_2$  nanoparticles on commercial Ni plaques allowed the fabrication of efficient electrodes for ECs, which showed high capacitance and excellent capacitance retention at high charge–discharge rates.

### **Recommendations**

This work solves many urgent problems, but it's also significant to give suggested guidances for the future works:

1. Devolepment of negative electrodes with higher capacitance utilizing novel materials such as nitrogen enriched activated carbon coating on CNTs or graphene.
2. Investigation of novel  $\text{AMn}_2\text{O}_5$  (A=Y, Yb, etc.) compound materials for higher capacitance.
3. Reduction of particle size for  $\text{BiMn}_2\text{O}_5$  with using novel surfactants during hydrothermal process to enhance its capacitive performance.
4. Establishing of models for capacitance and impedance analysis to optimize the electrodes.

5. Development of supercapacitor modules which are necessary for practical applications.